THE HENRYK NIEWODNICZAŃSKI
INSTITUTE OF NUCLEAR PHYSICS
POLISH ACADEMY OF SCIENCES

Using ALFA Detectors For Studies of the Beam-Related Background at the LHC

Bartosz Dziedzic

Supervisor
Dr. hab. Eng. Krzysztof Korcyl

Co-supervisor
Dr. Rafał Staszewski

A thesis submitted in partial fulfilment of
the requirements for the degree of

Doctor of Philosophy

in

The Henryk Niewodniczański Institute of Nuclear Physics Polish Academy of Sciences

Kraków 2021

Abstract

The thesis concerns the proton beam induced background at the LHC accelerator. The beam induced background originates mainly from the beam interaction with the LHC infrastructure and from scattering within particle bunch.

The measurements of the beam induced background are performed using a dedicated detectors. Such detectors need to be as close to the beam as possible and should allow measurements for each particle bunch separately. At the LHC beam background detectors are placed not closer than 50 mm to the beam core due to mechanical constraints.

The ALFA detector is devoted to elastic scattering measurements in the ATLAS interaction point. Detector elements are placed about 240 m from the interaction point on both sides of the ATLAS experiment. Moreover, they are installed in the so-called Roman Pots allowing insertion of the detectors into the LHC beam pipe, to a distance of a few millimetres from the beam core. These features of the detector allowed the author to formulate the thesis showing that it is possible to measure beam induced background using ALFA detector.

The elastic scattering measurements at the LHC injection energy, i. e. at 900 GeV in the centre-of-mass reference frame, and at special beam optics with $\beta^* = 100$ m were performed in 2018. The special runs were preceded by a number of tests with different collimation settings. To perform the beam induced background measurement there were additional non-colliding bunches injected (not colliding with a bunch from the counter-rotating beam in none of the interaction points). To support the measurements with ALFA, a special module monitoring ALFA trigger signals per bunch was programmed and maintained by the author.

The data analysis was performed for two LHC runs. One with use of the amorphous collimators like during normal LHC operation. The other one was assisted with crystal collimators. It was the first use of the crystal collimators during physics data-taking at the LHC.

The thesis introduces the basics of the beam dynamics and beam control which are essential to understand sources of the beam induced background and its evolution during the run. Detailed description of the detector design including its hardware and data acquisition system are also given. After a detailed introduction, the author presents the process of collecting data and partial results. The last chapter of the thesis author shows the time evolution of the trigger signals during the data-taking. The spatial distribution of the background and its time evolution are also discussed. The results are then compared with the simulations of the particle track spatial distribution, which allowed obtaining more knowledge about the beam induced background mechanisms. As a result the new collimation schemes allowing higher beam induced background reduction were developed.

Streszczenie

Rozprawa porusza problem indukowanego tła wiązki protonowej akceleratora LHC. Indukowane tło wiązki powstaje głównie w wyniku oddziaływania wiązki z infrastrukturą akceleratora oraz w wyniku rozpraszania wewnątrz pakietu protonów.

Pomiary indukowanego tła wiązki protonowej wykonuje się przy pomocy dedykowanych detektorów. Detektor taki musi być umieszczony możliwie blisko wiązki oraz powinien umożliwiać pomiary dla poszczególnych pakietów cząstek (ang. *bunches*). W praktyce detektory są umieszczane w odległościach nie mniejszych niż 50 mm od wiązki LHC, co wynika wprost z budowy akceleratora.

Detektor ALFA powstał w celu pomiaru elastycznie rozproszonych protonów w punkcie oddziaływania eksperymentu ATLAS. Elementy detektora są rozmieszczone po obu stronach punktu oddziaływania w odległości około 240 m. Dodatkowo elementy detektora zostały zainstalowane w tzw. Garnkach Rzymskich (ang. *Roman Pots*) umożliwiających wsunięcie detektorów do rury akceleratora LHC na odległość kilku mm od wiązki. Przedstawione wyżej właściwości detektora pozwoliły autorowi rozprawy postawić tezę że detektor ALFA umożliwia również pomiar indukowanego tła wiązki protonowej.

Pomiary rozpraszania elastycznego przy energii wstrzykiwania wiązki LHC, tj. 900 GeV w układzie środka masy oraz przy specjalnej optyce $\beta^* = 100$ m zostały wykonane w 2018 roku. Poprzedzone były testami przy różnych ustawieniach kolimacji wiązki. W celu przeprowadzenia pomiarów indukowanego tła wiązki protonowej wprowadzono do niej tzw. niezderzające się pakiety, czyli takie, które nie kolidują z pakietami pochodzącymi z drugiej wiązki w żadnym z punktów oddziaływania. Pomiary detektorem ALFA zostały dodatkowo wsparte przez specjalny moduł monitorujący częstotliwości wyzwalania niezależnie dla każdego z pakietów, za którego obsługę i konfigurację odpowiadał autor rozprawy.

Analiza została przeprowadzona dla dwóch tzw. *runów.* W jednym z nich zastosowano kolimatory amorficzne, które są stosowane podczas normalnej pracy akceleratora LHC. W drugim *runie* zastosowano dodatkowo kolimatory kryształowe. Było to ich pierwsze użycie podczas zbierania danych na akceleratorze LHC.

W rozprawie autor wprowadza podstawy dynamiki wiązki protonowej oraz najważniejsze aspekty jej kontrolowania, które są niezbędne do zrozumienia kształtowania się i ewolucji czasowej indukowanego tła wiązki protonowej podczas zbierania danych. Przedstawia również szczegółowy opis budowy detektora oraz przedstawia układy akwizycji danych. Następnie autor przedstawia w jaki sposób zostały zebrane dane wraz z komentarzem do poszczególnych testów kolimacji. W ostatnim rozdziale przedstawiona jest ewolucja czasowa częstotliwości wyzwalania zapisu w detektorach dla wspomnianych wyżej *runów*. Pokazano również rozkład tła oraz jego ewolucję czasową. Wyniki przedstawione w niniejszej rozprawie zostały porównane z symulacjami co pozwoliło na dokładniejsze poznanie mechanizmów powstawania indukowanego tła wiązki. W rezultacie zostały opracowane nowe schematy ustawień kolimacji, które mają pozwolić na dalszą redukcję indukowanego tła wiązki protonowej.

Acknowledgements

This thesis was funded by the Henryk Niewodniczański Institute of Nuclear Physics Polish Academy of Sciences. The author was the beneficiary of KNOW scholarship program. Significant part of work was done at CERN and covered by CERN Subsistence Allowance.

First I would like to thank to my supervisor Dr. hab. Eng. Krzysztof Korcyl and co-supervisor Dr. Rafał Staszewki for their support in the whole time of the PhD studies. Dr. hab. Eng. Krzysztof Korcyl was introducing me into technical stuff and supporting all my detector-related work. Dr. Rafał Staszewski was supporting me with data analysis and physics part of the thesis. Here, a special thanks to Prof. Dr. hab. Janusz Chwastowski who was providing many advices and help during dissertation preparation.

I would also like to thank to the ALFA/AFP community. Especially I would like to mention Dr. Eng. Elżbieta Banaś, Msc. Eng. Jolanta Olszowska and Dr. Maciej Trzebiński who introduced me into CERN life, when I was a new one. They made all technical aspect of the detector operation much easier to understand and they never said “I don’t have time”. Many thanks to Giulio Avoni for his support with all electronics-related jobs. Cooperation with him was always a grate experience and pleasure.

This dissertation couldn’t be written without support from the Collimation Working Group. Naming closest collaborators, acknowledgements to Dr. Roderic Bruce, Dr. Eng. Arkadiusz Gorzawski, Dr. Daniele Mirarchi and Dr. Hector Garcia Morales. They introduced me into basics of beam dynamics and beam collimation at the LHC.

Special thanks to my best friends – Rafał Sowa and Szymon Walosik who were always around in the most difficult moments. They always knew when and how to support me and how to encourage me to work.

Many thanks to all those who I met on the path of writing this thesis and not mentioned here explicitly.

Last, but not least thanks to my better half, Milena. Thank you for your patience, kindness and support. You made the time of preparing the thesis a way easier.

To my parents who have been always supporting me, even though they weren't aware what I am really working on...

Moim rodzicom, którzy zawsze mnie wspierali, nawet jeśli nie do końca wiedzieli czym się zajmuję...

Contents

Introduction

In experimental physics, background is an unwanted contribution to the process being measured. The presence of background determines the quality of data and contributes to the uncertainties of the measurement. The phenomenon of the background is present in many measurements and can have different origin. Typically, it is related to the imperfect experimental system, for example by introducing noise or by its finite resolution. The more complex the measurement apparatus, the more effects can be responsible for the background.

In high energy physics, a great majority of measurements are based on counting events of a given signature. In this case, the events that fulfill the experimental selection but do not originate from the processes of interest are considered as background. Depending on the situation, it might be easy or next-to-impossible to filter out the background events.

One of the main experimental tools in high energy physics are accelerators, like the Large Hadron Collider (LHC) at the European Organisation for Nuclear Research (CERN). During the normal accelerator operation some of the particles are lost from the beam core. Such particles create the so-called beam halo which is repopulated during the whole accelerator run. The background induced by the beam itself, by the accelerator, and its infrastructure is referred to a beam-induced or machine-induced background. In many measurements, the beam-induced background is negligible. However, for others, in particular for the measurements of elastic scattering at very low angles, it can be the most important source of the background. In fact, it may even lead to the dominant contribution to the final uncertainty of the measurement.

High level of beam-induced background is also correlated with the ionizing radiation surrounding the beam pipe. This is very dangerous to the superconducting magnets, which may undergo a quench – a sudden loss of their superconducting properties. The increased ionizing radiation may also cause failures of the electronics located in the accelerator area.

The consequences mentioned above lead to one conclusion: the necessity of minimizing the beam-induced background. The first approach is to build a dedicated shielding surrounding the beam pipe, which is able to absorb high doses of radiation. Solid absorbers are very robust to radiation, but due to relatively high distance from the beam core – few tens of centimetres – these are used mainly downstream to the experiments to absorb the collision products, at the injection point and in the beam extraction region, where the beam might be missteered. Another way, more sophisticated and more precise is using the movable absorbers – collimators. These devices, containing movable jaws, are able to move to a few mm from the beam core enabling the possibility of precise control of the beam-induced background. In case of the LHC there are 88 collimators of different type and purpose installed. Efficient usage of the collimators requires a detailed knowledge of the beam-induced background distribution.

There exists a number of methods allowing the background determination. First, one can use dedicated detectors. In case of the LHC, these are Beam Loss Monitors. It is a set of about 4000 radiation counters spread along the LHC tunnel and installed as close to the beam pipe as possible. Moreover, each experiment at the LHC has its own subsystems dedicated to measurements of the intensity of the beam halo.

In case of the ATLAS Experiment the Beam Condition Monitor equipped with diamond metallized sensors with high time resolution are installed very close to the beam – at a distance of a few centimetres. The time resolution of the order of nano seconds allows measurement of the halo particles incoming to the interaction point and distinguishing them from the collision products. ATLAS was also equipped with the Diamond Beam Monitor. It is a pixel tracking detector allowing measuring the luminosity and the background spatial distribution.

The present thesis exploits the ATLAS-ALFA detectors for beam halo measurements. This has two advantages. First, ALFA detectors operate very close to the beam and can provide unique information about the rate and spatial distribution of the beam halo and the time evolution of these quantities. This is possible because ALFA is a tracking detector. Second, small beam halo is crucial for the physics program of the ALFA detectors. Therefore, it is vital to monitor the beam-induced background during the data-taking to be able to quickly evaluate the quality of the data. This is possible due to a dedicated ALFA trigger module, which monitors and stores trigger rates separately for each LHC bunch crossing. In addition, precise measurements of background can help understanding its source and finding ways to reduce it in the future. These facts allow the author to formulate the thesis of the present work. Namely, that the ALFA detectors can be used to monitor background in ATLAS experiment using non-colliding bunch.

The analysis presented in this thesis is based on a special LHC run taken in 2018 with ALFA detectors inserted. The data were collected with different collimation settings and injected non-colliding bunches. The author supervised the data-taking process himself and was also responsible for the maintenance of the detector during the year 2018, including the commissioning after the winter shutdown and periodic detector condition checks.

The thesis is organised as follows. Chapter 1 introduces the general information related to the CERN organisation, ATLAS experiment and data acquisition basics. In Chapter 2 the ALFA detector and its scientific programme are introduced. The next two Chapters (3 and 4) introduce the basics of the beam optics and collimation. Chapter 5 is devoted to the trigger and data acquisition of the ALFA detector. The description is focused on the features allowing the use of the ALFA detector as a monitor of the beam-induced background reduction. The following two Chapters (6 and 7) are devoted to the data-taking and analysis of those data. After Chapter 7 a short summary and conclusions coming from this thesis are given.

Chapter 1

General Information

High energy physics, called also particle physics, is a field of sciences focused on the constituents of matter and their fundamental interactions occurring in the Universe. A valuable source of information about elementary particles is cosmic radiation. Although such particles have very high energy – the highest registered energy of a cosmic particles exceeded $E \approx 10^8$ TeV – the lack of knowledge of initial conditions and a large variety of the registered energies makes a precise determination of the particle parameters difficult, which leads to high uncertainties [1]. Another way to study physics of the elementary particles is colliding them using the accelerators.

Large Hadron Collider (LHC) [2] allows acceleration of particle beams up to 6.5 TeV and bringing them to head-on collisions at the centre-of-mass energy of 13 TeV. This results in well defined initial conditions and with high statistics experimental data [3] enables very precise measurements.

Modern high energy physics demands constant improvements of the accelerators which in turn requires a strong cooperation between scientists and engineers of various fields. Examples of such improvements and their impact on the collected data are also discussed within this thesis pointing that the LHC is a great testing ground for modern technologies and motivation to develop new ones, satisfying higher and higher ambitions of physicists.

1.1 CERN

The European Organization for Nuclear Research (CERN)[1] is the biggest laboratory for high energy physics in the world and is located in Geneva surroundings. One of the main goals of scientists at CERN is to study the Standard Model (SM) of particle physics and test its predictions. However, as the SM describes only about 4% of the Universe, efforts at CERN are also directed towards on the dark matter and antimatter research, searches for supersymmetry and many more.

---

[1] CERN - *french: Conseil Européen pour la Recherche Nucléaire*

During its many years of history, CERN has built a large complex of accelerators. Presently the leading one is the Large Hadron Collider – LHC [2], see Fig. 1.1.

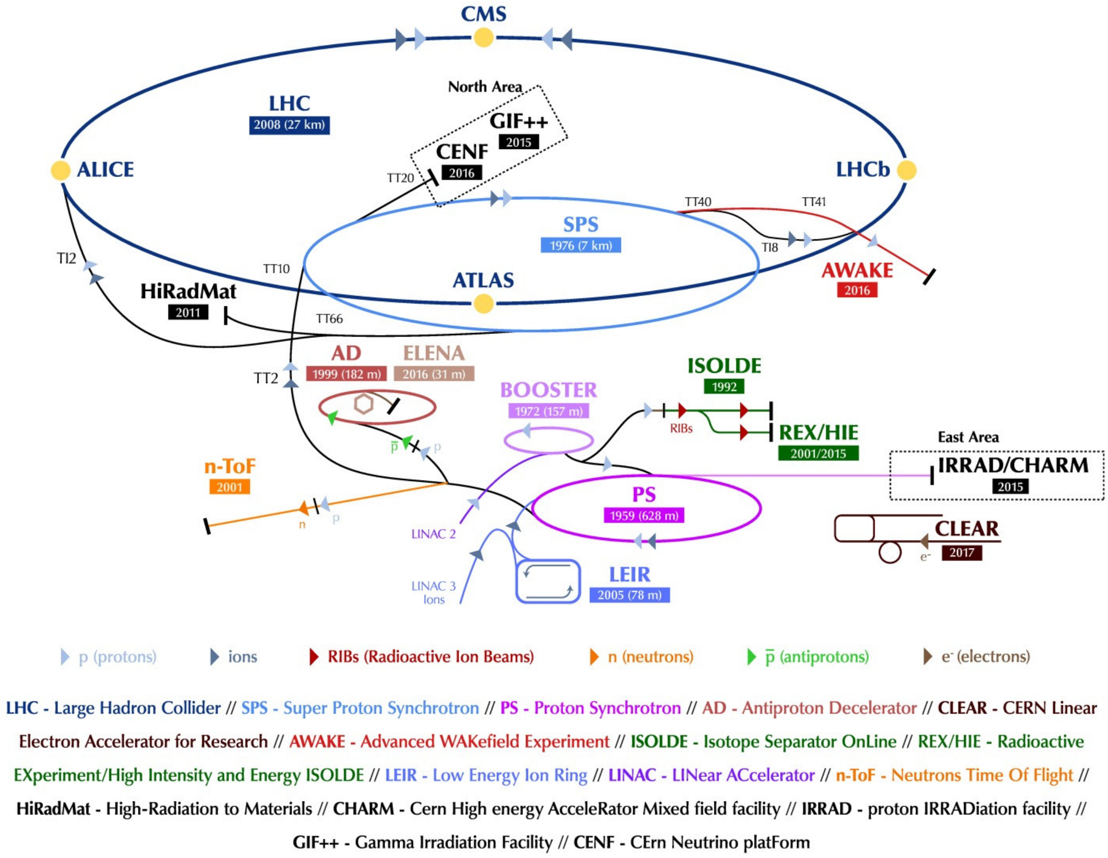

Figure 1.1: Sketch of the accelerator complex at CERN [4].

A variety of accelerators and scientific infrastructure offers a possibility to perform a wide spectrum of research ranging from elementary particle physics, through nuclear, atomic, and solid state physics to medical research, innovative technology, and engineering to applications. One should notice that the complexity of modern accelerators requires a strong cooperation of engineers of various fields from civil engineering through electrotechnics, electronics, IT, to advanced mechanics and cryogenics. Many of technologies developed at CERN for purely scientific purposes have plenty of applications. For example the pixel detectors were adopted among others for medical apparatus (Medipix) [5].

As the electronic parts in high energy physics experiments often have to work in environment with high radiation, the development of their radiation-hard versions is essential. Radiation hard electronics is widely applied in aerospace technologies – from planes, to artificial satellites and space probes deployed in the deep space research missions. As the CERN accelerator complex is a huge vacuum and cryogenics installation, those fields are also well developed. This includes also technologies related to high-current power converters and superconducting technologies.

1.2 LHC

Technically, the Large Hadron Collider is a storage ring with two counter-rotating beams. Its circumference is 26 659 m and the machine is located in a tunnel around 50-175 m underground [2]. A storage ring is a type of synchrotron optimised to store the beams for a long time [6].

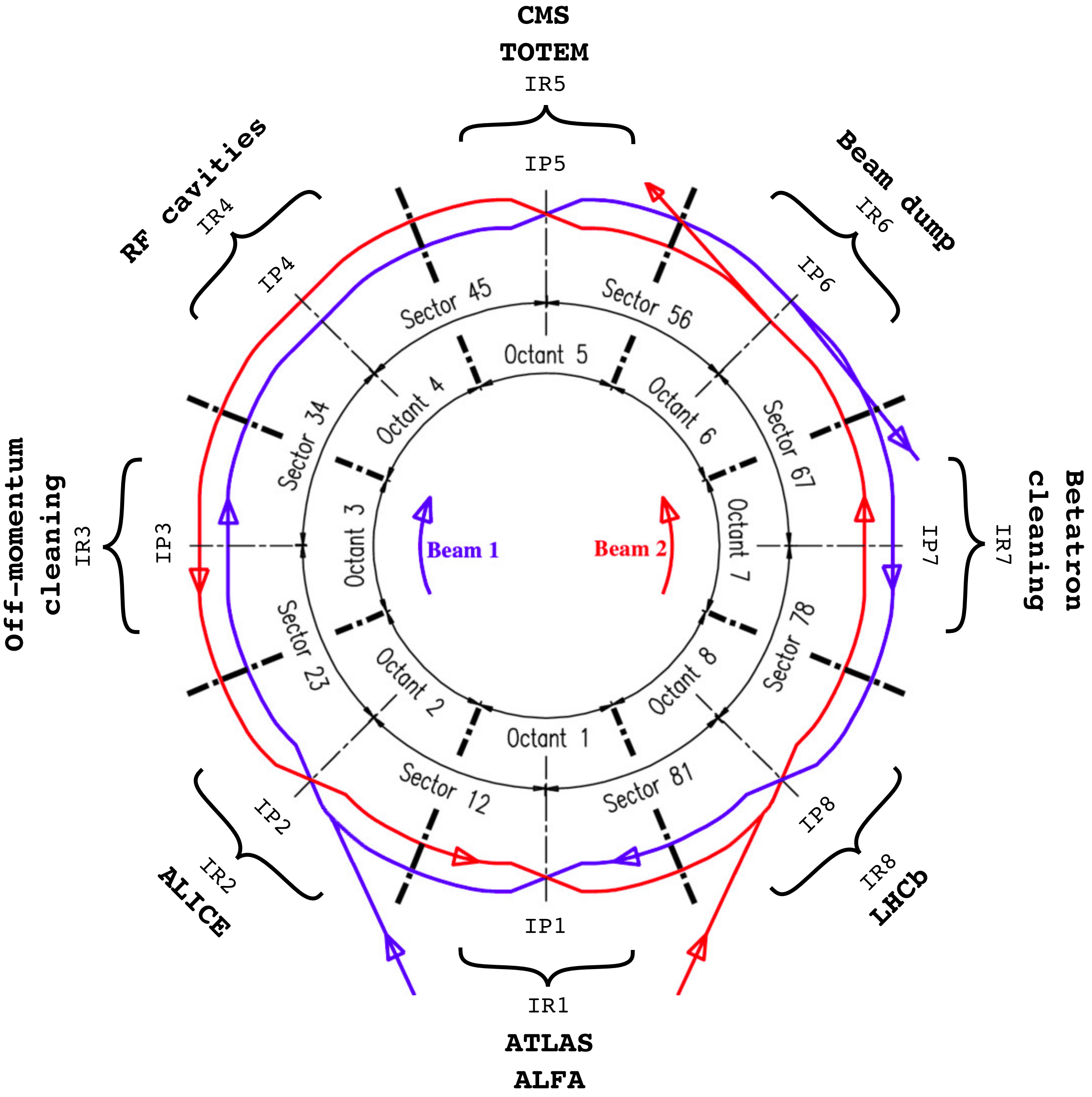

Figure 1.2: LHC layout [7].

The general layout of the LHC is presented in Fig. 1.2. The LHC ring is divided into eight sections called octants. In the centre of each octant there is a straight section called the Insertion Region (IR). Its centre is called a Point followed by its number. Each Point is devoted to a special collider facility or an experiment, see Table 1.1. Between the Points there are sectors which are named after the Point numbers, i. e. the Sector 12 is located between Point 1 (P1) and Point 2 (P2).

Table 1.1: The facilities in eight points around the LHC ring and their functionalities.

Point	**Facility**	**Description**
P1	ATLAS/LHCf	A Toroidal Large ApparatuS/LHC-forward
P2	ALICE	A Large Ion Collider Experiment
P3	Off-momentum cleaning	Off-momentum particle removal
P4	RF	Radio Frequency Cavities
P5	CMS/TOTEM	Compact Muon Solenoid/Total Cross Section, Elastic Scattering and Diffraction Dissociation
P6	Dump	Beam dumping system
P7	Betatron cleaning	Beam betatron cleaning
P8	LHCb/MoEDaL	LHC-beauty/Monopole and Exotics Detector at the LHC

The LHC was designed to reach unprecedentedly high centre-of-mass energy with high beam intensities. The designed parameters are summarized in Table 1.2 and details related to the beam parameters are discussed in Chapter 3.

Table 1.2: LHC beam parameters relevant for the peak luminosity [2].

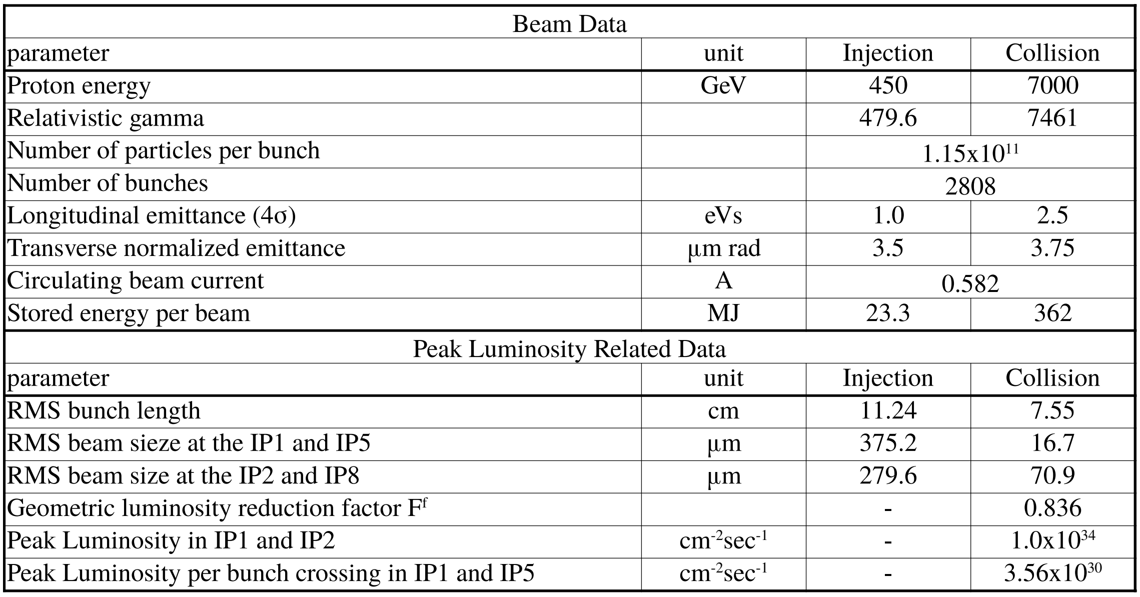

Beam Data			
parameter	unit	Injection	Collision
Proton energy	GeV	450	7000
Relativistic gamma		479.6	7461
Number of particles per bunch		1.15×10^{11}	
Number of bunches		2808	
Longitudinal emittance (4σ)	eVs	1.0	2.5
Transverse normalized emittance	μm rad	3.5	3.75
Circulating beam current	A	0.582	
Stored energy per beam	MJ	23.3	362
Peak Luminosity Related Data			
parameter	unit	Injection	Collision
RMS bunch length	cm	11.24	7.55
RMS beam sieze at the IP1 and IP5	μm	375.2	16.7
RMS beam size at the IP2 and IP8	μm	279.6	70.9
Geometric luminosity reduction factor F^f		-	0.836
Peak Luminosity in IP1 and IP2	$cm^{-2}sec^{-1}$	-	1.0×10^{34}
Peak Luminosity per bunch crossing in IP1 and IP5	$cm^{-2}sec^{-1}$	-	3.56×10^{30}

It is worth mentioning that some of the parameters of the LHC accelerator, were improved during the LHC Run 2 operation period (from 5th of April 2015 until 3rd of December 2018). On basis of the LHC measured performance the operation parameters were optimized to improve the beam quality and reduce the background. These parameters are listed in Table 1.3. More details about the LHC performance during Run 2 can be found in [3].

To reach the top energy of 13 TeV, a multi-stage accelerating system is required.

Table 1.3: The main LHC parameters obtained within Run2 [8].

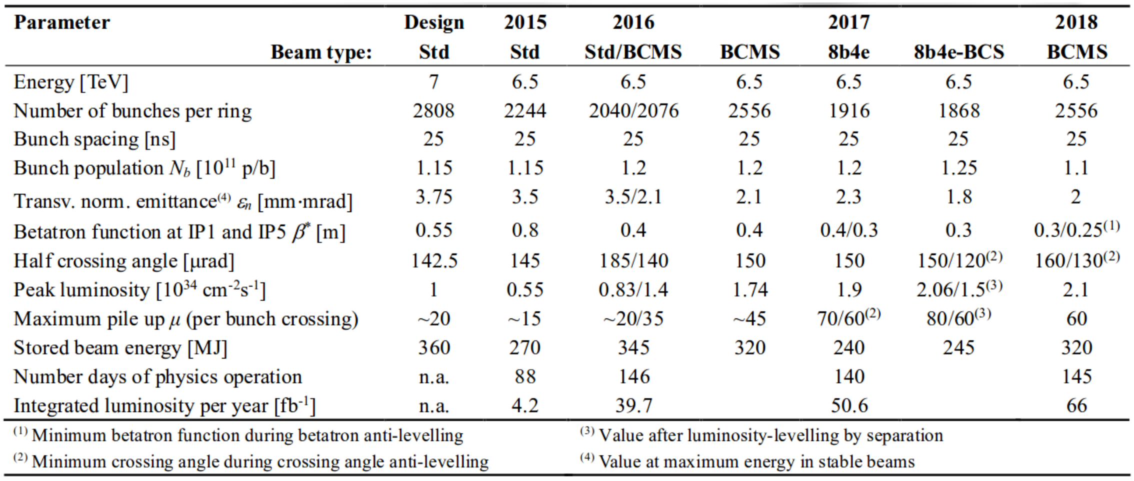

Parameter	**Design**	**2015**	**2016**		**2017**		**2018**
Beam type:	**Std**	**Std**	**Std/BCMS**	**BCMS**	**8b4e**	**8b4e-BCS**	**BCMS**
Energy [TeV]	7	6.5	6.5	6.5	6.5	6.5	6.5
Number of bunches per ring	2808	2244	2040/2076	2556	1916	1868	2556
Bunch spacing [ns]	25	25	25	25	25	25	25
Bunch population N_b [10^{11} p/b]	1.15	1.15	1.2	1.2	1.2	1.25	1.1
Transv. norm. emittance(4) ε_n [mm·mrad]	3.75	3.5	3.5/2.1	2.1	2.3	1.8	2
Betatron function at IP1 and IP5 β^* [m]	0.55	0.8	0.4	0.4	0.4/0.3	0.3	0.3/0.25(1)
Half crossing angle [μrad]	142.5	145	185/140	150	150	150/120(2)	160/130(2)
Peak luminosity [10^{34} cm^{-2}s^{-1}]	1	0.55	0.83/1.4	1.74	1.9	2.06/1.5(3)	2.1
Maximum pile up μ (per bunch crossing)	~20	~15	~20/35	~45	70/60(2)	80/60(3)	60
Stored beam energy [MJ]	360	270	345	320	240	245	320
Number days of physics operation	n.a.	88	146		140		145
Integrated luminosity per year [fb^{-1}]	n.a.	4.2	39.7		50.6		66

(1) Minimum betatron function during betatron anti-levelling

(2) Minimum crossing angle during crossing angle anti-levelling

(3) Value after luminosity-levelling by separation

(4) Value at maximum energy in stable beams

All accelerators taking part in the pre-acceleration of particles for the LHC are shown in Fig. 1.1.

The protons to be accelerated originate from hydrogen. First, hydrogen molecules are placed in a strong electric field, where they are stripped from electrons. Then they are accelerated by the linear accelerator LINAC2 up to energy of 50 MeV. The beam from LINAC2 is then injected into the Proton Synchrotron Booster (PSB) where the protons are accumulated inside the four accelerator rings. Once the protons reach the energy of 1.4 GeV, they are injected into the Proton Synchrotron (PS).

The PS, in addition to acceleration, forms the final bunched structure and strongly influences the LHC performance [9]. Each bunch contains a defined number of particles. In the PS the transition energy of 5.7 GeV the is achieved. It is the energy above which the protons act more like relativistic than classical objects and hence different machine settings must be provided [10]. Finally, the beam in the PS reaches its top energy of 26 GeV [11] and is transferred to the Super Proton Synchrotron (SPS).

In the SPS the protons are accelerated to 450 GeV and then injected into the LHC. There are two transfer lines between the SPS and the LHC allowing an injection of the clockwise (Beam 1) and anticlockwise (Beam 2) circulating beams. After the injection each bunch position is well defined and referred to using its identifier number – Bunch Crossing Identifier (BCID). Not all of the BCIDs are filled with particles – those which are not filled are called empty bunches.

The LHC magnet system contains about 9.5 thousands magnets – main bending dipoles, quadrupoles, field correctors and septum and kicker magnets that are used for the beam injection/extraction [2].

The system contains so-called warm magnets operating at the room temperature and superconducting ones operating in cryogenic temperatures – cold magnets. The use of the superconducting magnets is essential for the bending and focusing magnets in order to provide high enough magnetic field and to keep the beams on the trajectories designed for the LHC. Superconducting magnets are operated at temperatures between 1.8 K and 4.5 K. The nominal magnetic field in the dipole magnets at the maximum energy reaches 8.33 T.

1.3 ATLAS

The ATLAS (A Toroidal LHC ApparatuS) collaboration was established in the Spring of 1992. The ATLAS detector is a general purpose detector devoted to registering a wide spectrum of particles of various masses and transverse momenta p_T [12, 13]. It is a modular detector containing several sub-systems focused on different aspects of particle detection. Its size is 25 m in diameter, 44 m in length and the mass of about 7000 tones. Detector contains about 100 millions readout channels. Its design is presented in Fig. 1.3.

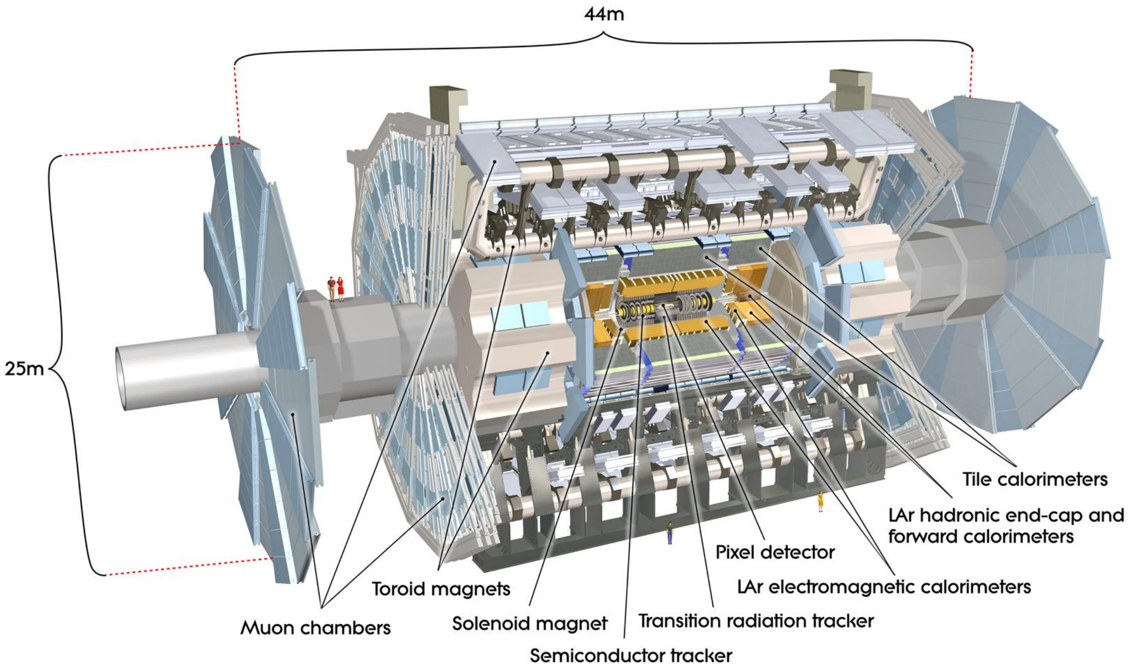

Figure 1.3: The ATLAS experiment.

ATLAS as a general purpose detector can provide a huge amount of data allowing observation of elementary particles of different types. The complexity of ATLAS and its high precision tracking system enables precise determination of particle properties and finally studies of many interactions occurring in proton-proton or heavy ion collisions. The main aim of the ATLAS design was to find the Higgs boson – the last missing element of the Standard Model, which discovery was announced in 2012 [14].

High luminosity provided by the LHC allows investigation of very rare processes and search for the so-called exotic particles. Complicated analysis of the unprecedented amount of data allows tests of the electro-weak symmetry breaking and of Quantum Chromodynamics (QCD) as well as searches for the Beyond Standard Model (BSM) phenomena.

1.3.1 ATLAS Sub-detectors

The ATLAS detector consists of several subdetectors, among them: the inner detector, the electromagnetic and hadronic calorimeters and the muon spectrometer [12].

Inner detector (ID) contains pixel spectrometer (Pixel/IBL), the SemiConductor Tracker (SCT) and Transition Radiation Tracker (TRT). It is submerged in the solenoidal magnetic field of 2 T. The main task of the inner detector is the measurement of the charged particle transverse momentum p_T from a precise reconstruction of its track accompanied by a simultaneous determination of the interaction vertex location. Total size of ID is 2.1 m in diameter and 6.2 m in length.

The closest to the beam line is the Insertable B-layer (IBL) [15] – the innermost layer of the Pixel detector [16] installed 33 mm from the beam center. The next two layers are installed at a distance of 88.5 and 122.5 mm from the beam. The pixel size is 50×200 μm^2. It is surrounded by the SCT [17] – a silicon strip detector containing about 6.3 million readout channels. Each strip is 64 mm long, and 80 μm wide. The TRT [18] tracker encompasses the SCT and is build out of straw tubes filed with xenon-based gas mixture and acting as drift chambers. In the central part of the TRT there are straw tubes parallel to the beam line and each of them is 140 cm long and 4 mm in diameter. In the forward direction, the straw tubes are 37 cm long and are set up in wheels radially to the beam. The TRT has 351 thousands readout channels.

Electromagnetic calorimeter (Liquid Argon electromagnetic calorimeter or LAr electromagnetic calorimeter) is suited for precision measurements of electrons and photons [19]. It consists of three parts – the barrel and two end-caps. LAr construction exploits the so-called accordion geometry. The lead absorbers and copper electrodes are shaped like the accordion waves to cover full azimuthal angle, without any cracks. The shapes of the waves vary to hold the liquid argon (LAr) gap between them constant. The calorimeter consist of about 173 thousand readout channels.

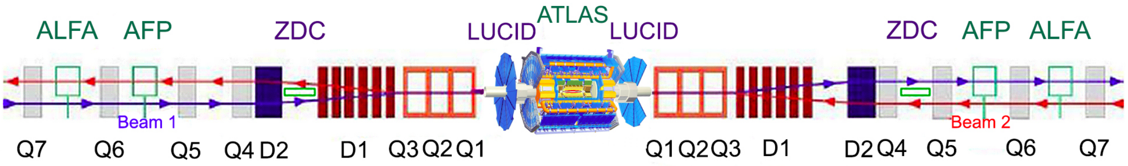

Figure 1.4: Location of the forward detectors around P1. [21]

Hadronic calorimeter contains three parts – the tile calorimeter, Liquid Argon hadronic end-cap calorimeter and LAr forward calorimeter (FCal) [19]. LAr hadronic end-cap calorimeter is located behind the LAr electromagnetic end-cap calorimeter. The Forward Calorimeter is installed between the beam pipe and the end-cap. FCal consists of three modules. The first one, closest to the IP, uses copper absorber plates and is optimised for electromagnetic measurements. The next two modules use tungsten absorber and serve as a hadronic calorimeter.

The tile calorimeter is made of scintillating tiles interleaved with steel absorber plates. Each tile is readout by two photomultipliers connected to the opposite sides of the tile via wavelength shifting fibres. The calorimeter consists of the central barrel part, 5.8 m in length, surrounding the LAr electromagnetic calorimeter, and two extended barrels, each 2.6 m in length, surrounding the end-cap calorimeters. Its external diameter is 8.5 m. The tile calorimeter is made of 25 mm and 50 mm copper plates (absorber) interleaved with 8.5 mm LAr gaps providing an active medium for the calorimeter. The total number of channels is 12248.

Muon spectrometer is built out of different types of muon chambers. It also contains three superconducting air-core toroid magnets [20]. It is devoted to precise tracking of muons which trajectories are bent in the magnetic field of two toroidal magnets. Monitored Drift Tubes (MDT) and Cathode Strip Chambers (CSC) are responsible for precise tracking. The Resistive Plate Chambers (RPC) and Thin Gap Chambers (TGC) deliver the trigger signals, identify the bunch-crossing, provide the p_T thresholds. The total amount of muon channels is about 1 million.

The ATLAS detector consists also of forward detectors – ALFA, AFP, LUCID and ZDC. Their locations are presented on the scheme in Fig. 1.4.

As this thesis is related to the data collected by the ALFA detector, Chapter 2 describes it in more details.

The Luminosity Cherenkov Integrating Detector (LUCID) is a detector dedicated to the online monitoring of luminosity with precision of ∼2-3 % [22]. The LUCID consists of twenty 1.5 m long tubes with a diameter of 15 mm and filled-in with C_4F_{10} gas. The Cherenkov radiation thresholds are 2.8 GeV for pions and 10 MeV for electrons. There are two sets of tubes installed symmetrically about 17 meters from the IP.

The Zero Degree Calorimeter (ZDC) is devoted to the forward neutron detection in heavy-ion collisions (lead-lead) [13]. Its main role is the collision centrality determination. The ZDC consists of four modules – one electromagnetic and three hadronic ones – installed on the each side of the IP at a distance of 140 m. They are installed inside of the Target Absorber Neutral (TAN, see Chapter 4.8).

The ATLAS Forward Proton (AFP) is a Silicon Tracker (SiT) based forward detector devoted to the measurement of the trajectory of protons scattered in diffractive processes [23]. The measurements can be used to reconstruct the scattered proton four-momentum. AFP uses the Roman Pot technology allowing for a horizontal insertion of the detectors into the beam pipe (in the accelerator plane). There are two detector stations on each side of the ATLAS IP. The near detector is located 206 m from the ATLAS IP, while the far one at the distance of 216 m.

The Minimum Bias Trigger Scintilator (MBTS) delivers primary triggers for selecting events from real LHC collisions with the smallest bias for the low luminosity LHC runs [24, 25]. The MBTS is an octagonal-shape detector placed 3.6 m from the ATLAS IP, on the inner face of the end-cap calorimeter. It consists of 16 plastic scintillators organized in two rings – inner (153-426 mm from the beam center) and outer one (426-890 mm).

The Beam Conditions Monitor (BCM) consists of two stations with four modules [26]. Each module contains two diamond sensors readout in parallel. The sensors are located 184 cm from the ATLAS IP and 55 mm from the beam core. A nanosecond scale time resolution allows distinguishing the beam halo from the collision products. It is devoted to measurements of the luminosity bunch-by-bunch and to detection of potential increase of the beam halo.

The Diamond Beam Monitor (DBM) was designed as an upgrade of the BCM giving additional capability of tracking features [27]. Its purpose is the bunch-by-bunch luminosity measurement and beam position monitoring. There are four DBMs on each side of the ATLAS IP in a distance of 1 m. The distance between DBMs and the beam core is 7 cm. Each DBM contains three modules stacked one behind the other one. Thus, it is capable of tracking the particles.

1.3.2 ATLAS TDAQ

The LHC collides proton bunches filled with $\sim 10^{11}$ protons each, almost every 25 ns. In each bunch collision, several proton-proton interactions may occur – the so-called pile-up in the Run 2 reached the mean value of around 37 and peaked up to about 70 individual interactions [3]. This translates into billions of interactions per second. The cross sections of some rare but interesting processes are presented in

Fig. 1.5. In case of rare processes, like Higgs boson production, interesting physics phenomena may happen every minute. Thus, a sophisticated filtering mechanism must be implemented to not miss the interesting interactions. In case of the ATLAS Trigger and Data Acquisition system (TDAQ), the final recorded event rate reached 1.2 kHz in the operation during 2018 [28].

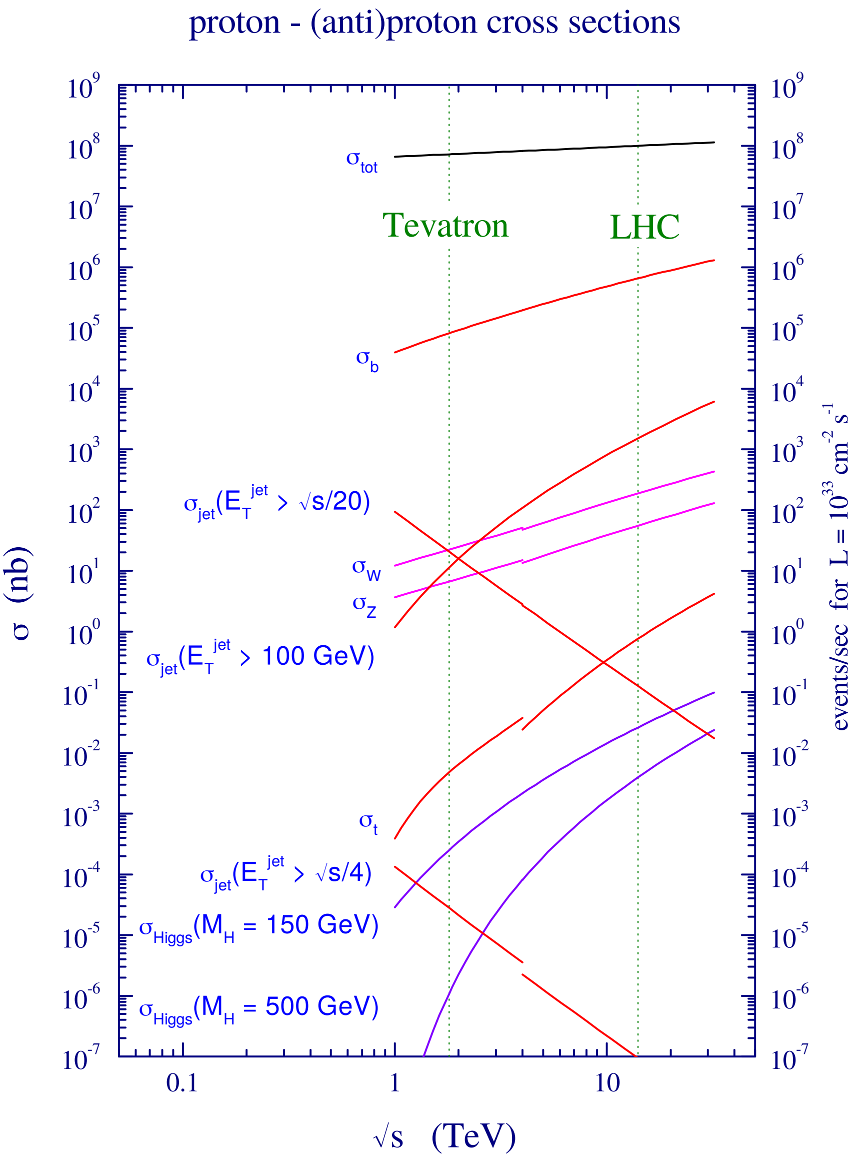

Figure 1.5: Proton-(anti)proton cross section diagram [29].

In the ATLAS experiment the trigger selects the bunch crossing BCX (identified with Bunch Crossing Identifier counted as a sequential number from the LHC start cycle (orbit signal)) which might be worth further analysis, while the data acquisition (DAQ) part of the system is responsible for the assembly of the data fragments recorded by sub-detectors for the selected BCID and for the transfer of these data to subsequent stages of the trigger system up to the permanent storage.

The scheme of the ATLAS TDAQ system is presented in Fig. 1.6. There are two main stages comprising the ATLAS trigger: the Level-1 Trigger and the High Level Trigger (HLT).

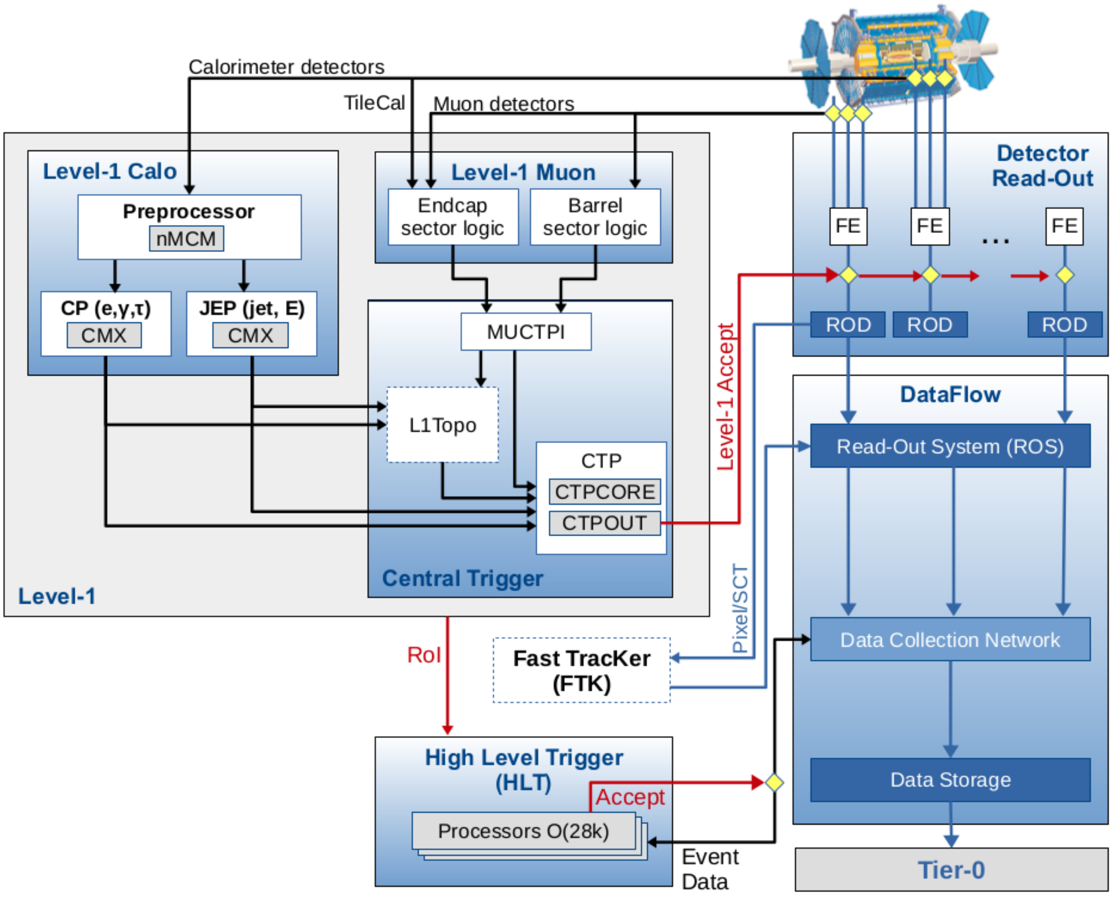

Figure 1.6: ATLAS TDAQ Scheme [30].

The Level-1 trigger is based on custom electronics which is highly optimized for execution of selection algorithms and its operation is fully synchronized with the LHC clock. The HLT executes the selection algorithms at a dedicated computing farm under control of Linux operating system and TDAQ infrastructure processes. The Level-1 trigger consists of three main parts. The Level-1 Calo (L1Calo) and the Level-1 Muon (L1Muon) correlates the trigger signals from the calorimeters and the Muon Spectrometer, respectively. At this stage also the pre-scaling of the selection signatures is performed. It is an algorithm reducing the event rate by rejection a defined fraction of events.

The third part is the Central Trigger which receives the trigger signals from the previously mentioned two blocks. The Central Trigger Processor (CTP) receives signals from the L1Calo directly and signals from the L1Muon via the Muon-to-CTP Interface (MUCTPI). The CTP combines them with signals from the topological processor (L1Topo) and generates the final decision at the first level. The Level-1 Accept (L1A) signal is generated if the referred BCID has passed the selection criteria and was still valid after pre-scaling. The lack of the L1A signal means that the decision is negative and the data registered for this BCID are not interesting and might be dropped. The dropped data are permanently lost.

During the time spent by the trigger system on processing the data, the information recorded by sub-detectors is temporarily stored – pipelined – in the Front-End electronics (FE) and waiting for the L1A acceptation signal from the CTP. Only the L1A accepted data are transferred to the ReadOut Drivers (RODs). To avoid blocking of the trigger operation (dead-time) the data fragments are copied to derandomizing buffers[2] located in memories of the FE electronics and then transferred to RODs when the link is free. These buffers share the front-end memories with the pipelines and have a major impact on dead time of the L1 trigger. At the output of Level-1, the event rate is reduced from 40 MHz down to 100 kHz (reduction by a factor of 400).

The ReadOut Drivers are designed to combine the data fragments from parts of the detector Front-Ends. In addition, they can perform some data processing which might be used at further stages of the trigger system and the results from this processing can be attached to the event data in case this BCID is finally accepted. Such information may contain the registered energy, the exact time of the interaction (within BCID) and other. It may also be dependent on the ATLAS sub-detector. The data from RODs are then forwarded to the HLT buffers located in the ReadOut System (ROS) where they await for the HLT processing and decision.

Concurrently to the L1A signal distributed to FE, ROD and ROS, the Level-1 trigger creates the Regions-of-Interest (RoI) and makes them available for the HLT. The main reason behind the introduction of the RoI idea in ATLAS was to limit the demand on the data transfer for the HLT processing. To refine the event selection criteria HLT uses data with full granularity available in the ROS buffers. This poses a high demand on link's bandwidth.

With the RoI concept, the first stage of processing at HLT starts with an analysis of the selected regions of the detector, where the L1 trigger found interesting information. In consequence, the full granularity data from these regions only are needed to be transferred.

Geometrically, the RoI is a virtual cone covering all the detector cells excited by the outgoing particles. The cone opening angle depends on the type of the

---

[2] The readout modules implement de-randomising buffers to accommodate for statistical fluctuations in detector data flow. In case of reaching the buffer capacity the readout system generates BUSY to stop generation of the new triggers. The ROD-busy module gathers busy signals from connected ReadOut Drivers. The busy signal is generated by the RODs when the amount of data fill the buffers, and there is no place to store more data.

interaction products. It is narrow, when the collision products are going along a straight line and is wider when for example a jet is produced. Thus the HLT at the first stage instead of processing the data from the whole ATLAS (about 100 millions channels), analyses only those regions of the detector which are covered by the RoI cone. RoIs reduce the amount of data to be processed typically by a factor of 10 [13]. This information helps also to initiate more accurate processing within the HLT and thus significantly reduces the required resources. The algorithms of RoIs are constantly developed to reduce inefficiencies and the required resources. If the data from at least one RoI are accepted then they are sent to the next step of the HLT. The HLT completes the data collection from the remaining parts of the ATLAS. The data are checked using their full granularity. The processing time at HLT takes up to one second. Finally, the data are directed to the Data Storage with frequency of about 1 kHz and wait there for free resources on the Tier-0 computing grid [31] to be reconstructed.

At each node where HLT algorithms are executed, there is also a constantly running Data Collection Manager (DCM) process which controls access and collection of data for the HLT. After the positive final trigger decision, the full granularity data, including results of intermediate processing at the HLT, are sent to Sub-Farm Output (SFO) nodes which keep track of various output streams and attach event data accordingly.

The ATLAS TDAQ consist of 1900 computers, where about 47 000 processes are running constantly. The data subsets from ROS and HLT trigger propagate via the Data Collection Network (DCN). DCN is only an exchange interface, it does not have any impact on the data shape or value.

A detailed discussion of the ATLAS Trigger and Data Acquisition in the context of the ALFA detector is given in Chapter 5.

1.3.3 ATLAS DCS

The ATLAS Detector Control System (DCS) [32] is a system ensuring safe operation of the experiment and its infrastructure. The DCS allows monitoring of the key parameters relevant for operation, manual control, and defining automatic actions to be taken based on the observed parameters. The key parameters are guarded with an alarm systems with severity gradation and notifications via e-mails or SMS messages sent to experts.

The DCS architecture is divided between two main parts – Front-End (FE) and Back-End (BE), see Fig. 1.7 [33]. The FE and BE are interconnected via the Controller Area Network (CAN) bus [34]. The Front-End consists of dedicated electronics and its infrastructures like power supplies, cooling, etc. Most of the sensors (ammeters, voltmeters, thermometers etc.) are connected via the Embedded Local Monitor Board (ELMB) – a general purpose I/O board developed by the DCS

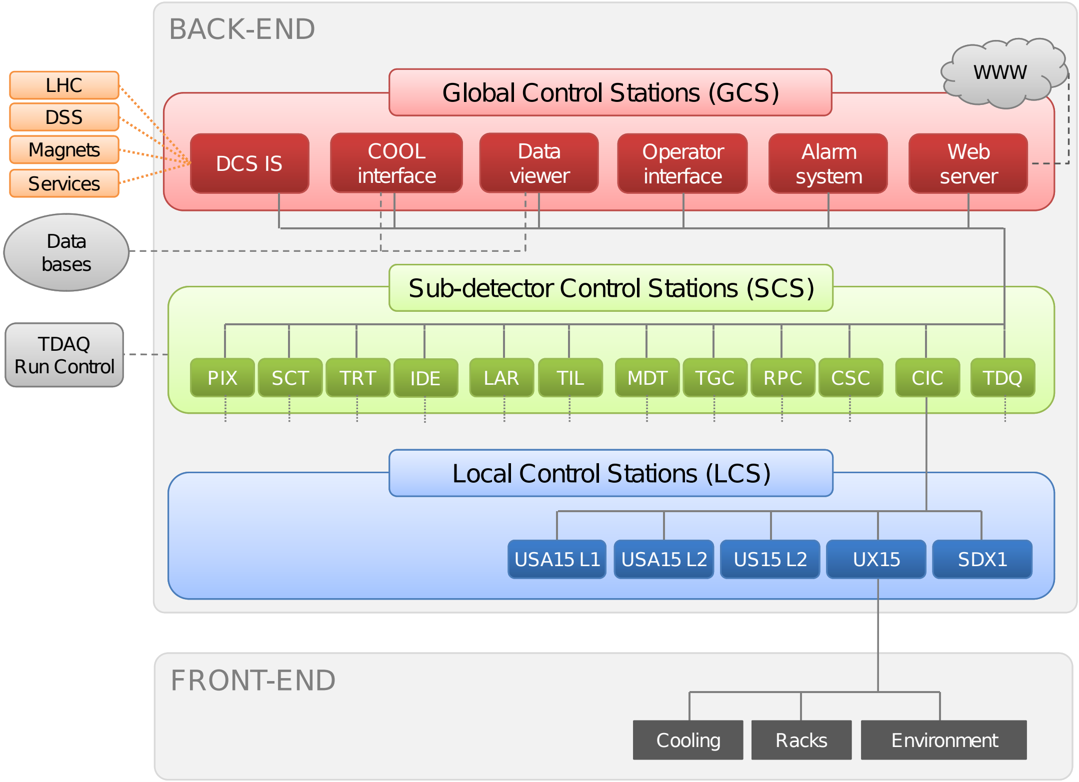

Figure 1.7: ATLAS DCS Scheme [33].

group [35]. The ELMB is a credit card-size, low cost board with 64 16-bit analogue channels and 32 digital I/O lines. The ELMB is radiation tolerant and certified to operate in locations where the radiation does not exceed 1 Gy/year and the magnetic field is below 1 T, including the safety margins [33]. The ELMB can operate in the stand-alone mode using a dedicated motherboard or being embedded in the custom made electronics.

The DCS Back-End consists of three layers (Fig. 1.7): Local Control Stations (LCS), Sub-detector Control Stations (SCS) and Global Control Stations (GCS). The LCS is responsible for the control of the smallest subsystems and individual devices. The SCS controls sub-detectors. Each of these has its own independent SCS which allows stand-alone operation of the detectors for diagnostics, calibrations or debugging purposes. It is also connected to the TDAQ using a bi-directional command protocol. The last one – the GCS – contains an application server and integrates all the sub-systems, serves the Human Interface (HI), records the data and allows accessing the stored technical data and many others.

The DCS provides also a mechanism for communication with the infrastructure. Those mechanisms monitor the status of services like cooling, ventilation, power supplies, etc. and deliver it to the experiment.Communication with the LHC is also provided by the DCS. Thus in case of any irregularity of the ATLAS subsystem, a signal is immediately propagated trough the DCS and gives a notification to the LHC experts in case of any danger to the LHC operation.

All sub-detectors and infrastructures controlled by the DCS are organized as a Finite State Machine (FSM). It is a basic concept of the DCS design allowing unification of all subsystems into a homogenous system.

The ATLAS Central DCS group provides a unified Graphical User Interface (GUI) for all other groups within the ATLAS experiment. The ATLAS DCS is based on the WinCC Open Architecture framework [36], which is commonly used in the industrial Supervisory Control And Data Acquisition (SCADA) systems and delivers also the Human-Machine Interface (HMI).

Chapter 2

ALFA Detector

This chapter presents the Absolute Luminosity For ATLAS (ALFA) [37] detectors. The main aim of these detectors was the determination of the absolute instantaneous LHC luminosity in the ATLAS experiment. First, the concept of luminosity will be introduced, followed by the ALFA physics programme and technical details of the ALFA design.

2.1 Luminosity at the Proton-Proton Machines

The instantaneous luminosity of an accelerator belongs to a set of its basic parameters. Its definition is given by the following equation:

$$R = \sigma \cdot \mathcal{L}. \tag{2.1}$$

where $\mathcal{L}$ is the instantaneous luminosity, σ is the cross section for some process, R is the rate with which this process occurs. The instantaneous luminosity can be also calculated from the parameters of the experiment. In the case of a particle collider:

$$\mathcal{L} = \sum_i \frac{N_{1,i} \cdot N_{2,i}}{A_{eff}} \tag{2.2}$$

with $N_{1,i}$ ($N_{2,i}$) – the number of particles in i^{th} colliding bunch of Beam 1 (Beam 2); A_{eff} – is the effective overlap transverse area, which for head-on collision is $4\pi\sigma_x\sigma_y$ with $\sigma_{x,y}$ being the Gaussian width of the beam in x- and y- coordinate at the Interaction Point. The sum runs over all colliding pairs of bunches.

The values of σ_x and σ_y are measured using the van der Meer scan [38]. During the scan, one of the beams is gradually displaced in small steps in one of the transverse directions (x or y). Observation of the count rate in a selected part of the experimental apparatus as a function of the displacement delivers the beam shape.

The other important part of this method is the knowledge of the beam currents. The measurements of the currents used to be the main ingredient of the uncertainty.

In case of the proton-(anti)proton collisions, determination of $\mathcal{L}$ suffered from large systematic uncertainties reaching 6% [39].

The method based on the Van der Meer scans and current measurements are presently used by the LHC experiments to determine the instantaneous luminosity. However, presently the systematics on the luminosity measurement is reduced to about 2%. The progress was connected with introduction of a new device, Beam Current Transformer (BCT) [40], allowing a precise measurement of the beam currents.

The luminosity measurement method based on counting events of a given process requires a well understood cross section for the selected process. This is relatively easy in case of the e^+e^- or lepton-hadron machines where, respectively, Bhabha or bremsstrahlung processes were selected (see for example [41] or [42]).

A precise luminosity measurement at hadron colliders would require selecting a QED process, where the calculation can be done with small uncertainties. One example of such a process is the elastic scattering at very small angles, which is dominated by a single photon exchange and depends on well-known proton form factors. However, such small scattering angles are not accessible by the standard detectors. Measurements of such processes are possible only with detectors which are installed far away from the interaction region and positioned inside the accelerator beam pipe.

In addition, the angular divergence of the colliding beams has to be very small, which leads to the necessity of special machine optics with β^{*}[1] much larger than the standard value. The ultimate aim of the ALFA system proposal was the $d\sigma/dt$ measurement in the interference region in runs with β^* value of 2500 m, cf. [37]. Optics characterised by $\beta^* \approx 6000$ m is considered for the LHC Run 3. Naturally, since these measurements can be performed only in special conditions, the method does not provide a continuous luminosity measurement but can serve for absolute calibration of other luminometers, similarly to the van der Meer scans.

2.2 Physics of Proton Elastic Scattering

The ALFA detectors [37] were designed to measure the process of elastic proton–proton interaction at very low scattering angles [37]. As a fixed centre-of-mass energy and for unpolarized beams, this process is characterised by a single kinematic variable. The common choice is the Lorentz-invariant four-momentum transfer squared, t, which is related to the scattering angle θ by $t = -2p^2(1 - \cos\theta)$, where p is the initial momentum of the proton in the centre-of-mass reference frame. The ALFA detectors deliver precise information on the trajectories of the scattered protons

---

[1] β is a betatron function which intuitively can be interpreted as a distance after which the beam doubles its transverse dimension and β^* is its value at the IP. More details are given in Chapter 3.1.2.

which in turn allows a precise determination of the scattering angle and t, finally leading to the measurements of the differential elastic cross section $d\sigma/dt$.

The mechanism of the elastic scattering is described by a colour-singlet exchange. This may occur either due to an electromagnetic process (an exchange of a photon) or due to a strong one which to a first approximation is represented by an exchange of a colour-compensated system of two gluons and called a Pomeron, see Fig. 2.1.

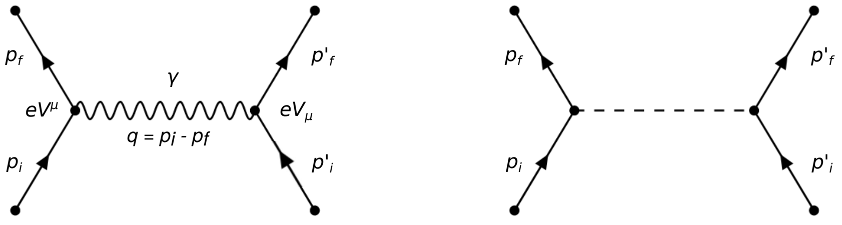

Figure 2.1: Proton-proton elastic scattering Feynman diagrams. *LEFT:* The wave line represents single-photon exchange. *RIGHT:* The dashed line represents a colourless exchange. The time on the diagrams is going upwards.

The full amplitude describing elastic scattering includes both mentioned parts and the differential cross section is given by:

$$\frac{d\sigma}{dt} \approx |f_{EM}(\theta) + f_{nucl.}(\theta)|^2, \tag{2.3}$$

where f_{EM} and $f_{nucl.}$ are the scattering amplitudes due to the electromagnetic and strong exchanges, respectively.

One can distinguish three domains of the four-momentum transfer values. They are related to:

- dominance of the EM processes (very small $|t|$) – Coulomb region,
- interference of the electromagnetic and strong amplitudes – Coulomb-nuclear interference domain,
- dominance of the strong exchange at large $|t|$, which includes also the hard scale processes described within perturbative QCD.

Perturbative QCD delivers a good description of the hard scale phenomena. However, it is not applicable in the domain of long-range, small four-momentum transfer processes. In this regime, the Regge theory founded on analytic properties of the scattering matrix and scattering amplitudes provides phenomenological description of the observed phenomena or data features. This theory describes an interaction in terms of an exchange of trajectories, which group particles along straight lines in the spin–mass-squared plane. The cross section related to the exchange of a trajectory changes with the centre-of-mass energy as $s^{\alpha-1}$, where α is the intercept of the trajectory.

For trajectories of known mesons, the intercept value is observed to be smaller than 1. In order to describe the raise of the total cross sections at high energies, a new trajectory with the intercept above 1 – the Pomeron – was introduced. A good description of data was obtained with $\alpha = 1.0808$ [43] for the Pomeron trajectory.

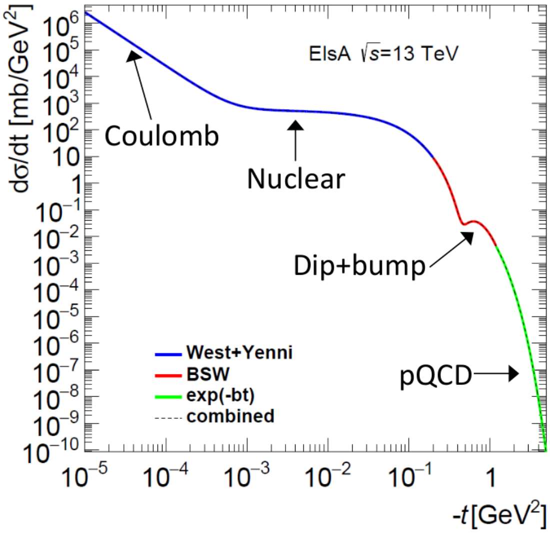

Figure 2.2: Predicted elastic differential cross section as a function of the absolute value of the four-momentum transfer at $\sqrt{s} = 13$ TeV [44]. Predictions cover the Coulomb and Coulomb-nuclear interference domain [45], the dip-region [46] as well as that of perturbative QCD.

Figure 2.2 shows the elastic differential cross section as a function of the absolute value of the four-momentum transfer squared. The West-Yenni [45] predictions describe the Coulomb (the photon exchange dominance) and Coulomb-nuclear interference (CNI) domains. The dip – influenced by the three gluon graph – and the following bump region are taken from the predictions of Bourrely, Soffer and Wu [46] and for larger $|t|$ values a dependence predicted by perturbative QCD is drawn.

Theoretical formula describing the differential cross section before the dip region is given by:

$$\frac{d\sigma}{dt} = \frac{4\pi\alpha^2(\hbar c)^2}{t^2}G^4(t) - \sigma_{tot}\frac{\alpha G^2(t)}{|t|}\left[\sin\alpha\phi(t) + \rho\cos\alpha\phi(t)\right]\exp\left(\frac{-b|t|}{2}\right) + \sigma_{tot}^2\frac{1+\rho^2}{16\pi(\hbar c)^2}\exp\left(-b|t|\right), \tag{2.4}$$

where α is the fine structure constant, $G(t)$ is the proton electric form factor, $\phi(t)$ is the Coulomb phase, b is the nuclear slope and σ_{tot} denotes the total cross section. The first term describes the Coulomb interaction, second the Coulomb-nuclear interference and the third is due to strong interaction. The value of σ_{tot} appears in the formula because of the optical theorem, which relates the amplitude of the elastic scattering at $t = 0$ to the total cross section.

Results of measurements performed at various $\sqrt{s}$ are subsequently used to constrain properties of the scattering amplitudes, in particular in the calculations using the dispersion relations. They will shed light on the presence of the Odderon [47] or taming of the increase of the total cross sections with energy [48] and therefore on the structure of the pp interaction at relatively low values of the four-momentum transfer. In addition, they can be used to test the energy dependence of the cross sections and its parametrisation.

Both ATLAS and TOTEM published the measurements of elastic proton-proton scattering at various $\sqrt{s}$ [49, 50, 51, 52, 53]. These measurements yielded also the total cross section and b values. Moreover, they play an important role for studies of the three-gluon (Odderon) exchange.

2.3 Location, Geometry and Naming of ALFA Detectors

ALFA is a moveable forward detector and a subsystem of the ATLAS experiment located in the straight section of P1. It consists of four Roman Pot stations, two stations on each side of the ATLAS Interaction Point (IP1) which allow a vertical movement (perpendicular to the machine plane) of the detectors. Each station is made of two pots – the upper and the lower one. Each pot contains a detector. Stations are installed symmetrically at a distance of about 237 m (the inner stations) and about 245 m (the outer stations) downstream from the IP1. The detector setup is presented in Fig. 2.3.

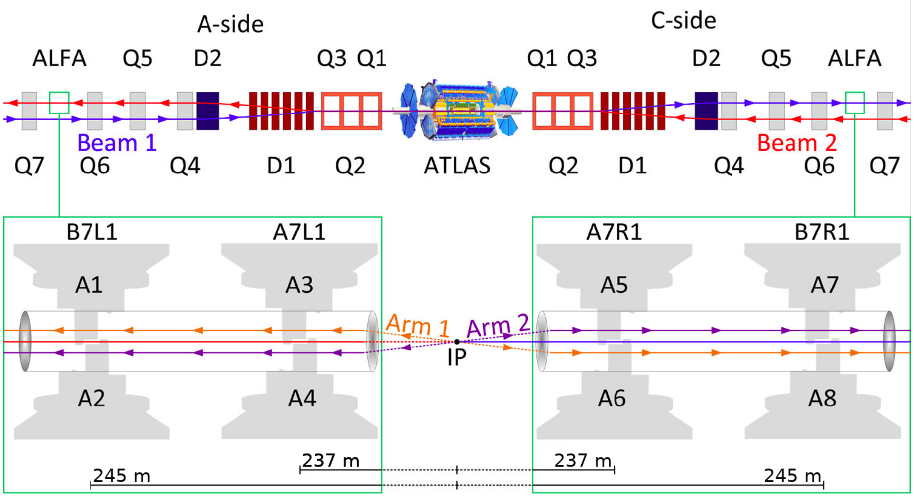

Figure 2.3: Schemes shows positions and naming convention of the ALFA detectors.

There are several naming conventions. The most regular and consistent with the LHC naming scheme is: B7L1U, B7L1L, A7L1U, A7L1L, A7R1U, A7R1L, B7R1U, B7R1L, with A (B) marking the inner (outer) station, 7 denoting the 7th cell (element of the magnetic lattice) in the insertion area while L(eft) or R(ight) correspond to the side of the Interaction Point as seen from the LHC ring centre and the lower and upper detectors are marked with appended L and U, respectively. The number 1 means that the device is located around P1. The same convention will be used in the description of other LHC devices and infrastructures, like collimators or absorbers.

The energy and momentum conservation leads to a correlation between the momenta of the two scattered protons. If proton on the left side is scattered with $p_y > 0$, then neglecting the angular divergence of the beam, the proton on the right side has $p_y < 0$. This leads to the concept of two elastic arms. As presented in the drawing, the detectors B7L1U, A7L1U, A7R1L, B7R1L form elastic Arm 1, while B7L1L, A7L1L, A7R1U, B7R1U form Arm 2 of the ALFA system. Another naming convention is also used, where the detectors are enumerated from 1 to 8 as presented in Fig. 2.3. The names B7L1, A7L1, A7R1 and B7R1 corresponds to the ALFA stations, each containing one upper and one lower detector.

2.4 Roman Pot Technology

ALFA detectors are installed inside of movable vacuum vessels called the Roman Pots. This is a technique used for devices operating very close to the beam invented in '70s by CERN Roman Group [54]. Normally, when the ALFA detectors are not used or during the beam injection, the Roman Pots are retracted to the HOME position. The insertion of the Roman Pots is a very delicate and precise process, thus it is done only from the CERN Control Center (CCC) in cooperation with the LHC operators. The idea of the Roman Pot is presented in Fig. 2.4.

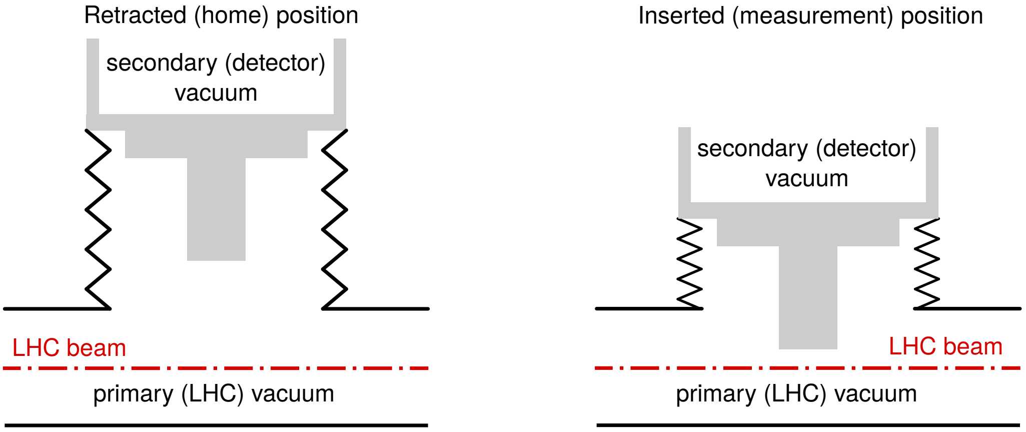

Figure 2.4: Idea scheme of Roman Pots.

A detector is placed inside the pot and is separated from the LHC primary vacuum. The pot is immersed in the LHC primary vacuum using the vacuum bellow. The bellow protects the vacuum and allows the movement of the pot. The detectors operate in a secondary vacuum, which is required to avoid deformations of the thin window of the pot.

A detailed view of the ALFA Roman Pot is presented in Fig. 2.5.

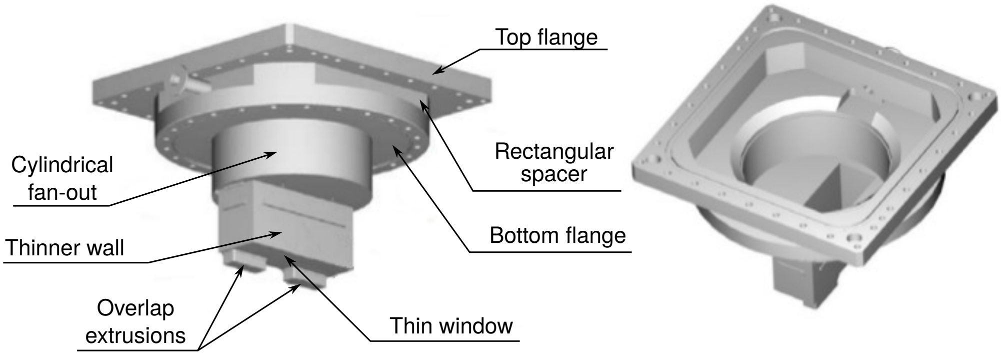

Figure 2.5: ALFA Roman Pot design visualisation.

The stainless steel walls surrounding the detector are 2 mm thick. In front of the detector the pot side wall is milled to 500 μm and under the detector there is a window which is machined to 200 μm.

The motion of the pot is driven by a stepping motor operating in the half-step mode giving 400 steps per revolution. The motor drives the 2 mm pitch roller screw. It gives the approaching resolution of 5 μm. In case of any malfunction, the motors can be switched off and the flange can be pushed from the working position to the HOME position by springs.

Each motor contains an integrated resolver, thus there is a feedback concerning the motor movement. The pot position is also monitored by a Linear Variable Differential Transducer (LVDT). The motors are driven by the micro-step drivers placed in the USA15 technical cavern located beside the ATLAS cavern. Apart from the drivers, the USA15 cavern accommodates all the motor control system based on the PXI system from National Instruments [55]. As the PXI is only a local control system, there is also an interface between the PXI and the LHC control system called FESA which is a standard for the CERN accelerators control.

2.5 Single Detector Description

Each detector consists of two parts: the Main Detector (MD) and two Overlap Detectors (OD) – one each side of the MD. Mutual position of the MD and the ODs is presented in Fig. 2.6. Main Detector is used for the scattered proton tracking, while the Overlap Detector is used for relative alignment between the upper and the lower detector.

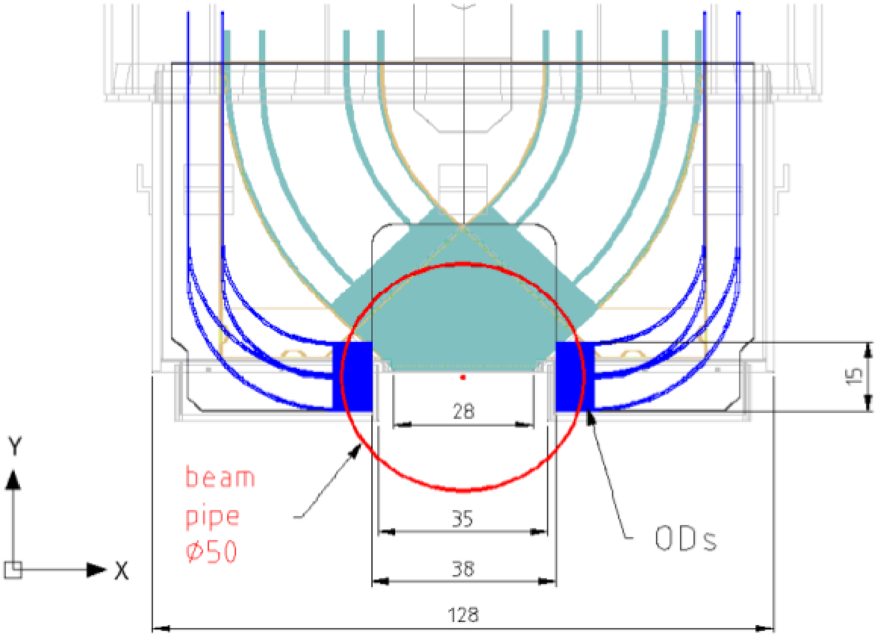

Figure 2.6: Front view drawing of the assembled detector.

2.5.1 Scintillators

Both, the MD and OD are made of the scintillating fibres (Sci-Fi). These are Kuraray Co LTD plastic single clad scintillating fibres SCSF-78 of S-type with square cross section of 0.5×0.5 mm^2, see Fig. 2.7, left panel. The scintillating fibre core is made of polystyrene (PS) and polymethylmethacrylate (PMMA) cladding reflects the light inside of the fibre, see Fig. 2.7, right panel. Contrary to non-S-type, the S-type fibre core has strong molecular organisation along the fibres, thus it is mechanically stronger and allows reduction of the bending radius needed to fit in the Roman Pot. This is very important feature as the ODs fibres are 90° bent, see Fig. 2.6. Such fibres unfortunately have higher attenuation by 10% than other tested ones, but as Sci-Fis in ALFA are relatively short (about 50 cm) the attenuation difference is not crucial. The peak of the wavelength induced by the scintillation is 450 nm.

The square cross section fibres have been chosen due to higher trapping efficiency – the amount of photons guided to the end of the fibre to the amount of photons produced in the scintillation process given in percents. In case of the tested fibres – 4.2% for square cross section vs. 3.1% observed for the round cross section ones with thinner cladding [56].

Even though the round fibres with double cladding have even higher efficiency, they were not used because of the smaller cross section of the active part.

All fibres are additionally clad with an aluminium layer to avoid the optical crosstalk. The aluminium cladding increases size of the fibre layer by about 2.2%.

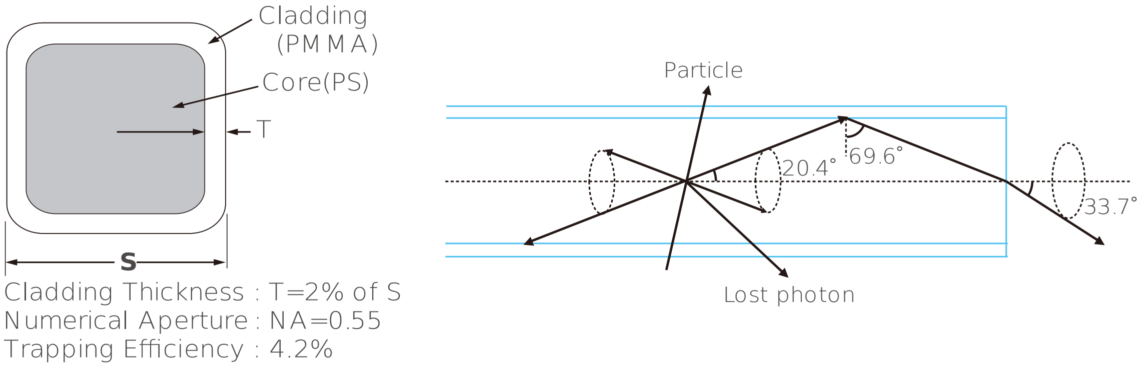

Figure 2.7: The cross section of the scintillating fibre (left) and scheme of the scintillation while the particle passes the fibre (right) [56].

Behind the active part of the detectors, as seen by the scattered proton, the trigger plates are installed. For this purpose the EJ-200 (Eljen Technology) scintillating tiles are used [57]. The tiles are made of polyvinyl toluene with maximum light emission at 425 nm wavelength. To improve the light yield, the tiles are clad with the white reflective paint. This allows an increase of the light yield of up to 50% including some additional conditions [58].

The scintillation light is transported with the light guides made of fibres with the round cross section to the photomultiplier tube (PMT). The fibres for light guides are Clear-PSM type from Kuraray Co LTD [56]. Each is read by one PMT.

2.5.2 Photomultipliers

The ALFA detector uses two types of the photomultiplier tubes – Hamamatsu SuperBialkali R9880 [59] and Hamamatsu R7400 [60] for MD and OD trigger plates, respectively. Also, a multi-anode photomultiplier tubes (MAPMT) of type Hamamatsu R7600-00-M64 [61] are used for the MD and OD trackers [58].

The Hamamatsu R7400 has 8 dynodes and its peak light wave length detection is at 420 nm. This suits very well the used scintillators with a peak at 425 nm. The quantum efficiency of those PMTs is 25%. The anode to cathode nominal supply voltage is 800 V. At the nominal voltage the PMT is able to exceed the gain of $7 \cdot 10^5$.

The Hamamatsu SuperBialkali R9880 consists of 10 dynodes powered with 1000 V anode to cathode voltage giving the gain of $2 \cdot 10^6$. The quantum efficiency is 35% at 350 nm of the light wavelength. At the scintillator wavelength peak it is still above 30%.

The third type, the MAPMT, has 64 channels with 12 dynodes each, which correspond to one layer of the MD tracker. Thus, 20 of those are used for the MD, and another 3 for the ODs for each detector. Each channel has a photocathode $2 \cdot 2$ mm^2 and is separated from the neighbours with a distance of 0.3 mm. The crosstalk between consecutive channels is about 2%. The gain of each channel is $\sim 10^6$ at the applied voltage anode to cathode of 1000 V. The gain varies between the channels with a factor of 2-3.

2.5.3 Main Detector

The main detector is used for the registration of the positions of the scattered protons. It consists of 10 double layers of scintillating fibres. Each layer contains 64 fibres. Fibres belonging to two adjacent layers are perpendicular to each other and attached to a titanium holder. The layers are positioned in the plane transverse to the beam and at the angle of $\pm 45°$ to the vertical axis. Those orthogonal layers are called the U-plane and V-plane. To obtain the spatial resolution of about 30 μm, the layers are staggered by 1/10 of the fibre. To allow the detector positioning close to the proton beam and thus optimising the detector acceptance, some fibres are cut at 45° (see Fig. 2.8). Each layer is connected to a separated MAPMT. Fibres have a very specific mapping to the MAPMT channels to avoid the internal crosstalk.

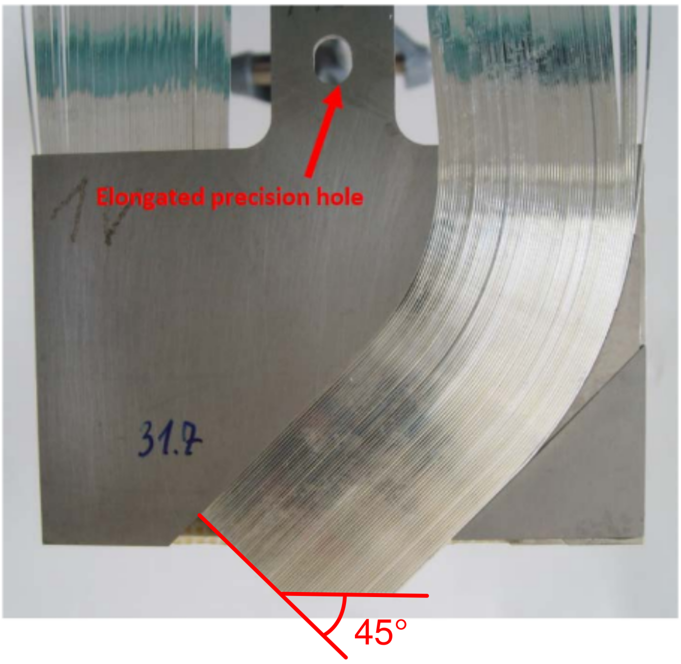

Figure 2.8: One layer of main detector – support and two crossed layers of 64 scintillating fibres.

2.5.4 Overlap Detector

The position of the detectors may vary from one insertion to the other. To be able to measure the relative position of the upper and lower detectors, the ODs are installed on the left and right side of the MDs.

Each Overlap Detector comprises three layers of 30 scintillating fibres each. Second and third layer are shifted by 166 μm and 333 μm, respectively, to increase the resolution of the vertical position measurement. They are oriented horizontally. Each OD contains a single 3 mm thick, 6×15 mm^2 scintillating tile covering the whole active area of the OD.

The OD are using the same readout system as the MD. It is worth mentioning that unlike the MDs, each OD has only single trigger tile.

2.6 Readout Electronics

The ALFA readout electronics is located directly on the detector. The path of the signal starts in the scintillating fibre in the form of a scintillation. The light is guided to the MAPMT where it is converted into electrical signal. The signal is processed by the PhotoMultiplier Front-end (PMF) and targets the motherboard (MB, ALFA-M) where the signals from all MAPMTs are buffered, serialized and sent to the local data acquisition system. Each step will be discussed in the following subsections. An overview of the readout electronics installation is presented in Fig. 2.9.

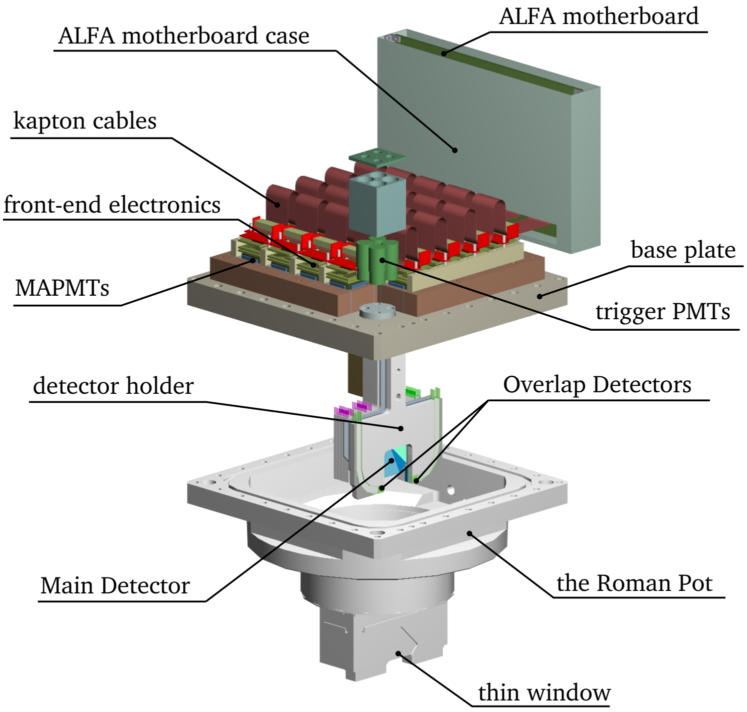

Figure 2.9: ALFA Roman Pot design visualisation.

The ALFA readout electronics is installed at the top of the Roman Pot and it is also moving together with the detector. Therefore, the connections between PMF and MB must be robust. Moreover, the electronics must be radiation tolerant as it is working about 20 cm from the LHC beam. More details concerning the radiation resistance of the ALFA electronics can be found in Appendix D.

2.6.1 PhotoMultiplier Front-End – PMF

The Roman Pot contains 25 spots for PMF structures. The PMF structure ($30\times30\times60$ mm^3) consists of: a single MAPMT, a stack of the three Printed Circuit Boards (PCB) and a connector to the kapton cable connecting PMF with the motherboard. The first PCB at the top of the MAPMT is the voltage regulator which supplies the PMT dynodes with High Voltage (HV). The second board is an adapter connecting 64 MAPMT channels, which are spread on the whole surface, to the last board. The third board comprises a Multi Anode ReadOut Chip (MAROC) and an FPGA-based interface between the MAROC and the ALFA motherboard. MAROC is an Application Specific Integrated Circuit (ASIC) designed for ALFA and its task is to process the electronic signal. A simplified scheme is presented in Fig. 2.10.

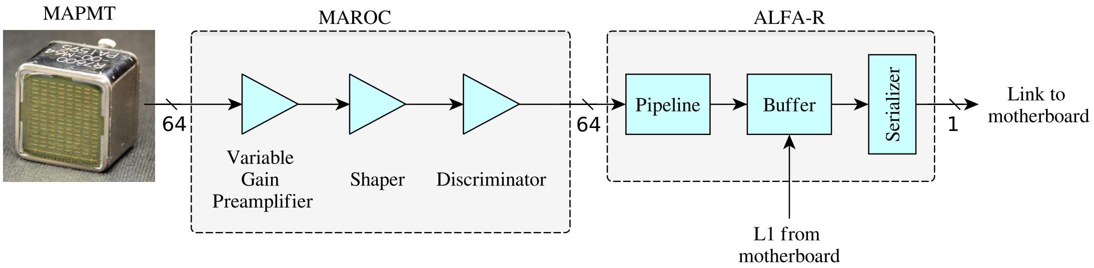

Figure 2.10: Simplified scheme of the readout chain scheme of the MAPMT.

Each input channel has its own tunable preamplifier to reduce the photo-multiplayer dispersion and its internal architecture is optimised to reduce the crosstalk in the silicon structure. The signal gets to the shaper and then to the discriminator which generates a strictly defined signal according to the setting of the threshold.

The FPGA, named ALFA-R, stores the signal coming from MAROCs and buffers it until the L1A signal arrives from the MB. Then, the data from 64 channels are serialised and transferred to the motherboard. Each kapton cable connecting the PMFs with the motherboard is able to serve up to 5 PMFs. Free PMF slots are terminated with a bridge-PCB.

In case of the trigger PMTs, the PMF architecture is analogous. The output signal from the PMF is delivered to the trigger mezzanine. More details is given in Section 2.7.

2.6.2 ALFA Motherboard

The ALFA motherboard is the main part of the readout electronics. It provides multiple functionalities starting from powering of the PMFs, through synchronising the data flow with the LHC clock and generating the trigger signal for the ATLAS Central Trigger Processor, to the monitoring of parameters of all readout components and allowing their configuration. Its simplified scheme is presented in Fig. 2.11.

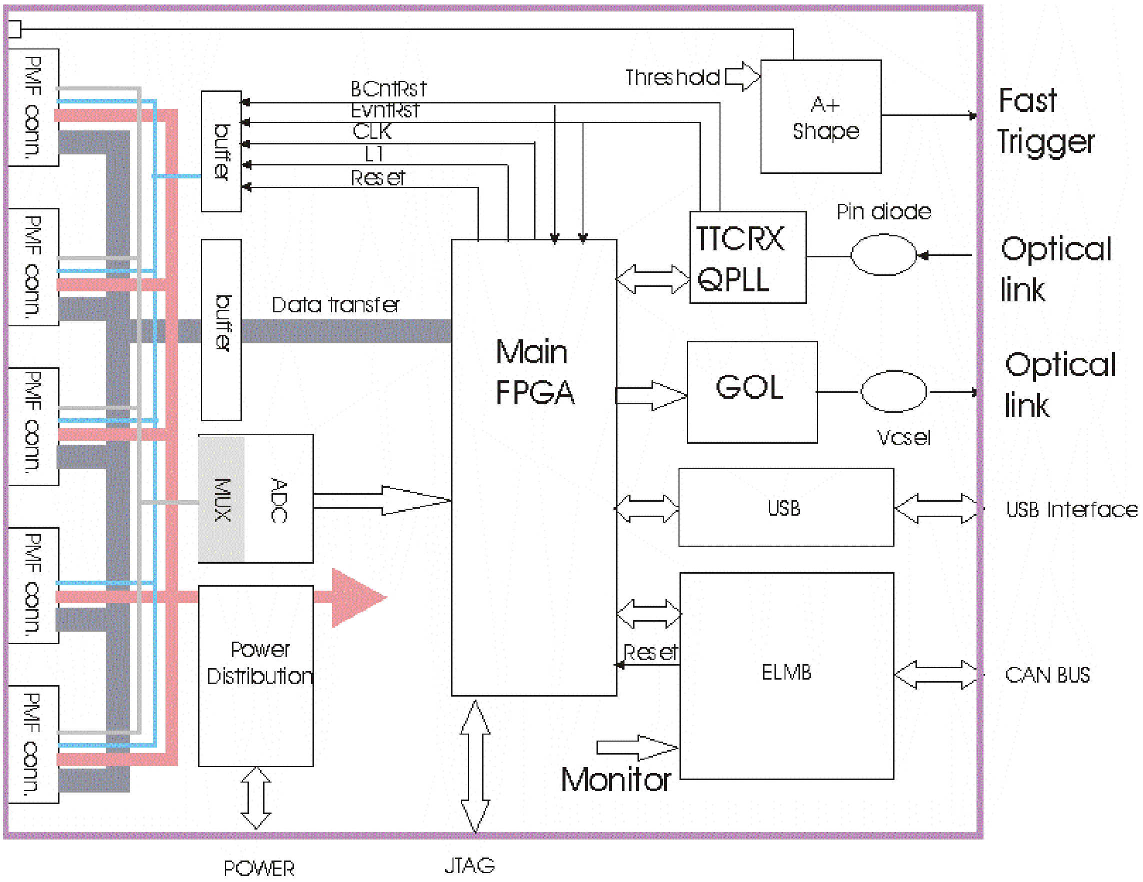

Figure 2.11: ALFA Motherboard main functional blocks.

The motherboard controls the data flow on all MAROCs and is designed to support up to 25 PMFs. In fact, each ALFA detector uses 23 of those. When the MB is ready to accept the data, it generates requests and all ALFA-Rs start sending serialised data from their buffers. Then, the MB rearranges the data, prepares a header and transfers them to DAQ. The integrated time from the proton hit on a single fibre to the data transfer stage at the MBs is about 10 μs corresponding to 400 BCIDs.

The ALFA motherboard is also equipped with a slot for ELMB, which is used for communication with MAROCs and measurement of voltages, currents and also for the PMF configuration [37]. The communication between the ELMB and MB is realised over the Serial Peripheral Interface (SPI) [62]. All readout parameters can be set via the ELMB.

The motherboard is also hosting a trigger mezzanine. The trigger board receives the PMT signals from the scintillating tiles (T1 and T2) and makes one of possible logic operations: T1, T2, T1 AND T2, T1 OR T2 and a special debugging trigger T_{LED}. In case of the last mode, the trigger can be generated on each LED blink, which allows determination of the trigger tiles efficiency by comparison of the number of triggers generated by the tiles with the number of LED blinks. If the trigger condition mentioned above is satisfied the trigger mezzanine sends the trigger signal to the CTP via the air-core cable. The use of the air-core cable is dictated by the fact that ALFA operates very close to the ATLAS L1 trigger latency limit (time of response) – actually ATLAS has to extend L1A latency by 8 BCIDs when operating with ALFA triggers. Thus, the trigger signal must be delivered from the station to the CTP as quickly as possible. The transmission speed in the installed type of the air-core cable approaches 91% speed of light, which allows the signal to reach the CTP within about 1030 ns through the 280 m long cable. For comparison, the signal propagation time over the same length standard cable lasts almost 1200 ns.

2.7 ALFA TDAQ

Triggering of the ALFA detectors starts in the scintillating tiles overlapping the detector active part. Electric signals from PMTs are received by the trigger PMF installed on the trigger mezzanine. The signal is preamplified and filtered according to the threshold set using DCS (see Section 2.8). The trigger signal can be generated by the Main Detectors or the Overlap Detectors. Then the trigger mezzanine logic analyses the trigger signals. If the trigger is accepted, the Trigger mezzanine forwards it to the ATLAS Central Trigger Processor through the ALFA_CTPIN Versa Module Eurocard (VME) module.

There is only one trigger cable per detector and the trigger mezzanine needs to prioritise the trigger signals. As the trigger from ODs is only used for detector calibration, signal from the MD has higher priority over the OD. Therefore, if there are signals from MD and OD, the trigger mezzanine sends the MD trigger as the trigger. The mezzanine encodes the triggers from the MD and OD using the trigger pulse length – 25 ns is the duration time of the MD trigger trigger pulse, while in the case of the OD it is 12.5 ns long. Schematically, it is shown in Fig. 2.12.

The ALFA_CTPIN module decodes the trigger type, and the CTP checks the combination of the triggers from 8 stations and subsequently qualifies them. If the event is accepted, the CTP sends the L1 accept signal to all ALFA motherboards and those generate a specific header, pack it into the package with respective data

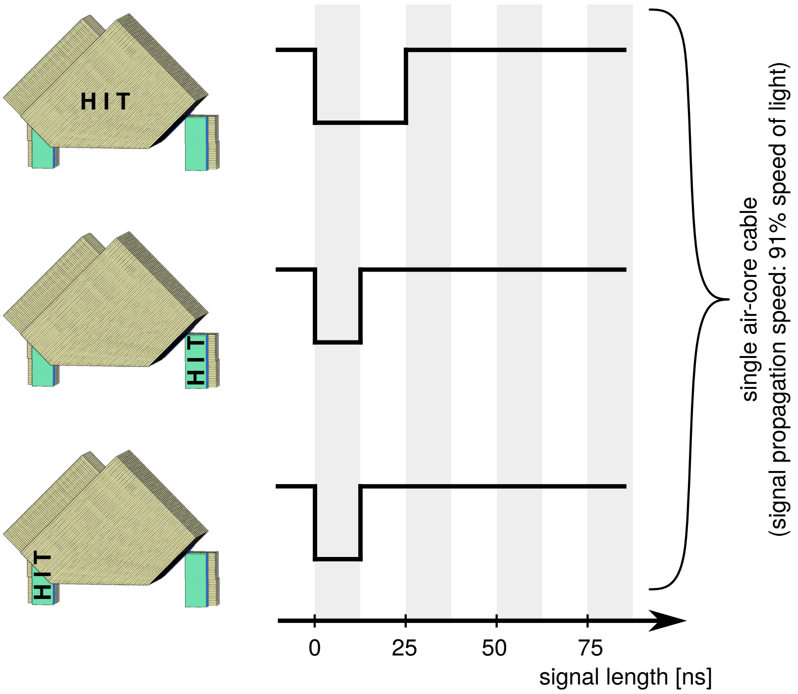

Figure 2.12: Different trigger pulse length for MDs and ODs gives a possibility to send two types of signals via air-core cable.

and send them to the MROD (Muon drift tube ReadOut Driver)[2] VME module via 300 m long optical fibre links.

In USA15 two MRODs are installed, one for each arm. The readout driver concatenates the data collected from four detectors (one elastic arm), forms packages and relays them to the ReadOut System.

The ROS is a PC-based system containing PCI card designed to receive data from several MRODs (up to 12 inputs). The ROS buffers the data and provides an access for the HLT trigger, in which more sophisticated algorithms of filtering physics events ca be applied. A detailed ALFA TDAQ description can be found in Chapter 5.

2.8 DCS

The ALFA DCS allows monitoring of all parameters of the ALFA detectors and their infrastructure, for example voltages and currents on the electronic components, positions of the Roman Pots, state of the vacuum and cooling etc. [37]. Moreover, the DCS is used to switch on/off the motherboards, low-voltage (LV) power-supply, HV on MAPMTs and PMTs, to set-up and configure PMFs and to tune the latency (the length of the pipeline in ALFA-R). DCS is also used to extract the Roman Pots

---

[2] ALFA is using RODs adopted from the Muon chamber. It was possible, as the ALFA data-stream format was adjusted to Muon data format.

in case of emergency.

For each monitored parameter, a set of alarm levels can be defined. If the parameter value is outside a pre-defined range then a corresponding warning or an error message is propagated through the DCS FSM tree, and related prompts are displayed. In case of critical issues the DCS notifies the experts directly. In case of warnings or errors not causing danger to the apparatus, the error is visible only for the shifter in the ATLAS Control Room and in the DCS GUI, Fig. 2.13.

ALFA DCS is connected to the Finite State Machine tree of the ATLAS DCS, thus any irregularity within the ALFA FSM tree is propagated to the top of the ATLAS DCS FSM tree. In case of the ALFA critical error, it may happen that the LHC beam injection is disabled by the interlock system.

Figure 2.13: ALFA DCS FSM GUI.

2.9 Track Reconstruction and Alignment

2.9.1 Track Reconstruction

The event reconstruction in the ALFA detectors starts from the local track reconstruction, which assumes that the proton has trajectory almost parallel to the beam

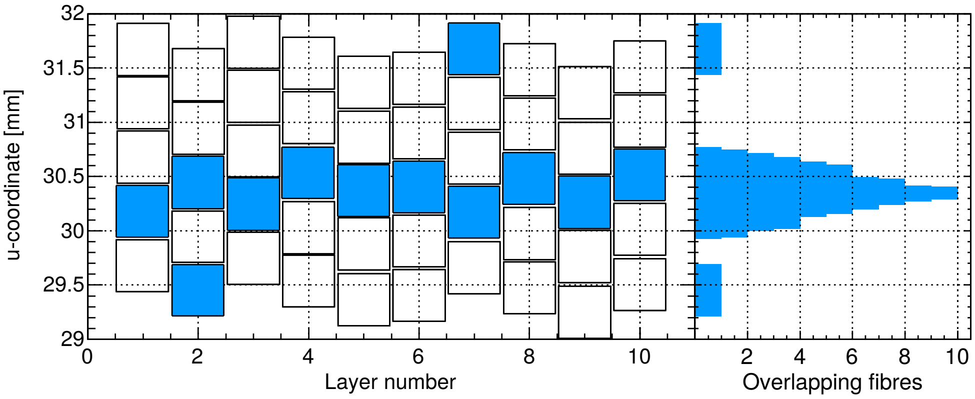

Figure 2.14: The proton track in the staggered fibres (left panel) and the histogram pointing the track position (right panel) [53].

line – small angle below 1 mrad can be neglected [53]. The track reconstruction is based on overlapping hits on staggered fibres, see Fig. 2.14. The centre of the overlap gives the coordinate of the track. The same overlap is performed independently for both directions of the fibres. Only layers with less than 10 hits are considered. To classify the track to be reconstructed, at least 3 layers out of 10 have to register between 1 and 3 hits. The last condition to be satisfied for the track reconstruction is the minimal number of overlapping fibres, which is 3. Then both profiles are transformed to the spatial positions in the beam coordinate system.

In case of multiple particles registered by the detectors, the fibres geometry does not allow a unique determination of the track position. The multiple hits usually comes from the halo and hopefully such events can be removed by matching them with the tracks from the opposite side of the IP. The elastic pile-up (more than one reconstructed track is coming from elastic scattering) is rather rare and it's fraction is only 0.1%.

Same method and criteria of track reconstruction is provided for both MDs and ODs.

2.9.2 Detector Alignment

The precise alignment of the detector is crucial for the physics analysis. This process is based on various distributions of the reconstructed tracks. The alignment uses three parameters: horizontal and vertical positions and the detector rotation. The horizontal alignment and rotation around the beam are based on the elastic pattern – vertical ellipse with a gap between the upper and lower detectors. The uncertainties of the alignment are 1-2 μm and 0.5 mrad for the horizontal alignment and rotation, respectively.

The vertical alignment uses data from the Overlap Detectors. It is determined by combining two vertical tracks from overlapped ODs. The main contribution to the alignment uncertainty comes from the fact the Overlap Detectors consists only of 3 layers and is about 10 μm. Another contribution comes from the precision of relative alignment of the MDs and ODs during manufacturing process and gives another 10 μm. Thus the uncertainty of the alignment of the inner stations is about 20 μm. For the outer stations it is increased due to showers induced by inner stations. The vertical alignment with respect to the beam is performed by comparison of the track densities between upper and lower detectors. This error is usually about 80 μm.

2.10 Reconstruction of Four-Momentum Transfer

The four momentum transfer t is determined from the ALFA measurements at special optics settings – high β^* with parallel-to-point property, which allows focusing all particles scattered at the same angle in the same point on the detector plane [53]. The parallel-to-point focusing is achieved only in the vertical angle. The four-momentum transfer t can be approximated by:

$$-t = (\theta^* \times p)^2 \tag{2.5}$$

where θ^* is a scattering angle measured at the IP and p is the nominal beam momentum. The beam optics is optimized to achieve highest possible scattering angle in the vertical direction, which allows to record tracks of the scattered protons with the smallest θ angles and yields the best resolution of the t determination.

A transport matrix formalism allows relating the parameters of the trajectory of a particle at two different positions. The trajectory $\big(w(s), \theta_w(s)\big)$, where $w \in \{x, y\}$ is the transverse position on the orbit at point s and θ_w is the angle of this trajectory between w and s, and is given by the transport matrix M and the coordinates at the interaction point (w^*, θ^*):

$$\begin{pmatrix} w(s) \\ \theta_w(s) \end{pmatrix} = M \begin{pmatrix} w^* \\ \theta_w^* \end{pmatrix} = \begin{pmatrix} M_{11} & M_{12} \\ M_{21} & M_{22} \end{pmatrix} \begin{pmatrix} w^* \\ \theta_w^* \end{pmatrix} \tag{2.6}$$

where the elements of the transport matrix can be calculated from the optics settings.

The transport matrix M must be calculated separately in the x and y planes and depends on s, thus 2.6 needs to be calculated for every detector and for both planes.

In case of the elastic scattering, the both scattered protons originate from the same vertex and their scattering angles are the same in magnitude and opposite in sign. This feature allows using the subtraction method. One can obtain the scattering angle using the formula:

$$\theta^*_w = \frac{w_A - w_C}{M_{12,A} + M_{12,C}} \tag{2.7}$$

where indices A and C corresponds to opposite sides of the IP. Finally, having the θ angles for x and y planes the t can be determined:

$$-t = \big((\theta^*_x)^2 + (\theta^*_y)^2\big)p^2. \tag{2.8}$$

2.11 ALFA Physics Results

The results of the differential cross sections at 7 TeV [53] and 8 TeV [50] are presented in Fig. 2.15. The red curve is a fit of the theoretical prediction in the range of $t = -0.01$ GeV^2 to $t = -0.1$ GeV^2. Such range was chosen for reduction of the extrapolation uncertainty. Finally the total cross section at 7 TeV yields $\sigma_{tot} = 95.35 \pm 1.30$ mb [53]. In case of the 8 TeV yields $\sigma_{tot} = 101.7 \pm 2.9$ mb [50].

The comparison of results performed by ALFA with other experiments and other energies are given in Fig. 2.16. The results are compatible with other published measurements.

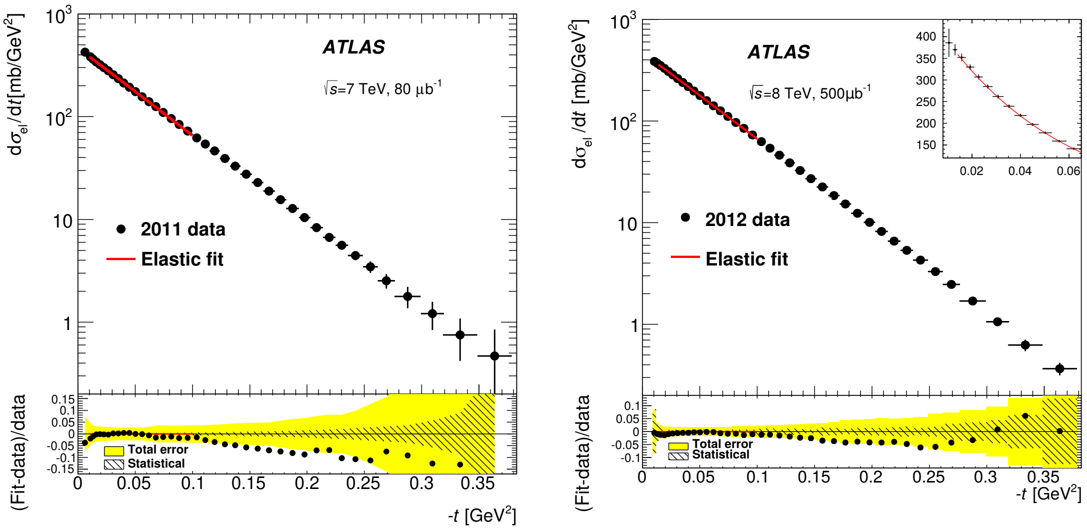

Figure 2.15: Total cross section measurement versus t-value (black dots) and the theoretical prediction fit (red line) – upper panel on both plots. In the lower panel the difference between theoretical prediction and data is given (black dots). Yellow area shows the total experimental uncertainty, while the hatched part shows the statistical component. *LEFT:* Measurements at 7 TeV [53]. *RIGHT:* Measurements at 8 TeV [50].

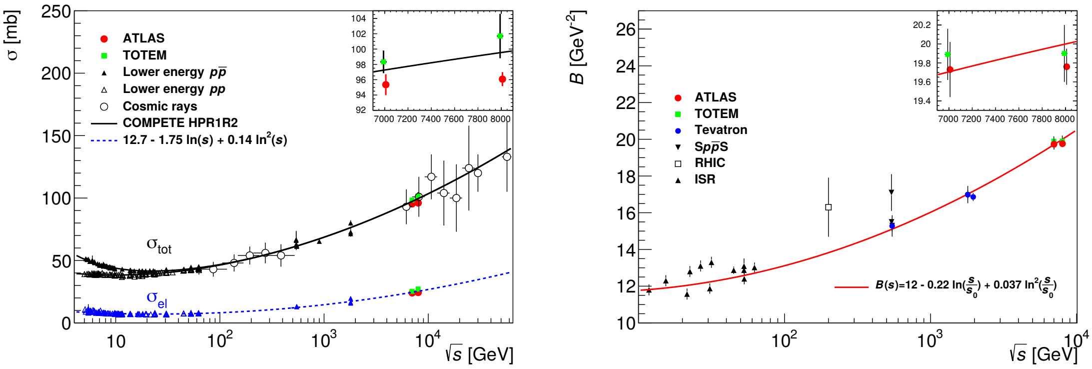

Figure 2.16: *LEFT:* Comparison of total and elastic cross section measurements performed by ALFA withe other published results [53]. *RIGHT:* Comparison of the nuclear slope measurements performed by ALFA with other published results [50].

Chapter 3

The LHC Proton Beam

Accelerator physics concerns many issues on the border between science and technology. Since 1920s, when the first particle accelerators were invented, many generations and types of these devices were developed. This chapter discusses the basics of the beam motion and the beam control for synchrotron machines like the LHC storage ring. If not mentioned explicitly, the contents of this chapter are based on [2, 10, 63].

3.1 Beam Dynamics

3.1.1 Basics of Linear Beam Optics

Trajectories of the LHC beam particles are very complex due to a complex magnet system and its settings, which may vary for different measurements. To investigate the particle motion, one introduces an ideal trajectory, fixed by the machine construction, and which is a closed curve. This fixed ideal trajectory is named the orbit. Since the transverse dimensions of the beam are typically small compared to the length (circumference) of the machine, it is natural to investigate the beam particle motion in the vicinity of the orbit using the co-moving reference frame. All further considerations will be carried out as a function of s – the position along the orbit from the starting point. At the LHC, by convention, the starting and ending points of the trajectory are chosen to coincide with the ATLAS IP. Next, the local right-handed Cartesian coordinate system is introduced, see (Fig. 3.1). At a given point of the orbit, the z-axis is tangent to it and the x-axis is in the LHC ring plane and points outside the ring.

For each LHC run, the particles are running around the orbit millions times – typically 300-400 millions – until they collide, are lost, or the beam is dumped. In the LHC case, the frequency with which particle pass the whole path of the ring – the revolution frequency – is 11 245 Hz.

In the simplest model of an accelerator, beam particles move along the orbit due

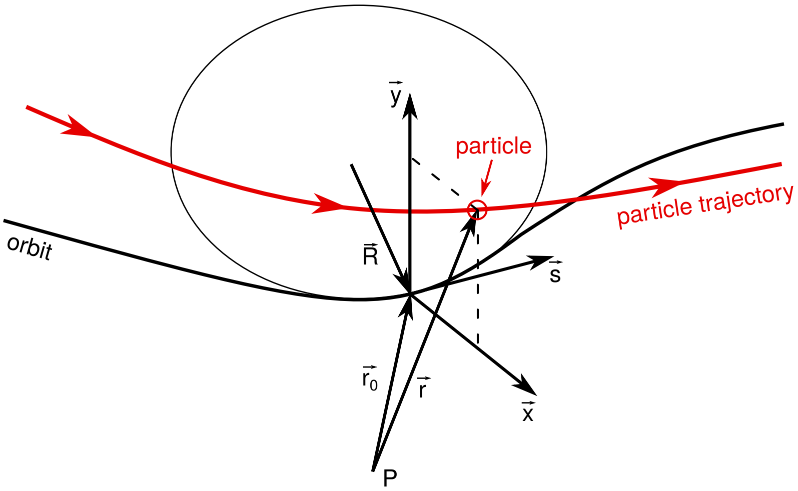

Figure 3.1: Closed orbit scheme reference frame [10]. The X–Y plane is transverse to the curve s being the orbit. The vector $\vec{S}(\vec{r})$ is tangent to the curve s. The red curve shows the trajectory of the particle oscillating along the orbit.

to electric and magnetic interactions caused by $\vec{E}$ and $\vec{B}$ fields, respectively. The Lorentz force acts on each proton:

$$\frac{d\vec{p}}{dt} = q(\vec{E} + \vec{v} \times \vec{B}) \tag{3.1}$$

where q is the electric charge, $\vec{p}$ is the proton momentum and $\vec{v}$ is its velocity. At the LHC, the magnetic fields are used for steering the trajectories (transverse dynamics) of the particles and electric fields for controlling their longitudinal dynamics.

3.1.2 Transverse Beam Dynamics

A charged particle in the $\vec{B}$ field travels along a bent path with the curvature radius ρ related to the field strength and particle momentum by:

$$\vec{B}\rho = \frac{m\vec{v}}{q} = \frac{\vec{p}}{q}, \tag{3.2}$$

were $\vec{B}\rho$ is also called magnetic rigidity and determines the maximum energy reachable in an accelerator.

The magnetic field does not have to be uniform. It is useful to consider its expansion in the vicinity of the orbit. For example, assuming $\vec{B}_y$ depending only on x one gets:

$$B_y(x) = B_y(0) + \frac{dB_y}{dx}x + \frac{1}{2!}\frac{d^2B_y}{dx^2}x^2 + \frac{1}{3!}\frac{d^3B_y}{dx^3}x^3 + ... \tag{3.3}$$

or

$$\frac{q}{p}B_y(x) = \frac{1}{\rho} + kx + \frac{1}{2!}mx^2 + \frac{1}{3!}ox^3, \tag{3.4}$$

with the expansion coefficients defined in Table 3.1.

Table 3.1: Main multipole expansion coefficients related to magnets used for beam steering at the LHC including their functionality[10].

multipole	**definition**	**functionality**
dipole	$\frac{1}{\rho} = \frac{q}{p}B_y(0)$	beam steering
quadrupole	$k = \frac{q}{p}\frac{dB_y}{dx}$	beam focusing
sextupole	$m = \frac{q}{p}\frac{d^2B_y}{dx^2}$	chromaticity compensation
octupole	$o = \frac{q}{p}\frac{d^3B_y}{dx^3}$	field errors or field compensation

The usefulness of the above expansion comes from the fact that it is possible to construct magnets for which only a single term is dominant, in particular the dipole or quadrupole one. These magnets can then be used as building blocks of the accelerator magnetic lattice. One should be aware of the presence of the higher multipoles in the LHC lattice. However, they either constitute the unwanted fields with $\vec{B}$-values few orders of magnitude smaller than the leading one (for example in quadrupole magnets) or are used to correct the beam chromaticity or orbit in special cases which are not of interest for the present thesis. Neglecting these higher terms and assuming the dipole moment affecting only the x axis (i.e. that the bending of the trajectory is confined to the accelerator plane), the equation of motion of a single particle traversing the magnetic structure can be written as:

$$x''(s) + \left(\frac{1}{\rho^2(s)} - k(s)\right)x(s) = 0, \tag{3.5}$$

$$y''(s) + k(s)y(s) = 0. \tag{3.6}$$

The qualitative behaviour of the solution depends of the sign of the quadrupole moment. If $k(s)$ is the quadrupole coefficient and if $k < 0$, the magnet structure is focusing the beam in considered plane, and it is defocusing if $k > 0$. Note that if the quadrupole magnet is focusing in one plane it is simultaneously defocusing the other one. Detailed derivation of the equations of motion can be found in [10, sec. 3.2].

The above equations describe a general case of particle traversing magnetic field. In a circular accelerator, each particle traverses the same magnetic structures many times. This can be described with periodic functions:

$$\rho(s) = \rho(s + L) \qquad \text{and} \qquad k(s) = k(s + L). \tag{3.7}$$

This leads to the following solution of the equation of motion:

$$x(s) = \sqrt{\varepsilon}\sqrt{\beta(s)} \cos\Big(\psi(s) + \phi\Big), \tag{3.8}$$

where ε and ϕ denote the integration constants termed the emittance and the phase, respectively, and their values are fixed by the initial conditions. The $\beta(s)$ and $\psi(s)$ functions introduced during solving the Hill's equation[1] are the amplitude of modulation and the phase advance of the betatron oscillation, respectively. The number of oscillations per turn is called the tune, Q [63]. The tune value is very important for the beam stability since integer numbers lead to resonances, which may destabilize the beam. The phase advance function can be calculated as:

$$\psi(s) = \int_0^s \frac{ds}{\beta(s)} \tag{3.9}$$

and takes large values when the $\beta(s)$ is small and *vice versa.* Derivation of Eq. 3.8 can be found in [10, sec. 3.7].

The first derivative of Eq. 3.8 gives the information about the evolution of the trajectory direction:

$$x'(s) = -\frac{\sqrt{\varepsilon}}{\sqrt{\beta(s)}}\Big[\alpha(s)\cos\big(\psi(s) + \phi\big) + \sin\big(\psi(s) + \phi\big)\Big], \tag{3.10}$$

where

$$\alpha(s) \equiv -\frac{1}{2}\frac{d\beta}{ds} = \frac{\beta'(s)}{2}. \tag{3.11}$$

The phase space of a particle[2] at fixed s is given by

$$\gamma(s)x^2(s) + 2\alpha(s)x(s)x'(s) + \beta(s)x'^2(s) = \varepsilon, \tag{3.12}$$

where

$$\gamma(s) \equiv \frac{1 + \alpha^2(s)}{\beta(s)} \tag{3.13}$$

and is shown in Fig. 3.2. Here, the area of the phase-space ellipse is directly proportional to the emittance value ($A = \pi\varepsilon$). The ellipse shape evolves depending on α and β functions as a consequence of the magnet lattice structure, see Fig. 3.3.

---

[1] Hill's differential equation is a second order linear ordinary differential equation described by the general formula $\frac{d^2u}{dt^2} + f(t)u = 0$, while $f(t)$ is a periodic function.

[2] To be precise the classical phase space is defined in (x, p_x) coordinate system. In accelerator physics it is adopted to call the (x, x') coordinates the phase space [63].

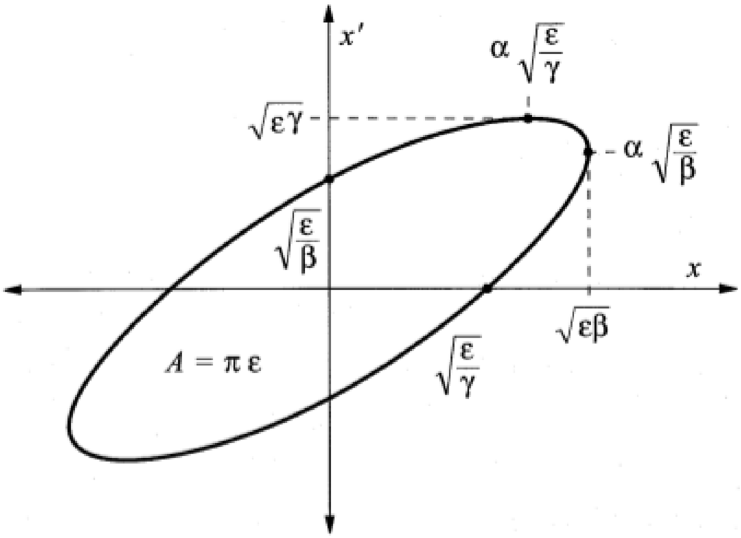

Figure 3.2: The phase space ellipse of particle motion in the $x - x'$ plane. Similar construction can be obtained for the $y - y'$ plane [10].

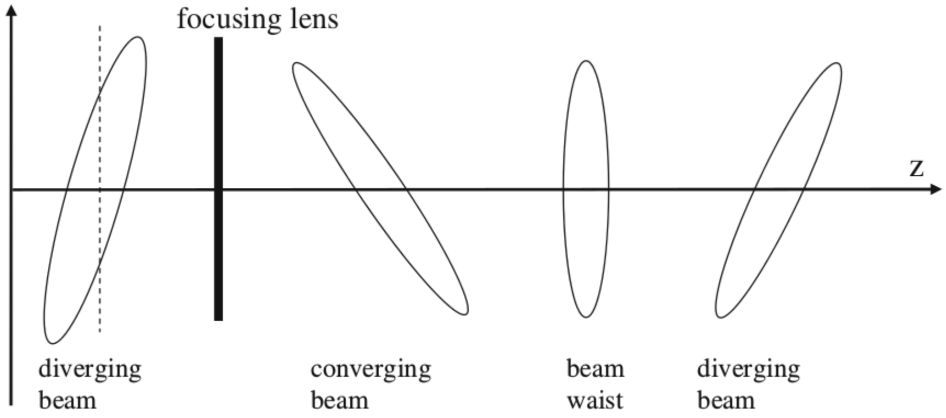

Figure 3.3: The phase space ellipse evolution [6].

The discussion above concerned trajectories of individual particles moving along the orbit. In case of a real storage ring, the beam can consist of even 10^{14} particles. Each of those particles has its own initial parameters, different trajectories and different phase-space ellipses. In this context, the term emittance is used for the average of the emittance values of all the individual particles.

When all forces acting on the beam particles are conservative, then according to Louville's theorem, the beam emittance is constant in time, similarly to the emittance of a single particle. Then, the beam emittance can be considered as the beam quality factors. The presence of particles with large amplitudes and angles leads to "bad quality" beam and large emittance. However, there are always some effects like intra-beam scattering and beam-beam interactions that lead to the emittance growth. Nevertheless, this growth is rather slow, up to a few percent per hour, and is typically neglected in the LHC context [64].

Knowing the emittance value and the betatron function, one may calculate the beam transverse size

$$\sigma_x(s) = \sqrt{\varepsilon\beta(s)},$$

and its angular spread

$$\sigma_{x'}(s) = \sqrt{\varepsilon/\beta(s)}.$$

The above equations provide an intuitive interpretation of the $\beta(s)$ value – it is a distance after passing which the beam doubles its transverse dimension (assuming no magnetic fields are present). The beam width considered as a function of s is often called the beam envelope, see Fig. 3.4.

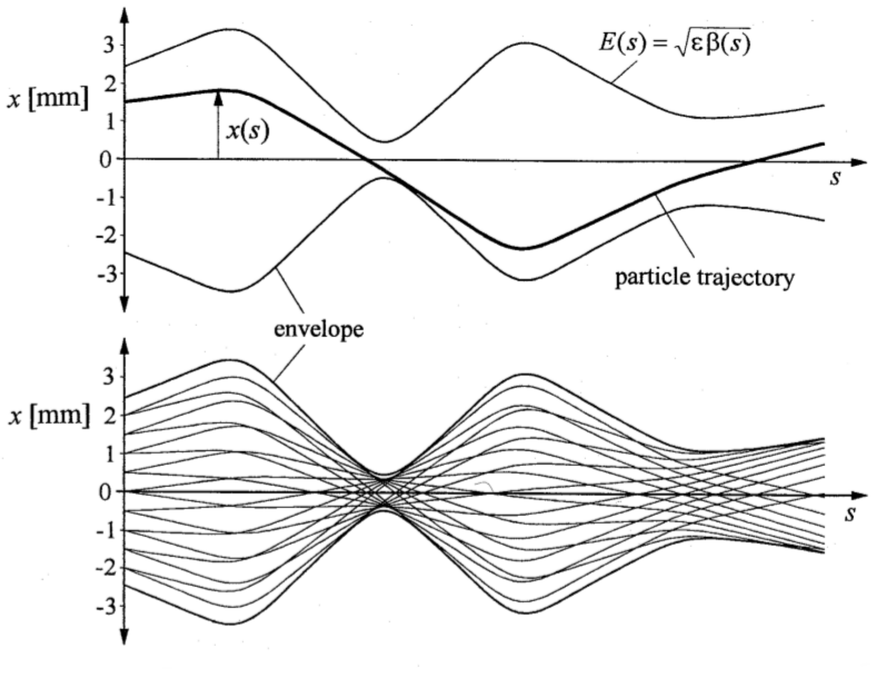

Figure 3.4: Particle trajectories and their envelope. The upper plot presents a single particle trajectory within an envelope, while the lower one presents trajectories of many particles creating the envelope [10].

3.1.3 Longitudinal Beam Dynamics

The main principle of the synchrotron-like machines is the particle trapping inside of the so-called radio frequency (RF) buckets. High voltage applied to the radio frequency cavities holds protons trapped in the RF buckets. The main task of the RF cavities during the normal running is to cover the beam particle energy losses due to synchrotron radiation, or to increase the particle energy during the beam acceleration phase. The energy change of a particle is given by:

$$\Delta E = qU_0 \sin\left(\Psi_0 + \Delta\Psi\right) - W \tag{3.14}$$

where ΔE is the energy change of each particle, q is the particle charge, U_0 is the peak value of the RF cavity voltage, Ψ_0 is the ideal particle phase relative to the RF phase and $\Delta\Psi$ is the phase deviation with respect to the ideal phase synchronous with the phase of the RF and W is the energy loss within one revolution.

As it was already mentioned, each particle has slightly different parameters. The same concerns its momentum which can differ from the designed value, see Fig. 3.5 left. Trajectory of a particle with slightly lower momentum is bent more than that of the nominal one, thus its path is shorter. It results in an earlier arrival of the particle into the RF cavity within the next turn. For a particle with slightly higher momentum the situation is opposite. The parameter connecting the relative path length change and the deviation in momentum is called the momentum compaction factor and is defined as:

$$\alpha = \frac{\Delta L/L}{\Delta p/p}. \tag{3.15}$$

Relativistic particles are synchronised with the radio frequency within the phase range of $\pi/2 < \Psi < \pi$. Particles with zero momentum deviation are coming in the proper phase Ψ_0. Other particles with non-zero deviation if are coming sooner – gain more energy as the voltage of the RF is higher according to equation 3.14. Those with higher momentum are coming later, when the voltage is lower, thus, they gain less or even loose energy, see Fig. 3.5 right. This phase variation is called the synchrotron motion or synchrotron oscillation and is described by a non-linear periodic differential equation:

$$\ddot{\Psi} + \frac{\Omega^2}{\cos\Psi}(\sin\Psi - \sin\Psi_0) = 0. \tag{3.16}$$

where $\ddot{\Psi}$ denoted the second derivative with respect to time.

The synchrotron oscillation frequency is given by:

$$\Omega = \omega_{rev}\sqrt{-\frac{qU_0(\omega_{RF}/\omega_{rev})\cos\Psi_0}{2\pi\beta_{rel}^2 E}\left(\alpha - \frac{1}{\gamma^2}\right)} \tag{3.17}$$

where q is the particle charge, $\beta_{rel} = v/c$ – its relative speed, E – the particle energy, U_0 is the voltage peak value, α – denotes the momentum compaction factor, γ – the Lorentz factor, ω_{rev} and ω_{RF} are the revolution and cavity radio frequencies, respectively. The value of the harmonic number, $h = \omega_{RF}/\omega_{rev}$ has to be an integer number to hold the synchronisation between the RF cavity and the revolution

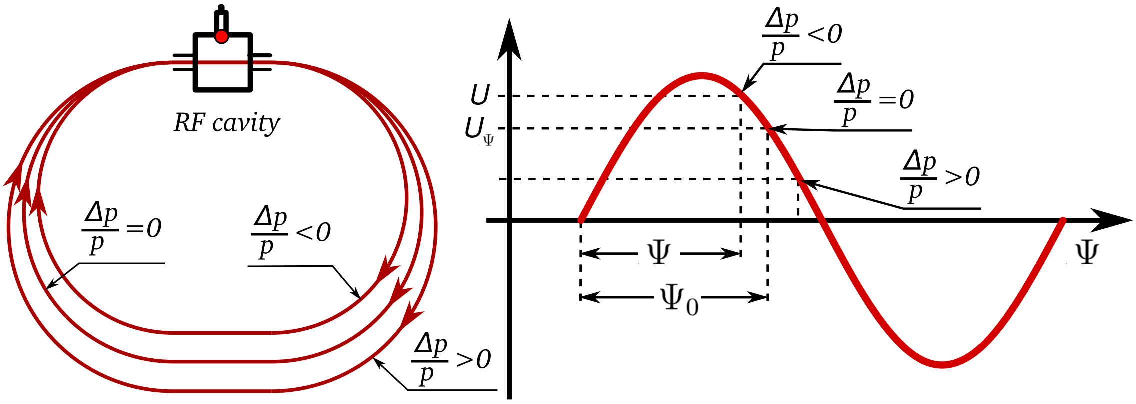

Figure 3.5: The principle of synchrotron oscillation [10].

frequencies.

The solutions of Eq. 3.16 are stable only in some regions of the $(\Delta E, \Delta\Psi)$ phase space plane, see Fig 3.6. The stable and unstable regions are separated by the separatrix. This leads to the bunched structure of the beams. The stable regions are often called the buckets.

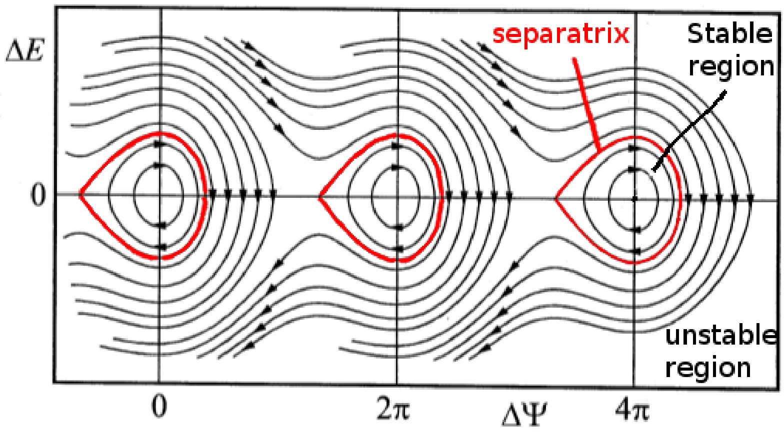

Figure 3.6: Particle motion in an accelerator RF field. [10].

The area of the separatrix determines the maximum longitudinal acceptance of the synchrotron. A detailed derivation of equations describing the particle motion in the RF field and separatrix can be found in [6]. Once a particle gets outside of the separatrix it cannot return back. Particles outside of the separatrix are out of control from the machine side and may hit elements of the accelerator and its infrastructure.

3.1.4 Dispersion Function

The particles within a bunch are oscillating with a certain momentum deviation which can be described:

$$\frac{\Delta p}{p_0} = \frac{p - p_0}{p_0} \tag{3.18}$$

where p_0 is the reference momentum, p – particle momentum and Δp is the momentum deviation. At the LHC, the Δp value is of the order of 1‰[63].

The dispersive effects impact mostly the horizontal plane due to accelerator curvature. Thus the equation 3.5 turns into:

$$x''(s) + \left(\frac{1}{\rho^2(s)} - k(s)\right) x(s) = \frac{1}{\rho(s)} \frac{\Delta p}{p_0}. \tag{3.19}$$

The solution describes the oscillation amplitude of particles oscillating around the designed trajectory.

$$x(s) = \sqrt{\epsilon}\sqrt{\beta(s)} \cos\left(\Psi(s) + \phi\right) + \left(\frac{\Delta p}{p}\right) D(s) \tag{3.20}$$

where D is a dispersion function. It quantifies the sensitivity to the momentum dispersion and is defined as:

$$D(s) = \frac{x(s)}{\frac{\Delta p}{p}}. \tag{3.21}$$

Typical values of the dispersion at the LHC are about $1 - 2$ m [63]. The dispersion also implies the following extension of the the beam size definition:

$$\sigma_{RMS}(s) = \sqrt{\varepsilon_{RMS}\beta(s) + \left(\frac{\Delta p}{p}\right)^2_{RMS} D^2(s)}. \tag{3.22}$$

Note the emittance and the momentum spread in 3.22 are also taken as the RMS values.

The α, β, γ are called the Twiss parameters [63]. Functions α, β, dispersion D and its derivative D' are enough to describe the exact linear beam optics [10].

The LHC optics is not fixed but changes during each fill depending on the LHC operation state. Different optics is used at the injection, during squeeze, and during data-taking at the LHC top energy. Some example values of β and $D(s)$ are given in Fig. 3.7. During injection the maximum values of the β function do not exceed 250 m (Fig. 3.7 a). During the squeeze the β^* is reduced, while the top values of the β on both sides of the IP are increased (Fig. 3.7 b). The lower β^* is expected, the higher values are required on the sides of the IP (3.7 c, d). The Figure shows

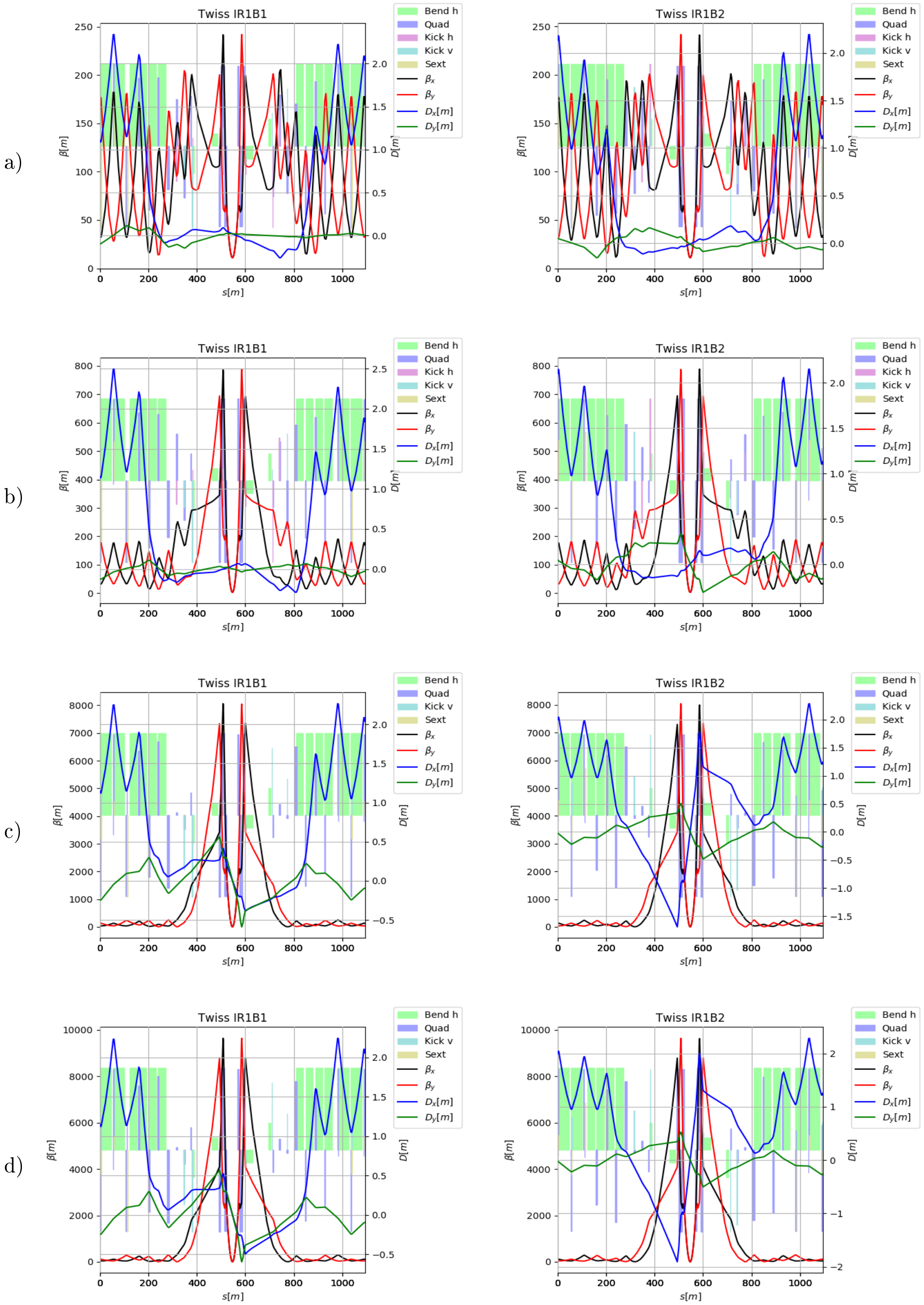

Figure 3.7: LHC optics in surroundings of IP1 examples: a) injection, b) squeeze at 3.1 m, c) collisions at 0.3 m, d) collisions at 0.25 m. The IP1 is located in the middle of each plot.

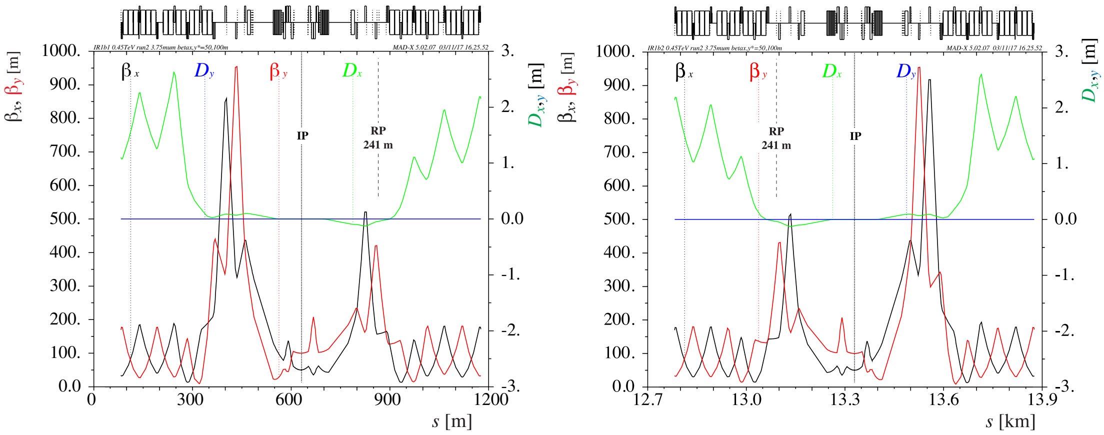

Figure 3.8: LHC optics for Beam 1 (left panel) and for Beam 2 (right panel) for 900 GeV special runs.

also that, the Beam1 and Beam2 optics, are not exactly symmetric, and there are some differences for each beam.

The LHC optics is also constantly improved and new settings are applied every few weeks. Also for each special run a new optics is designed. Optics designed for ALFA 900 GeV special runs is given in Fig. 3.8.

3.2 Beam Structure

The revolution frequency of the LHC is $\omega_{rev} = 11.245$ kHz, while the radio frequency cavities operate at $\omega_{RF} = 400.8$ MHz then the harmonic number is $h = \omega_{RF}/\omega_{rev} = 35640$. It determines the maximum number of stable regions – the RF buckets – where the particles can be controlled. The RF bucket length is 2.5 ns. The LHC design allows filling of every 10^{th} bucket with protons, but not more than 2808 per beam, since the total stored energy is limited to 362 MJ. Practically, the number of filled bunches is limited to 2655 for normal runs (during the LHC standard operation in 2018) and the maximum stored energy to 320 MJ. Typically it did not exceed 300 MJ after the declaration of the *stable beam* status [3].

For each LHC settings, a filling scheme is designed. The bunches cannot be uniformly spread along the storage ring to avoid electric fields induced by the charged particles destabilizing the beam due to resonances. Therefore, the bunches are organised into the trains. Typically, each train consists of 144 bunches and the trains are separated by 32-36 empty bunches which corresponds to 800 – 900 ns.

Dividing the LHC circumference – $L = 26\,659$ m by the number of available buckets one gets that the next bucket starts about every 75 cm and, thus, the distance between two consecutive bunches is about 7.5 m. The half-length of the ATLAS detector is about 22 m then to avoid parasitic collisions inside of the experiment area, the machine has to be run in the non-head-on collision mode by providing a non-zero crossing angle of the beams. During the Run 2 standard data-taking, a typical value of the half-crossing angle was 130 – 160 μrad. In case of the ATLAS experiment the crossing was in the vertical (y, z) plane. The crossing angle affects the luminosity value. Equation 2.2 needs to be modified by the luminosity reduction factor $S(\phi)$, which is given by:

$$S(\phi) = \frac{1}{\sqrt{1 + (\frac{\sigma_s}{\sigma^*} \tan \frac{\phi}{2})^2}} \tag{3.23}$$

where σ^* is the transverse beam size and σ_s is the bunch length.

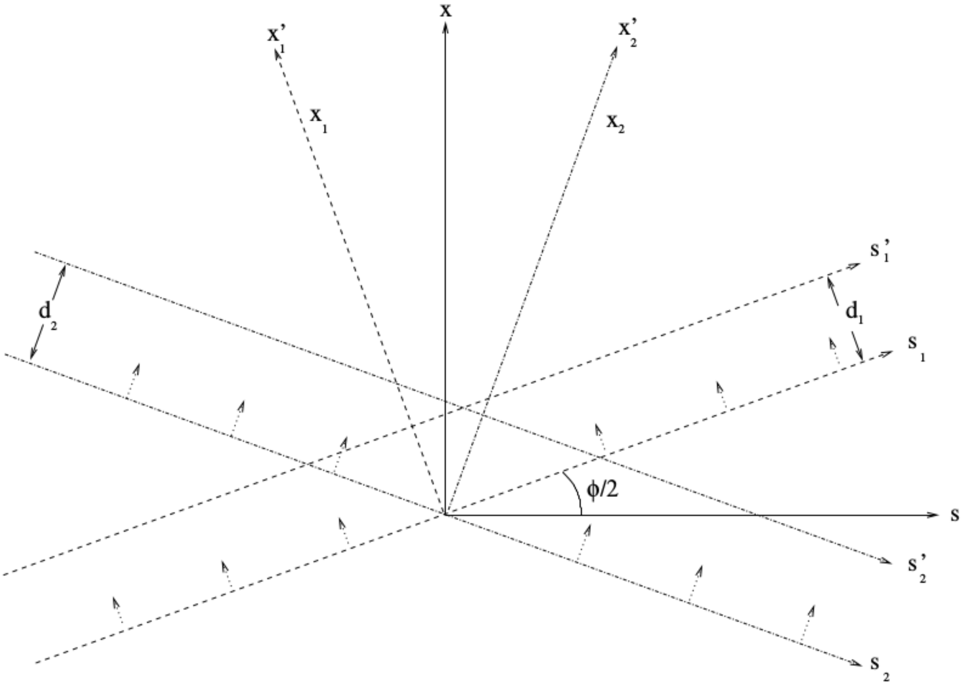

Figure 3.9: Beam crossing angle and beam offset scheme [65]

Another correction is due to the transverse separation factor, $D(d)$, of the beams:

$$D(d) = e^{-\frac{(d_2-d_1)^2}{4\sigma^{*2}}} \tag{3.24}$$

where d_1 and d_2 are the beam offsets for the Beam 1 and Beam 2, respectively. Those offsets are coming from the beam displacement from the ideal trajectory, see Fig. 3.9.

Including other corrections and the number of colliding bunches, the luminosity formula turns into:

$$\mathcal{L} = \frac{N_1 N_2 \omega_{rev} N_b}{4\pi \sigma_x \sigma_y} \cdot S(\phi) \cdot D(d) \cdot W(\phi, d) \tag{3.25}$$

where N_1 and N_2 correspond to the number of protons in a single bunch in the Beam 1 and Beam 2, respectively, ω_{rev} is the revolution frequency, σ_x and σ_y – are the beam sizes in x and y direction, respectively. The term $W(\phi, d)$ is an additional reduction factor which appears only in the presence of both $S(\phi)$ and $D(d)$.

3.3 Beam Losses

During the run, the beam intensity constantly drops over time. This beam loss is an unavoidable phenomenon at the particle accelerators. A detailed understanding of the beam loss mechanisms is essential to avoid beam instabilities and the damage of the infrastructure, experiments or other instrumentation.

Beam losses in the accelerator can be regular or irregular. The irregular ones usually are due to equipment failures during the beam operation or injection errors. There are also different random events which may cause a beam dump triggered by the Beam Loss Monitor (BLM); for example UFOs (Unidentified Falling Objects) may cause a shower of secondary particles which leads in consequence to the beam dump [66].

Apart from the irregular losses, there are always unavoidable regular ones. The regular losses related to the proton-proton interactions or imperfections of the machine are measured during the low intensity runs devoted to the loss map creation. Losses caused by normal machine operation like the beam halo cleaning, tune shift, orbit change, etc. are also considered as the regular beam losses.

In the simplest case, assuming a smooth LHC operation with no parameter changes, the change in beam intensity can be expressed [67] as:

$$N(t) = N(0) \exp\Big(-\frac{t}{\tau}\Big) \tag{3.26}$$

where $N(0)$ is the initial beam population, $N(t)$ denotes the beam population after time t and τ is the beam life-time.

3.3.1 Intra-Beam Scattering

The main physics phenomenon causing the regular beam losses is the intra-beam scattering (IBS). Particles within a bunch are charged so they act with repulsive Coulomb force on each other. Having 10^{11} protons within a bunch acting on each other, the multiple small-angle Coulomb scattering effect shows up leading to growth of the beam emittance.

According to Bjorken-Mtingwa theory, the IBS growth rate can be expressed as[68]:

$$d\sigma_p(t) = \sigma_p(0) \exp\left(\frac{t}{\tau_{long}}\right) \tag{3.27}$$

$$\sqrt{\varepsilon_x}(t) = \sqrt{\varepsilon_x}(0) \exp\left(\frac{t}{\tau_{trans.x}}\right), \qquad \sqrt{\varepsilon_y}(t) = \sqrt{\varepsilon_y}(0) \exp\left(\frac{t}{\tau_{trans.y}}\right) \tag{3.28}$$

where τ_{trans} and τ_{long} are the transverse and longitudinal emittance growth time, respectively, σ_p denotes the relative energy spread and ε_x, ε_y corresponds to the horizontal and vertical emittance, respectively. In case of the LHC at the injection energy, the emittance growth due to IBS is 38 and 30 hours in the transverse and longitudinal direction, respectively.

3.3.2 The Toushek Effect

If IBS causes sufficiently high energy transfer from the transverse phase space to the longitudinal one, the scattered particles may cross the separatrix. Such a phenomenon is called the Touschek effect [69]. The loss rate due to the Touschek effect is:

$$\frac{dN}{dt} = -\alpha N^2 \tag{3.29}$$

where N is the beam population and α is the geometrical coefficient depending on the beam cross section shape. Integrating 3.29 one gets the Toushek lifetime:

$$\tau_{Touschek} = \frac{1}{\alpha N_0} \tag{3.30}$$

where N_0 is the initial beam population. For the LHC at the injection energy the $\tau_{Touschek}$ is 4830,9 hours [67] which is much larger than length of a typical period between the consecutive refills of the LHC.

3.3.3 Beam-Beam Effects

Another important contribution to beam losses comes from the beam-beam interactions at the 4 collision points. Elastically scattered protons populate the beam halo causing the transverse beam emittance growth. This effect contributes mainly to the luminosity decay:

$$\mathcal{L}(t) = \frac{\mathcal{L}(0)}{1 + \frac{t}{\tau_0}} \tag{3.31}$$

where $\mathcal{L}(0)$ is the luminosity of the beam at the initial time and the τ_0 is the initial decay time described by:

$$\tau_0 = \frac{N(0)}{\mathcal{L}(0)\sigma_{tot}k} \tag{3.32}$$

were $\sigma_{tot} = 10^{-25}$ cm $^{-2}$ is the total cross section at 7 TeV and k is the number of interaction points. The beam luminosity lifetime due to the beam-beam interaction is 29 hours.

3.3.4 Residual Gas Beam Scattering

In the LHC beam pipe, the ultra-high vacuum (UHV) ranges between 10^{-10} and 10^{-11} mbar [2]. Usually, the LHC UHV is described by normalizing to the equivalent hydrogen gas density. To satisfy the requirement of the beam lifetime exceeding 100 hours it should remain below 10^{15} $\mathrm{H_2m^{-3}}$. In the interaction regions it is less than 10^{13} $\mathrm{H_2m^{-3}}$ to minimize the background [2]. Due to the distributed vacuum pumping system, the vacuum pressure is considered to be stable.

The remaining gas consists mainly of hydrogen (about 90%), methane, carbon monoxide and carbon dioxide [70]. The gas mixture combines the so-called residual gas. The gas composition depends on the local temperature (warm/cold aperture), LHC section (straight/arc section) and on the material of the vacuum chamber. To reduce the desorption effects some parts of the warm aperture are covered with the Non-Evaporable Getter (NEG) coating [2]. The desorption of the gas can be induced by thermal effects (mostly in warm aperture) or by the beam phenomena: e. g. ion, photon, electron induced molecular desorption [70]. In arcs also the synchrotron radiation can induce the desorption. Thus, it is roughly proportional to the luminosity of the LHC.

The main process causing the background due to the beam-gas interaction is the multiple Coulomb scattering resulting a slow diffusion of the protons from the beam core resulting in the emittance growth [70]. The emittance growth causes the the increase of betatron amplitude of particles. Such particles are feeding the beam halo, and after many turns they are intercepted by collimators. Similar behaviour can be observed for small-angle elastic nuclear scattering. In case of the very small scattering angle it is not possible to distinguish the elastically gas-scattered particles from the beam halo [71].

The inelastic residual gas-beam scattering results secondary particles with much larger polar angles. Such particles are lost in the LHC aperture within few tens to few hundreds of meters [70]. The rates of the inelastic nuclear interactions are expressed in the units of $\mathrm{m^{-1}s^{-1}}$. Typical values for Point 1 are about 10 in the experimental cavern region, 20–30 in the warm aperture within the straight section, 400 in the inner triplet and $8 \cdot 10^3$ within the arcs, while the total number of elastic and inelastic nuclear interactions upstream of the ATLAS IP is $3.07 \cdot 10^6$ p/s per beam [70]. The values given above are typical for the standard LHC beam operation.

3.4 Beam Loss Diagnosis

The Beam Loss Monitor system consists of a set of about 4000 detectors measuring radiation installed along the LHC ring. The BLMs located in the LHC straight sections have 89 μs time resolution, which corresponds to one single revolution of particles. In case of the beam losses exceeding the threshold, the BLM system triggers a beam dump within 3 revolutions [72]. The thresholds are calibrated during special runs with low beam intensity – only a few bunches are injected. In such runs the beam instabilities are increased by setting the tune close to the integer number, which moves the transverse oscillations into the resonance region (see Section 3.1.2), or adding the transverse noise using the transverse damper system, intentionally designed to damp the instabilities during injection and ramping. The second method is preferred by the beam experts, as allows to set different transverse noise for each injected bunch separately.

The map of the beam dump thresholds for the BLM is called the loss map. The map must be prepared for all LHC settings used during the data-taking, as different positions of the collimators, Roman Pots or other equipment may have non-negligible impact on the amount of beam losses in certain locations along the beam pipe.

Chapter 4

LHC Beam Collimation

The LHC accelerator stores the energy of over 300 MJ within the beams, see Table 1.3. Since there always exist some beam losses which uncontrolled may affect the accelerator operation, cause the superconducting magnet quench or damage sensitive apparatus then proper measures have to be taken to minimise their influence. A multistage collimation system is used for this purpose. Additionally, this system covers other tasks. The most important in the context of this thesis are:

- minimisation of the beam-induced background,
- beam halo scraping,
- cleaning of the betatron and off-momentum halos.

The collimation system also provides a passive protection of the machine, protects the radiation sensitive equipment by absorbing the radiation, concentrates the radiation doses inside of the collimator jaws, removes the collision products (the so-called physics debris), and supported by the Beam Loss Monitors can be used for the beam halo diagnostics [73].

4.1 Beam Amplitude and Machine Aperture

As it was already pointed in Chapter 3.1, a bunch contains particles oscillating around the designed orbit with some transverse amplitude given by Eq. 3.20. The bunch consists of two main parts – the core containing particles traversing within 3 σ from the ideal trajectory and the tails – located outside this range. The beam core to a good approximation is considered as Gaussian. Particles belonging to the tails create the so-called beam halo. The value of 3 σ is rather arbitrarily established [73]. The beam cross section is illustrated in Fig. 4.1.

The beam width is also used as a unit for specifying the distance of movable

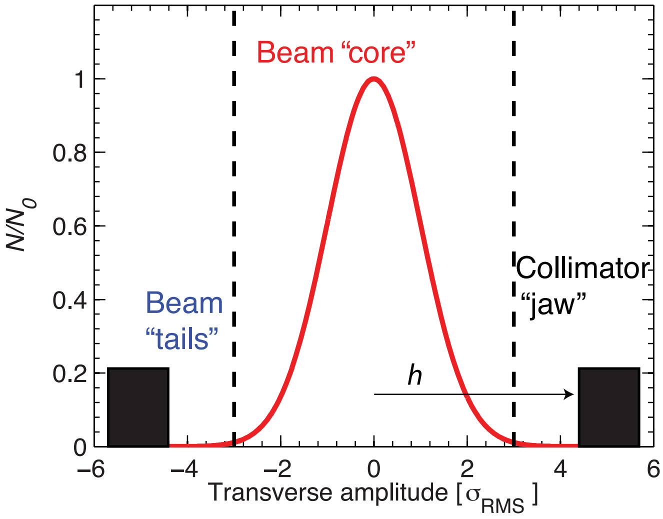

Figure 4.1: The Gaussian beam cross section [73].

devices like collimators or Roman Pots from the beam:

$$n_\sigma(s) = \frac{h}{\sigma(s)} \tag{4.1}$$

where $\sigma(s)$ is the beam transverse size at the particular location, h – the distance between the beam centre and the movable device. Those units are based on the betatron size of the beam, which means that only the betatron term of Eq. 3.22 is considered.

Another important parameter is the geometrical aperture – A_{geom} – which describes the amount of the space available to the beam within the vacuum chamber (vacuum pipe), including the instrumentation installed inside the chamber. The aperture is usually given in the units of σ. Its value must always be larger than the beam, otherwise the particles will hit the vacuum chamber walls or other instrumentation and they will be lost.

4.2 Collimators

The LHC collimation system consists of 88 moveable ring collimators, (44 per beam) which were used during Run 2 beam operation [2, 74]. The layout of a complete collimation system is presented in Fig. 4.2. Collimators in the IR3 section intercept the particles with high momentum deviation (off-momentum cleaning). The IR7 collimators perform the betatron cleaning function, i.e. they remove halo particles with large betatron oscillation amplitude [67]. The other collimators located downstream of the experiments are used for the physics debris removal and those upstream ones to protect the final focusing magnet triplets. In addition, there are collimators protecting most sensitive points of the LHC – at injection (IR2 and IR8 for Beam 1 and Beam 2, respectively) and in IR6 – protecting the beam extraction facilities.

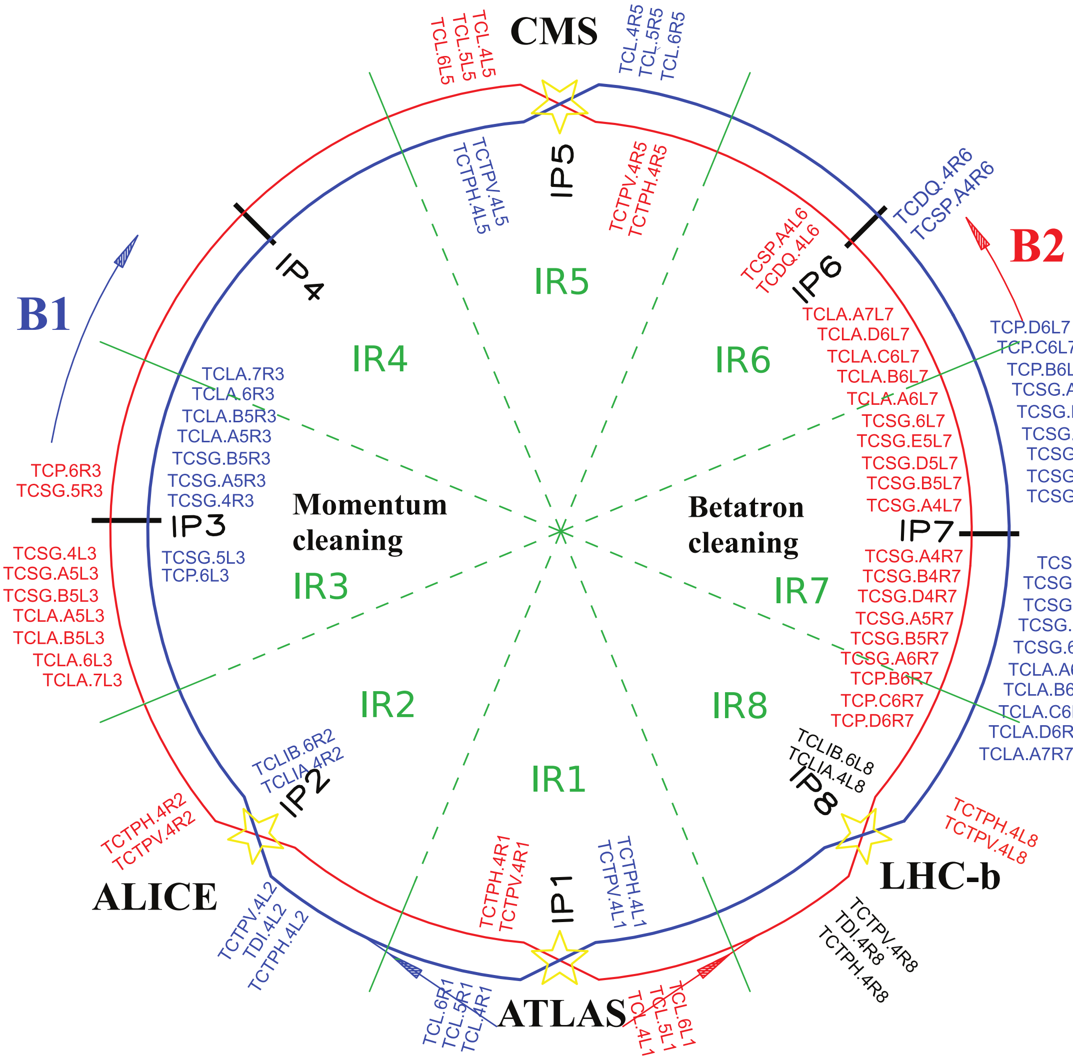

Figure 4.2: The layout of the collimation system used at the LHC during Run 2 [74]. Collimation layout in the LHC as of Run 2, for both beams. Bent crystals acting on the vertical plane are placed between TCSG.A6[L,R]7 and TCSG.B5[L,R]7 in beam [1,2].

The naming of the collimators follows the standard convention used for devices installed in the LHC tunnel. As an example, TCLA.A5[L/R]3.B[1/2] refers to a collimator type TCLA; A5 – corresponds to the 5th cell of the LHC section (cf. Chapter 2.3). [L/R]3 means Left or Right side of the IP3 and B[1/2] defines which beam the collimator acts on [75]. A short description of each type of the collimator is given in Table 4.1.

A typical collimator is presented in Fig. 4.3. It consists of two movable jaws. Each jaw is controlled by two stepping motors which allow the transverse movement

Table 4.1: Collimator types used during the LHC operation in Run 2.

Collimator	type	jaw material	location	Comments
TCP	Target Collimator Primary	CFC	IR3, IR7	Primary stage collimators for beam cleaning
TCPCV	Target Collimator Primary Crystal Vertical	Si	IR7	Primary stage one-sided crystal collimators for beam cleaning
TCSG	Target Collimator Secondary Graphite	CFC	IR3, IR7	Secondary stage collimators for beam cleaning
TCTPH/ TCTPV	Target Collimator Tertiary with ***Pick-Up Horizontal/Vertical	Tungsten	*IR1, IR2, IR5, IR8	Tertiary stage collimators for triplet magnets protection with ***Pick-Up
TCLA	Target Collimator Long Absorbers	Tungsten	IR3, IR7	Shower absorbers downstream of the cleaning insertion
TCL	Target Collimator Long	Copper	**IR1, IR2, IR5, IR8	Absorbers for physics debris from experiments
TCLI	Target Collimator Long for Injection	CFC	IR2, IR8	Injection magnets protection, A,B suffics corresponds to protected magnet
TCDI	Target Collimator Dump Injection	graphite/ CuZrCr alloy	IR2, IR8	Injection protection in the case of a malfunction of the injection kickers
TCDQ	Target Collimator Dump Quadrupole	CFC	IR6	Beam extraction magnets protection
TCSP	Target Collimator Secondary with ***Pick-Up	Tungsten	IR6	Secondary stage collimator with ***Pick-Up supporting TCDQ
TAS	Target Absorber Secondaries	Copper	IR1, IR5	Protects the inner triplet from the physics debris (secondary particles)
TAN	Target Absorber Neutral	Copper/ concrete	IR1, IR5	Protects the Dipole 2 from the neutral particles outgoing from the IP
TCHS	Target Collimator Horizontal Scraper	****vary	****IR3, IR7	Single-jaw collimators used only for special runs devoted to beam and halo diagnosis

*installed upstream of the interaction region

**installed downstream of the interaction region

***Pick-up is a type of BPM embedded in the collimator jaw

****TCHS collimators are under development, thus meterials, number of installed devices and locations are varying over time

and angular adjustment [67]. In case of the motor failure, the jaws can be retracted by the return springs. The collimator is installed inside of a vacuum tank. Another stepping motor allows adjustment of the full collimator assembly in the perpendicular direction to the jaws movement line [76]. This feature allows to present a fresher jaw surface to the beam in case of significant radiation damage in the beam impact area.

The jaws are equipped with water cooling to dissipate the heat load from the energy deposited by the intercepted particles. To facilitate the heat transport from the jaws to the heat exchanger, special clamps improving the contact between them were developed. Another function of the clamps is the compensation of the mechanical stress due to different thermal coefficients of the used materials. It is worth mentioning that the collimator surroundings are highly radioactive areas. To reduce the time required for any repair service or maintenance jobs, special quick connectors and flanges were developed.

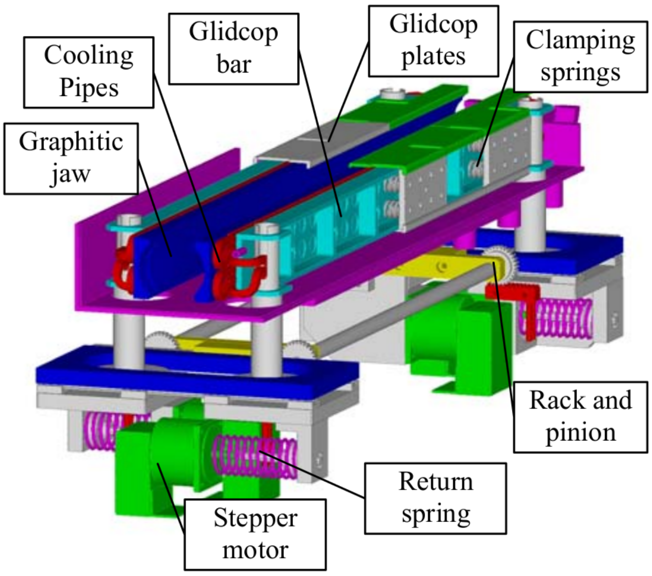

Figure 4.3: An overview of the collimator assembly. [76].

An ideal collimator should have a circular inner aperture. Such a solution would be very problematic since the aperture has to be adjustable. Therefore, the jaws are flat, but installed in three planes. Horizontal (H) – used for both – the off-momentum and betatron cleaning. Vertical (V) and skew (S) planes are used only for the betatron cleaning area. The off-momentum dispersion propagates mostly horizontally, thus the use of the horizontal collimators is sufficient.

At the LHC the collimators are divided into four classes according to their tasks:

- Collimators (TCP, TCSG),
- Movable Absorbers (TCT, TCLA, TCL),
- Diluters (TCLI, TCDQ, TCDI),
- Scrapers (TCHS).

The following description of the collimator classes is based on [77].

The main task for the collimator class devices is cleaning the beam halo. They scatter the halo particles by inducing the inelastic interactions in their jaws material. The jaws are made of carbon-reinforced composite (CFC) and graphite which are very robust to radiation, making the collimators most robust devices along the LHC ring. On the other hand, due to small jaws material density they absorb only a small

fraction of the particle energy and, thus, cause the secondary and tertiary halo. The secondary task for collimators is the machine protection.
Movable absorbers are very similar to collimators, but their jaws are made of different material. Instead of scattering, the movable absorbers intercept the tertiary halo (TCTs), particle showers from cleaning insertions (TCLA) and the collision products (TCL). As they are very delicate and can be damaged by higher beam losses, they are always kept in the shadow of the collimators of the first class – further from the beam expressed in σ.

Diluters are mainly the machine protection devices. They are installed in the injection and beam-dump areas. In case of the injection error or emergency beam-dump, the mis-kicked beam impacts onto the diluters. They partially absorb the lost beam energy and cause strong emittance growth (dilution).

The scrapers are used only during the special runs devoted to the machine development and diagnostics.

In case of a regular LHC operation only the first two classes of the collimators are used. Their exact positioning follows from precise calculations and simulations.

4.3 Multi-stage Collimation

The LHC collimation is a multi-stage system. Such collimation paradigm is used to increase the cleaning efficiency. Schematically the multi-stage collimation idea is presented in Fig. 4.4.

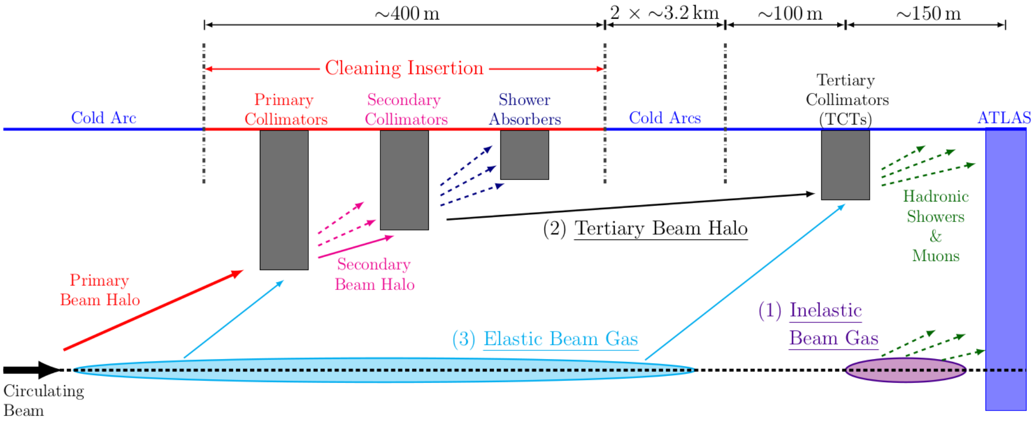

Figure 4.4: Idea of the multi-stage collimation [78].

The beam halo particles hit the primary collimators, which are the closest devices to the beam. The halo particles interacting with the TCP jaws cause the secondary halo and hadronic showers. The same idea serves the secondary collimation stage. The secondary collimators are placed in the shadow of the primary ones.

Hadron showers caused by the collimators are absorbed by movable absorbers – TCLAs. The tertiary halo caused by secondary collimators and not absorbed by TCLAs travels in the close vicinity of the beam and is absorbed by tertiary collimators made of a high density material to absorb as much energy as possible.

An example of the betatron cleaning set-up is presented in Fig. 4.5 for an injection energy (upper panel) and collision energy (lower panel). The scheme shows that during the injection the main limitation is the cold aperture – the aperture available in the superconducting magnets with safe margin established as 7.5 σ [67]. With the acceleration, the arc aperture becomes less critical and at the top energy it is 32 σ. Due to optics settings the main limitation are triplet magnets. Thus in the collision phase, the tertiary collimators are inserted.

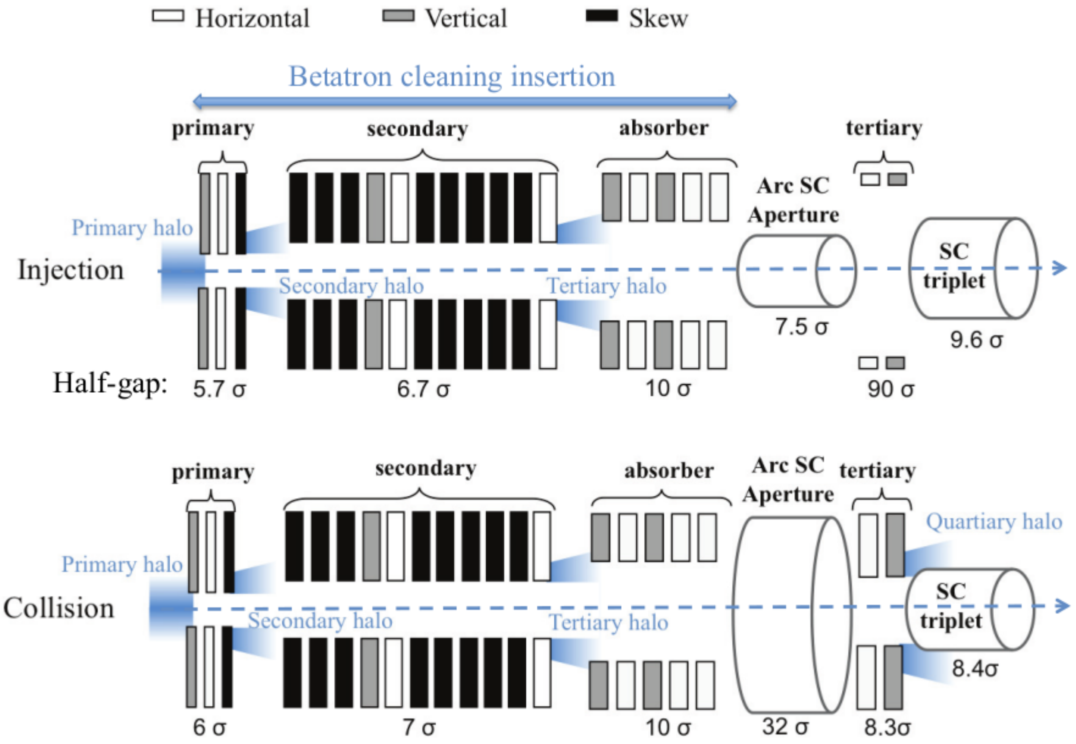

Figure 4.5: Typical positions of collimators at the injection energy (upper panel) and at the collision energy (lower panel) [67].

For the rest of the collimation system, the settings are given in Table 4.2. One can see that the off-momentum collimation is tight only during injection. When the LHC is at the top energy the collimation is looser – 15-20 σ, depending on the collimation stage.

A proper positioning of the collimation system elements confines the beam losses to the cleaning areas, keeping the losses in the cold aperture (superconducting surroundings) below the magnet quench limits. It is very important to reach the

Table 4.2: Positions of the collimators at the injection energy and during collisions. [67].

Location	Collimator type	Half-gap [σ]	
		Injection	Collision
IR7	TCP	5.7	6
	TCSG	6.7	7
	TCLA	10	10
IR3	TCP	8	15
	TCSG	9.3	18
	TCLA	10	20

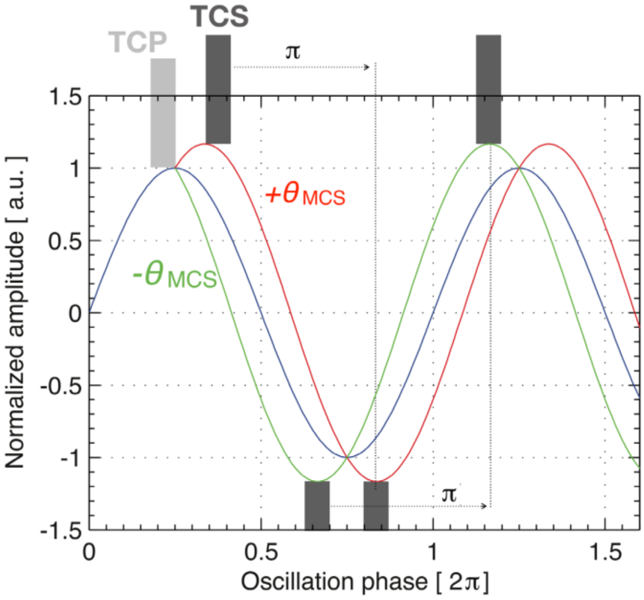

Figure 4.6: The principle of arranging collimators in a multi-stage hierarchy [73].

highest betatron oscillation amplitude in the location of the primary collimators to obtain maximum collimation efficiency. The TCPs cause the secondary halo alternating the oscillation phase advance of the particles. This is caused by the Multiple Coulomb Scattering (MCS). The MCS causes the phase advance offsets by $-\Theta_{MCS}$ and $+\Theta_{MCS}$ angles, see Fig. 4.6. Thus, the secondary collimation uses more devices to cover a wider spectrum of the oscillation phases. An optimal efficiency of the collimation can be achieved by placing two secondary collimators at unique phase advance locations after the primary collimators [79].

The above discussions shows the general idea using one-dimension model, but the reality is more complex as the MCS occurs in all directions. Thus, the number of secondary collimators is much higher than number of the primary ones, however these effects are beyond the scope of this thesis.

4.4 Collimation Performance

The main parameter characterizing the collimation system is the global cleaning inefficiency, η_c, [67]. It describes the leakage rate of particles that should be removed from the beam halo. The inefficiency considers only particles with a higher oscillation amplitude A (measured in n_σ) than the aperture A_c.
It is given by:

$$\eta_c(A_c) = \frac{N_{\text{leak}}}{N_{\text{impact}}} \tag{4.2}$$

where N_{leak} is the number of particles escaping the cleaning area with amplitude A higher than the aperture A_c and N_{impact} is the total number of particles which have inelastically interacted with jaws of the collimators. In case of the LHC, during a regular operation the aperture A_c is considered as the distance between TCLA absorbers and the beam core and is around 10 σ. The η_c is required to be below 10^{-3}.

Apart from the global inefficiency, the local one is important, as even though the global one meets the requirements, in some locations the losses might exceed the quench limit.

4.5 Amorphous Collimation

The collimators used so far at different accelerators, including the LHC, are based on the same idea – the use of the amorphous jaws to intercept or scatter the halo particles. The main parameter which is considered in the design of the collimator jaws is the stopping power $-dE/dx$ expressed by the Bethe-Bloch formula:

$$-\frac{dE}{dx} = Kz^2\frac{Z}{A}\frac{1}{\beta^2}\left[\frac{1}{2}ln\frac{2m_ec^2\beta^2\gamma^2W_{max}}{I^2} - \beta^2 - \frac{\delta(\beta\gamma)}{2}\right] \tag{4.3}$$

where K is a constant coefficient, z – the charge of incident particle, Z – the atomic number of the absorber (jaw material), A – the atomic mass of the absorber expressed in g/mol, m_e – the electron mass, c – the speed of light, β and γ are the Lorentz coefficients, I – the mean excitation energy, W_{max} – the maximum energy transferred to an electron in a single collision, $\delta(\beta\gamma)$ – the density effect correction to the ionization energy loss [80]. This formula describes the mean rate of the energy loss per unit length with an accuracy of a few percent.

Second process taking place in the jaw material is the Multiple Coulomb Scattering. A charged particle traversing the jaw material interacts with it via the Coulomb force. Due to many such interactions its path is deflected and the resulting deflection

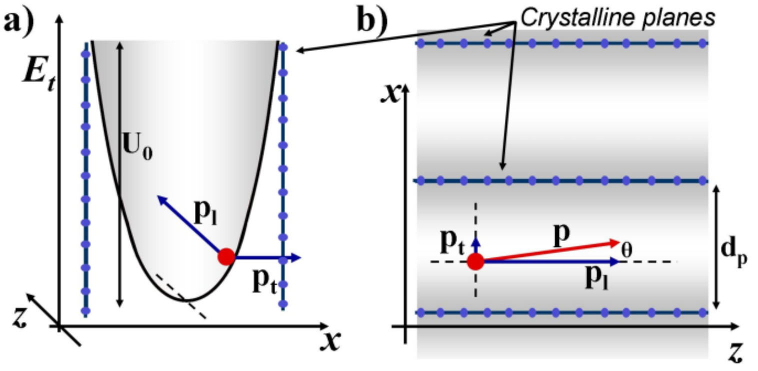

Figure 4.7: *LEFT:* Potential well between crystal planes. *RIGHT:* Reference frame for protons entering the crystal. [75].

angle, $\theta_x(s)$, is given by:

$$\theta_x(s) = \frac{13.6\ MeV}{\beta_{rel} c p} z \sqrt{\frac{s}{X_0}} \left[1 + 0.038 \ln\left(\frac{s}{X_0}\right)\right] \tag{4.4}$$

where, p – the particle momentum, s – the traversed material thickness, c – the speed of light, z – the incident charge, X_0 – the material radiation length. The last one is defined as the distance after which the particle looses $1/e$ of the initial energy.

4.6 Crystal Collimation

In contrast to the amorphous collimation, where the halo particles are scattered in all directions, the crystal collimators are in a sense guiding the halo particles and bending their trajectories into the absorber. It is due to the coherent interactions with atoms belonging to the crystal lattice. The crystal collimation is described in [75].

In Fig. 4.7 the reference system is defined. Assume the particle enters a crystal in between the lattice planes with momentum p, marked with the red arrow. One can decompose the momentum into the transverse and longitudinal components – p_t and p_l, respectively. Trapping between the crystal planes is possible only if the p_t is very small. Such trapping of particles is called the crystal channelling and the space between the crystal planes is called a channel. As the crystal lattice is acting on a particle in the transverse direction the transverse energy is given by:

$$E_t = \frac{p_t^2 c^2}{2E} + U(x) \approx \frac{p^2 c^2 \theta^2}{2E} + U(x) \tag{4.5}$$

where $p_t \approx \theta p$ is assumed due to the smallness of θ. The potential of the crystal lattice acting on the particle traversing it can be approximated by:

$$U(x) \approx U_{max}\left(\frac{2x}{d_p}\right)^2 \tag{4.6}$$

where d_p is the crystal plane spacing. As the total particle energy is conserved and forces act only in transverse direction, the longitudinal component of the energy is constant and transverse energy is conserved. The crystal channelling effect is possible only if the transverse energy is smaller than the maximum lattice potential U_{max}. U_{max} depends on the physical properties of a crystal. In case of the crystals used at the LHC, the $U_{max} \approx 20\ eV$, $d_p = 1.92$ Å. One can introduce a critical channelling angle, θ_c, describing the maximum θ angle value for which the channelling is still possible:

$$\theta_c = \sqrt{\frac{2U_{max}}{pv}} \tag{4.7}$$

where v is the particle velocity. In case of the LHC θ_c is 9.4 μrad for the injection energy and for the top beam energy (6.5 TeV) $\theta_c = 2.5$ μrad.

The equation of motion of a particle trapped in the crystal lattice can be written as:

$$pv\frac{d^2x}{dz^2} + \frac{8U_{max}}{d_p^2}x = 0. \tag{4.8}$$

Such a particle will follow a sinusoidal trajectory, given by:

$$x(z) = \frac{d_p}{2}\sqrt{\frac{E_t}{U_{max}}}\sin(\frac{2\pi z}{\lambda} + \phi) \tag{4.9}$$

where λ is the oscillation period, which is usually about a few tens of micrometres and ϕ is the oscillation phase depending on the initial conditions at the edge of the crystal.

To deflect the channelled particle trajectory to the absorber and to clean the beam, the crystal is bent. For a small bending angle the particle behaviour is not changing a lot and to a first approximation introduction of only the centrifugal component pv/R into Eq. 4.8 is sufficient:

$$pv\frac{d^2x}{dz^2} + \frac{8U_{max}}{d_p^2}x + \frac{pv}{R} = 0 \tag{4.10}$$

where R is the bending radius. The radius cannot be too big, as the channelling effect might be lost due to increase of the transverse momentum. In case of the LHC the minimal bending radius is 1.1 m at injection energy and 15.6 m at the top energy. In general the particle trajectory in the bent crystal is still sinusoidal, however its equilibrium is offset due to the centrifugal force. One can defined an effective potential acting on the particle as:

$$U_{eff}(x) = U(x) + \frac{pv}{R}x. \tag{4.11}$$

In consequence the potential wells in Figs 4.8 – 4.10 have increasing potential deeps.

The channelled particle might loose the conditions of channelling due to the interaction with the crystal nuclei or electrons. Those interactions cause de-channelling if the energy of transverse oscillation of a particle increases above the U_{max} potential. The process can be modelled as an exponential decay using the characteristic de-channelling length L_D:

$$N(x) = N_0 \exp\left(-\frac{x}{L_D}\right) \tag{4.12}$$

where $N(x)$ is the number of the channelled particles after the path x and N_0 is the initial number of the channelled particles. L_D can be calculated using diffusion theory [75].

The idea of the de-channelling effect is presented in Fig. 4.8. The left panel shows a particle entering the bent crystal, channelled properly and after some path the particle transverse energy is increased enough to cross the potential barrier and in consequence it is lost. The right panel shows the potential diagram with a particle marked in one of the potential wells.

In a similar way the particle can be captured in the middle of the crystal, see Fig. 4.9. Such a phenomenon is called the volume capture. The left panel shows a particle entering the crystal at θ greater than θ_c. Such particle cannot be channelled. After some path the angle between the particle trajectory and the crystal layers gets smaller due to the crystal bending. If θ gets small enough – smaller than θ_c – the particle can be captured by the potential between the crystal layers. The right panel presents the potential diagram of the described phenomenon. Once captured a particle behaves like the one channelled from the beginning of the path, and might be de-channelled as other particles.

Another important process is the volume reflection. If a particle impinges on the bent crystal at the angle slightly grater than θ_c, but still smaller than the crystal bending angle, the volume reflection process is possible. The particle entering the crystal cannot be chanelled, but as its trajectory is tangent to the crystal plane, it can be reflected. This effect can be determined only via geometrical considerations. Such process is very efficient – 90% of particles satisfying conditions of the volume reflection is indeed reflected. The idea is presented in Fig. 4.10.

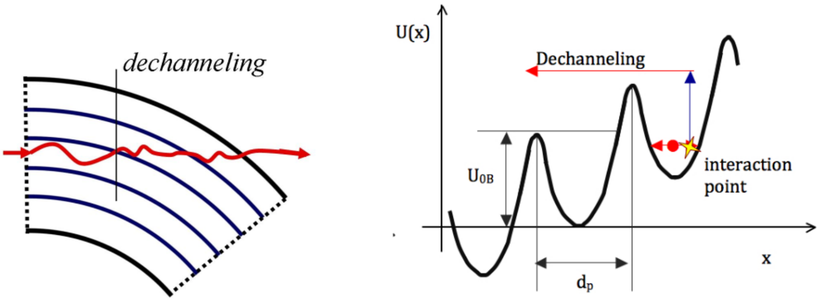

Figure 4.8: Dechannelling effect. [75].

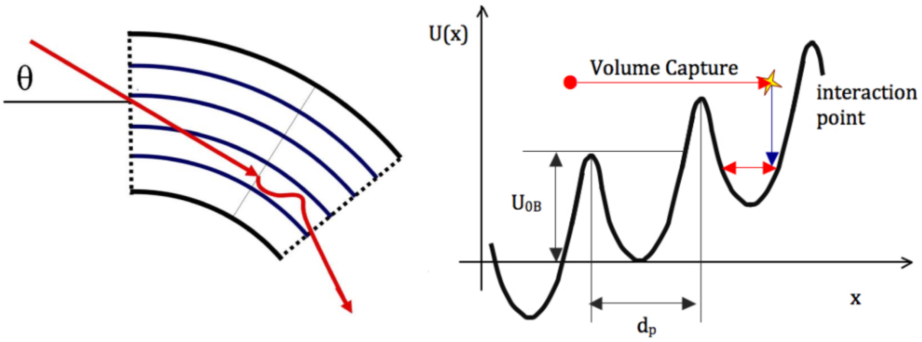

Figure 4.9: Volume capture [75].

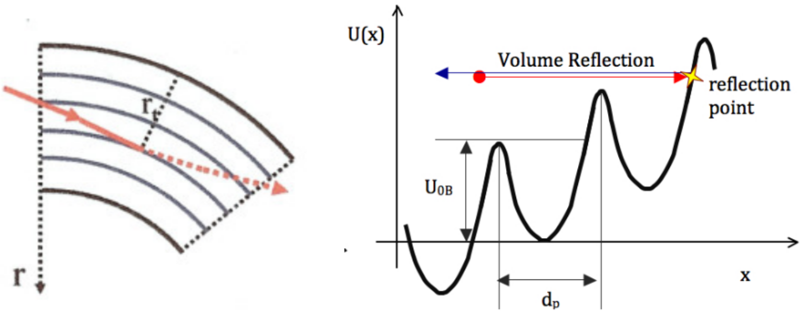

Figure 4.10: Volume reflection [75].

4.7 Beam-Based Alignment – BBA

The beam trajectory is very complex due to many variables which influence it. Also, the beam position evolves with time. In fact, there are several effects adding to a slow evolution of the beam position even if the machine settings are fixed: long exposition of the infrastructure to ionizing radiation, apparatus ageing etc.

On the other hand there are several movable equipment pieces which positions need to be adjusted very precisely with respect to the beam with accuracy of the order of a few tens of micro metres. These devices are collimators and movable detectors, like ALFA, AFP or TOTEM [2, 37, 23, 81]. Such precision cannot be solely based on the Beam Position Monitor readout. It can be obtained only via a direct beam position check using the beam-based alignment (BBA) method.

The BBA is performed using a low intensity beam. When the beam parameters are stabilised, the LHC operators move the collimators towards the beam until the jaws "touch" it. This moment can be recognized by a sudden appearance of a peak in the number of counts seen by the beam loss monitors (BLM) installed near the collimator. The relative positions of the BLMs are presented in Fig. 4.11.

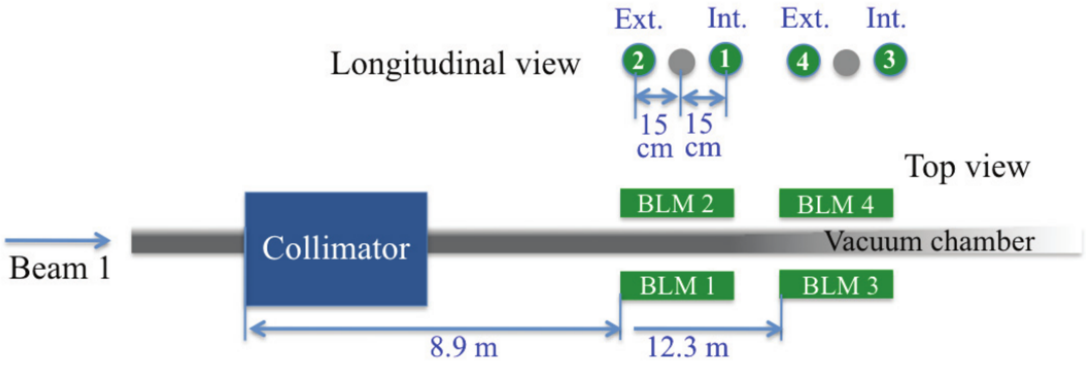

Figure 4.11: Mutual positions of the beam loss monitors and collimator being aligned [67].

This procedure must be performed after each long or technical shutdown, and each time when the key parameters of the LHC are changed. This procedure for all collimators takes about 4.5 hours and is fully automated [82].

4.8 Source of the Beam Background – Tertiary Halo

The tertiary halo consists of particles escaping the betatron and momentum cleaning insertions. As this term is related to the inefficiency of the main collimation system, it is also called "collimation tails" [83]. This source of the background being caused by the machine collimation is also referred to as the machine induced background (MIB). Effects originating from the tertiary halo are the main point of considerations within this thesis, see Chapters 6 and 7.

The tertiary collimators are located about 150 meters from the interaction point upstream of the IP, see Fig. 4.12. The ATLAS IP is located at 0. The copper Target Absorber Secondaries (TAS) is located between $|z| = 19$ m and $|z| = 20.8$ m. Its inner diameter is 17 mm [78]. It is followed by the inner triplet installed between $|z| = 23$ and $|z| = 54$ m. At $|z| = 70$ m the Dipole 1 (D1) is positioned, the so-called separation magnet. The recombining Dipole 2 (D2) is located at $|z| = 160$ m. After D2, the beams trajectories are separated by a distance of 194 mm and parallel. The D2 is protected against the physics debris by the Target Absorber Neutral. The TCT is located between the TAN and the D2 on the incoming beam.

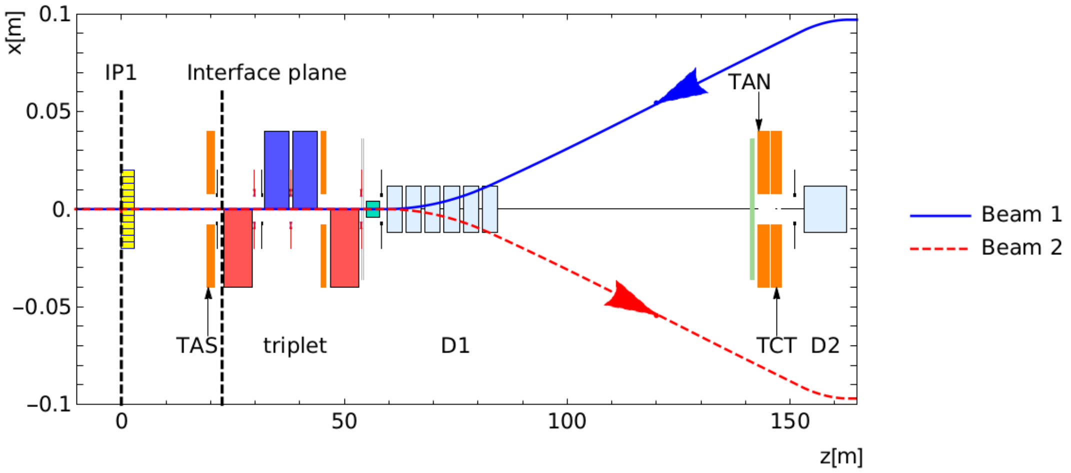

Figure 4.12: A relative position of the TCT upstream of the ATLAS interaction point. It is located behind inner triplet and separation dipole D1 at about 140 m from the ATLAS IP [78].

During the normal LHC beam operation, the tertiary halo is removed by tertiary collimators. Due to localisation of the betatron and momentum cleaning insertions the tertiary halo is highly asymmetric, thus, in the experiments, the rate of tertiary halo will be different in each beam. For example, the rate of the loses on the TCTs, in the typical LHC run, is $4.28 \cdot 10^6$ p/s for the Beam 1 approaching the ATLAS IP [70]. For Beam 2 outgoing from the off-momentum cleaning insertion the loss rate on the TCTs is about 10% less. The losses on the TCTs contain also a contribution of particles scattered from the residual gas. Dedicated tests have proven that the contribution of the TCTs inefficiency to the background seen in the ATLAS experiment is negligible – below 1% of the total observed background [84].

In case of the ALFA special runs the situation is more complicated as the functions of collimators were changed – the TCTs were used as the secondary stage collimators [85]. Detailed discussion is given in Chapters 6 and 7.

Chapter 5

ALFA TDAQ and ALFA_CTPIN

In the ATLAS experiment the trigger and data acquisition are systems operating in real time and designed to select a BCID with interesting physics phenomena using a chain of filtering algorithms and transfer the corresponding data from detectors to a permanent storage.

The Central Trigger Processor upgrade for Run 2 reduced the first level trigger latency (time of response), which could exclude ALFA from operation in a combined mode with other ATLAS sub-detectors. To participate in the combined running, ALFA designed and developed a module that delivers ALFA signals directly to the core of CTP. This allowed reducing the time elapsing from the moment when protons cross ALFA detectors till the moment when CTP receives ALFA signals and can use them to produce the final ATLAS L1A decision. The module named ALFA_CTPIN [86] was developed and will be introduced within this chapter, including a presentation of its capabilities useful for beam-induced background determination.

This chapter introduces detailed description of ALFA TDAQ system. Sections 5.1 and 5.2 describe architecture of the system and Section 5.3 is devoted to the TDAQ software. ALFA_CTPIN module is described in Section 5.4. Its commissioning and dedicated tools are discussed in Sections 5.5 and 5.6. The last Section presents the commissioning of the ALFA_CTPIN module.

5.1 ALFA Trigger and Data Acquisition

The implementation of the ATLAS TDAQ system at the sub-detector level has to comply with requirements on bidirectional communication between central and peripheric trigger systems. The synchronization signals (LHC clock, orbit) and L1 trigger decisions generated at the central level have to be distributed to the front-end electronics in one way but the trigger and BUSY signals generated at the detector level have to be sent to the central system in the other way.

The ALFA TDAQ uses an ATLAS-wide set of modules to synchronize with the

ATLAS central trigger system. The LTP (Local Trigger Processor) is the main module in the set. The main task of this module is to generate and distribute synchronization signals and L1 trigger decisions. The module can be configured to receive signals from the ATLAS Central Trigger Processor. This is the configuration used in ALFA dedicated runs when ALFA participates in the ATLAS combined run with other sub-detectors. The LTP is then set to operate as a slave module with respect to the ATLAS Central Trigger Processor and all synchronization signals together with L1 trigger decisions are received from the CTP.

Alternatively, the module can be configured in the stand-alone mode when it can generate synchronization signals based on a local 40 MHz oscillator and L1 trigger decisions based on predefined patterns of signals from the ALFA detectors. This configuration is used when ALFA experts perform tuning and calibration of the Front-End electronics independently of ATLAS TDAQ operation.

The LTP acts also as an interface to receive the BUSY signal from sub-detectors and forward it to a higher level to stop generation of L1 triggers. In the combined configuration the BUSY signal is forwarded to CTP. In the stand-alone mode the active BUSY signal blocks generation of subsequent L1 triggers. The ability to set the LTP either as a slave in the combined runs or as a master in the stand-alone mode allows construction of hierarchical setups with a number of daisy chained[1] LTPs forming a large partition with common synchronization signals and L1 triggers, see Fig. 5.1, left. In such a complex configuration the BUSY from the lower levels is propagated towards the top LTP which controls the generation of L1 triggers.

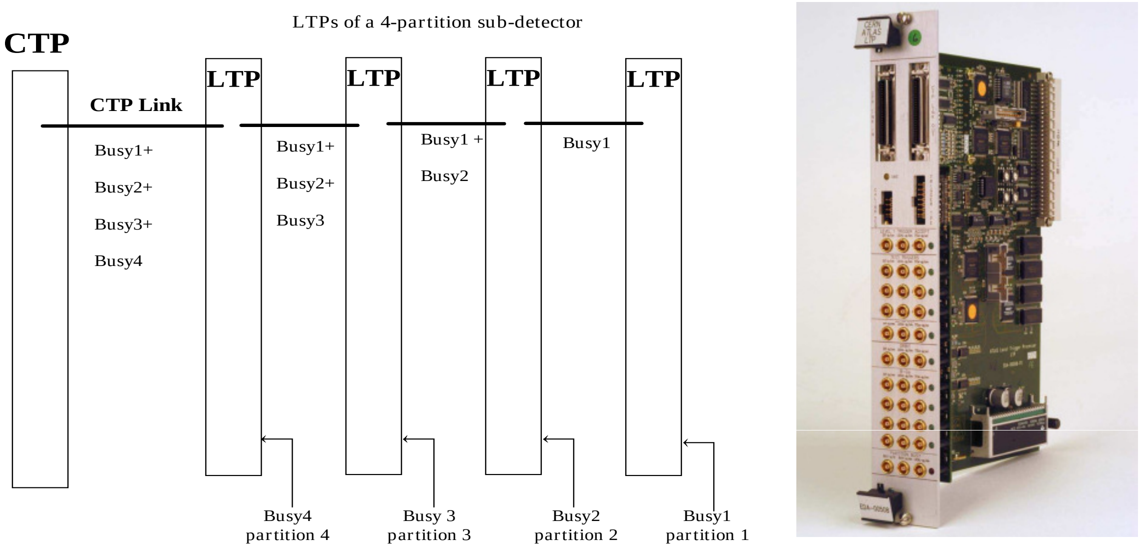

Figure 5.1: *LEFT:* Daisy chain of the BUSY signals of different partitions of a sub-detector [88]. *RIGHT:* Picture of the LTP module [88].

---

[1] A method of propagating signals along a bus in which the devices are connected in series and the signal passed from one device to the next without prioritisation [87].

The LTP is shown in Fig. 5.1, right. On the front panel it has 4 sets of inputs, which can be used to deliver signals from detectors which LTP will use as L1 triggers. The triggers can be produced in corresponding 4 outputs together with 40 MHz clock and Orbit signals. On the front panel there are also 2 connectors – one input and one output to receive (input) and forward (output) electrical signals in case the module is configured as a slave. The signals from the input connector can be duplicated and sent to electrical outputs, clock and orbit. On the front panel there is a BUSY input which can be used to stop generation of next triggers. The low latency trigger and other synchronization signals have to reach the Front-End electronics in a precise moment in time. The LTP can also generate encoded commands which can be used in configuration of the Front-End electronics but they are not required to be precise in time. There is so-called B channel and 4 B-GO outputs which given detector can use to propagate such commands. In case of ALFA TDAQ, the B channel is used in fine tuning of detectors by moving the clock phase in 200 ns steps.

The electrical signals from an LTP can be sent to remaining modules forming the TTC (Time, Trigger and Control) system. The electrical signals of the clock, orbit and L1 trigger are sent to the TTC system which encodes this information into the light pulses distributed to Front-End electronics via optical fibres. A scheme of connections between above modules and the LTP is displayed in Fig. 5.2. In case of the ALFA partition, there is only one set of modules (LTP and TTC) connected to the CTP.

The TTC system allows to merge the low latency trigger and timing commands (A channel) with other commands (B channel) on a single fibre. In the implemented time-sharing mode the signals from A channel have absolute priority and only in case of idle time, the fibre can be used to transfer commands from the B channel.

Short description of the signals exchanged between LTP and CTP is given in Table 5.1.

5.2 Trigger Signal Distribution for ALFA Detector

As it was already mentioned in Chapter 2, each ALFA detector consists of a tracker based on the scintillating fibres and trigger tiles overlapping the active region of the detector. These tiles generate signals which are received by the trigger mezzanine attached to the ALFA motherboard. The trigger mezzanine collects all signals from the respective detector – two from MD and one from each (left and right) ODs, encodes them as 25.0 ns NIM standard pulses for the MD or as a 12.5 ns pulse for the OD. In case there are active signals from MD and OD for the same BCID the trigger mezzanine gives the priority to MD and sends 25 ns long pulse. Moreover, trigger mezzanine can operate in one of a number of modes: single MD tile – only from tile 1 or only from tile 2, coincidence of MD tiles, alternative of MD tiles (at

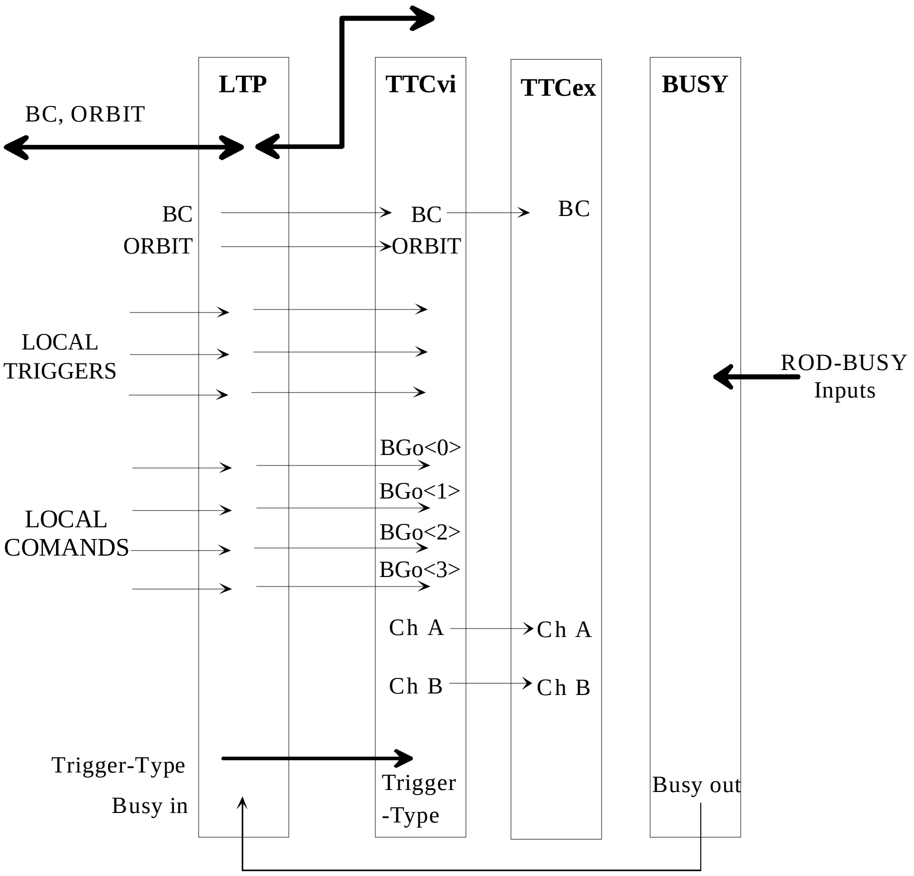

Figure 5.2: Scheme of the TTC partition running in a stand-alone mode [88].

Table 5.1: Signals exchanged between the LTP and CTP.[88].

Name	Function
BC	LHC clock
ORBIT	LHC ORBIT signal used for instance to issue the Bunch Counter Reset (BCR) signal to synchronise counting of bunches.
L1A	L1 Accept signal.
Trigger-Type	8-bit trigger-type word issued by the CTP with each L1A.
ECR	Event Counter Reset signal. Signal used to reset the 24 low-order bits and to increment the 8 high-order bits of the L1ID.
Pre-Pulse	A signal issued by the CTP indicating that in N BC a L1A will be issued. This signal can be used, for instance, to fire a calibration or test pulse at the right time during data taking.
BUSY	The BUSY signal generated by the RODs of the sub-detector when their buffers are almost full. Used by the CTP to introduce dead-time.
Calibration	3-bit word issued by the sub-detector and used by the CTP to generate calibration triggers.

least on of the trigger tiles), left OD, right OD. Encoded trigger signals from all 8 detectors are transmitted through 8 air-core cables to the ALFA_CTPIN module, where those signals are decoded.

Depending on ATLAS trigger menu settings, the ALFA triggers might be pre-scaled with different values depending on the condition of the run. In case of ALFA dedicated runs, only a few BCIDs are filled with protons, which limits the maximal rate for L1A. Moreover, the high β^* value amplifies the effect. Such running conditions allow setting the pre-scale for ALFA triggers to 1 and such settings are considered in this thesis.

The L1A signal generated by the CTP is distributed to all detectors participating in the run, and the receiving module in each sub-detector is the Local Trigger Processor, see Fig. 5.3. The LTP/TTC block in the scheme means that the LTP includes the TTC partition according to Fig. 5.2; The L1A signal for the accepted BCID arrives at the ALFA motherboard at the moment when the data for this BCID are at the end of the FIFO[2] pipeline located in the Front-End. In case the L1 decision is positive the data are copied to the de-randomising buffer and subsequently sent to ROD when the link becomes free. The motherboard attaches information about the selected BCID to the data fragment. This allows verifying the consistency of the fragments with the similar information delivered to MROD from the TTC system. The MROD then combines data from 4 ALFA detectors (the other 4 are received by another MROD) and forwards these data to buffers in ROS.

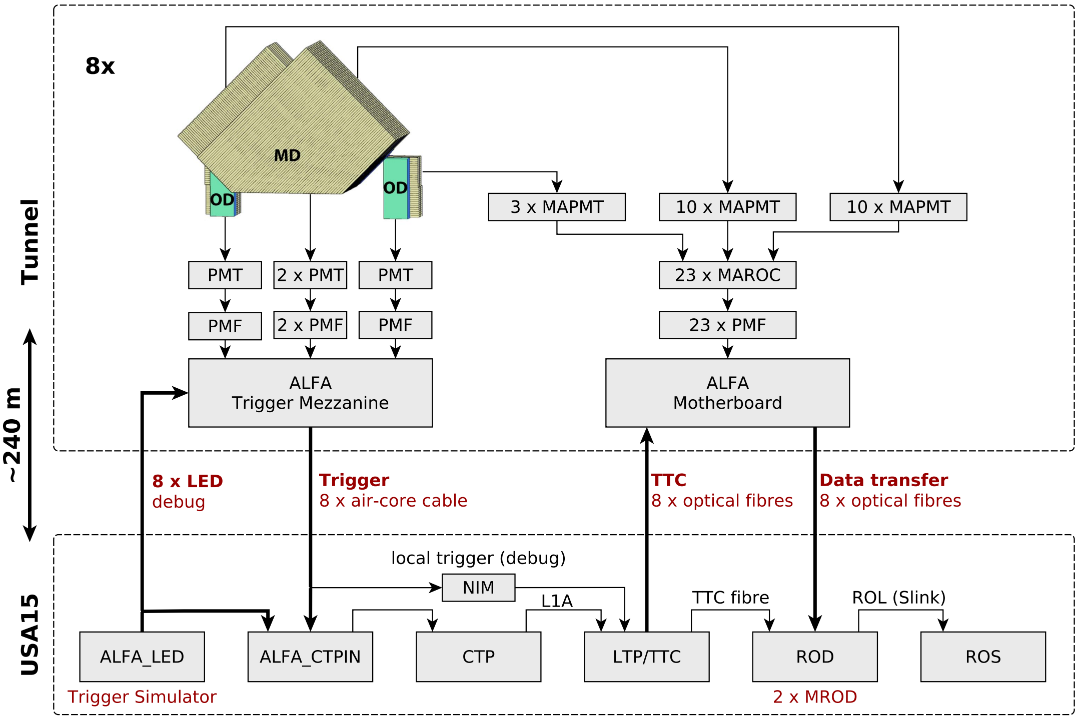

Figure 5.3: ALFA daq cabling [89].

The ALFA trigger signals arrive to CTP via the ALFA_CTPIN module. This

---

[2] FIFO is a type of buffer, where the oldest data (First In) is processed first (First Out).

module bypasses the CTP interfaces and communicates directly with the CTP core what minimizes propagation time of ALFA triggers to ATLAS CTP. The module was introduced in Run 2 when ATLAS shortened the L1 latency and time of flight of protons to ALFA stations and trigger signal travel via the air-core cable became too long.

After 350 m of air-core cable the ALFA trigger signals arrive at the USA15 (counting room) where they are split and delivered to the CTP and to ALFA local trigger electronics. The ALFA local trigger is based on NIM modules where MD/OD decoding is performed and simple logical OR operation producing a trigger when any of the MD or OD sends a signal. This setup allows running local test outside of ATLAS combined runs.

Another module, ALFA_LED visible in Fig. 5.3 is a hardware simulator of the trigger signals designed by the author for ALFA_CTPIN tests [89]. More details about ALFA_LED are given in Appendix B.

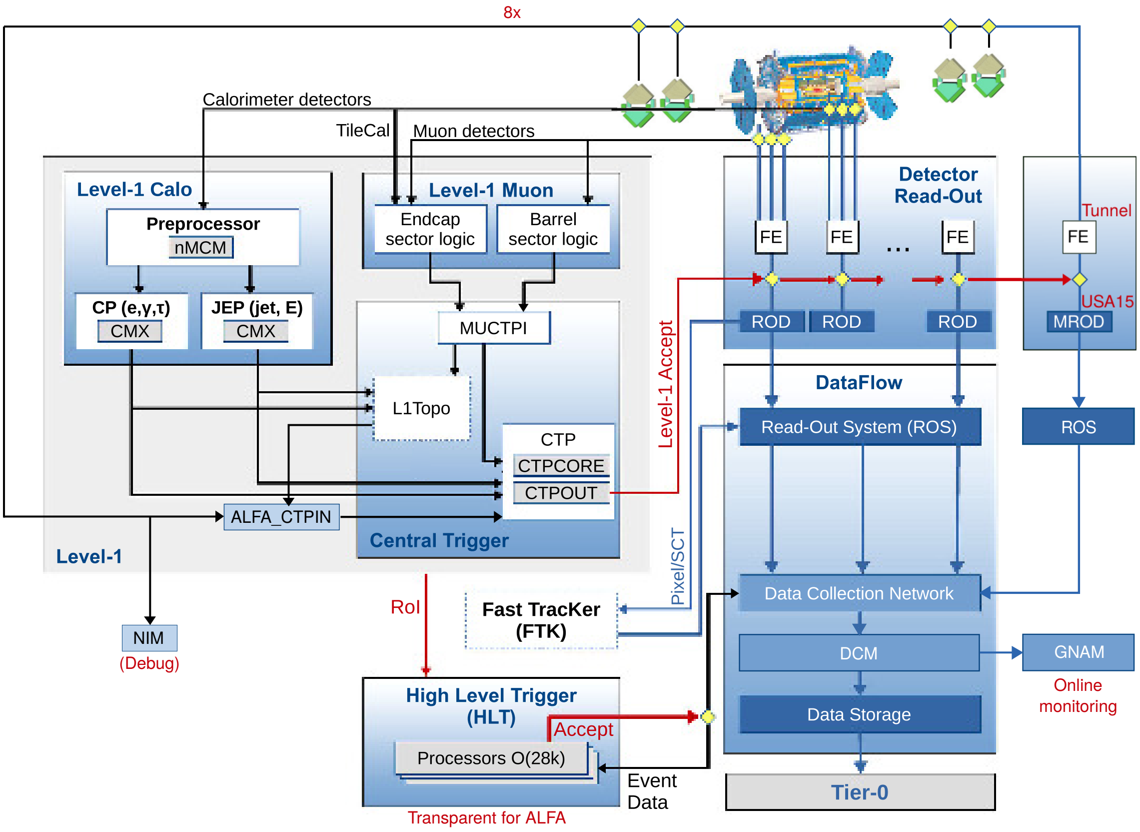

Figure 5.4: ATLAS TDAQ Scheme with ALFA detectors included [30].

The relation of the ATLAS TDAQ and the ALFA is presented in Fig. 5.4 (compare to Fig. 1.6 in Chapter 1.3.2). The ALFA detectors operate very close to the beam and they are out of acceptance of any other ATLAS sub-detectors. Thus, there is no RoI signal covering ALFA detectors. All BCIDs selected by ALFA triggers are thus accepted at the HLT.

ATLAS TDAQ scheme was already presented in Fig. 1.6 in Chapter 1.3.2. The scheme suplemented with elements related to ALFA detector is presented in Fig. 5.4.

5.3 ALFA TDAQ Software

During data-taking it is extremely important to monitor the performance of the detector. In case of ALFA two additional factors contribute – the detectors are moved close to the beam, hence monitoring of detectors response is critical, but also ALFA dedicated runs consist only of a few days per year and collecting unknown data may result in significant loss. Therefore, a big effort was put into development and installation of software packages focused on online data monitoring.

At the CPU farm nodes where DCM and HLT processes are running there can also be activated a GNAM spy process – a process which has access to fully built events using DCM and samples of copies of events can be forwarded to the node where detector quality process (GNAM) is running. When ALFA participates in the ATLAS combined run, 100 GNAM spy processes are distributed across the HLT farm. They are configured to send copies of events from the ALFA calibration stream. The ALFA calibration stream collects events with active ALFA triggers. The event data from the ALFA calibration stream consists of data fragments from ALFA detectors and trigger pattern recorded at the CTP. This allows the GNAM process to recognize ALFA detectors that contributed to ALFA trigger.

The GNAM process decodes data stream and builds histograms with tracks reconstructed using simplified algorithms. This allows experts to deduce if detectors perform as expected and if there are no issues with event data transfers. An example of a GNAM plot is presented in Fig. 5.5.

The Information Service (IS) system is used by the ATLAS online TDAQ applications to access various information spread across a distributed environment. Some of the applications publish information acquired from the event data stream as a snapshot of the current status of detectors in form of objects, histograms etc. Other applications running as clients can access these information and analyse their contents to warn ATLAS operators about possible malfunctioning. The information provided by the publishers is held in memories of IS servers and saved on local hard disks when they terminate.

The IS system does not provide persistency and the information which is exchanged via IS is transient. To allow following the time evolution of certain information, another service PBEAST – Persistent Back-End for the ATLAS Information System of TDAQ – was introduced [90]. It allows gathering information by subscribing to IS servers and getting a callback when the monitored information changes. In the callback the information can be analysed (filtered) and prepared for inser-

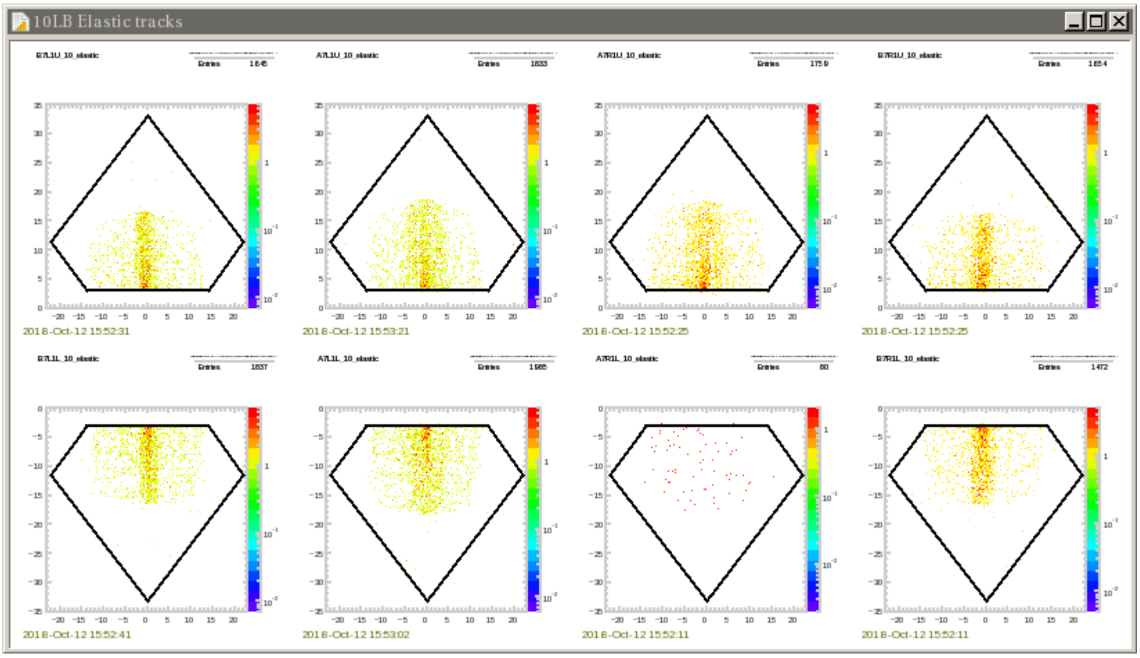

Figure 5.5: An example GNAM plot showing the elastic track reconstruction collected within 10 lumiblocks. Each plot corresponds to respective detector. From the presented plot an expert can conclude there is an issue with A7R1L detector as an amount of reconstructed tracks is 2 rows of magnitude smaller than for other detectors and characteristic elastic pattern does not show up and the proper action must be taken.

tion into a database. In addition, PBEAST provides an interface to retrieve stored information in form of time slice queries. The PBEAST database was used by the author many times during the thesis preparation and those data are very important for the analysis. The scheme of the PBEAST is presented in Fig. 5.6

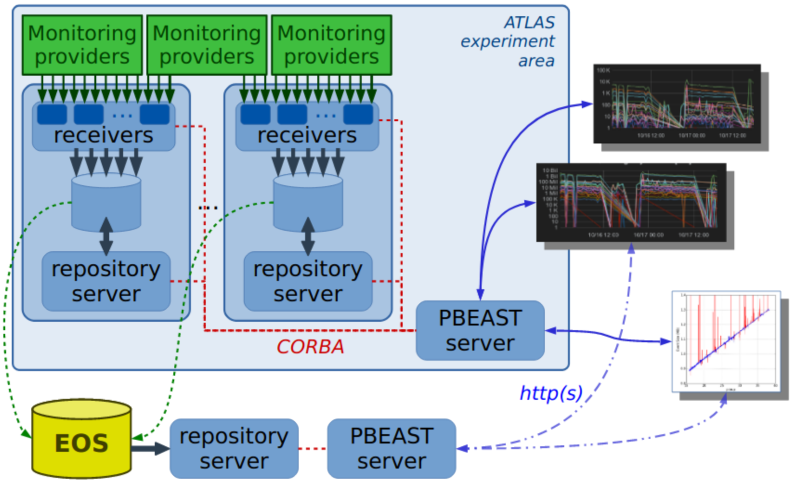

Figure 5.6: PBEAST scheme [90].

Trigger Rate Presenter (TRP) [91] is an application which accesses IS to retrieve information published by the ATLAS central trigger. It allows presenting the information in real time during the data-taking. The TRP is an essential tool used by ALFA experts. The limitations of TRP is that the stored information are the trigger rates averaged over different BCIDs; the bunch-by-bunch rates are not available. Anyway, those data were helpful during beam-induced background investigation and can be useful for debugging purposes as well.

All above discussed software and their relations are presented on the scheme in Fig. 5.7.

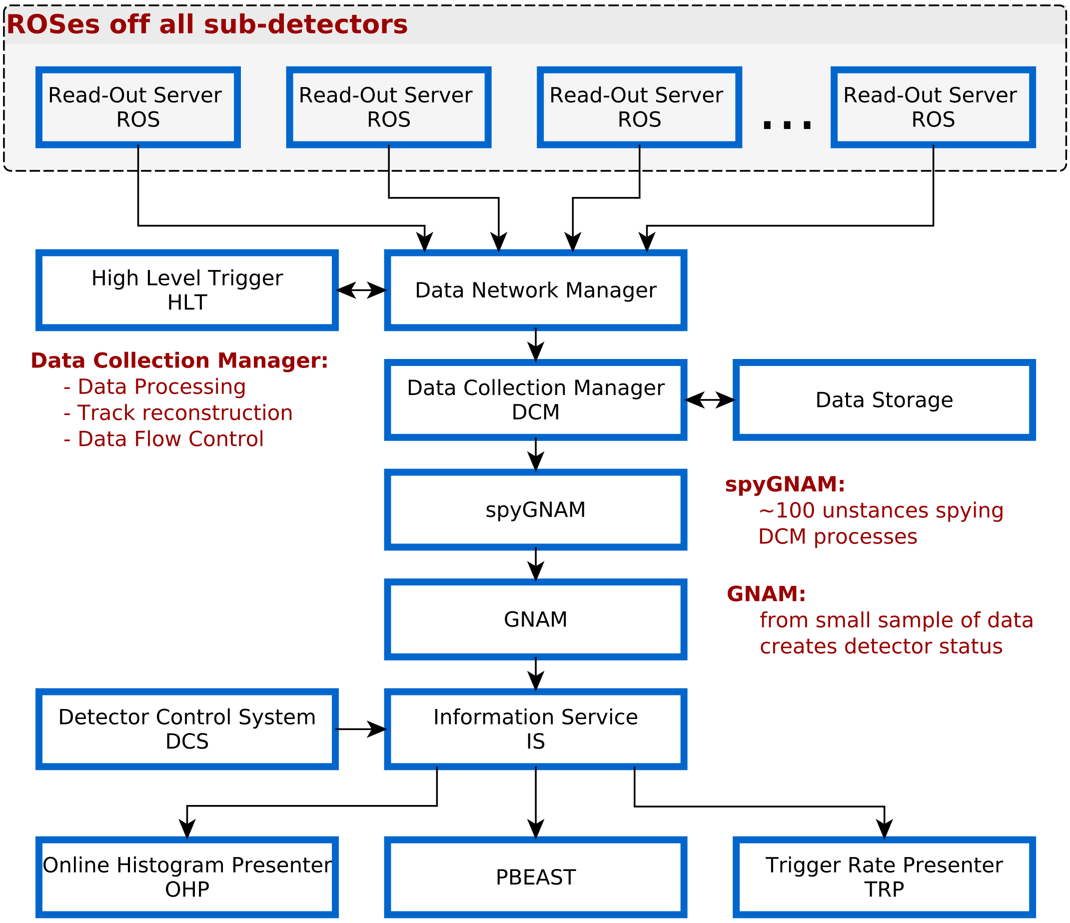

Figure 5.7: ATLAS TDAQ software relations scheme.

5.4 ALFA_CTPIN Module Description

The main motivation for the design and implementation of the ALFA_CTPIN module was to reduce latency of ALFA trigger signals and allow ALFA to participate in ATLAS combined runs. After CTP upgrade for Run 2 the maximum ATLAS

Table 5.2: Comparison of the ALFA latency budget before and after ALFA_CTPIN installation. Grayed fields shows were a latency reduction was achieved [92].

Without ALFA_CTPIN		With ALFA_CTPIN	
Source of latency	Latency [ns]	Source of latency	Latency [ns]
Time of flight	800	Time of flight	800
Scintillator	3	Scintillator	3
Photomultiplayer	6	Photomultiplayer	6
LEMO-cables (tunnel)	25	LEMO-cables (tunnel)	10
MAROC2 (analog FE)	13	MAROC2 (analog FE)	13
Digital Front-End	50	Digital Front-End	37.5
Air-core cable	1051	Air-core cable	1051
LEMO-cables (USA15)	15	LEMO-cables (USA15)	10
MROD separation	60	ALFA_CTPIN	37.5
NIM to LVDS convertion	5		
CTPIN logic	25		
CTPIN PITbus	50		
CTP functionality	125	CTP functionality	125
CTP_OUT	25	CTP_OUT	25
TOTAL	**2253**	**TOTAL**	**2118**

latency was reduced to 2175 ns, which was lower than minimal latency achievable by the ALFA, see Table 5.2. In fact, during normal operation ATLAS works even with a smaller latency. Interfacing the module directly to the Central Trigger Processor core bus allowed ATLAS to use ALFA trigger signals to produce L1 trigger at the cost of extending the L1 trigger latency of only 8 BCIDs from the nominal one. The further extension of latency, needed in case of runs without the module, would provoke significant increase of dead time from other ATLAS detectors participating in the ALFA runs.

Location of the module in the path between the ALFA detectors and CTP allows to monitor precisely ALFA trigger activity. Running with the LHC clock the module monitors ALFA triggers with BCID accuracy and publishes this information to the Information Service. The data published by ALFA_CTPIN allow ALFA operators to estimate backgrounds and request LHC to clean-up the beams in case the their rates grow above the limits.

ALFA_CTPIN is a VMEbus standard triple wide, 6U size module forming an interface between the ALFA trigger mezzanine and the CTP. The front panel and block diagram of the ALFA_CTPIN module are presented in Fig. 5.8.

The ALFA_CTPIN is equipped with 16 trigger signal inputs but uses only 8 of them and two clock inputs – one for the LHC Bunch-Crossing Clock (~40 MHz), marked as BC and one for the LHC Orbit Clock signal (revolution frequency,

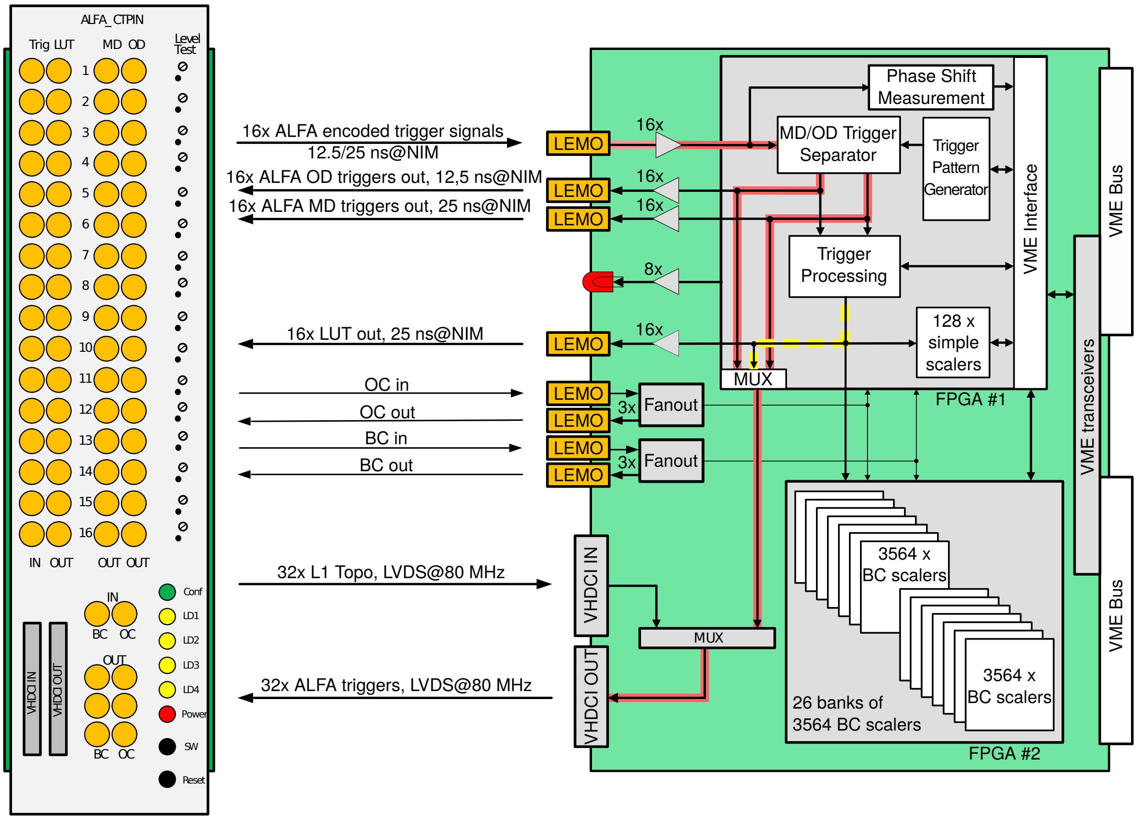

Figure 5.8: The ALFA_CTPIN block diagram [86]. *LEFT:* The front-panel layout. *RIGHT:* General block diagram of the module.

∼11 245 Hz), marked as OC. It has also 16 Look-Up Tables (LUT) outputs and 16 pairs of outputs for selected triggers from MD and OD. Another six outputs are devoted to sharing LHC Bunch-Crossing Clock and Orbit Clock, three outputs for each clock. The trigger outputs allow monitoring trigger activity using an oscilloscope and the 6 clock outputs are meant for synchronization with external devices. All of described above connectors are LEMO sockets.

A VHDCI OUT connector is the main interface to ATLAS CTP. Via this connector the decoded OD and MD triggers are delivered to the CTP core. VHDCI IN is used for connecting L1Topo in an ALFA_CTPIN by-pass mode. In Run L1Topo and ALFA will share one socket in the CTP rack, thus, the ALFA_CTPIN was designed to be also a bridge for L1Topo. As ALFA runs do not require L1Topo this solution is sufficient, however ALFA_CTPIN requires firmware upgrade. Each switch between by-pass mode, and ALFA trigger mode requires ALFA_CTPIN reconfiguration via the VME interface. Switching between by-pass mode for L1Topo and ALFA triggers is done by an embedded multiplexer.

The heart of the module consists of two FPGAs. First one decodes if the trigger is from MD or OD, processes the triggers and communicates with the VME bus. It contains also trigger pattern generator – a dedicated memory which can be loaded with pre-set combinations of trigger signals and used for debugging (see next Section). The other FPGA contains 26 banks of scalers with 3564 channels each. Each channel corresponds to one BCID, and each bank counts rates generated by different triggers. This allows observing evolution in time of the signal bunch-by-bunch which makes it a unique and powerful tool for beam parameters measurements and helps to collect information about background associated with the LHC bunches. These scalers take decoded ALFA triggers as inputs and produce rates according to predefined logic.

As Fig. 5.8 shows, the trigger signals coming into the ALFA_CTPIN module first are decoded into MD and OD triggers by the MD/OD Trigger Separator. The MD/OD Trigger Separator drives them through multiplexers to the CTP via VHDCI OUT output. Moreover the outgoing signals are aligned to the Bunch-Crossings phase. The latency of the separator is 50 ns. The thick red line in fig. 5.8 shows the path of the trigger signal from inputs to VHDCI OUT providing the shortest path for the signals to the CTP.

In parallel to the mentioned path there is also Trigger Processing Unit. It is an FPGA based trigger processor which was designed to process incoming triggers and generate additional information for more sophisticated combinations of incoming signals. The processor allows defining up to 128 logical functions with incoming trigger signals (MD and OD) and the results of the corresponding logic functions are stored as LUTs. The results of the first 16 functions are also sent to the module's front panel outputs for monitoring with an external device (like an oscilloscope). The scalers counting rates of those logic functions are located in the second FPGA. Positive value of the processor's function causes corresponding counter to increment. Depending of the module's configuration the values from the scalers are copied every second or 10 seconds (for slow trigger rates) to a set of registers which are accessible via the VME interface. Every 1.3 sec. ROD Crate DAQ (RCD) software performs the readout of the registers and either publishes them directly to the IS service or divides the values by 10 before publishing in case of the slow trigger rates. The values published on IS can then be used by clients like TRP presenter or PBEAST to monitor evolution of rates in time.

Phase Shift Measurement unit monitors the presence of the signal and phase shift between the incoming signal from ALFA and the LHC clock received by the module. The results of the measurements of the phase shift with resolution of 2.5 ns are available via the VME register and are also part of the RCD readout every 1.3 sec. The data is then published in dedicated histograms via the IS service.

5.5 ALFA_CTPIN – Trigger Processing Unit

The design of the ALFA_CTPIN module is based on FPGAs' internal memories to program various logic functions. The ALFA triggers received on ALFA_CTPIN inputs are decoded to MD and OD and then the resulting trigger pattern is used as an address to refer to a memory location previously loaded with desired results of logic functions related to the received trigger pattern (Look-up Table style).

```
<item>
     <id> 17 elast15 </id>
     <det> MD </det>
             <level>
                     <level>
                             <st> B7L1U </st>
                             <st> A7L1U </st>
                             <func> OR </func>
                     </level>
                     <level>
                             <st> A7R1L </st>
                             <st> B7R1L </st>
                             <func> OR </func>
                     </level>
                     <func> AND </func>
             </level>
     <det> OD </det>
             <level>
                     <st> B7R1U </st>
                     <st> B7R1L </st>
                     <func> AND </func>
             </level>
     <lutf> F2 </lutf>
     <bgroup> 0 </bgroup>
</item>
```

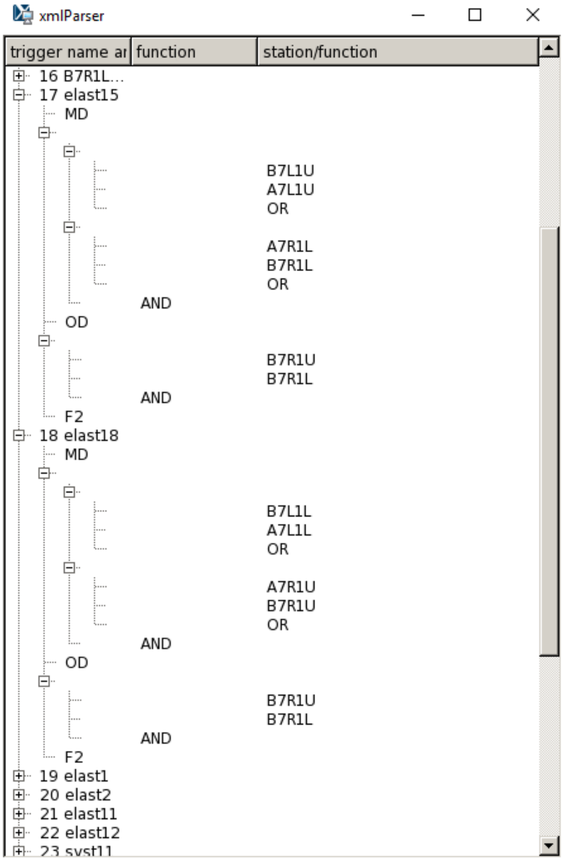

```
16 B7R1L...
17 elast15
  MD
                               B7L1U
                               A7L1U
                               OR
                               A7R1L
                               B7R1L
                               OR
               AND
  OD
                               B7R1U
                               B7R1L
               AND
  F2
18 elast18
  MD
                               B7L1L
                               A7L1L
                               OR
                               A7R1U
                               B7R1U
                               OR
               AND
  OD
                               B7R1U
                               B7R1L
               AND
  F2
19 elast1
20 elast2
21 elast11
22 elast12
23 syst11
```

Figure 5.9: *LEFT:* Fragment of XML configuration file with definition of ALFA elastic trigger item elast15 (see text for details). *RIGHT:* Visualisation of XML configuration file for ALFA elastic trigger items elast15 and elast18.

To prepare desired contents of the memory a dedicated tool has been developed with a significant help of author. The logic function of desired triggers is prepared in a text file using the XML format. An example of so-called ALFA golden trigger (elastic trigger – ELAST15) encoded in the XML format is presented in Fig. 5.9, left panel. The `<id>` tag specifies ALFA_CTPIN trigger number (17) and name of this trigger (ELAST15) – to be used later on histograms. The next tag `<det>` specifies the section of detectors (either MD or OD) for which the trigger function will be defined. Details of the logic are specified in the number of `<level>` tags. Inside a level there are name(s) of the station(s) contributing to the logic and selected logical function. In the presented example there is logical OR between B7L1U and A7L1U (upper detectors for A side), A7R1L OR-ed with B7R1L (lower detectors from C-side) and these two functions will be inputs to the logical AND. The definitions for OD detectors is irrelevant in this example as the function `<lutf>` F2 defines that only status of MD will be used in the final trigger definition.

The dedicated tool takes as input the trigger logic encoded in the XML file. To facilitate understanding of the trigger configuration and verify whether the encoded logic matches the desired triggers, the tool produces also graphical output presented in right panel of the Fig. 5.9. The upper part of the figure presents the logic encoded in the XML file with ELAST15 trigger pattern discussed above. The mirror configuration for elastic trigger – ELAST18 – is presented in the lower part of the figure. The logic definition presented in this example corresponds to the loose definition of the ALFA elastic triggers. It is also possible to define another set of elastic triggers where with veto from the other 4 detectors not contributing to the ALFA golden elastic triggers.

When the XML configuration is ready and verified by the user using the graphical representation, the tool produces an output text file with contents of all memories (LUTs). The text file is then parsed by the online DAQ software and used to load contents of the all LUT memories used in the trigger monitoring.

5.6 Commissioning of the ALFA_CTPIN

For debugging and commissioning purposes, the module was augmented with a Trigger Pattern Generator part. This part, designed as a programmable memory, is able to simulate signals arriving from the ALFA detectors and send them to the MD/OD Separator. The width of the test memory word is 8 bits – to simulate the arrival of trigger signals from 8 ALFA detectors. To generate signals with 12.5 ns period required to simulate the OD trigger signals, the generator operates at 80 MHz clock. The memory implemented for these tests is large enough to store signals for a full LHC cycle. As the generation of OD triggers requires half of the LHC clock cycle, the total number of memory locations for these tests has depth of 3564×2 locations (for the addressing purpose the depth is 8192)

The commissioning of the module in the lab was based on programming of the input memory with expected pattern needed to generate preprogrammed trigger and observing evolution of trigger rate in the corresponding histogram published in the IS. The main drawback of this solution was that the preprogrammed trigger pattern was firing at least once per LHC orbit due to buffer limitation. This resulted with about 11 kHz as the minimal rate of the trigger due to the revolution frequency.

To solve this issue another commissioning solution was proposed and implemented by the author. The solution was based on sending patterns of electrical pulses from counting room USA15 to the detectors in the tunnel. The old OD cables from ALFA initial installation were used as the medium for sending the pulses (these OD cables planned for calibration runs with OD detectors were abandoned during Run 1 and OD signals were sent encoded over the main air-core cables soon after). The electrical pulses arriving at the detectors were then used to illuminate LEDs and provoke triggers in the trigger PMFs. The electrical tests could thus be driven from an intelligent device installed in USA15. The author designed and implemented an FPGA based pattern generator: ALFA_LED. Details of this device are presented in Appendix B. With this solution any rate of triggers could be generated. Using the LHC clock and counting the BCIDs the ALFA_LED was synchronous with the LHC timing and taking into account delay of the OD cables, the electrical pattern was arriving at the detectors precisely at the moment corresponding to LHC bunch of protons. This commissioning setup allowed to not only testing the logic of the ALFA_CTPIN module but also commissioning the whole trigger channel from the detectors to the back-end electronics.

5.7 ALFA_CTPIN in Background Measurements

Access to the module inserted into the ATLAS trigger path with full synchronization with the LHC orbit cycle allowed a remarkable increase of monitoring capabilities of background and trigger conditions generated from ALFA detectors. This feature is extremely important in case of detectors operating near the beam, which increases the risk of beam dumps or damage of the detectors. An instant access to the ALFA rates generated in each BCID gave new possibilities to monitor the conditions for the individual BCIDs. The rate informations, collected continuously from the module by the readout software and published in IS allowed ALFA operators to react instantly on changing background conditions. The archiving of the IS information via PBEAST and further access to the rates evolution was the foundation of the background analysis presented in this thesis.

Chapter 6

Detector Preparation and the Data Taking

The data considered in this thesis were taken at the LHC injection energy i. e. 450 GeV per beam. The main motivation for such low collision energy was the lack of proton–proton elastic scatering measurements between the ISR[1] and LHC energies, i. e. $\sqrt{s} = 62.5$ GeV [93] and $\sqrt{s} = 7.0$ TeV [49], respectively. The results of measurements at $\sqrt{s} = 1.8$ TeV performed at the Tevatron concern proton–antiproton collisions and suffered large discrepancy. The total cross section measured by three experiments – CDF, E811 and E710 – ranges between 71 and 80 GeV [94], and differs by a few standard deviations between CDF and other experiments, see details in Table 6.1.

Table 6.1: Results from Tevatron experiments [94].

$\sigma_{tot}[mb]$	$\sigma_{el}[mb]$	σ_{el}/σ_{tot}	experiment
80.03 ± 2.24	19.70 ± 0.85	0.246 ± 0.004	CDF
71.42 ± 2.41	15.79 ± 0.87	0.220 ± 0.008	E811
72.80 ± 3.10	16.60 ± 1.60	0.230 ± 0.012	E710

Collissions at injection energy are unusual at LHC, which was designed to operate in different conditions. Thus, the data-taking required a lot of preparations and was preceded by a number of test runs which are reported in Section 6.4.

6.1 Beam Parameters and Run Preparation

Typical LHC beam consists of $1.2 \cdot 10^{11}$ protons per bunch and there is up to 2655 filled bunches (during the standard operation in 2018). In case of the special data-taking at the injection energy, the beam was limited to 4-6 colliding isolated bunches with a reduced number of injected protons each.

---

[1] Intersecting Storage Rings – accelerator (collider) operated at CERN in 1971-1984.)

Colliding bunch means a bunch filled with protons that crosses with a corresponding one belonging to the opposite beam. In the ATLAS case both such bunches are identified by the same Bunch Crossing Identifier [71]. Isolated means there are at least three empty bunches in both of the beams within at least 3 BCIDs ahead nor behind of the considered one. In an empty bunch the number of injected protons is lower than in the filled one by four orders of magnitude [95]. During the test and the final data-taking, the beam parameters were slightly different, thus for each run details are given in corresponding sections.

In some runs one of the injected bunches was an isolated non-colliding one. The non-colliding bunch is the main point of considerations further within this thesis, as the data coming due to such a bunch contain only pure non-collision background.

The optics β^* value for the ATLAS IP was set differently in x and y planes, see Table 6.2. According to beam experts, these are the most optimal β^* values at the LHC injection energy within ATLAS Interaction Point concerning all pros and cons. For comparison, β^* for ATLAS IP was typically 30-50 cm at 13 TeV (2018). As the ALFA detectors operate in vertical direction, the y index was skipped in many documents related, so the campaign was called simply $\beta^* = 100$ m or just high β^* run.

Table 6.2: Optics β^* value during special ALFA runs.

Plane	**Beam 1**	**Beam 2**
Horizontal (β_x^* [m])	53	53
Vertical (β_y^* [m])	98	101

The chosen β^* value was a trade-off between many technical and physical constraints [44, 96]. From the machine point of view the smaller β^* value the better as the LHC was optimized to run with the value of tens of centimetres. From the physics point of view it is very important to reach the Coulomb-Nuclear Interference region, i. e. $-t \approx 6.5 \cdot 10^{-4}$ GeV. According to the formula:

$$-t_{min} = \frac{2pn_\sigma^2 \varepsilon_N m_p}{\beta^*} \tag{6.1}$$

where p is the proton momentum, n_σ – the distance from the beam centre, ε_N – normalized emittance, m_p proton momentum [96]. Unfortunately at low energy the beam is more sensitive to machine imperfections, and effects like IBS have much stronger influence on the beam stability. Thus, the β^* was established to about 100 m in the vertical plane (Table 6.2). According to simulations performed by ALFA experts, the 100 m optics should satisfy the required t acceptance.

Another strong discussion was about the collision energy, whether it should be 900 GeV or 1.8 TeV center of mass energy [96]. Due to time constraints – limited time for the data-taking, complicated machine studies and commissioning required at the 1.8 TeV it was decided to run the LHC at higher energy only if necessary. Thus, all the efforts and manpower were focused on simulations and preparations for the LHC run at the injection energy.

6.2 Background

A number of backgrounds is considered in ALFA measurements. The background can be estimated in different ways. The online background estimation was based on the trigger rates, while the offline one was based on the collected data.

6.2.1 Online Background Estimation From the Trigger Rates

During the tests as well as during the physics runs, the rates of four triggers called L1_ALFA_ELAST_15, L1_ALFA_ELAST_18, L1_ALFA_SYST_17 and L1_ALFA_SYST_18 were monitored. First two of those corresponds to the elastic signal, while last two – to the background. In the following, these two types of trigger rates are called shortly elastic and background trigger rate, respectively. Definition of those triggers can be found in Table 6.3 and in Fig. 6.1.

Table 6.3: Trigger definitions.

trigger	**definition**
L1_ALFA_ELAST_15	(B7L1U or A7L1U) and (A7L1L or B7L1L)
L1_ALFA_ELAST_18	(B7L1L or A7L1L) and (A7L1U or B7L1U)
L1_ALFA_SYST_17	(B7L1U or A7L1U) and (A7L1U or B7L1U)
L1_ALFA_SYST_18	(B7L1L or A7L1L) and (A7L1L or B7L1L)

6.2.2 Offline Background Estimation From the Data

The offline estimation based on the collected data used a more sophisticated analysis. It consists of a few steps which are discussed below.

In an offline analysis elastic event candidates were selected based on their back-to-back topology (golden events) within a geometrically defined fiducial volume [49]. The irreducible background in this sample consists predominantly of accidental coincidences of the halo protons and events from diffractive processes. The background contamination in such a signal sample is determined using the anti-golden events, which consist of pure background.

6.3 ALFA Beam-Based Alignment

The BBA procedure related to the ALFA detector is carried out before each data-taking campaign. The procedure is performed manually, usually in tandem with

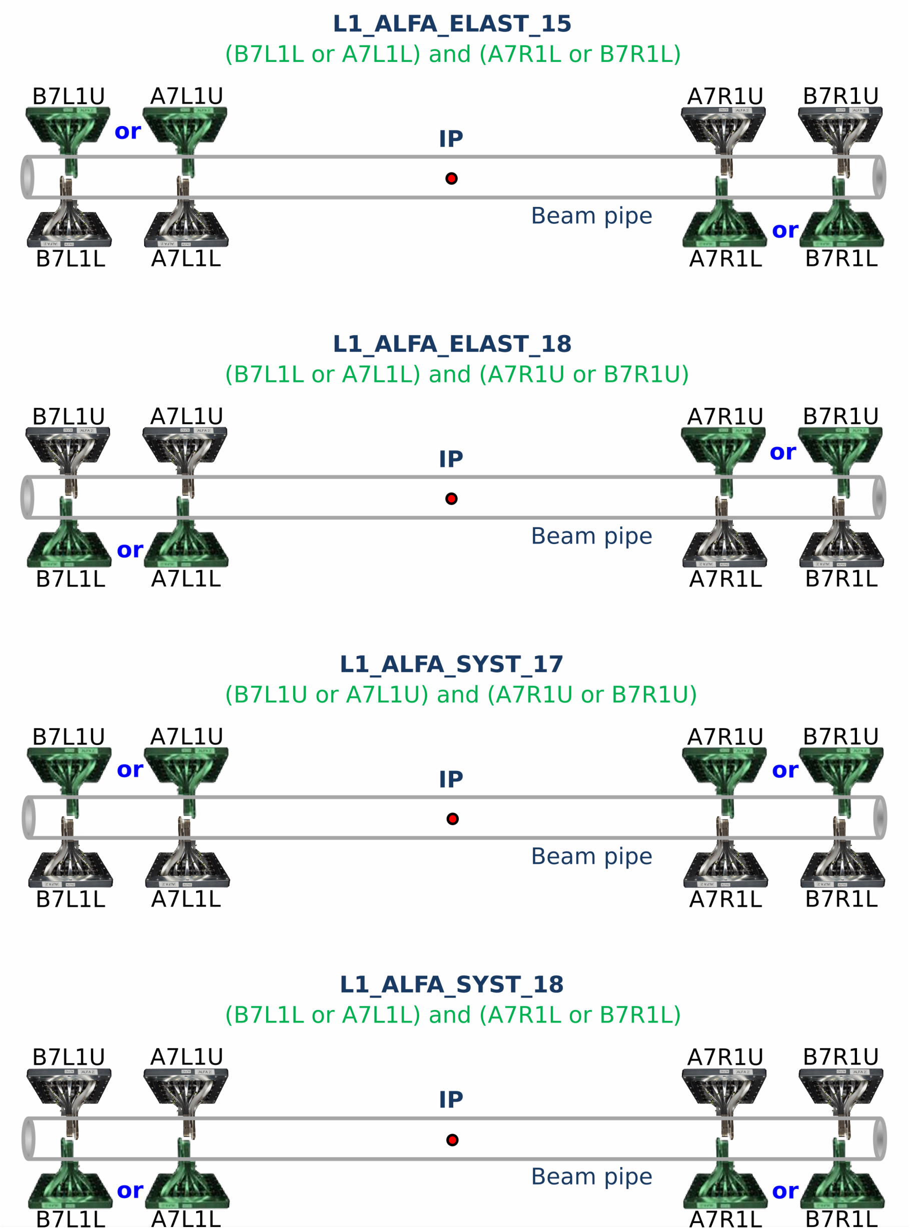

L1_ALFA_ELAST_15
(B7L1L or A7L1L) and (A7R1L or B7R1L)

L1_ALFA_ELAST_18
(B7L1L or A7L1L) and (A7R1U or B7R1U)

L1_ALFA_SYST_17
(B7L1U or A7L1U) and (A7R1U or B7R1U)

L1_ALFA_SYST_18
(B7L1L or A7L1L) and (A7R1L or B7R1L)

Figure 6.1: Visualisation of trigger definitions [97].

TOTEM detector, and takes up to 2 hours. If ALFA is being aligned in case of the TOTEM absence, the time required for the BBA is about 30 minutes. Graphs of the detector position during the BBA and the BLM readouts are presented in Fig. 6.2. It is very important to keep in mind that the peak in the BLM counts means that the Roman Pot "touched" the beam. It means to that position read from the DCS a distance 200 μm has to be added covering the bottom window thickness and also 150-200 μm of the distance between the detector edge and the pot bottom (different for each detector).

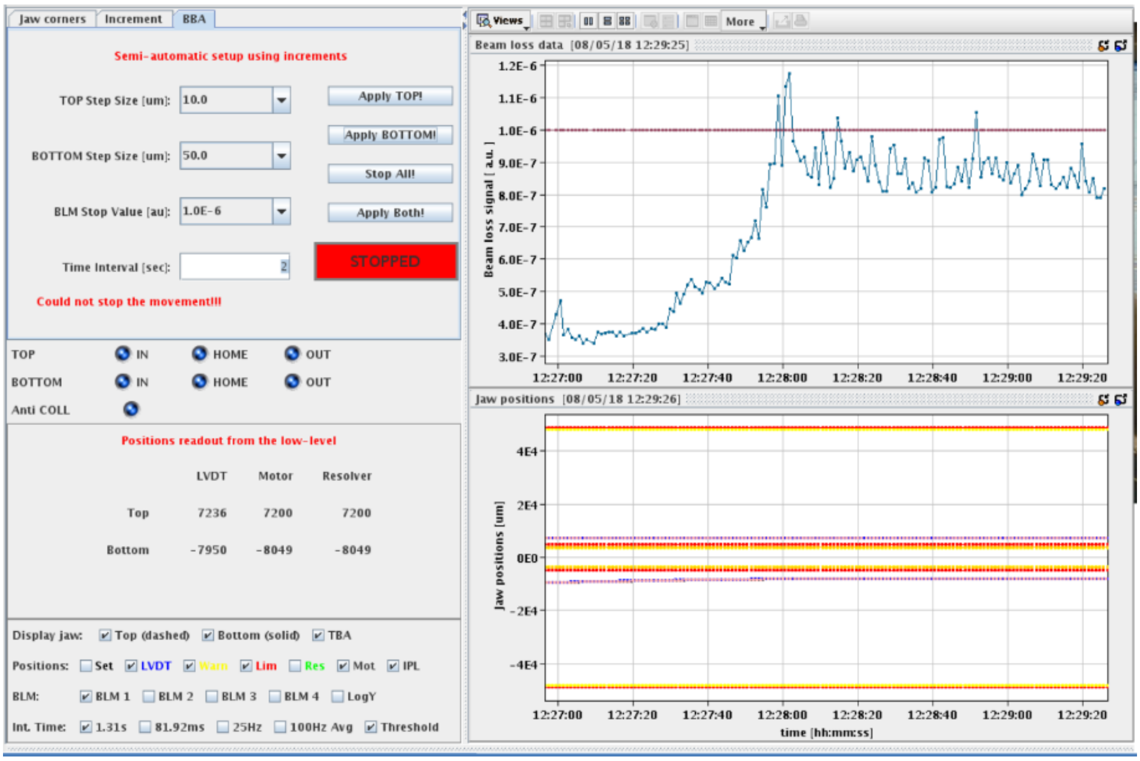

Semi-automatic setup using increments

TOP Step Size [um]: 10.0

BOTTOM Step Size [um]: 50.0

BLM Stop Value [au]: 1.0E-6

Time Interval [sec]: 2

Could not stop the movement!!!

TOP ● IN ● HOME ● OUT
BOTTOM ● IN ● HOME ● OUT
Anti COLL ●

Positions readout from the low-level

	LVDT	Motor	Resolver
Top	7236	7200	7200
Bottom	-7950	-8049	-8049

Display jaw: ☑ Top (dashed) ☑ Bottom (solid) ☑ TBA
Positions: ☐ Set ☑ LVDT ☑ Warn ☑ Lim ☐ Res ☑ Mot ☑ IPL
BLM: ☑ BLM 1 ☐ BLM 2 ☐ BLM 3 ☐ BLM 4 ☐ LogY
Int. Time: ☑ 1.31s ☐ 81.92ms ☐ 25Hz ☐ 100Hz Avg ☑ Threshold

Figure 6.2: BLM GUI. Upper plot shows the BLM count rate, while the bottom one actual Roman Pot positions (blue line), warning limit (yellow line) and alarm limit (red line). If the Roman Pot cross the red line it will cause immediate self extraction and beam dump. In case of crossing the yellow line, the warning shows up.

The moment the detector "touches down" can be also observed using the Trigger Rate Presenter Graphical User Interface application (TRPgui) – an application that allows online observation of the trigger rates as well as checks of the archived runs. Decreasing the distance between the detector and the beam results in the trigger rate increase. The moment of touching the beam can be recognised by a sudden growth of the trigger rate followed by its small drop and a form of a plateau. Unfortunately, this method is much less precise than the one using BLMs, it is used rather as a supporting method. Another disadvantage of basing the BBA procedure on the trigger rates follows from the fact that after the detector reaches the beam, it creates strong particle showers, which can also affect ALFA electronics. This may cause a Single-Event Upset (SEU) and lack of the detector readout.

Fig. 6.3 presents the trigger rates in case of the BBA concerning only the ALFA detectors. At first the outer stations and then the inner ones were aligned. After the BBA procedure the detectors got retracted by 10 mm. The ellipse marks the point when one detector readout "died" due to SEU. Usually, the power cycling of the ALFA motherboard solves this problem, but as each power cycle takes about

10 minutes and obviously prolongs the BBA procedure, it is rather avoided. On the right side of the plot a situation when all detectors got inserted together into the measurement positions is visible.

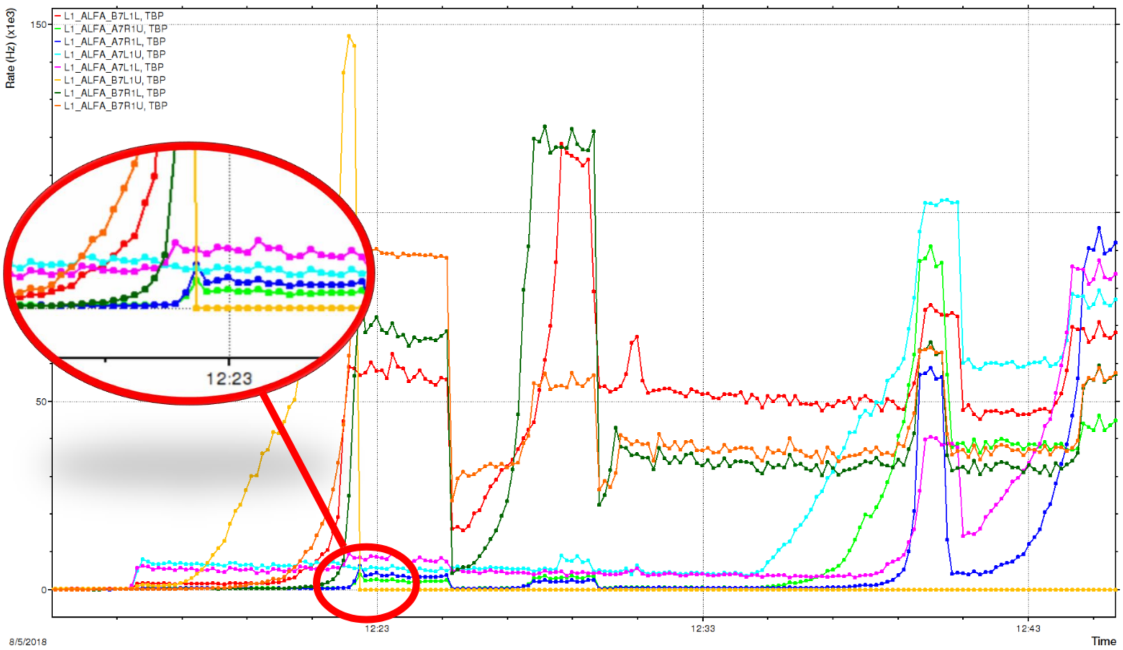

Figure 6.3: TRP GUI. Beam-based alignment. The plot displays the trigger rates over time during the BBA. The moment of the detector "touch down" the beam is much less obvious than when using BLMs, moreover it is possible that the readout may hang due to particle showers and ensuing SEU (marked and magnified using red ellipses).

6.4 Collimation Tests in 2017 and 2018

In a typical LHC operation the collimators made of carbon-fibre-composite or graphite are used as the primary and secondary stage – TCPs and TCSGs, respectively. Relatively low density of their jaws material increases the robustness to radiation from the beam halo. On the other hand, smaller density means also less absorption of the halo particles, and thus, induces more secondary halo, which is intercepted by TCTs and TCLAs made of tungsten.

During ALFA runs the beams have much lower intensity – 4-6 bunches of protons instead of 2655 nominal bunches, and in some cases with reduced population, thus collimation experts decided to change the typical approach, described in Chapter 4.3. The tungsten absorbers were used as the primary collimators. Such a change allows the primary collimation stage to absorb much more halo protons and thus to reduce the secondary halo. This approach was already developed during previous ALFA dedicated runs and succesfully tested [98].

In case of ALFA special runs at injection energy a similar approach was applied. The following subsections discuss the used collimation schemes, online observations, and results from the offline analysis in the context of usability of collected data.

6.4.1 Collimation Test – Preevaluation

Before any data-taking each collimation scheme had to be evaluated. At first, Collimation Working Group performed transport simulations using SixTrack programme [99]. This tool allows simulation of multi-turn transport and evolution of the multi-particle halo population in time. The CWG took into account also particle interactions with collimators, Roman Pots and geometrical aperture of the LHC. In case of SixTrack simulations, the Roman Pots were considered as the so-called "black hole collimator", i. e. every hit was absorbed to increase the statistics [100].

After simulations, the most promising schemes were chosen for the background test run. Four test runs were performed starting from November 2017. Each test run had to be preceded with a BBA (see Chapters 4.7 and 6.3). The ALFA experts monitored elastic and background trigger rates. Physics simulation results implied that the rate of elastic events should be around 10 Hz. Assuming that data is usable if the background trigger is not larger than the elastic one, the maximal trigger rate should be about ∼20 Hz [44].

6.4.2 1st Collimation Test

The first test run was performed on the 8th of November 2017. Four colliding bunches were injected and there was no non-colliding bunch. Thus, the detailed observation of beam induced background was more complicated. The bunch intensity was typical for LHC run, around $1.2{\cdot}10^{11}$ particles. The measured emittance was $\varepsilon \approx 1.5$ μm and the crossing angle was set to 0°.

During the test run 7 single-stage collimation schemes were evaluated. The timeline of the test run:

- 16:30 – 17:50 – beam-based alignment,
- 18:00 – 18:30 – first scheme,
- 18:35 – 19:20 – second scheme,
- 19:30 – 19:45 – third scheme,
- 19:55 – 20:15 – fourth scheme,
- 22:15 – 22:30 – fifth scheme,
- 22:45 – 22:55 – sixth scheme,

- 23:00 – 23:05 – seventh scheme,
- 23:10 – 23:20 – fourth scheme repeated.

A detailed description of the collimation schemes is presented in Table 6.4.

Table 6.4: Collimation schemes used during the first background test [101]. The collimator positions are given in σ.

Collimators	Beam	IP	plane	Scheme 1		Scheme 2		Scheme 3		Scheme 4		Scheme 5		Scheme 6		Scheme 7	
				Scr	D-T	Scr	D-T	Scr	D-T	Scr	D-T	Scr	D-T	Scr	D-T	Scr	D-T
TCP	B1; B2;	3; 7;	V	2.0	2.5	3.0	3.0	3.0	3.0	3.0	3.0	3.0	3.0	3.0	3.0	3.0	3.0
TCP	B1; B2;	3; 7;	H	3.0	5.5	3.0	5.5	3.0	5.5	3.0	5.5	3.0	5.5	3.0	5.5	3.0	5.5
TCLA	B1; B2;	3; 7;	V	R	R	2.0	2.5	R	R	2.0	2.5	2.0	2.5	R	R	R	R
TCT	B1	2	V	R	R	R	R	2.0	2.5	2.0	2.5	2.0	2.5	2.0	2.5	R	R
TCT	B2	2	V	R	R	R	R	R	R	R	R	R	R	2.0	2.5	2.0	2.5
TCT	B1	8	V	R	R	R	R	R	R	R	R	R	R	2.0	2.5	2.0	2.5
TCT	B2	8	V	R	R	R	R	2.0	2.5	2.0	2.5	2.0	2.5	2.0	2.5	R	R
TCT	B1/B2	1/5	V	R	R	R	R	R	R	R	R	?.?	3.0	R	R	R	R
TCT	B1/B2	1/5	H	R	R	R	R	R	R	R	R	?.?	5.0	R	R	R	R

Scr – Scraping, D-T – Data-taking, R – retracted, V – vertical, H – horizontal

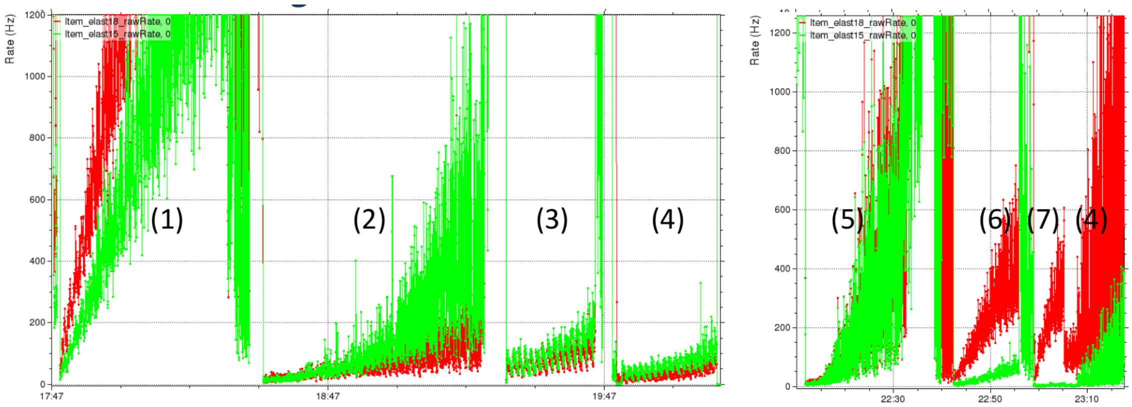

Figure 6.4: Elastic trigger rates over time during the test run 340308. Presented trigger rates represents sum of trigger rates from all 4 colliding bunches. Values in the parenthes correspond to the number of the tested scheme [101].

The elastic trigger rate is presented in Fig. 6.4. Unfortunately, for this run the background trigger rate was not stored. Nevertheless, the most promising scheme (scheme 4) had the trigger rate of about ∼50 Hz after the beam scraping, which was still higher than assumed 20 Hz including the background. Therefore, the data-taking using scheme 4 was repeated, however in the second attempt, the elastic trigger rate growth was much faster, and its value quickly reached a level of hundreds of Hz.

The trigger rates from individual detectors are shown in Fig. 6.5 (upper panel). The plots present the trigger rates integrated over all injected bunches. In the lower panel, Roman Pots positions in mm from the centre of the beam pipe are presented.

Inner stations were inserted into 10 mm positions with no alignment, while the outer ones into 3 σ positions according to performed BBA.

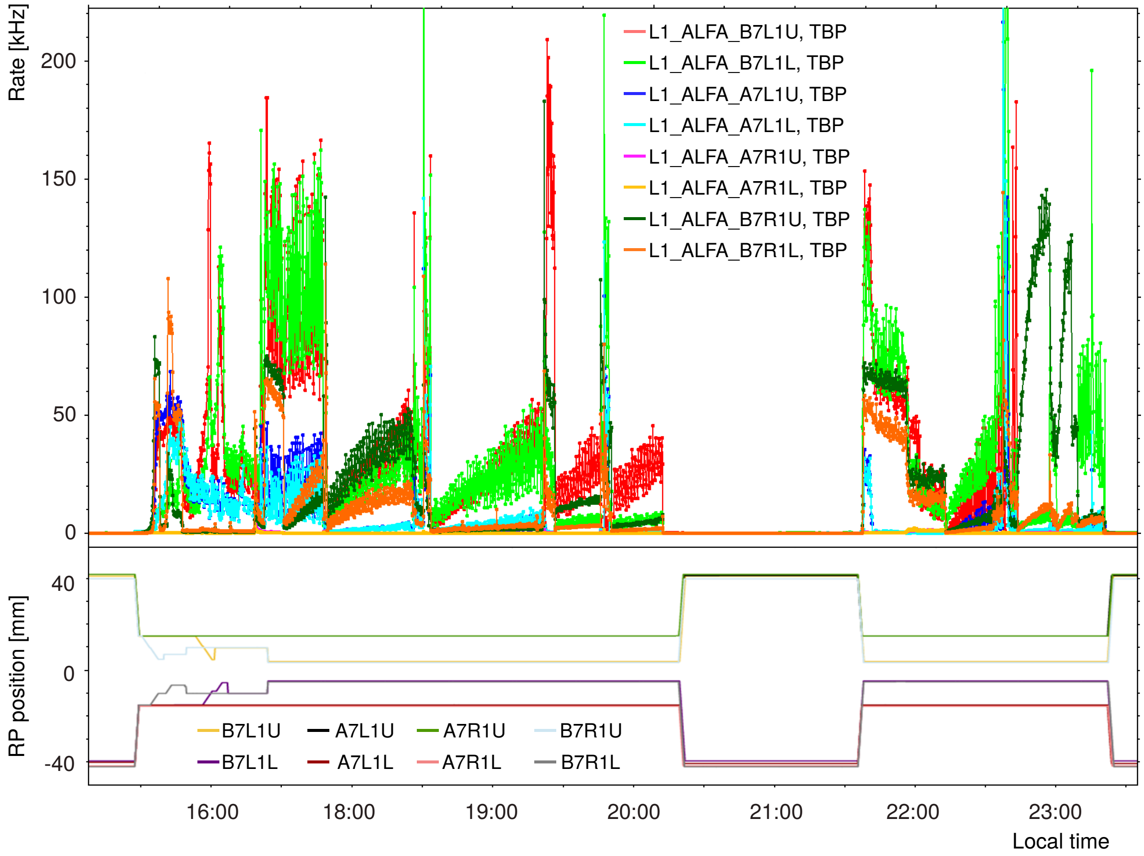

Figure 6.5: *UPPER PANEL:* The time dependence of the trigger rates for all injected bunches, run 340308, LHC Fills 6368 and 6369. *LOWER PANEL:* Roman Pots positions in mm. Inner detectors were inserted into 10 mm positions, while outer ones into 3 σ positions.

The offline analysis confirmed that the background was too high and the elastic signal was dominated by the background, thus there was no possibility to select elastic events from data. According to ALFA experts opinion, the background had to be reduced at least by factor of ten, thus another test had to be performed.

Although lack of success, the run gave important information about the LHC beam behaviour at the injection energy. In particular, from the Beam Synchrotron Radiation Telescope (BSRT) [102] measurements one can conclude the scraping did not grow the emittance as experts expected. Contrary – this operation improved the beam emittance reducing its value by up to 20%, see Fig. 6.6.

6.4.3 2nd Collimation Test

Thirteen days after the first unsuccessful test a new run was taken. This time there were four colliding bunches injected with intensity reduced from $1.2{\cdot}10^{11}$ to $0.8{\cdot}10^{11}$.

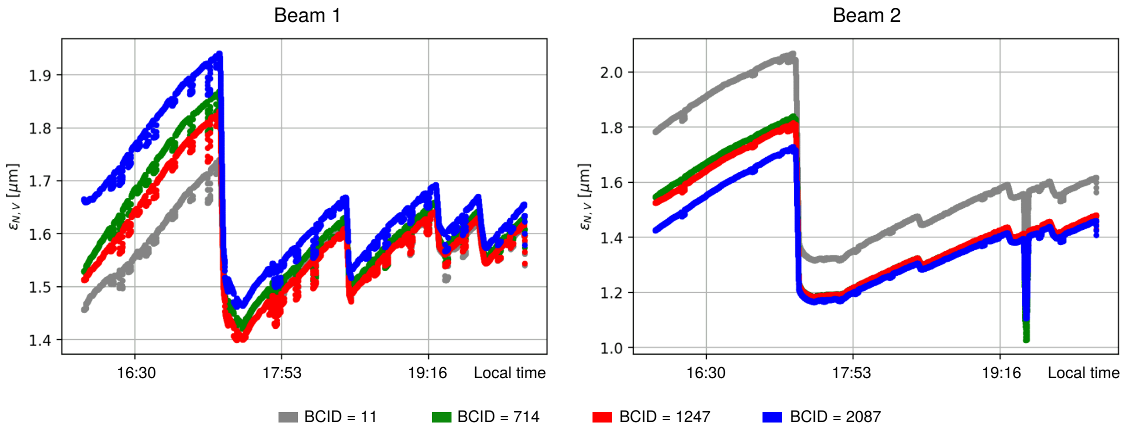

Figure 6.6: The BSRT measurements of the emittance during the LHC Fill 6368. The emittance is improved by each scrapping by 10-20% for Beam 1 and up to 5% for Beam 2.

Also an additional non-colliding bunch was injected. The emittance was reduced and finally the measured value was about $\varepsilon \approx 1.0$ μm with zero crossing angle.

The timeline of the test:

- 14:50 – 15:35 – first scheme,
- 15:50 – 16:20 – second scheme,
- 16:30 – 16:55 – third scheme,
- 17:05 – 17:20 – third scheme with Roman Pot retracted to 3.5σ,
- 17:30 – 18:00 – fourth scheme,
- 18:10 – 18:40 – fifth scheme,
- 18:50 – 19:05 – sixth scheme.

Detailed description of the collimation schemes is presented in Table 6.5.

Table 6.5: Collimation schemes used during the second background test [101].

Collimators	Beam	IP	plane	Scheme 1		Scheme 2		Scheme 3		Scheme 3’		Scheme 4		Scheme 5		Scheme 6	
				Scr	D-T	Scr	D-T	Scr	D-T	Scr	D-T	Scr	D-T	Scr	D-T	Scr	D-T
TCP	B1; B2;	3; 7;	V	3.0	3.0	3.0	10.0	2.5	10.0	2.5	10.0	3.0	3.0	3.0	3.0	3.0	3.0
TCP	B1; B2;	3; 7;	H	3.0	5.5	3.0	10.0	2.5	10.0	2.5	10.0	3.0	5.5	2.5	5.5	2.5	5.5
TCLA	B1; B2;	3; 7;	V	2.0	2.5	5.0	5.0	5.0	5.0	5.0	5.0	2.5	2.5	2.5	2.5	2.5	2.5
TCT	B1	2	V	2.0	2.5	2.0	2.5	2.0	2.5	2.0	2.5	2.0	2.0	2.0	2.0	2.0	2.0
TCT	B2	2	V	R	R	R	R	R	R	R	R	R	R	R	R	R	R
TCT	B1	8	V	R	R	R	R	R	R	R	R	R	R	R	R	R	R
TCT	B2	8	V	2.0	2.5	2.0	2.5	2.0	2.5	2.0	2.5	2.0	2.0	2.0	2.0	2.0	2.0
TCT	B1/B2	1/5	V	R	R	R	R	R	R	R	R	R	R	R	R	R	R
TCT	B1/B2	1/5	H	R	R	R	R	R	R	R	R	R	R	R	R	R	R
Rps	B1/B2	1	V	3.0	3.0	3.0	3.0	3.5	3.5	3.0	3.0	3.0	3.0	3.0	3.0	3.0	3.0
RF-voltage	n/a	n/a	n/a	6.6		6.6		6.6		6.6		6.6		6.6		12.0	

Scr – Scraping, D-T – Data-taking, R – retracted, V – vertical, H – horizontal

The elastic and background trigger rates are presented in Fig. 6.7. The test was started with repeating scheme 4 from the previous test. During this test it was also checked whether retracting of the Roman Pots from 3.0 σ positions to 3.5 σ position could improve the background reduction. To reduce the bunch length and thus decrease the de-bunching effect, the fifth scheme was also repeated with the RF voltage increased from 6.6 MV to 12.0 MV.

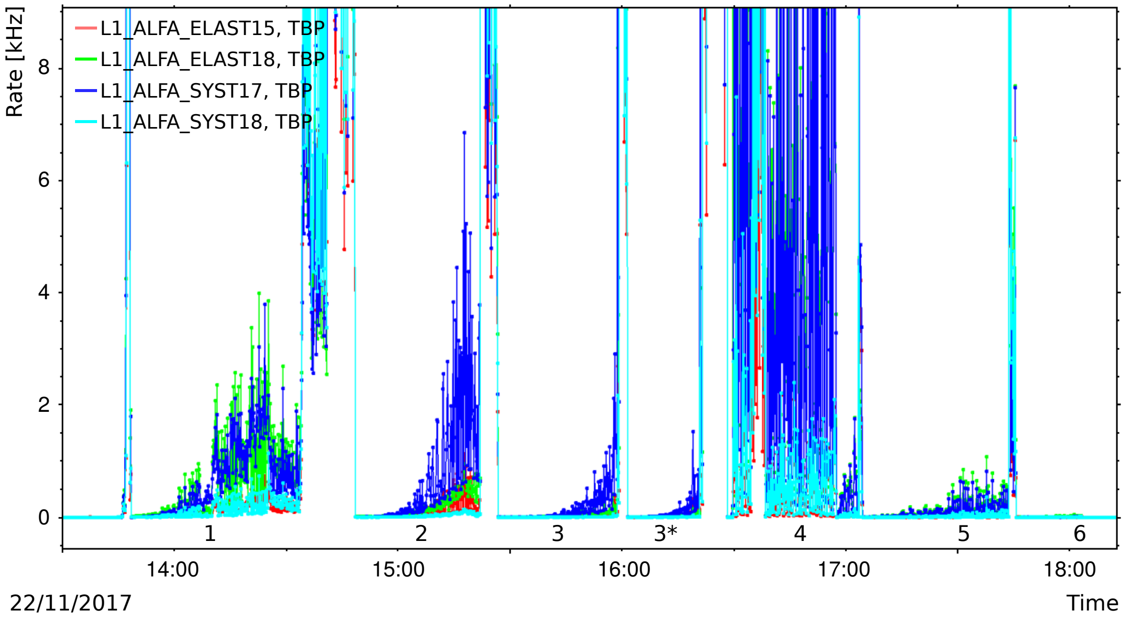

Figure 6.7: Elastic and background trigger rates over time during the test run 341367. Presented trigger rates represents sum of trigger rates from all 4 colliding bunches and the non-colliding one. Values under the plots correspond to the number of the tested scheme.

The trigger rates from each detector are presented in Fig. 6.8, upper panel. The rates are integrated from all colliding and non-colliding bunches. In the lower panel the Roman Pots positions are presented. Unfortunately all tested schemes gave too high background. Measures taken as an outcome from the previous test like bunch intensity reduction or increasing the detector distance did not give a satisfying improvement of the background reduction. Another test had to be performed.

6.4.4 3rd Collimation Test

Another collimation scheme was tested on 8th of May 2018. The CWG modified settings of one collimator during the run, thus in fact two schemes were tested. The beam intensity was limited to $0.5{\cdot}10^{11}$ protons per bunch and there were 6 colliding bunches injected instead of planned 8 colliding bunches. The number of the injected bunches was reduced during injection as the total beam intensity exceeded the safety limit. No non-colliding bunches were injected. The emittance was set to $\varepsilon = 2.0$ μm with zero crossing angle. During this test the RF voltage was increased from nominal

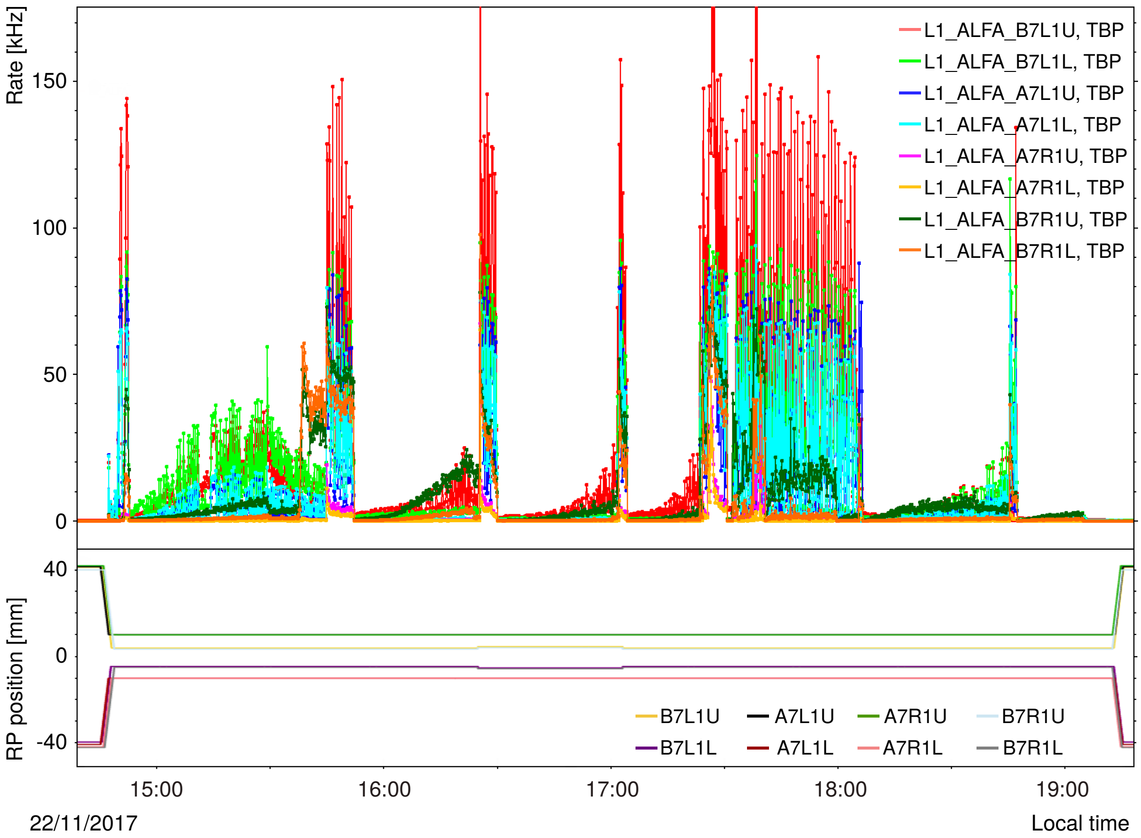

Figure 6.8: *UPPER PANEL:* The time dependence of the trigger rates for all injected bunches, run 341367, LHC Fill 6410. *LOWER PANEL:* Roman Pots positions in mm. Inner detectors were inserted into the distance of 10 mm from the beam pipe centre, while outer ones into 3 or 3.5 σ positions, dependent on the collimation scheme

6 MV (nominal for operation at 13 TeV at the beginning of 2018) to 12 MV for the first LHC Fill and to 16 MV for the second one, see Fig. 6.9

The timeline of the test:

- 12:00 – 14:30 – Beam-based alignment,
- 16:55 – 17:55 – test of prepared scheme at 12 MV,
- 18:00 – 18:30 – modified scheme at 12 MV,
- 21:45 – 22:15 – modified scheme at 16 MV.

During this test the trigger rate was much higher than during previous tests, exceeding 10 kHz for some of the detectors. The trigger rate plots for all 8 detectors are presented in Fig. 6.10 upper panel. All of the Roman Pots were positioned at 3 σ – see Fig. 6.10, lower panel.

The online monitoring of the elastic triggers demonstrated that none of the tested schemes is proper for the elastics data-taking at the injection energy. The offline analysis confirmed the impossibility to distinguish the signal from the background. In fact the condition were much worse than in the previous tests.

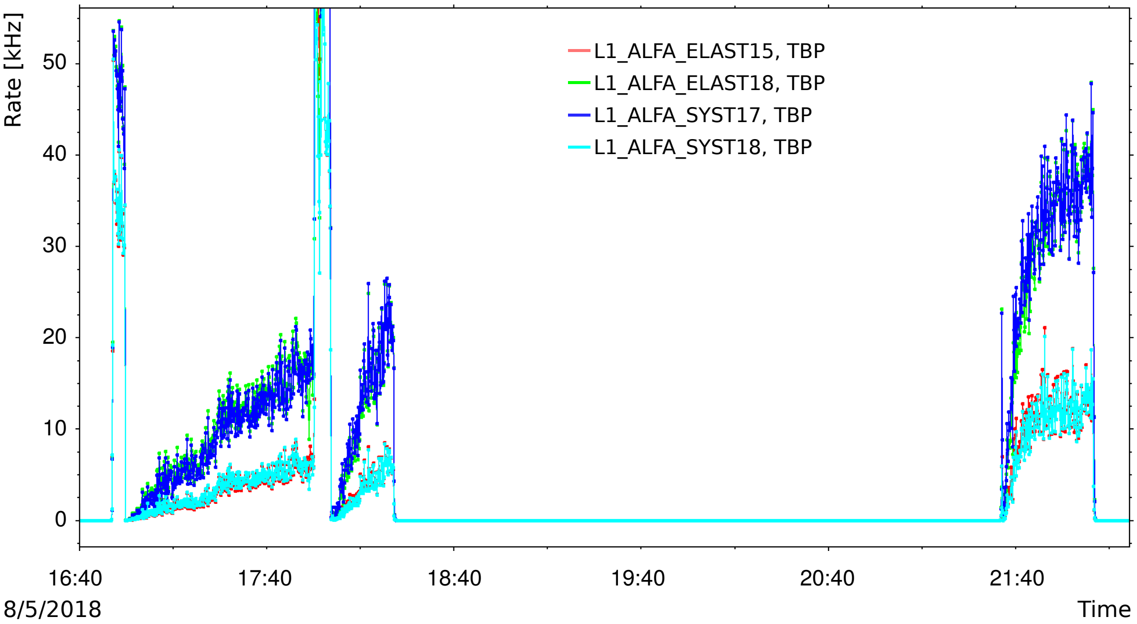

Figure 6.9: Elastic and background trigger rates over time during the test run 349769. Presented trigger rates represents sum of trigger rates from all 6 colliding bunches.

6.4.5 4th Collimation Test

To prepare the fourth test the Collimation Working Group analysed once again the previous simulations and investigated which particles were mostly recorded by the forward detectors [100]. The results of the analysis are presented in Fig. 6.11. The majority of particles detected by the Roman Pots were coming straight from the collimators which were set as a first device on the particles path and which did not interact with any other collimators. According to the analysis, higher loss rate on the off-momentum collimator could improve the background. Thus, a new idea was offered – the two-stage collimation scheme.

In the two-stage scheme, the collimators were divided into three groups – first stage at 2.5 σ, second stage at 2.7 σ intercepting beam induced background and halo induced by the first stage, then the Roman Pots at 3.0 σ and the rest of collimators further from the beam than the detectors for the machine protection. Contrary to previous schemes, only tungsten collimators were used for the background reduction – TCLA at betatron cleaning area as the primary and TCTs with TCLAs at the off-momentum cleaning area as the secondary stage. Their high density allowed to intercepting much more background than TCPs and TCSGs.

Simulations of the hits on the Roman Pots performed for both solutions – single and two-stage collimation schemes were performed. The results of the simulation were very promising, as is visible in Fig. 6.12. It is clearly visible that the background reduction is significant. The simulation shows also the asymmetry between Beam 1 and Beam 2, which is consistent with observations.

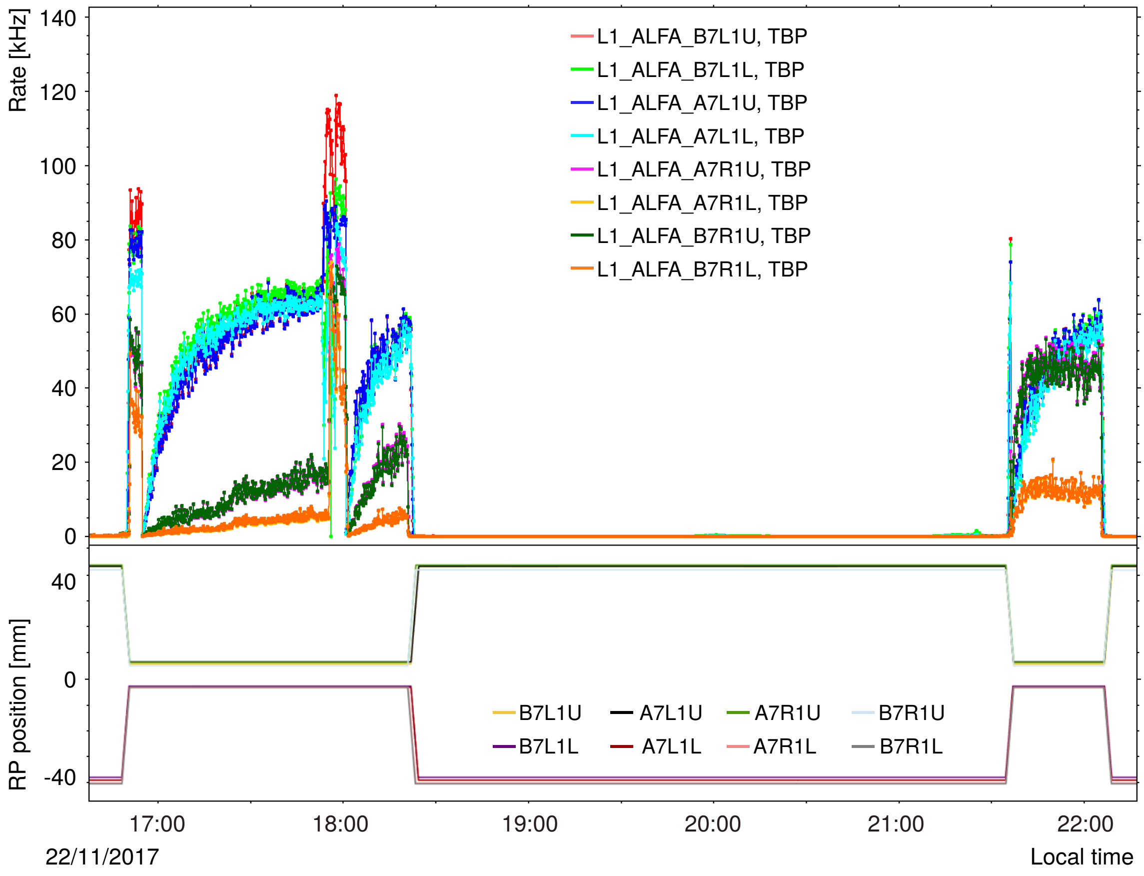

Figure 6.10: *UPPER PANEL:* The time dependence of the trigger rates for all injected bunches, run 349769, LHC Fill 6410. *LOWER PANEL:* Roman Pots positions in mm. Inner detectors were inserted into the distance of 10 mm from the beam pipe centre, while outer ones into 3 or 3.5 σ positions, dependent on the collimation scheme

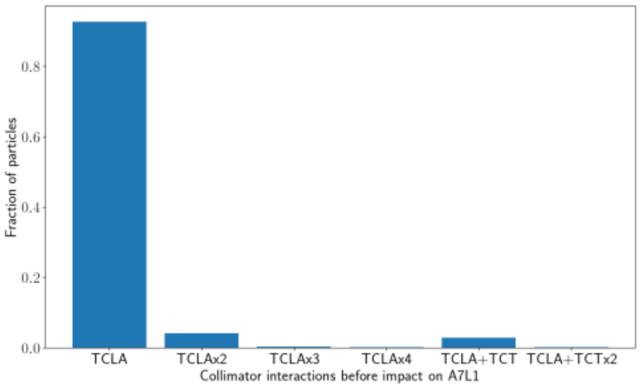

Figure 6.11: Fraction of particles impacting on the ALFA detector as a function of the collimator they scattered on [100].

Moreover the CWG proposed to use a new type of collimators based on crystal channelling effect (see Chapter 4.6). In the scheme containing the crystal collimators,

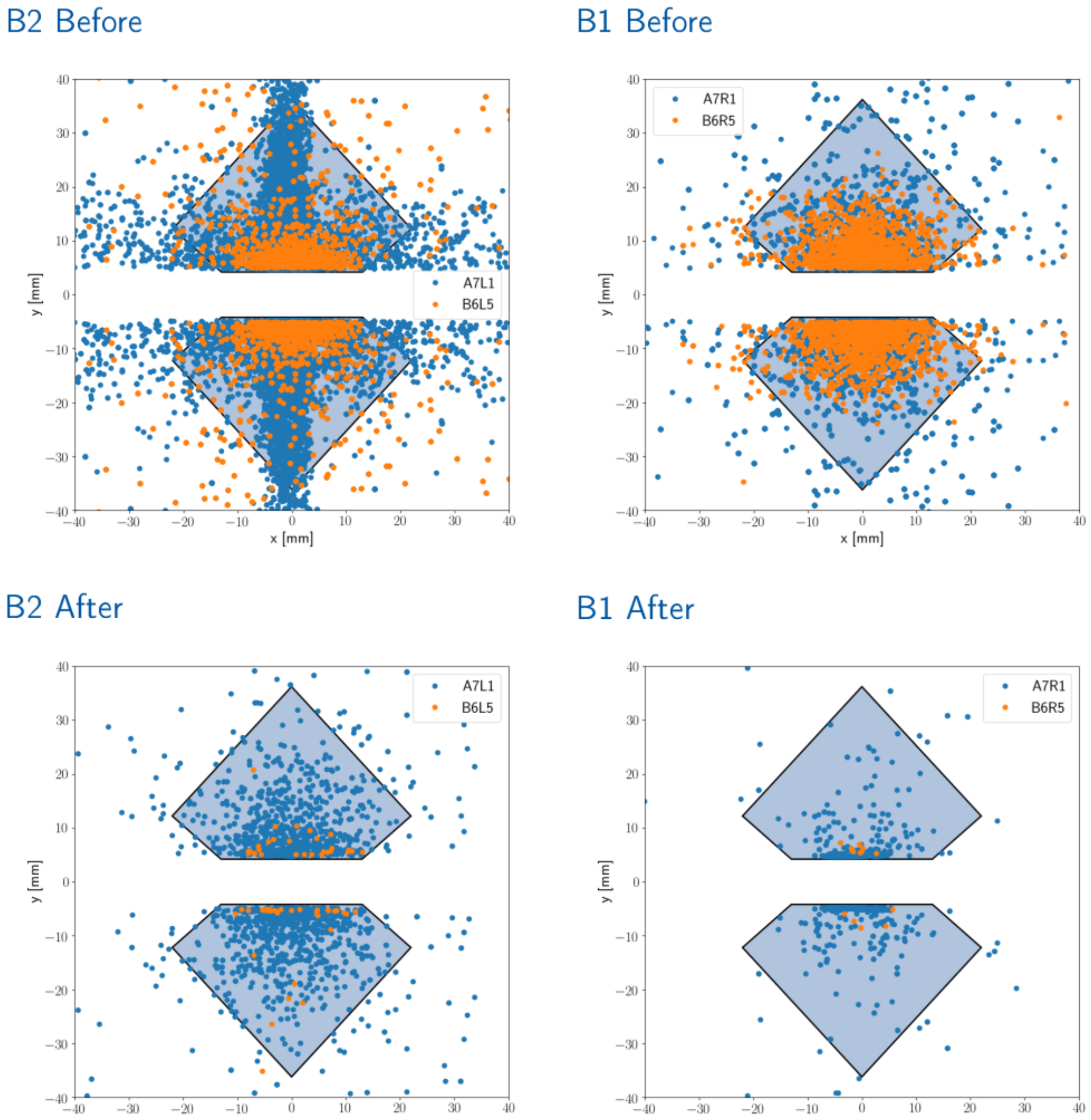

Figure 6.12: Simulation of the spatial distribution of the hits on the detector for the single-stage collimation scheme (upper plots) and for the two-stage collimation scheme (lower plots) [100]. Blue dots correspond to ALFA detectors located in stations A7L1 and A7R1 and the orange ones to TOTEM detectors located in stations B6L5 and B6R5.

these were used as primary collimators and the TCLAs at the betatron cleaning area were set at 2.7 σ, see Table 6.6.

The emittance was set to $\varepsilon = 2.0$ μm with zero crossing angle. The beam intensity was at the level of $0.8 \cdot 10^{11}$ protons per bunch, with six colliding bunches injected. The test was performed on 2nd of October 2018.

The elastics and background trigger rates collected during the test run are presented in Fig. 6.13. The low elastic trigger rate values not exceeding 25 Hz and much lower background trigger rate were very promising. According to simulations the level of elastics should be only twice smaller.

Table 6.6: Collimators positions in σ for runs with two-stage collimation scheme (Setting 1) and for run with crystal collimation scheme (Setting 2). The Plane column corresponds to the collimator orientation. Symbols H, V and S refers to a horizontal, vertical and skew orientation, respectively. Table contains only collimators inserted during the run. Collimators related to the injection protection and beam dump are not included.

Collimator	Plane	IR	Scheme 1	Scheme 2
TCP.6[L/R]3.B[1/2]	H	3	5,3	5,3
All TCSGs@IR3	H,S	3	6,3	6,3
TCLA.A5[L/R]3.B[1/2]	V	3	2,7	2,7
Rest of TCLAs@IR3	H	3	9	9
TCP.D6[L/R]7.B[1/2]	V	7	3.2/3.0	3.2/3.0
TCP.C6[L/R]7.B[1/2]	H	7	4	4
TCP.B6[L/R]7.B[1/2]	S	7	5,7	5,7
All TCSGs@IR7	H,V,S	7	5	5
TCLA.A6[L/R]7.B[1/2]	V	7	2,5	2,7
TCLA.B6[L/R]7.B[1/2]	H	7	8	8
TCLA.C6[L/R]7.B[1/2]	V	7	2,7	2,7
TCLA.D6[L/R]7.B[1/2]	H	7	10	10
TCLA.A7[L/R]7.B[1/2]	H	7	8	8
TCTPH.4[L/R]1.B[1/2]	H	1	13	13
TCTPV.4[L/R]1.B[1/2]	V	1	2,7	2.7/13.0
TCTPH.4[L/R]2.B[1/2]	H	2	13	13
TCTPV.4[L/R]2.B[1/2]	V	2	2,7	13
TCTPH.4[L/R]5.B[1/2]	H	5	13	13
TCTPV.4[L/R]5.B[1/2]	V	5	2,7	13.0/2.7
TCTPH.4[L/R]8.B[1/2]	H	8	13	13
TCTPV.4[L/R]8.B[1/2]	V	8	2,7	13
Crystal*	V	7	n/a	2,5
Roman Pots	V	1/5	3	3

*Regular names of the Crystal collimators used during ALFA run are TCPCV.A6L7.B1 and TCPCV.A6R7.B2

Also, the trigger rates from each detector were pretty low, see Fig. 6.14, upper panel. In the previous test, during the re-scraping some of the detectors required a power-cycle and reconfiguration of the PMFs due to the single event upset effect. Such a procedure takes at least 10 minutes and there is always risk of additional complications. To avoid such time loss, it was decided to test the detector behaviour if the Roman Pots were retracted to 10 σ for the time of re-scraping. Such a procedure could save about 6 minutes on moving the Roman Pots in and out completely, see Fig. 6.14, lower panel. Unfortunately the trigger rates during the beam re-scraping were still very high, causing the risk of the detector trip due to SEU. Thus, it was decided to move out the detectors completely for the beam re-scraping which takes about 8 minutes.

In comparison to the previous tests the background was reduced by factor of 1000. Moreover the trigger rate growth was very small, which suggests pretty stable conditions. Indeed, the offline analysis proved that the background level allowed selecting a clean sample of elastic events. It gave a green light for both tested schemes for physics data-taking. Details of the successful collimation schemes and procedures established for the data-taking are provided within the next Section.

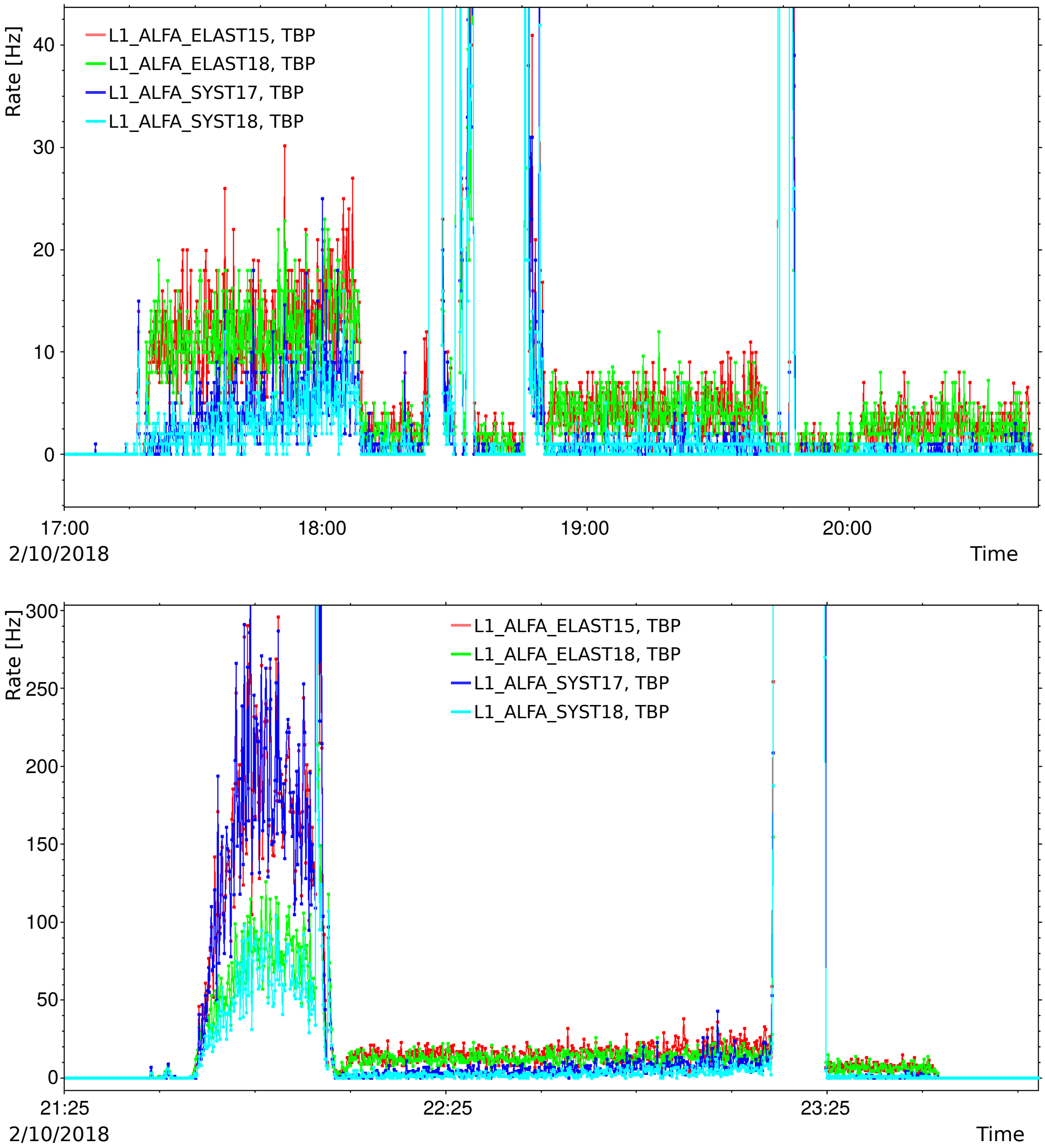

Figure 6.13: Elastic and background trigger rates over time during the test runs 362501 (upper) and 362547 (lower). Presented trigger rates represents sum of trigger rates from all 6 colliding bunches.

6.5 Physics Data Taking

During the 900 GeV campaign a number of runs at the LHC injection energy were performed using two collimation schemes mentioned in previous subsection. Only two runs were performed with non-colliding bunch injected – Runs 363469 (LHC fill 7284) and 363500 (LHC fill 7289) using the two-stage and the crystal collimation scheme, respectively. In total there were 12 runs including 3 that used the crystal

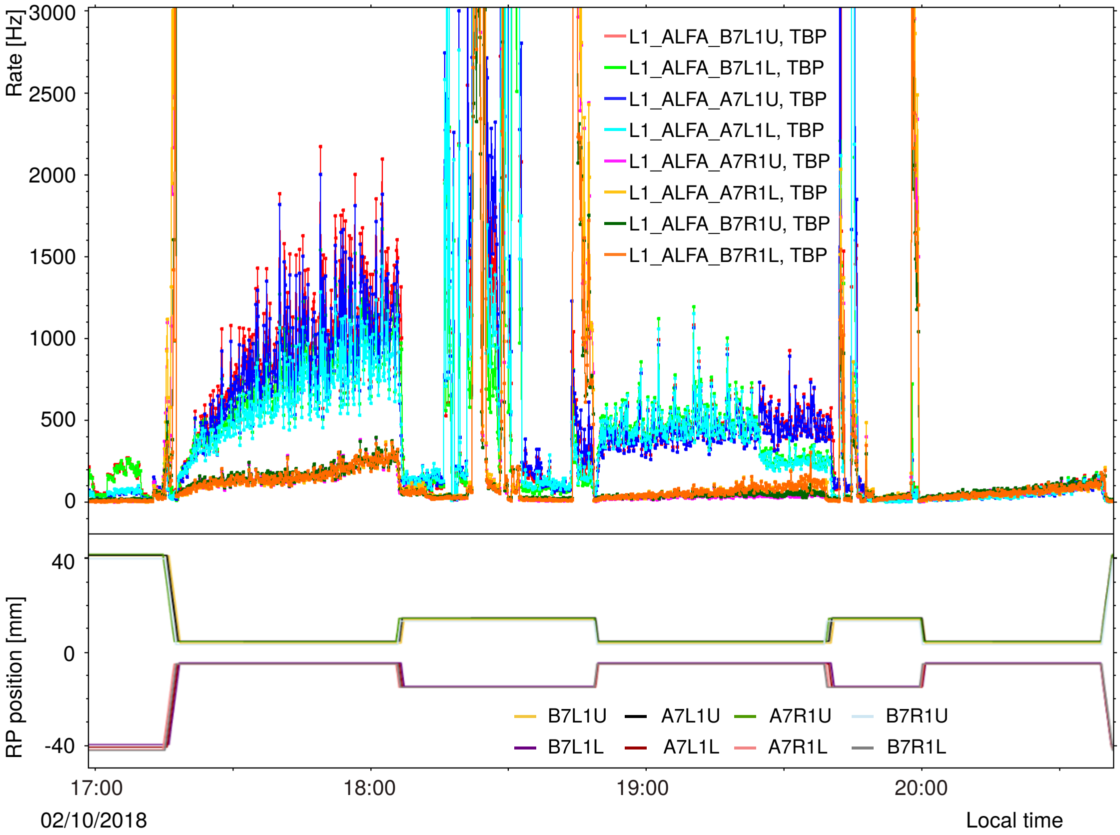

Figure 6.14: *UPPER PANEL:* The time dependence of the trigger rates for the Run nr 362501, for all colliding and non-colliding bunches. LHC fills 7249 and 7250. *LOWER PANEL:* Roman Pots positions given in mm. During rescraping the Roman Pots were retracted to 10 σ positions while during the data-taking all detectors were positioned at 3 σ.

collimation scheme. Moreover two of the runs were performed with PIX and SCT detectors included in the ATLAS partition. The details about runs can be found in Table 6.7 and in Fig. 6.15.

The target number of elastic events to reach was one million. The online estimation pointed to 1.011 millions of events collected using two-stage collimation scheme and about 400 thousands of events using the crystal-assisted collimation scheme.

The detailed collimation schemes are presented in Table 6.6. Before the injection the ALFA detectors were parked in the home position – about 40 mm from the beam centre. When the beams were injected and stabilised an initial scraping was performed:

- the TCP.D6[L/R]7.B[1/2] collimators were moved down to 2.5 σ;
- rest of collimators were moved from the injection to the data-taking positions according to the values in Table 6.6;
- the TCP.D6[L/R]7.B[1/2] collimators were retracted to the data-taking position

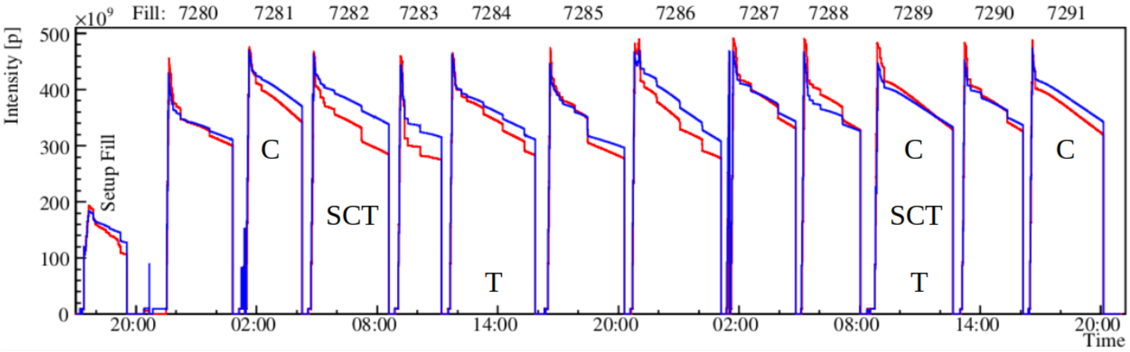

Figure 6.15: Beam intensities of the fills during ALFA high-β^* campaign. Characters marks on the plots corresponds to: "C" – runs with crystal-assisted collimation scheme, "SCT" – runs with PIX and SCT detectors included in the ATLAS partition, "T" – runs with non-colliding bunch injected in the partition, considered within this thesis.

Table 6.7: List of runs performed during data taking at injection energy.

LP	Run nr	LHC fill	Scheme	PIX+SCT	Events**	duration
1	363452	7280	two-stage	not included	105k	5:07
2	363460	7281	crystal	not included	122k	3:26
3	363461	7282	two-stage	included	126k	4:07
4	363462	7283	two-stage	not included	55k	2:30
5	363469*	7284	two-stage	not included	112k	4:36
6	363489	7285	two-stage	not included	48k	4:13
7	363495	7286	two-stage	not included	155k	4:47
8	363498	7287	two-stage	not included	163k	3:41
9	363499	7288	two-stage	not included	123k	3:14
10	363500*	7289	crystal	included	160k	3:46
11	363506	7290	two-stage	not included	123k	3:21
12	363510	7291	crystal	not included	118k	3:55

*Injected with non-colliding bunch, subject of this thesis. **Online estimation.

according to Table 6.6;

- the TCLA.A6[R/L]7.B[1/2] collimators were moved from 2.5 σ down to 2.0 σ position;
- the signal in the BLM stabilised, meaning the halo above 2.0 σ was cleaned;
- the TCLA.A6[R/L]7.B[1/2] collimators retracted to the data-taking positions – 2.5 σ as presented in Table 6.6;
- the ALFA Roman Pots were moved into their operational positions, i.e. 3.0 σ.

During the data-taking, the background trigger rate was slowly rising and when its rate reached the elastic one, re-scraping of the beam was requested – the ALFA Roman Pots were retracted to the home positions and the TCLA.A6[R/L]7.B[1/2] collimators were moved from 2.5 σ down to 2.0 σ position. After the BLM read-out got stabilised the TCLA.A6[R/L]7.B[1/2] collimators were retracted to 2.5 σ positions and the Roman Pots were reinserted.

The criterion of the re-scraping was the ratio of the elastic trigger and background trigger rates – if the ratio was around 1, re-scraping was requested. In case of the two-stage collimation run, the re-scraping was requested about every 45 minutes. For the crystal-assisted collimation scheme the background growth was low enough that the re-scraping was not required. Since during the 4th collimation test run the elastic trigger rate was reaching 20 Hz before the scraping, it was decided to call the beam dump and to re-fill the machine once the elastic trigger rate decreased to about 10 Hz.

6.5.1 Physics Data-Taking Using Two-Stage Collimation Scheme – Run Number 363469

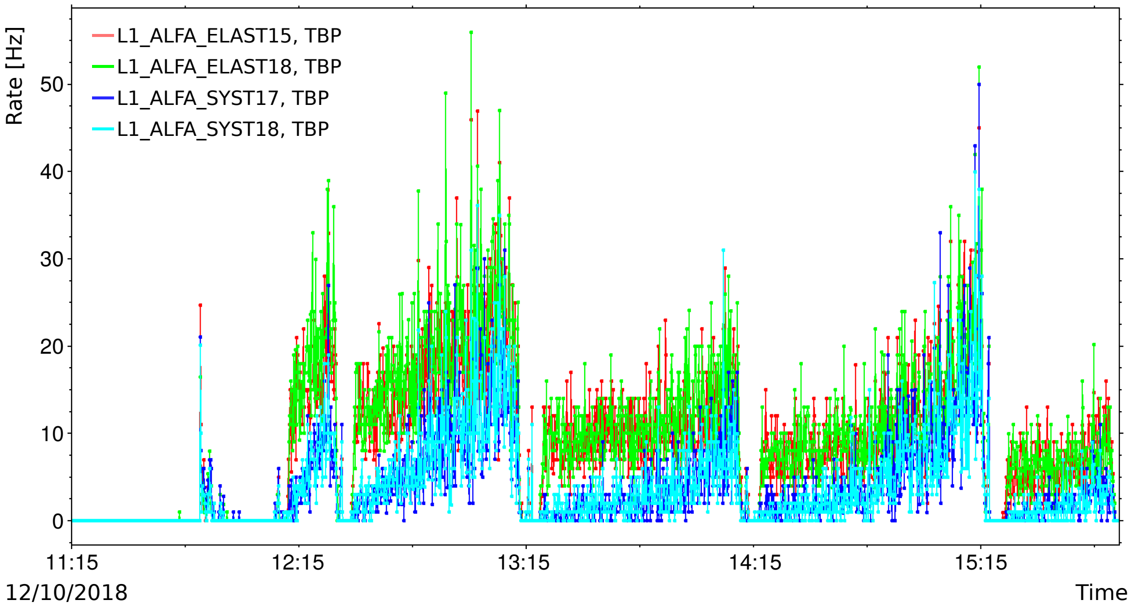

Figure 6.16: Elastic and background trigger rates over time during the data-taking, run nr 363469 – run with two-stage collimation scheme. Presented trigger rates represents sum of trigger rates from all 5 colliding bunches and non-colliding one LHC Fill 7284.

The timeline of this run was the following. The run was started at 11:17, Geneva local time, and the beams were injected at 11:30. The first peak visible on the plots in Figs 6.16 and 6.17 (upper panel) represents the initial scraping which started at 11:47. Later on, when the beams were stabilised, the Roman Pots were inserted at 12:16. After few minutes of the data-taking the background pattern and the rate growth were not satisfying, thus a re-scraping was requested. The final data-taking started at 12:32. As the background was slowly growing, three re-scrapings were requested at 13:14, 14:13 and 15:18. At 15:51 the beams were dumped and the run was ended.

The elastic and background trigger rates for the run with two-stage collimation

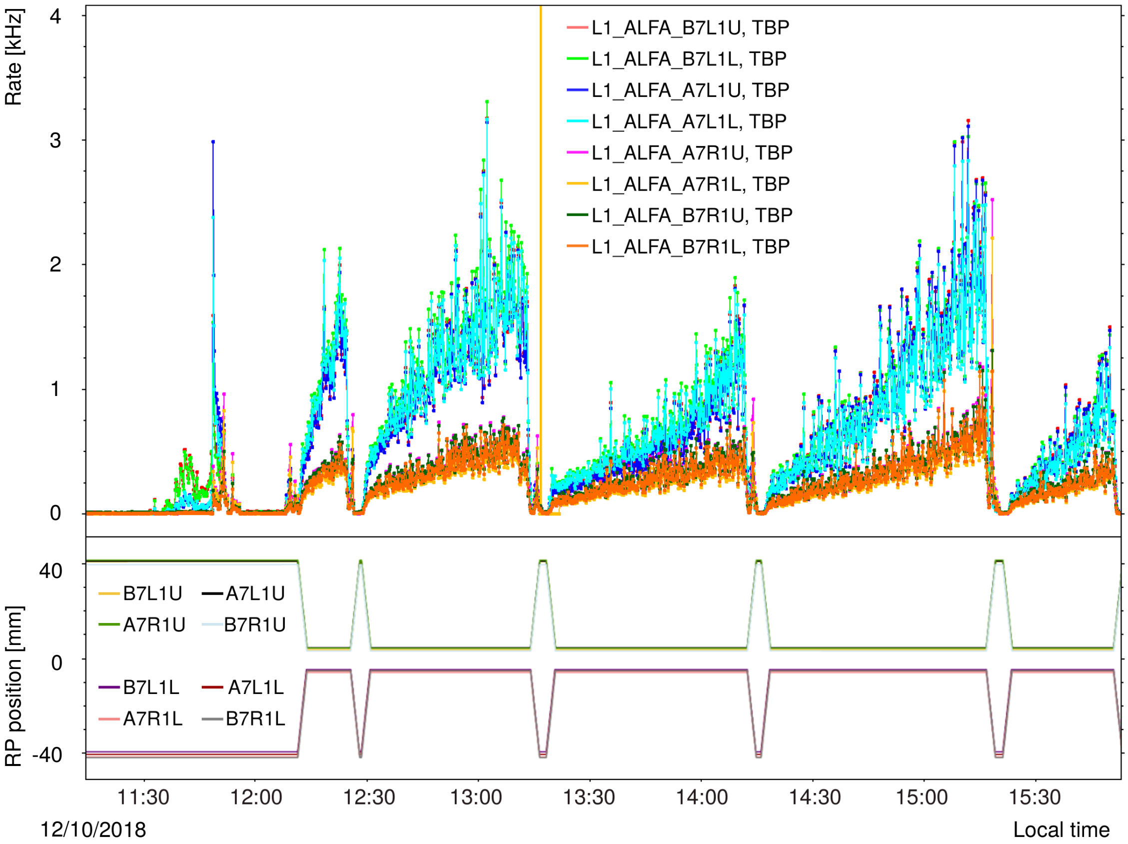

Figure 6.17: *UPPER PANEL:* The time dependence of the trigger rates during the data-taking with the use of the two-stage collimation scheme for run nr 363469, integrated over all colliding and non-colliding bunches. LHC Fill 7284. *LOWER PANEL:* Roman Pots positions given in mm. During rescraping fully extracted, while during the data-taking all detectors were positioned at 3 σ.

scheme are presented in Fig. 6.16. It is clearly visible from the plot that the elastic trigger rate is slowly growing, starting from about 15 Hz at the beginning of the run and exceeding 30 Hz before the first re-scraping. The background trigger rate starts from a level comparable to a few Hz and grows over time reaching the elastic trigger rate before re-scraping. As after the third re-scraping the trigger rate at the beginning of the data-taking period was less than 10 Hz, the beam dump was requested once the background trigger rate reached that of the elastic trigger.

The rates from the detectors are presented in Fig. 6.17 (upper panel) for the colliding and non-colliding bunches and corresponding Roman Pots positions in Fig. 6.17 (lower panel). The first observation is the difference between the rates measured by the detectors sensitive to Beam 1 and Beam 2. Detectors on the left hand side from the IP, looking from the center of the LHC, show much higher rates than the detectors on the opposite side. A detailed discussion will be provided in Chapter 7.

6.5.2 Physics Data-Taking Using Crystal-Assisted Collimation Scheme – Run Number 363500

The timeline of this run was the following. The beam was injected at 8:50 and the initial scraping followed by the crystal collimators insertion happened at 9:09. The Roman Pots were inserted at 9:17. At 11:43 the wire-scan measurements of the beam emittance requested by the ALFA were performed, see Figs 6.18 and 6.19 (upper panel). The beams were dumped at 12:38.

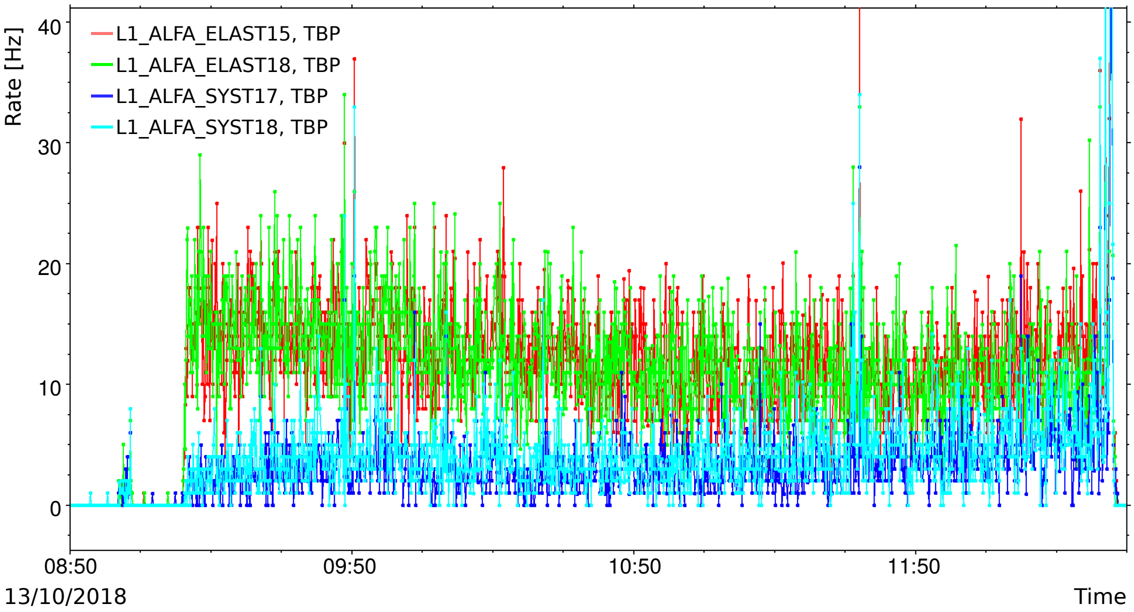

Figure 6.18: Elastic and background trigger rates over time during the data-taking, run nr 363500 – run with crystal-assisted collimation scheme. Presented trigger rates represents sum of trigger rates from all 5 colliding bunches and non-colliding one. LHC Fill 7289.

The elastic and background trigger rates for the run with crystal-assisted collimation scheme are presented in Fig. 6.18. Contrary to the run using the two-stage collimation scheme, the elastic trigger was slowly decreasing. Starting from the level of about 15 Hz and finishing at the level of about 11 Hz. The background trigger rate was slowly growing from 2 Hz at the beginning to about 5 Hz at the end of the run. The drop of the elastic trigger rate was much slower than the growth during the two-stage collimation scheme and allowed to run for over three hours without re-scraping.

The trigger rates integrated over all of the colliding bunches and the non-colliding one from each detector separately are presented in Fig. 6.19 (upper panel) and corresponding Roman Pots positions (lower panel). The rates measured by the detectors on the left side (Beam 2) are comparable in all detectors. In case of the right side (Beam 1) they are spread, the rates from each detectors do not overlap. Another observation is similar to the one done with the elastic and background

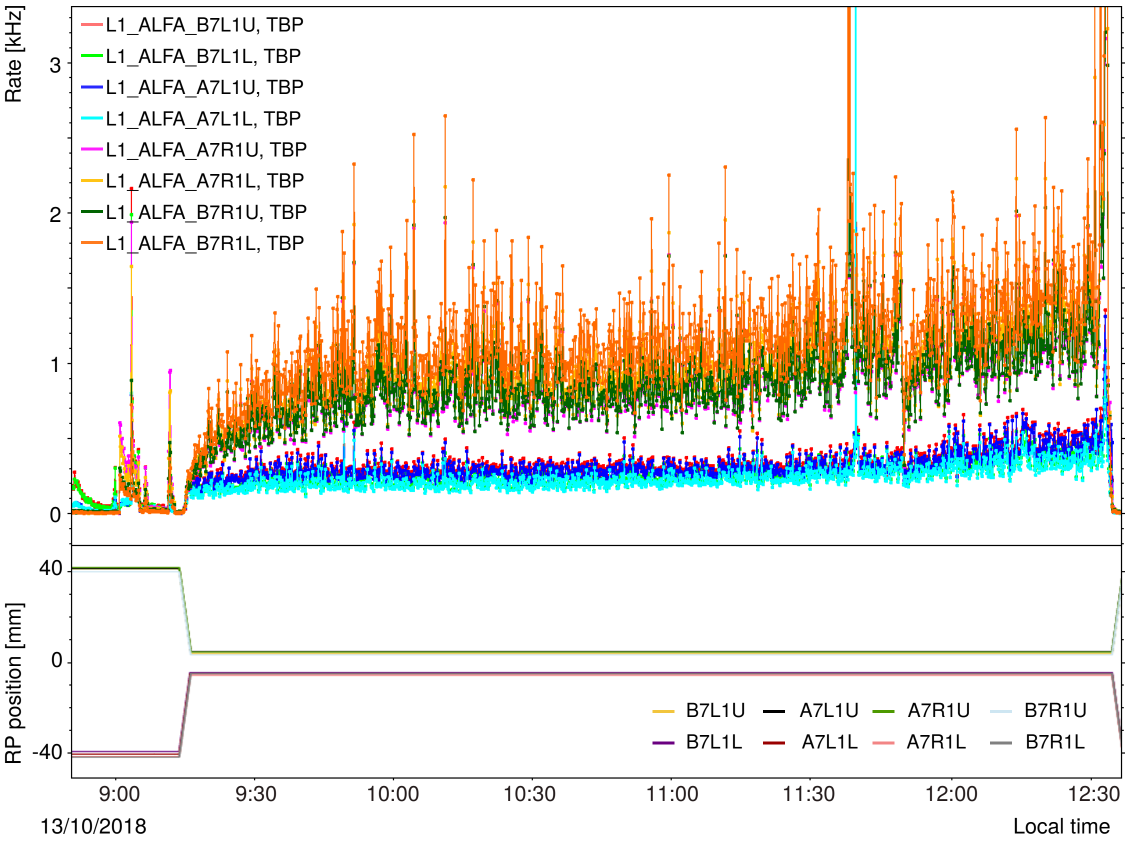

Figure 6.19: *UPPER PANEL:* The time dependence of the trigger rates during the data-taking with the use of the crystal-assisted collimation scheme for run nr 363500, integrated over all colliding and non-colliding bunches. LHC Fill 7289. *LOWER PANEL:* Roman Pots positions given in mm. During the data-taking all detectors were positioned at 3 σ and no re-scrapings were performed.

trigger rates. The rates from each detectors are growing but this growth is much slower than the one observed for the two-stage collimation. Moreover the rates are much lower than in case of the two-stage collimation. Details are discussed in the next Chapter.

Chapter 7

Data Analysis

This chapter presents the analysis of the data taken during two ALFA special runs at the LHC injection energy. Run 363469 and Run 363500, where data were taken using two-stage and crystal-assisted collimation schemes, respectively. The first part of the analysis, presented in Section 7.1, is focused on ALFA trigger rates of the different ALFA detectors. Second part of the analysis is presented in Section 7.2 and concerns reconstructed tracks and their spatial distributions.

7.1 Trigger Rates Analysis

First part of the analysis concerns comparison of the trigger rates between the detectors located on the left and right side of the ATLAS IP. Fig. 7.1 shows the trigger rates from the non-colliding bunch during the run with the two-stage collimation scheme. In contrast to the online plot presented in previous Chapter (Fig. 6.17, upper panel), this one is prepared from the data collected by the ALFA_CTPIN module, described in Chapter 5.4. Presented data are averaged every 100 readouts, which correspond to about 130 seconds, then smoothed using embedded procedures in ROOT analysis software. As it was already mentioned, due to the background growth, the beam had to be re-scraped every 45-50 minutes; three re-scrapings were performed, see Chapter 6.5.1. Further within this thesis, only the second data-taking period is taken into account due to a good detector performance, good data quality and to make the comparison of the background behaviour within considered runs more reliable. Beam 2 (left side) had twice higher trigger rate than Beam 1 (right side) and the ratio is presented in Fig. 7.2. On this plot and in the following text the ratio for the two beams means the ratio of the trigger rate from detector on Beam 1 divided by the trigger rate from detector on Beam 2.

In case of the trigger rates within the run using the crystal-assisted collimation scheme, the situation was different. The trigger rates are presented in Fig. 7.3. The plot was prepared from data collected in the same way as the plot for Run 363469

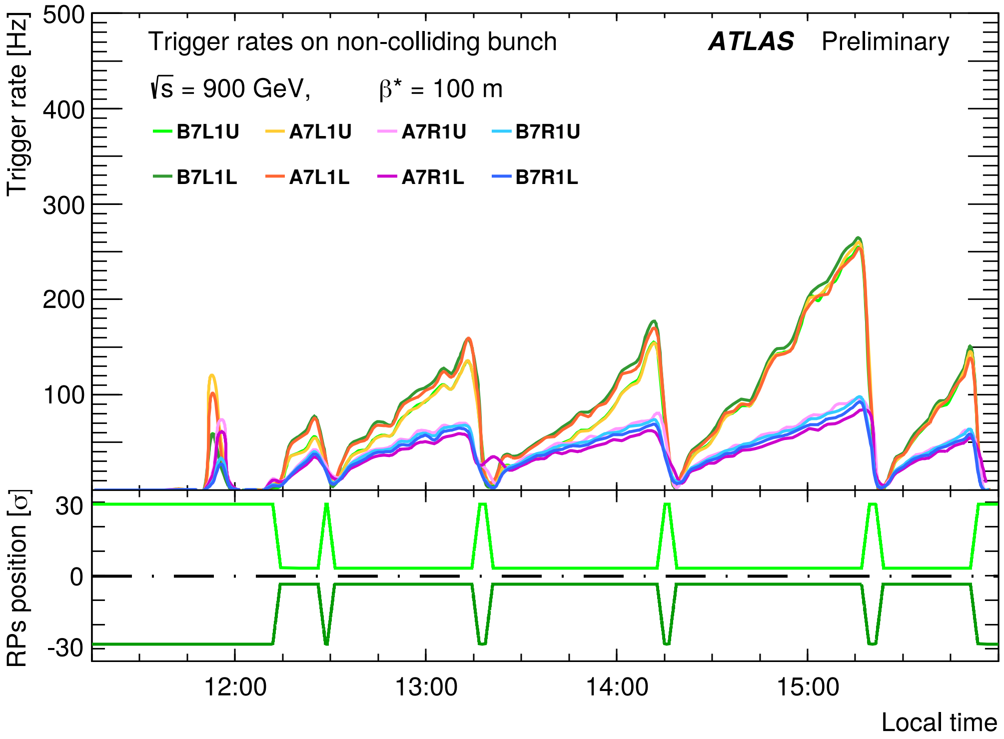

Figure 7.1: The time dependence of the trigger rate on non-colliding bunches for Run 363469 (upper panel) [85]. The plot was prepared for two non-colliding bunches – 462 and 520 on Beam 1 and Beam 2, respectively. The lower panel presents Roman Pots position in σ units.

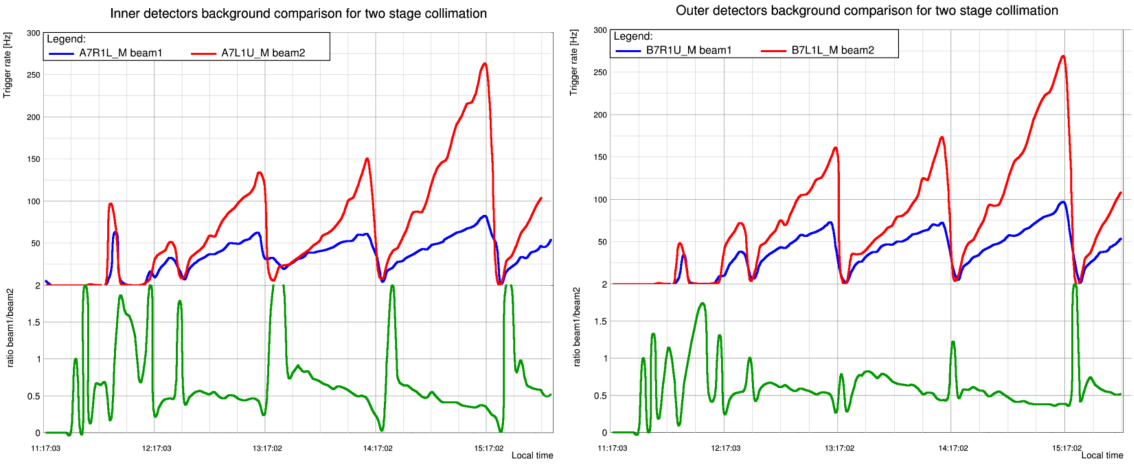

Figure 7.2: The ratio between rates of 2 detectors belonging to the same detector arm during the run with use of the two-stage collimation scheme. Left plot shows comparison between inner detectors and right plot shows the same comparison for outer detectors.

(Fig. 7.1). The rate from Beam 1 is similar to the one obtained with use of the two-stage collimation scheme. The speed of growth is also comparable. The main difference comparing to the two-stage collimation scheme is the spread of the trigger rates between the detectors on the right side. The difference between the rates from the B7R1U (lowest rate) and B7R1L (highest rate) is 25 Hz at the beginning of the run, and reaches level of 50 Hz before the beam dump. Detectors from Beam 2 all have comparable rates, no spread is observed.

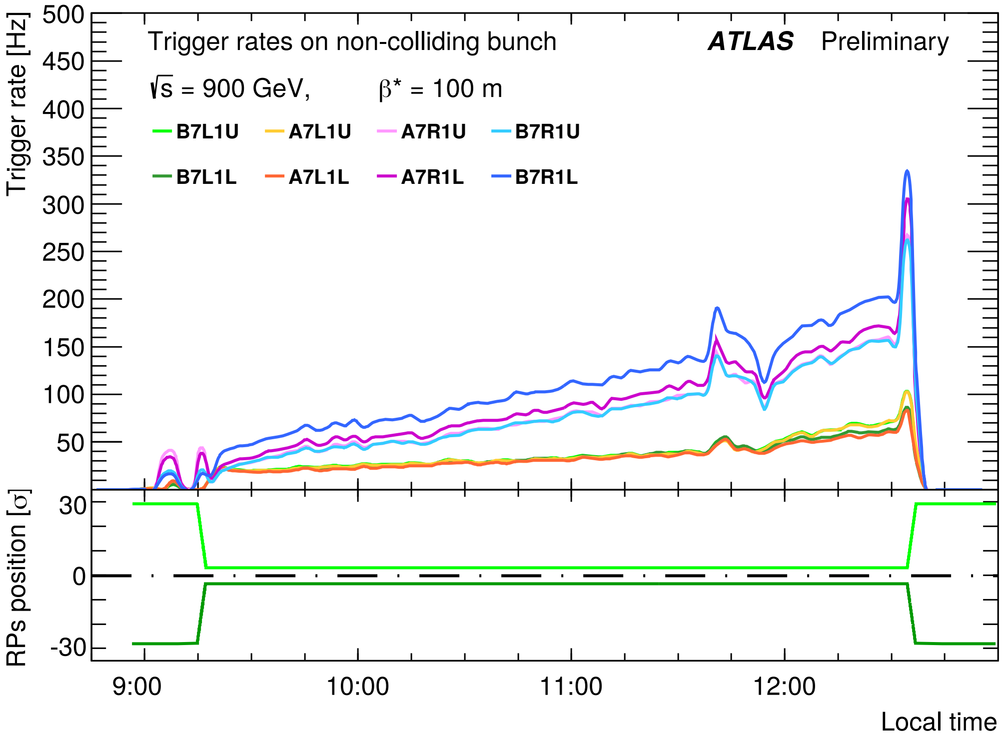

Figure 7.3: The time dependence of the trigger rate on non-colliding bunches for Run 363500 (upper panel) [85]. The plot was prepared for two non-colliding bunches – 2655 and 2755 on Beam 1 and Beam 2, respectively. The lower panel presents Roman Pots position in σ units.

The ratio Beam 1/Beam 2 is opposite to the one observed in the case of the two-stage collimation, see Fig. 7.4 and is about 2.0-2.5, depending on the compared detector. The trigger rate from Beam 2 is about 4 times lower than the one obtained in case of the two-stage collimation meaning significant improvement in the beam-induced background reduction. The ratio is more fluctuating over the time.

7.2 Analysis of the Track Spatial Distribution

The second stage of the analysis is focused on the spatial distributions of halo particles registered in the detectors. The spatial distribution of the reconstructed tracks collected within Run 363469 is displayed in Fig. 7.5. The plot presents events from the non-colliding bunches – left four panels present tracks from BCID

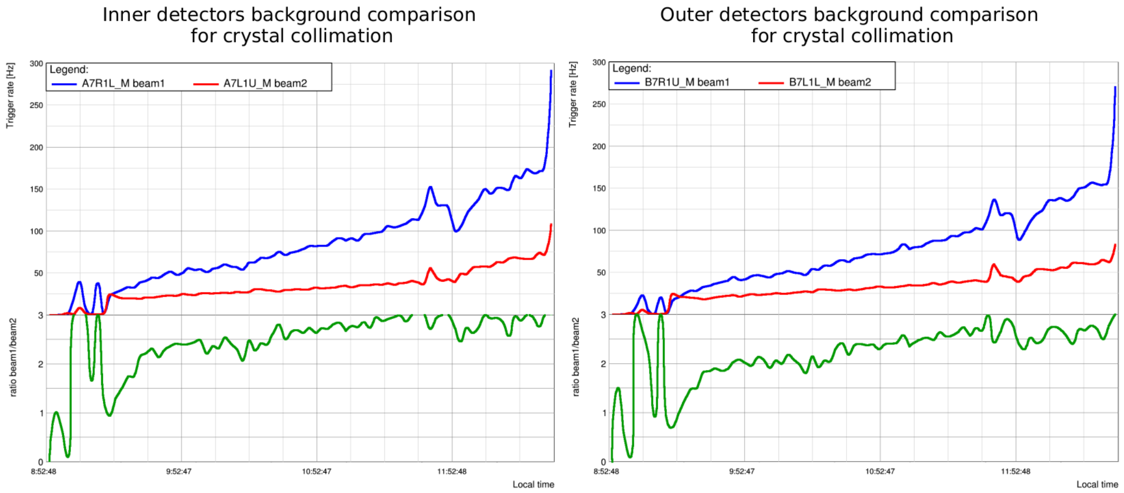

Figure 7.4: The ratio between rates of 2 detectors belonging to the same detector arm during the run with use of the crystal-assisted collimation scheme. Left plot shows comparison between inner detectors and right plot shows same comparison for outer detectors.

520 (Beam 2), right four panels show BCID 462 (Beam 1). The presented data were collected only within the first period, as mentioned in the previous section.

In the plots, the distribution fill the whole shape of the detector – square 32×32 mm^2 with cut edge. The green colour corresponds to a region limited by the LHC aperture. In the close vicinity of the beam, the colours turn to yellow, orange and red showing higher intensity of the beam halo.

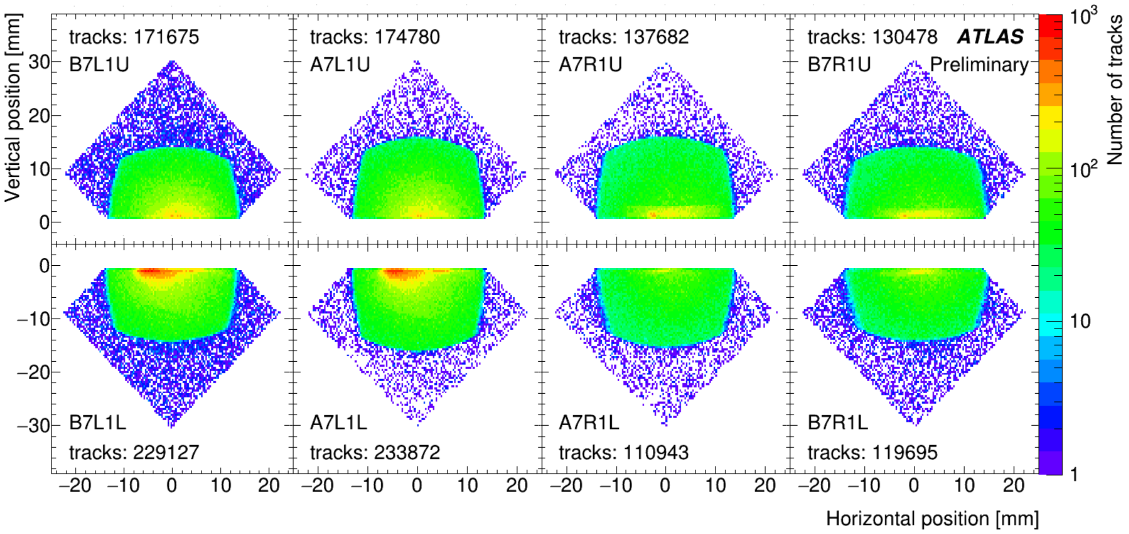

Figure 7.5: Spatial distribution of reconstructed tracks during Run 363469 (two-stage collimation scheme). Plot represents data collected between lumiblocks 130 and 175 on non-colliding bunches – left four panels are related to BCID 520 (Beam 2) and right four – BCID 462 (Beam 1).

For run 363500 (crystal-assisted collimation scheme), the spatial distribution is displayed in Fig. 7.6. This plot presents reconstructed tracks only from non-colliding bunches. Thus, left four panels display tracks from BCID 2755 (Beam 2) and right four – BCID 2655 (Beam 1). Plot shows a period starting after the Roman Pots were inserted to the measurement position. The ending time was chosen to show the same amount of time as for Run 363469. Such a period was chosen to ease the comparison of the same length data-taking with similar initial conditions (after initial scraping). The colour scale is the same as for Fig. 7.5 to make the comparison even more direct.

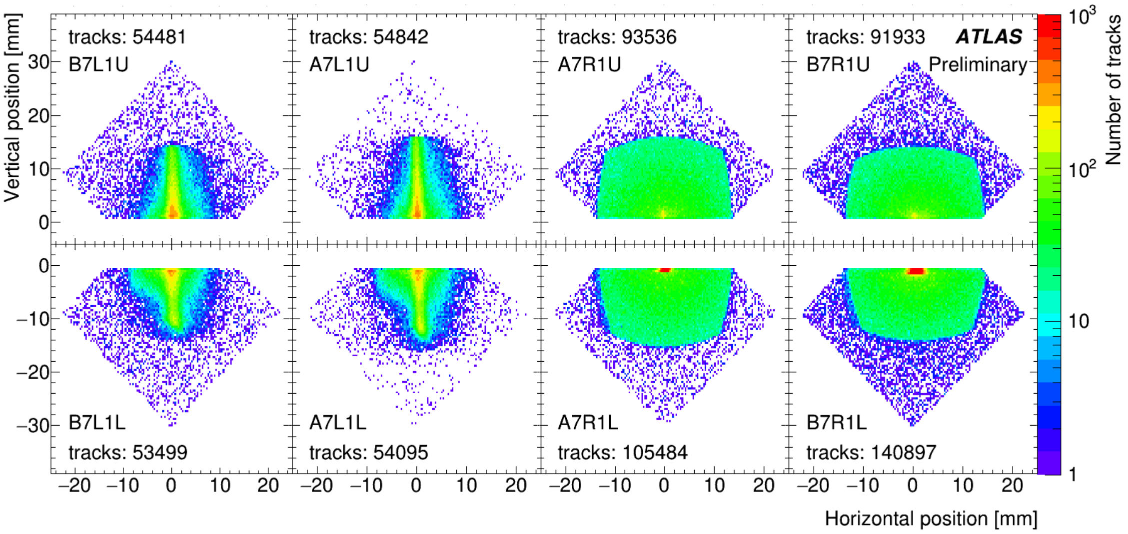

Figure 7.6: Spatial distribution of reconstructed tracks during Run 363500 (crystal-assisted collimation scheme). Plot represents data collected between lumiblock 32 and 77 on non-colliding bunch. Plot presents reconstructed tracks from two different non-colliding bunches – left four panels are related to BCID 2655 (Beam 2) and right four – BCID 2755 (Beam 1).

Beam 1 (right side) looks quite similar for both collimation schemes. In case of the crystal-assisted scheme, high intensity halo in close vicinity of the beam is more intensive but limited to a smaller region.

The shape of the distribution for the left side (Beam 2) is more interesting. The beam halo is narrower in comparison to the two-stage collimation scheme, but more spread in the y-axis direction. Also amount of the reconstructed tracks is smaller by a factor of 3 for upper detectors and by a factor of 4 for the lower detectors. The obtained pattern looks similar to the elastic one. Obviously there is no elastic scattering as the plot in Fig. 7.6 was created only for tracks related to the non-colliding bunch.

The origin of the phenomenon was a subject of research performed by the Collimation Team. Finally the simulation of 10^8 protons intercepted by the collimation system allowed to reproduce the pattern, see Fig. 7.7.

From the simulation the mechanism behind the observed background is deduces,

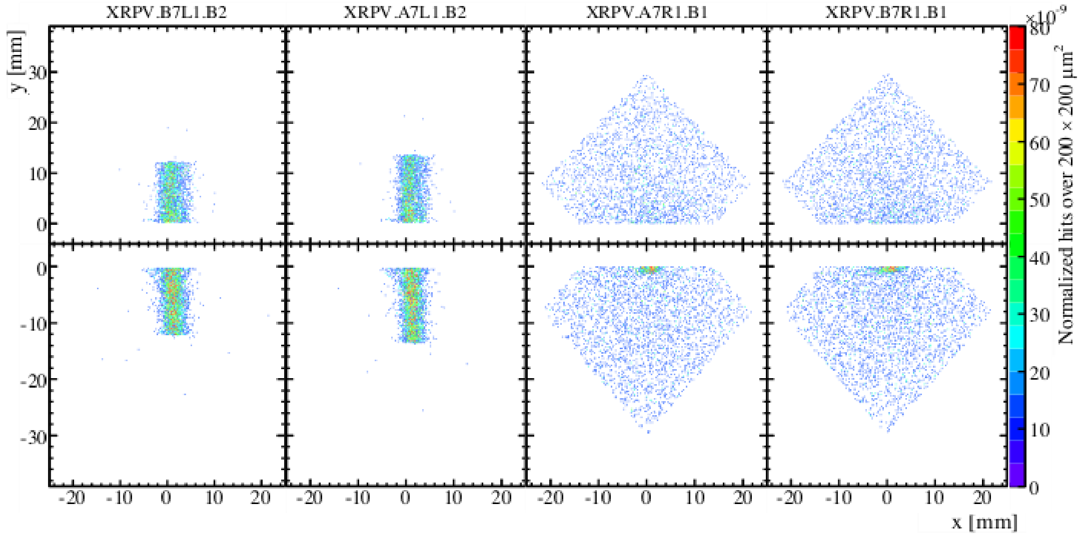

Figure 7.7: Simulation of Run 363500 [74]. The developed tools allowed to reproduce the conditions during the run with very nice agreement with the collected data.

see Fig. 7.8. Some protons intercepted by the crystal collimators undergo the dechannelling effect. As the dechannelled particles got less deflection from the particles following the crystal channel properly, they bypassed the absorber placed behind the crystal collimator and travelled along the beam. Then they were running typically 10 turns around the machine until they hit the TCLA.A5L3.B2 collimator in IR3. Some fraction of the particles that hit the collimator got elastically deflected and then hit the ALFA detectors on the left side of the ATLAS IP. The scattering process on the collimation itself is isotropic, thus the particles got the same deflection in every direction. However, due to different optics parameters in the x and y direction, the trajectories of the particles are different.

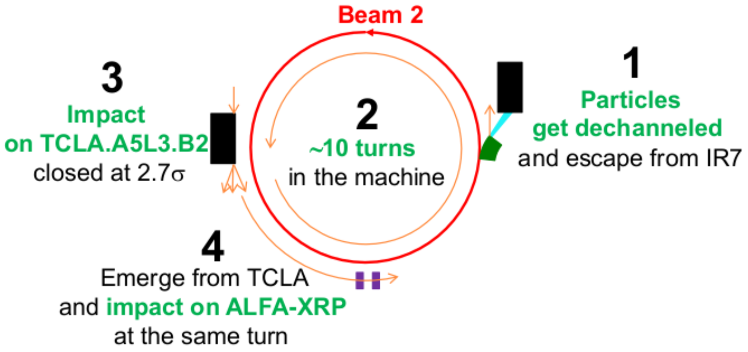

Figure 7.8: Explanation of the source of the pattern seen on the spatial distribution of the reconstructed tracks from Run 363500 [74].

The deflection acquired by the particles at the TCLA.A5L3.B2 can be calculated from [74]:

$$\frac{\Delta y(\theta_{el})}{\Delta x(\theta_{el})} \propto \frac{\theta_{el}\sqrt{\beta_y^{TCLA}\beta_y^{XRP}}sin(\Delta\mu_y^{XRP-TCLA})}{\theta_{el}\sqrt{\beta_x^{TCLA}\beta_x^{XRP}}sin(\Delta\mu_x^{XRP-TCLA})} \approx 20. \tag{7.1}$$

where $\Delta x(\theta_{el})$ and $\Delta y(\theta_{el})$ are deflections acquired in directions of the x and y axis, respectively, and are measured in mm in the plane of the detector. β_x^{TCLA} (β_y^{TCLA}) and β_x^{XRP} (β_y^{XRP}) are values of the the β function in the location of the collimator and the ALFA Roman Pots, respectively. Indices x and y corresponds to the considered axis. $\Delta\mu$ is the phase advance difference between the collimator and the detector and the values are:

$$\Delta\mu_x^{XRP-TCLA} \approx 4^\circ. \tag{7.2}$$

$$\Delta\mu_y^{XRP-TCLA} \approx 244^\circ. \tag{7.3}$$

As the main source of the pattern seen on the plot 7.6 was the TCLA.A5L3.B2 collimator, another simulation for the Beam 2 was performed. This time the collimator was “retracted” to 13 σ position. The result of the simulation is presented in Fig. 7.9 where, there is no peculiar pattern. In general, the amount of background is much smaller and is more evenly distributed in both directions, around the beam centre.

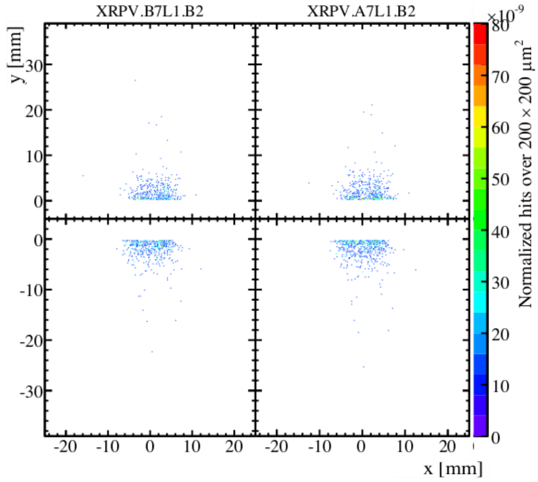

Figure 7.9: Simulation of Run 363500 with the TCLA.A5L3.B2 retracted to the 13 σ position [74].

The next step of the spatial distributions analysis is a check of their time evolution. Fig. 7.10 (left panel) shows the mean x position of the hits over lumiblocks (time in bins equal to five lumiblock). For six detectors it is rather stable. For detectors B7L1L and A7L1L the mean x position moves by about 0.4-0.5 mm. Indeed it corresponds to the plots of Fig. 7.5 which shows a little different, and quite spread distribution for the mentioned detectors.

A similar behaviour is observed in the y direction. The mean value on the y-position moves by about 0.5 mm for B7L1L and A7L1L, see Fig. 7.10 (right panel). Signals from rest six detectors are rather stable over time.

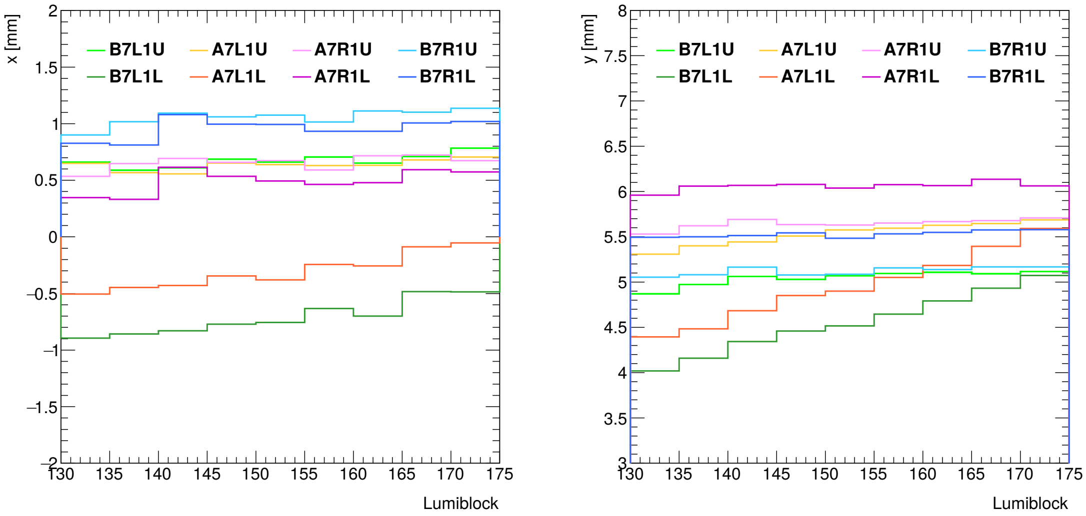

Figure 7.10: Mean value of the x-axis position (left panel) and y-axis position (right panel) of the track position as a function of lumiblocks for Run 363469 (two-stage collimation scheme).

The next step is to check the standard deviation of the distributions on x- and y-axis, see Fig. 7.11 left and right panel, respectively. Standard deviation informs about the stability of the beam conditions, thus it is another good indicator of the background growth and the beam quality. In case of the x-axis, the standard deviation is about 6.7 mm on the right side. In case of the detectors located on the left side, the deviation is constantly growing over time. At the beginning of the data-taking period (right after the re-scraping of the beam) it is about 5.7-6.2 mm, depending on the detector and at the end of the data-taking period (before the next beam re-scraping) it is 6.2-6.4 mm, depending on the detector. The growth is linear over time, and the speed of the growth is higher for the lower detectors than for the upper ones.

In case of the y-axis, the standard deviation is about 4.0-4.5 mm, depending on the considered detector and is stable over time. This result shows the beam related background on the y-axis time dependence is stable.

In case of the run using the crystal-assisted collimation scheme the x- and y-axis mean track positions as a function of time are given in Fig. 7.12 left and right panel, respectively. Values presented are the mean values per five lumiblocks. The mean track position values on x-axis are stable over time. Similar situation is with the y-axis.Stable position of the mean value of the background hit distribution

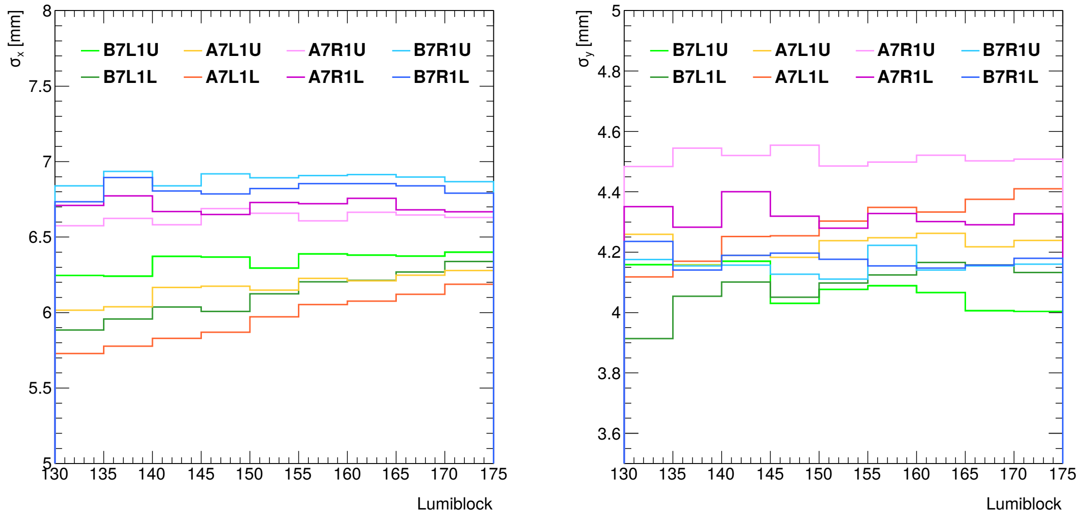

Figure 7.11: Standard deviation of the track spatial distribution x-axis position (left panel) and y-axis position (right panel) of the tracks over lumiblocks for Run 363469 (two-stage collimation scheme).

means stable beam conditions and thus, easier further physics data analysis, mainly distinguishing signal from the beam-induced background.

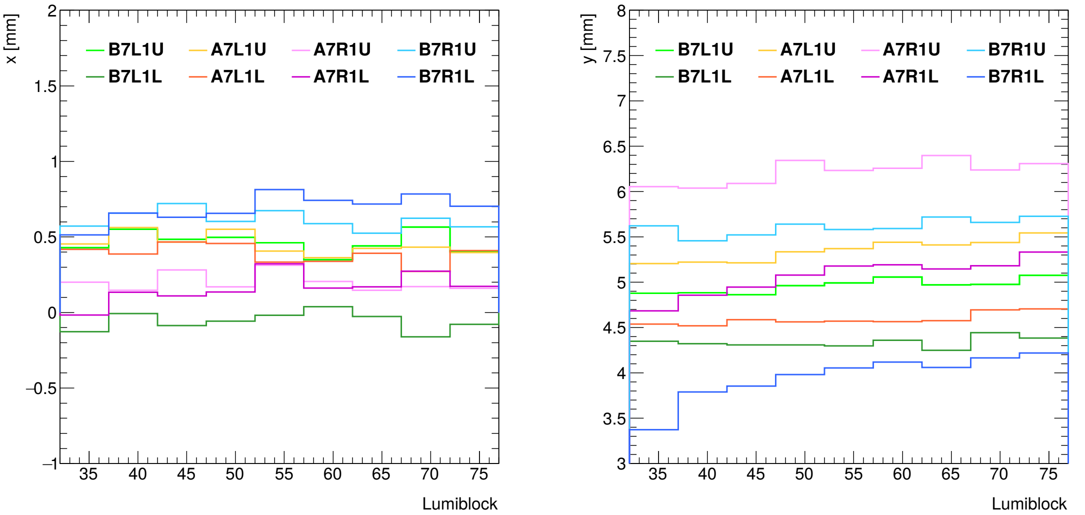

Figure 7.12: Mean value of the x-axis position (left panel) and y-axis position (right panel) of the track position as a function of lumiblocks for Run 363500 (crystal-assisted collimation scheme).

Another item to study is the standard deviation of the reconstructed track spatial distributions for the run using the crystal-assisted collimation scheme, see Fig. 7.13 left and right panel for x-axis and y-axis, respectively. The standard deviation for Beam 1 is quite similar to the one obtained in case of the two-stage collimation scheme. Values are different for each detector in range from 5.2 mm to 6.8 mm.

Values are slowly growing over time to reach the range of 5.7-7.0 mm after 45 minutes. In case of the Beam 2 the values are in the range of 2.5-3.5 mm after the initial scraping and very slowly decreasing – downto 2.4-3.3 mm after 45 minutes of the data-taking. Much smaller standard deviation on the left side comes from the fact that the background particles are concentrated around the center part of the detector, Fig. 7.6.

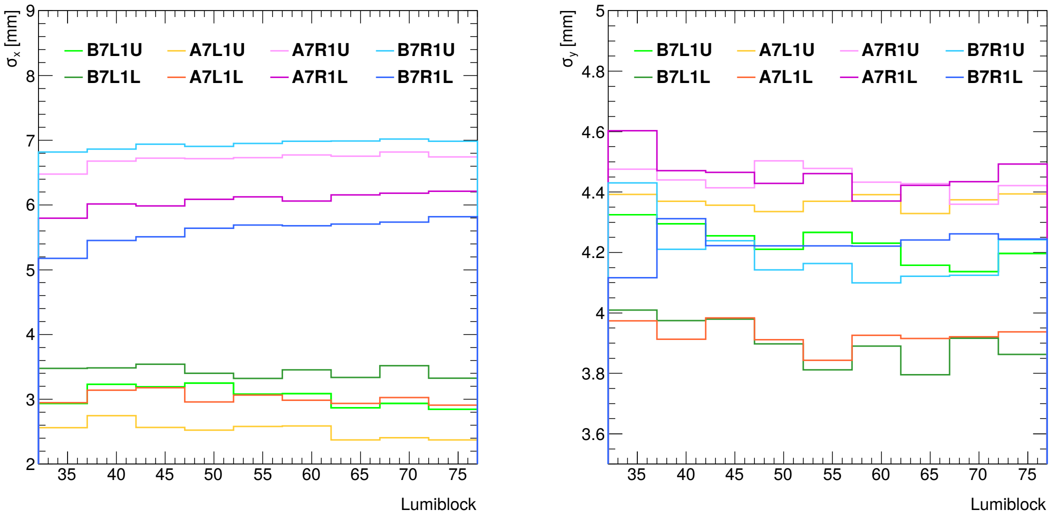

Figure 7.13: Standard deviation of the track spatial distribution x-axis position (left panel) and y-axis position (right panel) of the tracks over lumiblocks for Run 363500 (crystal-assisted collimation scheme).

On the y-axis the standard deviation is more stable. After initial beam scraping these values are between 4.0 and 4.6 mm. These values depend on the detector. Over time the standard deviation decrease is about 0.1 mm. The value of the standard deviation for the crystal-assisted collimation scheme is similar to the one obtained in case of the two-stage collimation scheme, see Fig. 7.11 (right panel). Such stable conditions are very good from the data analysis point of view. It means the background distribution pattern is constant over time, thus the further separation of the signal from the beam-related background is much easier.

7.3 The Background Reduction Factor

Having background rate measured by the ALFA detectors for both – two-stage and crystal-assisted collimation schemes, one could compare them with the simulations for validation and then to each other to extrapolate models and future collimation schemes. The simulation of the crystal-assisted collimation scheme was already presented and discussed in previous section. Similar simulation was also performed for Run 363469 with use of the two-stage collimation scheme. The result of such simulation is presented in Fig. 7.14.

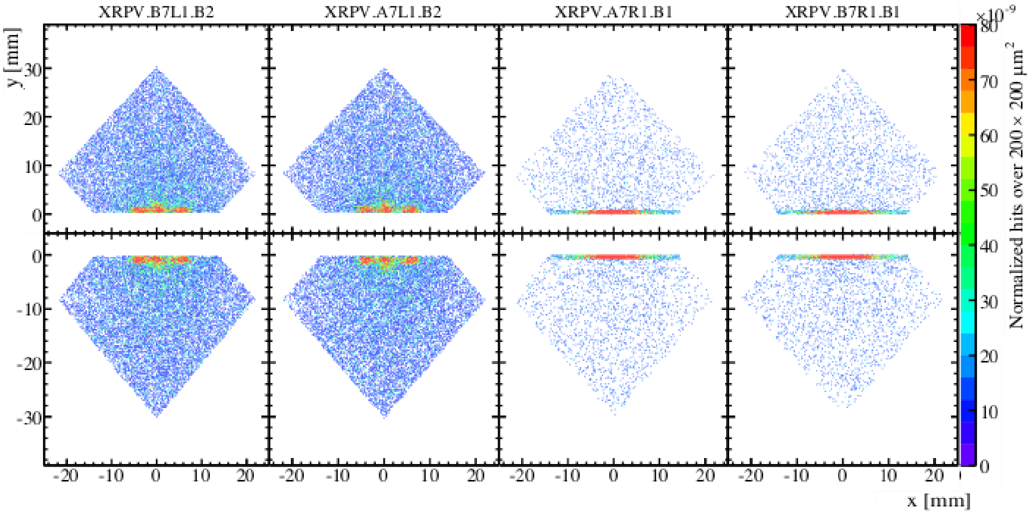

Figure 7.14: Simulation of Run 363469 [74]. The developed tools allowed to reproduce the conditions during the run with very good agreement with the collected data.

Dividing the number of events collected during two-stage collimation data-taking by the amount of events from the crystal-assisted collimation scheme one can get the background reduction factor. Same ratio was calculated for simulated data. The result is presented in Fig. 7.15. The agreement between ratio from the data and from the simulation is very good and the simulated ratio fits in the uncertainty of experimental data [74]. The background reduction factor for the Beam 1 (left side) is about ∼4.5, while for the other side is about ∼1.6. The data shows background reduction factor about ∼5 for the left side, while for the right side ∼1.4.

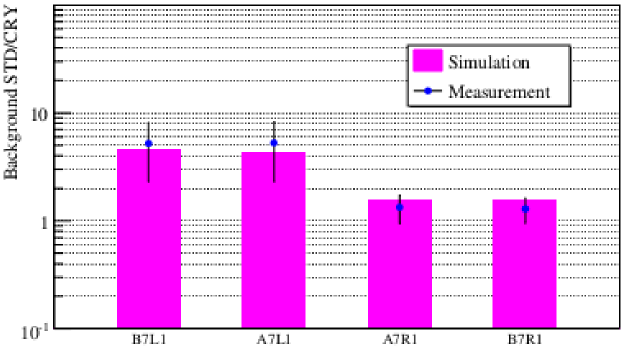

Figure 7.15: Background reduction factor for crystal collimation scheme. The comparison with the experimental data shows a good agreement of the simulation with the reality [74].

The background reduction factor was also calculated for the improved crystal-

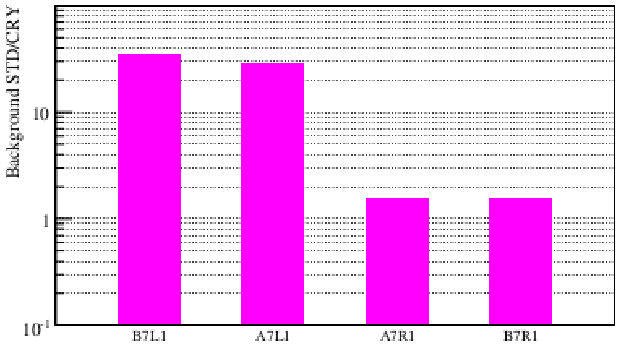

Figure 7.16: Background reduction factor for improved crystal collimation scheme [74]. The result from the simulation is very promising for the future data-taking using crystal-assisted collimation scheme.

assisted collimation scheme. The result is presented in Fig. 7.16. The simulation shows that new improved collimation scheme allows to reduce the background by the factor of ∼30 in comparison to the two-stage collimation scheme.

From the above discussion, one can conclude that the collimation based on bent crystal is more efficient and gives more stable background rate over time. This can be related to the multi-turn halo processes [74]. Such a process is possible if the number of the particles impinging the collimation is larger than the number of removed particles. The CWG performed simulations of multi-turn halo and obtained distributions of particles removed within certain number of turns. The results are given in Fig. 7.17.

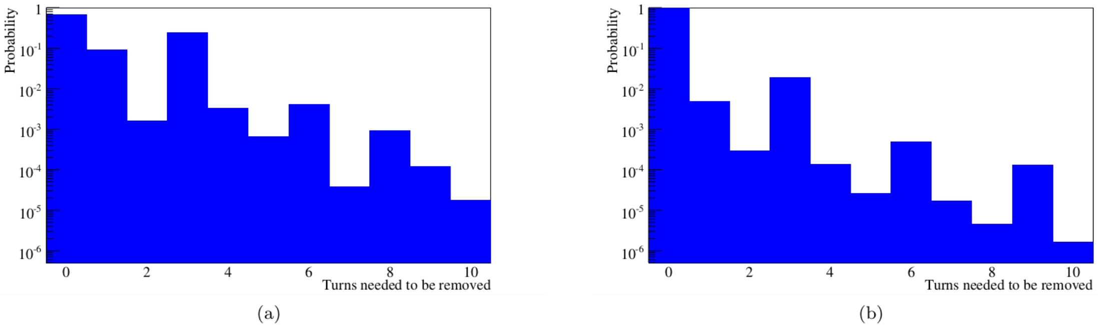

(a)

(b)

Figure 7.17: Probability of the number of turns needed to be removed from the circulating beam after being intercepted by the primary stage using a) two-stage and b) crystal-assisted collimation scheme [74].

The simulation shows that for the two-stage collimation only 66% of the particles impinging into the collimators used as a primary stage are removed within the one turn. Thus, 34% of the particles are repopulating the beam halo, and requires more than one turn to be removed. In case of the collimation scheme assisted with bent crystals, 98% of halo particles are removed within one turn.

The simulation also shows peaks of absorption every three turns. It is especially visible for the simulation of the crystal-assisted collimation scheme. The reason of such behaviour comes from the LHC tune which was about $Q \approx 1/3$. It is worth to mentioning that for the crystal collimation scheme there was only one single-sided collimator at the primary stage, while for two-stage collimation scheme the TCLA.A6 used as a primary stage was inserted symmetrically (two jaws on both sides of the beam). It shows much higher effectivity of the halo removal by the crystal collimators.

7.4 Event Reconstruction and Physics Background

The detailed analysis of the data recorded during 900 GeV campaign is still ongoing. However, reconstruction of events was done a few days after the data-taking. The number of reconstructed events normalised to the run duration shows that in runs assisted with crystal collimators, there were about 15% more events within the same time of the data-taking [103]. This value roughly corresponds to the time spent on the beam re-scraping.

The background to elastic processes for the runs using two-stage collimation was between 0.13 and 0.5%, depending on the run [103]. In case of the runs assisted by crystal collimators, the background fraction was about 1.5-1.6%. Even though the amount of background was much higher for the runs with use of crystal collimators, it was still relatively low and still allows gathering more useful data within the same run duration. Moreover, it is very likely that the new collimation scheme will improve the background level.

7.5 The Beam Background Asymmetry Explanation

The source of the beam-related background can be discussed in the context of the phase-space coverage of the collimators and Roman Pots [74]. The particles registered by the Roman Pots had to pass the primary and secondary-stage collimators first. Then hits the detectors, and all is happening within one turn. Detectors sensitive to the Beam 1 are fully covered by two collimators and partially covered by one collimator. This gives in total from 2 to 3 metres of tungsten, that particles have to cross before impacting on the detector. In case of the Beam 2, detectors are fully covered by only one collimator, and partially covered by three others. Thus they are covered in total by 1 to 4 metres of tungsten. This difference cause the asymmetry in the trigger rates observable on both sides of the ATLAS IP.

Summary and Conclusions

The background in high energy physics experiments is an inherent contribution to the collected data. Its minimization is indispensable for gathering high quality data and precise determination of the measured quantities. This is possible only by detailed studies of the backgrounds occurring in the experiment. It is very important to understand the source of the background and measure its amount. For this purpose a special measurement methods and specialized detectors can be used.

ALFA – Absolute Luminosity For ATLAS is an ensemble of detectors designed to determine the LHC luminosity by measurement of the elastic scattering in a forward direction. It consists of 8 detectors – 4 on each side of the ATLAS interaction point. Each detector is installed inside of a Roman Pot which allows to move the detector towards the LHC beam to a distance of a few mm. Each detector consists of 20 layers of crossed scintillating fibres with a square cross-section 0.5 x 0.5 mm^2. Such a construction allows track reconstruction with 30 μm spatial resolution. The detector features allowed the author to assume the ALFA detectors could be used to measure LHC beam-induced background in ATLAS experiment using data from non-colliding bunches.

The results presented within this thesis confirm possibility to use the ALFA detector for beam-induced background measurement. ALFA delivers additional information about the time evolution of the background and its spatial distribution which are not available using other existing detectors at LHC. The special info obtained from the ALFA detectors is in addition complemented by information on the per BCID ALFA trigger rates published by the ALFA_CTPIN module which was programmed and maintained by the author. ALFA measurements allow also cross-checking other beam-induced background measurements in an independent manner.

The analyzed data were taken at the LHC injection energy i. e. 900 GeV in the centre of mass reference frame. The optics β^* at the ATLAS interaction point was set to 50 and 100 metres in the x and y planes, respectively. The beam intensity was reduced by injecting only 5 colliding bunches and 6th non-colliding one and each bunch contained $0.8 \cdot 10^{11}$ protons.

The data-taking was preceded with a series of tests of collimation schemes, to find optimal parameters allowing the data collection. Finally, two collimation schemes were chosen for the final data-taking. The first one – two-stage collimation scheme with only amorphous collimators. The second one supported by the crystal collimators, which were never used before for the physics data-taking at the LHC.

During the test runs only the trigger rates were measured and compared with the physics models. Although the tracker data were recorded, the level of the background was 3-4 orders of magnitude too high, and thus, it was not possible to distinguish the physics data from the background. In the final data-taking, all data were stored allowing the background studies presented in this thesis.

This thesis contains an analysis of two runs, in which the non-colliding bunches were injected, and thus, the background was measured. The trigger rates for both amorphous and crystal collimation schemes were compared proving improvement of the background level in the runs using crystal collimation scheme. For the detectors on the left side the background trigger rate was about four times smaller when using the crystal assisted collimation than for the other run. Moreover, the time evolution of the trigger rates showed much more stable conditions during the runs assisted by the crystal collimators. The scraping of the beam for the runs with the two-stage amorphous collimation scheme was required every 45-60 minutes. In case of the run assisted with crystal collimators, the re-scraping was not required. This allows to save 20-30 minutes during the run.

Having the spatial distribution of the particles registered by the ALFA Main Detectors the beam halo shape was measured. Again, the conditions were more stable in the run using the crystal collimation scheme. The mean value of the tracks positions during the run was rather stable when the crystal collimation scheme was used. The standard deviation of the track positions in the x direction was smaller, especially on the left side of the ATLAS IP.

On the other hand, the physics background during the runs using the crystal-assisted collimation scheme was three times higher than during the other one – 1.5% in compare to about 0.3% in the runs without the crystal collimators. However, no need of the beam re-scrapping and, as mentioned above, more stable measurement conditions allowed for a larger amount of data to be processed within the same time, making the crystal-assisted scheme more efficient. Using the data collected by ALFA and presented in this thesis, the Collimation Working Group improved the collimation scheme. The new crystal assisted collimation scheme presents a non-negligible improvement of the background reduction in simulation. The results will be considered during preparation phase of the data-taking in the LHC Run 3.

The results presented in this thesis allowed understanding the source of the beam background and stimulated improvement of the simulation tools. Thus, it was possible to find a solution allowing the beam background reduction, which also was discussed.

The data presented within the thesis were collected with active participation of the author. The author was also engaged in all jobs related to detector maintenance and preparation to the data collection.

Appendix A

Abbreviation List

AFP	ATLAS Forward Proton
ALFA	Absolute Luminosity For ATLAS
ASIC	Application-Specific Integrated Circuit
ATLAS	A Toroidal LHC Apparatus
BCID	Bunch Crossing Identifier
BCM	Beam Condition Monitor
BCT	Beam Current Transducer
BLM	Beam Loss Monitor
BSRT	Beam Synchrotron Radiation Telescope
CAN	Controller Area Network
CCC	CERN Control Center.
CDF	Collider Detector at Fermilab
CERN	Conseil Européen pour la Recherche Nucléaire
cf.	latin: *confare*; compare with
CFC	Carbon-Reinforced Composite
CMS	Compact Muon Solenoid
CTP	Central Trigger Processor
CWG	Collimation Working Group
DAQ	Data Acquisition
DBM	Diamond Beam Monitor
DCM	Data Collection Manager
DCN	Data Collection Network
DCS	Detector Control System
e. g.	latin: *exampli gratia*; for example
ELMB	Embedded Local Monitor Board
FE	Front-End
FIFO	First In, First Out
FPGA	Field-Programmable Gate Array
FSM	Finite State Mashine
GUI	Graphical User Interface
HLT	High Level Trigger
HV	High Voltage
i. e.	latin: *id est*; that is
IP	Interaction Point
IR	Insertion Region
IS	Information Service
ISR	Intersecting Storage Rings
L1A	Level-1 Accept
LAr	Liquid Argon
LED	Light Emitting Diode
LHC	Large Hadron Collider

LTP	Local Trigger Processor
LUT	Look-Up Table
LVDT	Linear Variable Differential Transducer
MAPMT	MultiAnode PhotoMultiplier Tube
MAROC	Multi Anode ReadOut Chip
MB	MotherBoard
MBTS	Minimum Bias Trigger Scintillator
MCS	Multiple Coulomb Scattering
MD	Main Detector
MDT	Monitored Drift Tube
MROD	MDT ReadOut Driver
MUCTPI	Muon-to-CTP Interface
NIM	Nuclear Instrumentation Module
OD	Overlap Detector
OHP	Online Histogram Presenter
PBEAST	Persistent Back-End for the ATLAS Information System of TDAQ
PCI	Peripheral Component Interconnect
PMF	PhotoMultiplier Front-end
PMT	PhotoMultiplier Tube
PSB	Proton Synchrotron Booster
PXI	PCI eXtensions for Instrumentation
QCD	Quantum Chromodynamics
QED	Quantum ElectroDynamics
RCD	ROD Crate DAQ
RF	Radio Frequency
RMS	Root Mean Square
ROD	ReadOut Driver
RoI	Region of Interest
ROS	ReadOut System
RP	Roman Pot
SCADA	Supervisory Control And Data Acquisition
Sci-Fi	Scintillating Fibres
SEU	Single-Event Upset
SFO	Sub-Farm Output
SiT	Silicon Tracker
SPI	Serial Peripheral Interface
SPS	Super Proton Synchrotron
TAN	Target Absorber Neutral
TCL	Target Collimator Long
TCLA	Target Collimator Long Absorber
TCP	Target Collimator Primary
TCSG	Target Collimator Secondary Graphite
TCT	Target Collimator Tertiary
TDAQ	Trigger and Data Acquisition
TOTEM	Total Cross-Section, Elastic Scattering and Diffraction Dissociation
TRP	Triger Rate Presenter
TRT	Transition Radiation Tracker
TTC	Time, Trigger Control
UFO	Unidentified Falling Object
UHV	Ultra-High Vacuum
VHDCI	Very-High-Density Cable Interconnect
VME	Versa Module Eurocard
ZDC	Zero Degree Calorimeter

Appendix B

ALFA_LED – the Test Tool for ALFA_CTPIN

This appendix shortly describes the ALFA_LED module designed for debugging, calibration and commissioning of the ALFA_CTPIN module. Detailed description of the ALFA_LED can be found in [104, 89, 105].

B.1 Introduction

The main aim of the ALFA_LED is generation of short pulses synchronised with the LHC clock and the ORBIT signal. ALFA_LED is able to generate signals analogous the those generated by the detectors. Thus, it is called also a hardware simulator of the trigger signals. These signals can be either 25 ns either 12.5 ns long, thus, can simulate both – OD and MD triggers. The generated signals can be connected directly to the inputs of the ALFA_CTPIN module or into the LEDs located inside of the Roman Pots. The connection scheme is presented in Chapter 5.2 and in Fig. 5.3. The first configuration – ALFA_LED connected directly to the ALFA_CTPIN module allows to debug or calibrate the module. The other configuration with signals connected to the LEDs allows to investigate the whole trigger chain starting from the trigger PMTs, through MAROCs, PMFs to the trigger mezzanines and finishing on the ALFA_CTPIN. The LED blinks excite the trigger PMTs similarly to the signals induced by the particles traversing the trigger tiles, thus, the module works exactly in the same way as during the normal physics run.

The ALFA_LED module is based evaluation board ZedBoard [106] and a NIKHEF converter from LVDS to NIM signals. All installed on the steel plate (see Fig. B.1) in size of the 6U NIM module and inserted into a VME crate. Additional two custom-made mini-modules with relays and converters NIM to TTL allow to switch on/off the ZedBoard and send the reset signal, respectively. The NIM to TTL converter is required, as those relays are controlled via NIM digital output module.

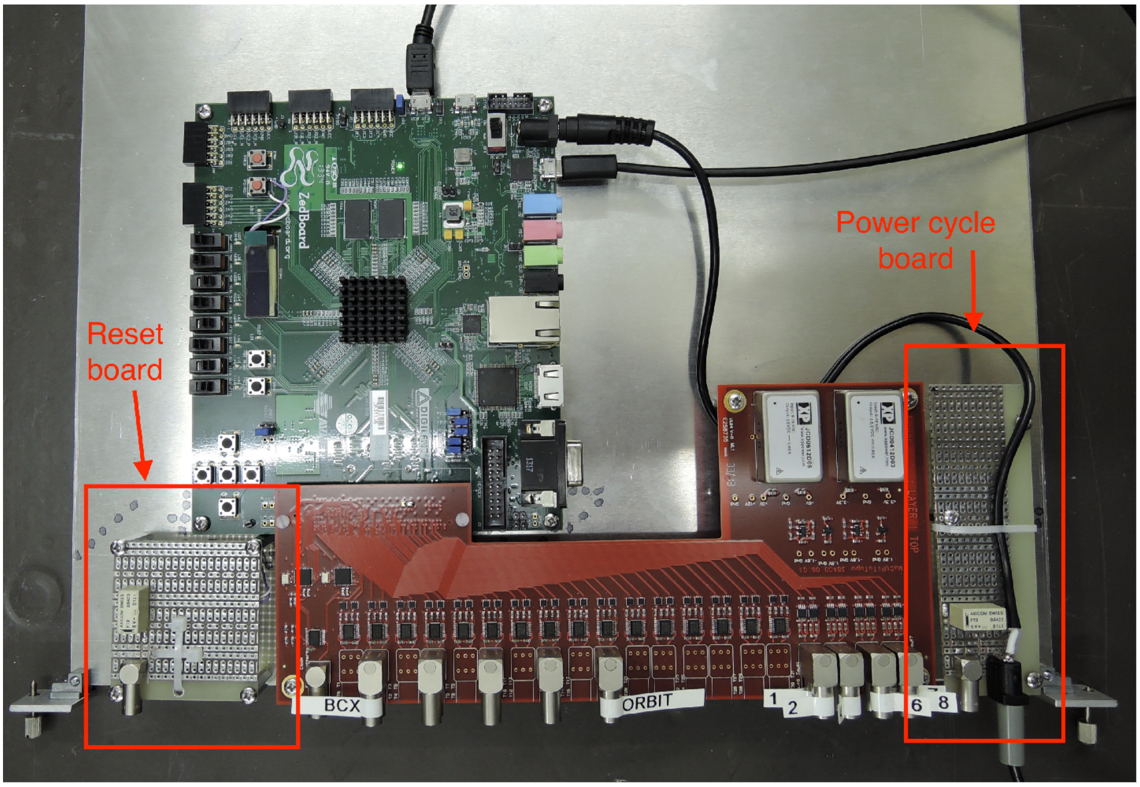

Figure B.1: ALFA_LED – overview of the module [107].

B.2 Architecture

The main part of the ALFA_LED module is the ZedBoard. It is an stock evaluation board containing Zynq Z-7020 System-on-Chip (SoC) microcontroller uniting dual-core ARM Cortex A-9 processor – refered as Processing System (PS) and 7-th generation Artix FPGA – referred as Programmable Logic (PL) [108]. The block scheme is presented in Fig. B.2.

The Processing System runs ARCH Linux ARM [109] embedded operating system, which is installed on the SD Card. The operating system runs the ALFA_LED software. The communication with the board is done over UART interface via one of the ALFA PCs installed in the ALFA rack in the USA15 cavern. The communication is required to load the ALFA_LED configuration and control the test. The configuration data contains detailed parameters like trigger scheme in certain BCID and information about type of the trigger (MD/OD). The main menu of the ALFA_LED application and memory content is presented in Fig. B.3

For the test, the memory content is sent to the Programmable Logic via AXI bus into the block RAM via Port A, see Fig. B.3. The Port B used to read the memory

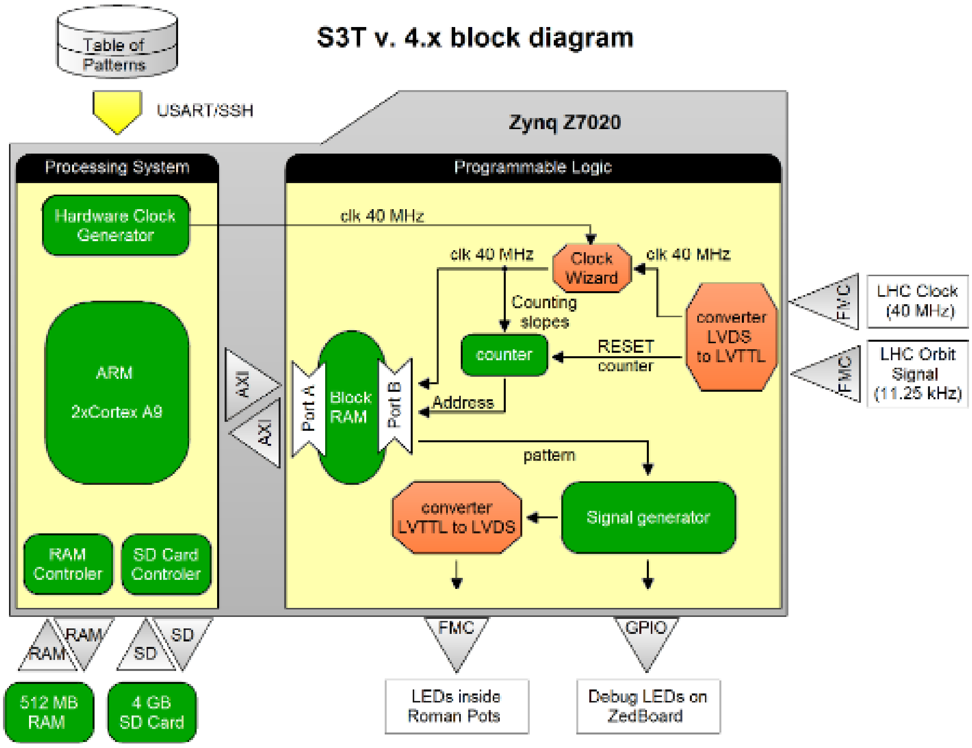

Figure B.2: ALFA_LED – block diagram of the system architecture [89].

by the Signal Generator. The last one decodes the memory content and sends it to the LEDs located on the Zynq board (ALFA_LED debugging mode) or converts them to the LVDS signals and sends them to the NIM outputs via the LVDS to NIM converter. The Signal Generator contains also a pipeline used to synchronise the output with the BCID.

The PL is synchronised with the LHC clock or with the internal clock by the Clock Wizard block. This block controls the clocking signal in the PL part. Depending on the test, the internal clock frequency can be equal to the LHC clock (40 MHz) if only MD signal are generated, or doubled (80 MHz) if the simulation contains also OD signals. The counter is used to address the memory according to the BCID number. The ORBIT is used to reset the counter, then memory is read from the first cell.

B.3 Summary

The ALFA_LED is a hardware simulator of the ALFA trigger signals allowing debugging and calibration of the ALFA_CTPIN module. The simulated triggers can be sent directly to the trigger inputs on the ALFA_CTPIN module or can be used to

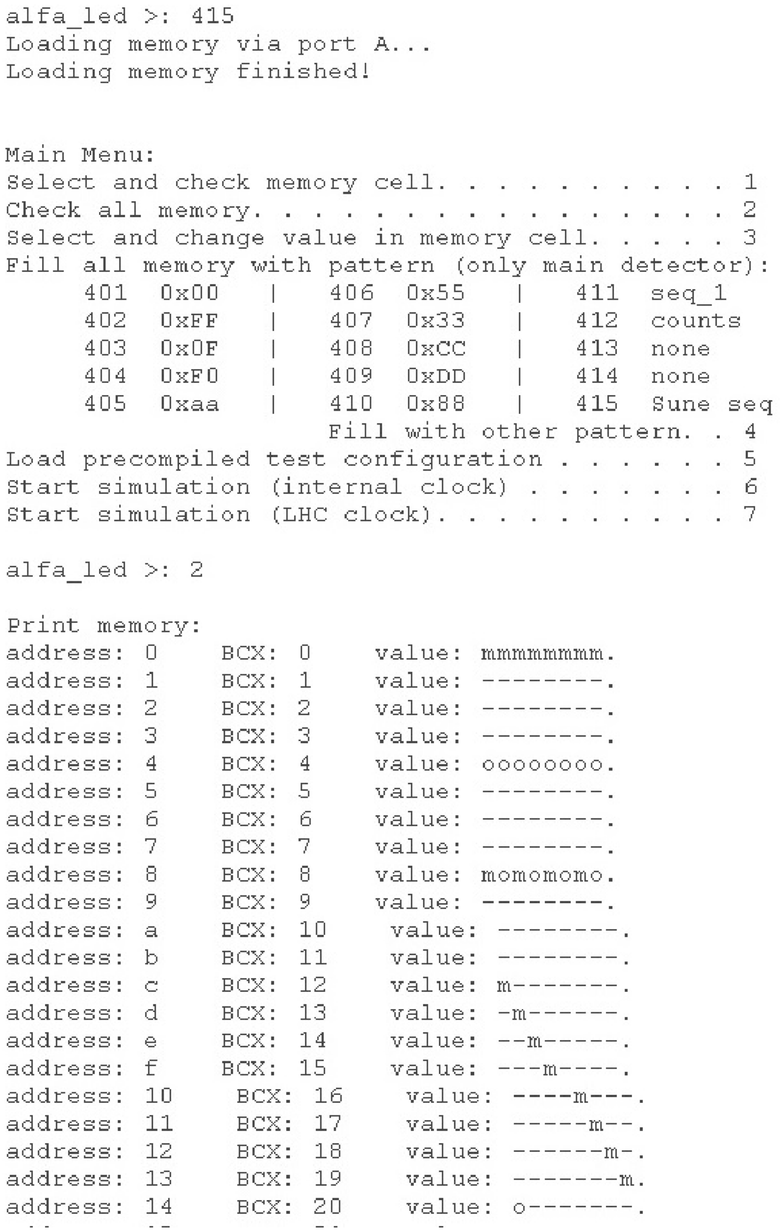

```
alfa_led >: 415
Loading memory via port A...
Loading memory finished!


Main Menu:
Select and check memory cell. . . . . . . . . . 1
Check all memory. . . . . . . . . . . . . . . . 2
Select and change value in memory cell. . . . . 3
Fill all memory with pattern (only main detector):
     401  0x00   |   406  0x55   |   411  seq_1
     402  0xFF   |   407  0x33   |   412  counts
     403  0x0F   |   408  0xCC   |   413  none
     404  0xF0   |   409  0xDD   |   414  none
     405  0xaa   |   410  0x88   |   415  Sune seq
                     Fill with other pattern. . 4
Load precompiled test configuration . . . . . . 5
Start simulation (internal clock) . . . . . . . 6
Start simulation (LHC clock). . . . . . . . . . 7

alfa_led >: 2

Print memory:
address: 0    BCX: 0    value: mmmmmmmm.
address: 1    BCX: 1    value: --------.
address: 2    BCX: 2    value: --------.
address: 3    BCX: 3    value: --------.
address: 4    BCX: 4    value: oooooooo.
address: 5    BCX: 5    value: --------.
address: 6    BCX: 6    value: --------.
address: 7    BCX: 7    value: --------.
address: 8    BCX: 8    value: momomomo.
address: 9    BCX: 9    value: --------.
address: a    BCX: 10    value: --------.
address: b    BCX: 11    value: --------.
address: c    BCX: 12    value: m-------.
address: d    BCX: 13    value: -m------.
address: e    BCX: 14    value: --m-----.
address: f    BCX: 15    value: ---m----.
address: 10    BCX: 16    value: ----m---.
address: 11    BCX: 17    value: -----m--.
address: 12    BCX: 18    value: ------m-.
address: 13    BCX: 19    value: -------m.
address: 14    BCX: 20    value: o-------.
```

Figure B.3: The listing presenting the main menu of the ALFA_LED application. In this example the user printed the memory content. Each line corresponds to one bunch crossing, so there is 3564 lines in total. The value represents the generated trigger – each character corresponds to respective detector. The "m" and "o" corresponds to the trigger in the Main Detector and Overlap Detector respectively. "-" means no trigger will be generated.

illuminate the LEDs installed in the Roman Pots. The last method allows debuging the whole trigger chain starting from the trigger PMTs.

Appendix C

Software Tools

During the thesis preparation a number of software tools were developed. Short description of those is presented within this appendix.

C.1 NTuple Creator v. 3.x

NTuple Creator is a C++ console application developed for generating ROOT [110] ntuple files from a raw experimental data files. Such procedure allows saving significant amount of storage place. The raw data for each ALFA Run is saved into a number of 10 GB files. The ntuple file containing only essential data for further processing from all raw data files utilizes typically 20-50 MB.

The NTuple Creator requires a config file containing basic parameters like time range of the data to be enclosed in the ntuple files, BCID numbers, Run number and raw data file names. For each input raw data file there is one output ROOT ntuple file generated, thus it is required to concatenate the output files using the ROOT hadd tool.

C.2 Plot Creator v. 3.x

The Plot Creator is a C++ console application for processing and plotting the data stored in the ROOT ntuple files. This software contains a number of ROOT macros, which are set via config files and according to those generates proper plots. The macros support ATLAS style [111]. All plots presented in the Chapter 7 were generated by the Plot Creator.

C.3 Script Generator v. 1.x

Script Generator is a graphical application originally designed to facilitate writing scripts for downloading the data from the pbeast database. Later on, new features were developed according to needs of the author. The Graphical User Interface (GUI) was developed using QT libraries [112] and the code was written using C++ programming language. The application window is presented in Fig. C.1.

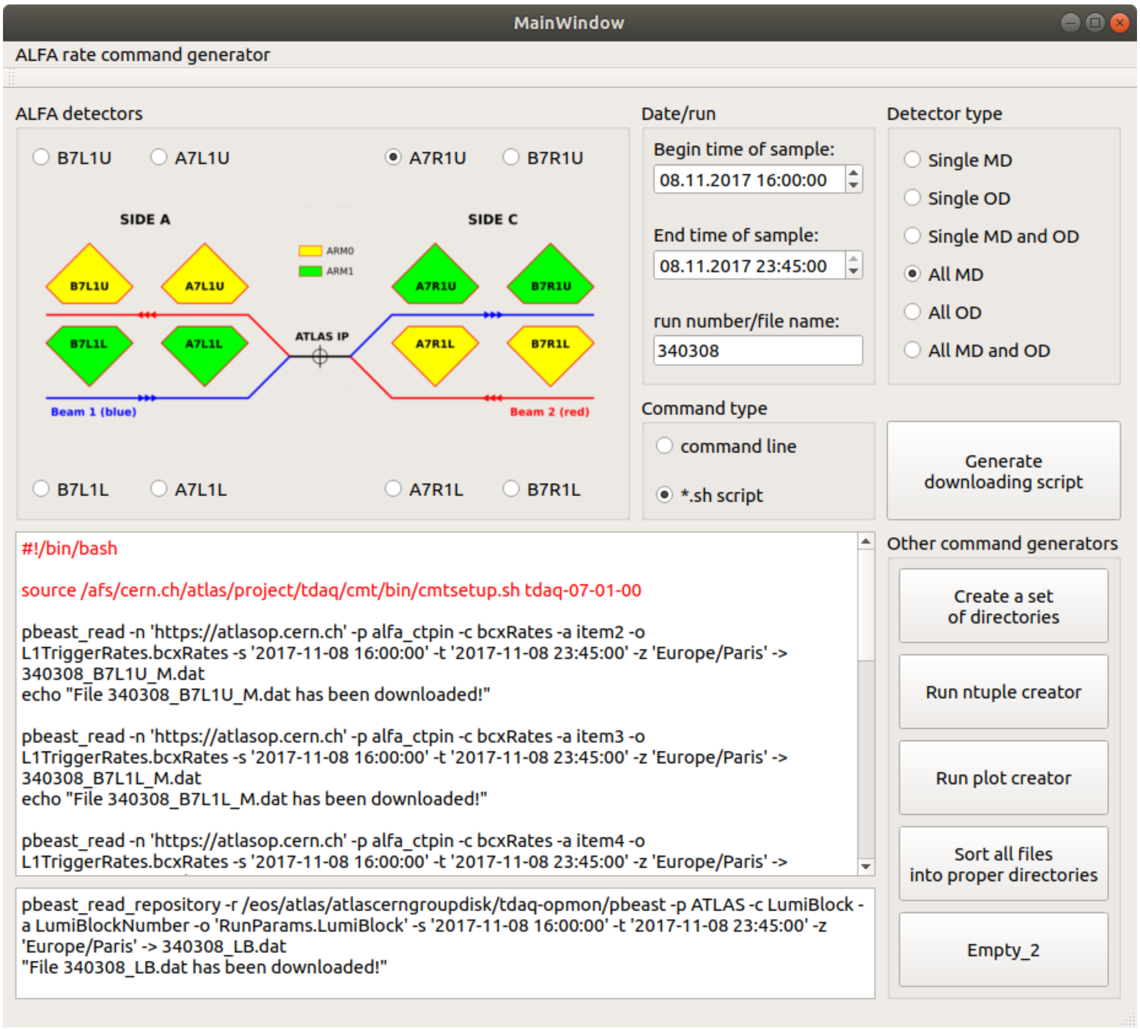

ALFA detectors: ○ B7L1U ○ A7L1U ● A7R1U ○ B7R1U ○ B7L1L ○ A7L1L ○ A7R1L ○ B7R1L

Date/run

Begin time of sample: 08.11.2017 16:00:00

End time of sample: 08.11.2017 23:45:00

run number/file name: 340308

Detector type: ○ Single MD ○ Single OD ○ Single MD and OD ● All MD ○ All OD ○ All MD and OD

Command type: ○ command line ● *.sh script

```
#!/bin/bash

source /afs/cern.ch/atlas/project/tdaq/cmt/bin/cmtsetup.sh tdaq-07-01-00

pbeast_read -n 'https://atlasop.cern.ch' -p alfa_ctpin -c bcxRates -a item2 -o
L1TriggerRates.bcxRates -s '2017-11-08 16:00:00' -t '2017-11-08 23:45:00' -z 'Europe/Paris' ->
340308_B7L1U_M.dat
echo "File 340308_B7L1U_M.dat has been downloaded!"

pbeast_read -n 'https://atlasop.cern.ch' -p alfa_ctpin -c bcxRates -a item3 -o
L1TriggerRates.bcxRates -s '2017-11-08 16:00:00' -t '2017-11-08 23:45:00' -z 'Europe/Paris' ->
340308_B7L1L_M.dat
echo "File 340308_B7L1L_M.dat has been downloaded!"

pbeast_read -n 'https://atlasop.cern.ch' -p alfa_ctpin -c bcxRates -a item4 -o
L1TriggerRates.bcxRates -s '2017-11-08 16:00:00' -t '2017-11-08 23:45:00' -z 'Europe/Paris' ->
```

```
pbeast_read_repository -r /eos/atlas/atlascerngroupdisk/tdaq-opmon/pbeast -p ATLAS -c LumiBlock -
a LumiBlockNumber -o 'RunParams.LumiBlock' -s '2017-11-08 16:00:00' -t '2017-11-08 23:45:00' -z
'Europe/Paris' -> 340308_LB.dat
"File 340308_LB.dat has been downloaded!"
```

Figure C.1: The Script Generator overview.

User can choose graphically the detector for which he wants to download the data, sets the time range and run number. It is also possible to generate the downloading script for all MDs, all ODs or all MDs and ODs at single application run. After clicking the proper push button the downloading script is available in the text box, in the application window. Generator also generates a short script for downloading timestamps of lumiblocks.

Later on, new features to the software were developed:

- “Create a set of directories” – generates a script creating a directories tree for the full set of plots, and other files related to certain run;
- “Run ntuple creator” – generates a script running the code converting down-

loaded raw data into ROOT ntuple files;

- “Run plot creator” – generates a script running the code reading the data from the ROOT ntuple files and generates plots according to defined config files;
- “Sort all files into proper directories” – sorts outputs from above scripts into proper directories.

There is also a number of features under development:

- Config File Generator for Ntuple Creator and Plot Creator;
- Database containing run numbers and time ranges;
- Export output into a file;

Appendix D

Irradiation Tests

D.1 Introduction

The ALFA detectors are installed very close to the beam as it is described in Chapt. 2. Thus, they are exposed to high radiation from the beam halo. Although the radiation levels were acceptable for a typical electronic devices, the situation got complicated – according to simulations, after AFP detector installation, the radiation levels got increased by factor of 5-10. Thus, the FLUKA group at CERN performed studies related to protecting ALFA detectors from increased radiation. Several ideas were simulated and the final solution – double 40 cm thick shielding installed upstream of each detector allowed to reduce the radiation doses by factor of 2.

The radiation doses absorbed by the detectors were measured from the beginning. Table D.1 shows the results of those measurements until 2017. The doses presented in Table D.1 are calculated as a mean values from a number of detectors type TLD100 and TLD800 placed in three points around the detector and readout electronics. The values are given in grays (Gy).

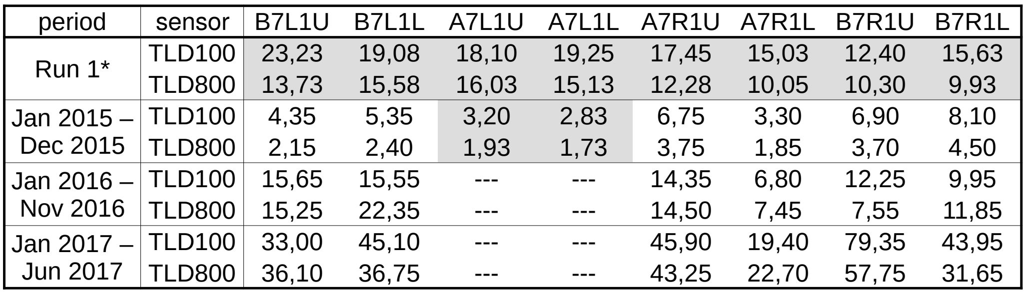

period	sensor	B7L1U	B7L1L	A7L1U	A7L1L	A7R1U	A7R1L	B7R1U	B7R1L
Run 1*	TLD100	23,23	19,08	18,10	19,25	17,45	15,03	12,40	15,63
	TLD800	13,73	15,58	16,03	15,13	12,28	10,05	10,30	9,93
Jan 2015 – Dec 2015	TLD100	4,35	5,35	3,20	2,83	6,75	3,30	6,90	8,10
	TLD800	2,15	2,40	1,93	1,73	3,75	1,85	3,70	4,50
Jan 2016 – Nov 2016	TLD100	15,65	15,55	---	---	14,35	6,80	12,25	9,95
	TLD800	15,25	22,35	---	---	14,50	7,45	7,55	11,85
Jan 2017 – Jun 2017	TLD100	33,00	45,10	---	---	45,90	19,40	79,35	43,95
	TLD800	36,10	36,75	---	---	43,25	22,70	57,75	31,65

* TLD800 installed later in June 2011.

Figure D.1: Measurements of the doses absorbed by the ALFA detectors. The grayed values are given for measurements from both sides – downstream and upstream. The rest results are given only from upstream sensors.

The radiation absorbed by the ALFA was still much higher than it was assumed in the design, thus it was necessary to check empirically how much radiation can be absorbed by the ALFA readout electronics before damage.

D.2 Results

For the irradiation campaign two sets of ALFA electronics were prepared later referenced as MB21 and MB22. Each set contained a motherboard, trigger mezzanine, ELMB and 2 PMFs. Designers of the readout electronics analysing the electronic design prepared a number of points to measure the voltages, which should indicate any abnormalities in the electronics work. Most of those points were related to operational amplifiers, analog-to-digital converters and voltage regulators. The author prepared the measurement procedures allowing the most efficient measurements and performed a numbers of iteration which were continued and finalized by a summer student. The electronics was irradiated using the proton beam extracted from Proton Synchrotron in the CERN High energy AcceleRator Mixed field facility (CHARM). Two sets of the ALFA electronics were installed inside of the CHARM and irradiated with the dose of about 30 (MB21) and 100 (MB22) Grays per week, respectively. After a week of irradiation electronics had to be cooled down (relaxed from activation) for another week and then tested for another week. Thus, each measurement series took 3 weeks. Detailed results and procedures are described in the mentioned student's master thesis [113].

As an example of the measurements, the pedestal voltage of the ADC on the motherboards MB21 and MB22 are presented, see Fig. D.2. It is clearly visible the pedestal voltage increased after certain doses.

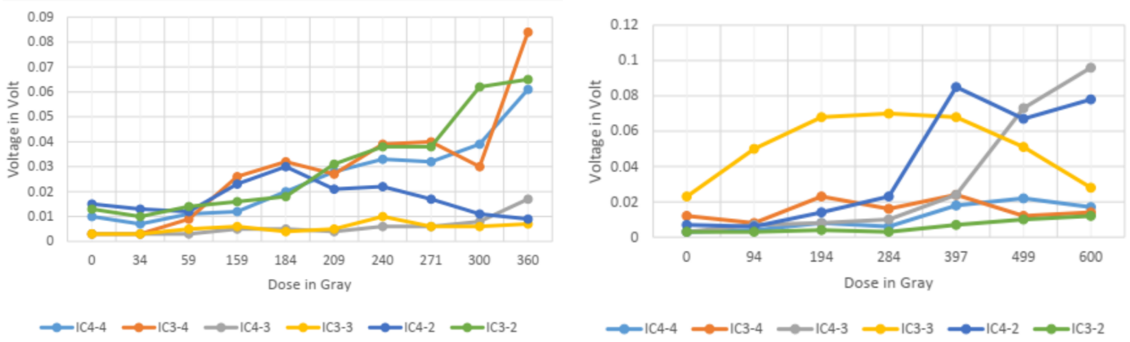

Figure D.2: Measurements of the ADC pedestals for the MB21 set (left panel) and for the MB22 set (right panel).

The measurements of the MB22 were stopped after 600 Grays as the motherboard was damaged. The criteria was if the motherboard didn't start after a number of power-cycles and 3 cycles of reloading the firmware it was irreversibly damaged. The MB21 motherboard measurements where not continued, as the electronics was working properly without any loose of the performance and the total absorbed dose was above the foreseen limit at the end of the ALFA scientific programme. The results allowed assuming that the motherboards will survive Run 2 and the foreseen data-taking at the beginning of the Run 3.

The trigger mezzanine was more resistant to radiation, as it was still working properly after the dose of 600 Grays, however one of the trigger PMFs from MB22 stopped working after the dose of 284 Gy and the second one stopped working after the dose of 600 Gy. The rest of trigger PMFs as well as the MAPMT PMFs were working properly and the parameters were not significantly different from the reference values (measured before the irradiation).

The test showed that the weakest point of the ALFA readout electronics was the ELMB. Its digital part required for loading the PMF configuration stopped working after dose of 159 Gy, however, the analog readouts were highly corrupted already after dose of 60 Gy.

D.3 Summary

The irradiation campaign ensured ALFA experts that the readout electronics should survive the ALFA scientific programme till Run 3. However the ELMB is more sensitive to radiation, and thus all ELMBs are foreseen to be replaced before Run 3. To ensure that ALFA will be fully operational after LS2, new motherboards were ordered to replace those most irradiated during Run 1 and Run 2.

Appendix E

Detector Run - General Information

During the tests as well as during final data-taking several parameters indicating quality of the data taking as well as the detector performance were checked. Experts in ACR were responsible for the proper detector configuration, the data quality and detector performance control. In their hands was communication with ATLAS Run Control desk and Trigger experts. ALFA experts in CCC were responsible for the Roman Pots movement control, cooperation with machine and CMS/TOTEM experts and also for the LHC refill requests. The observed parameters are described below.

First screen refers to the main ATLAS partition and TDAQ system status, Fig. E.1. Left panel shows IGUI – software used for control the ATLAS DAQ partition. As the ATLAS partition can be controlled only from Run Control desk in ACR, ALFA experts, used it only in the observer mode to access information about common ATLAS status and TDAQ errors or warnings. The IGUI error console on the ALFA desk in contrary to the IGUI displayed on the Run Control desk was printing only errors and warnings related to ALFA. Such configuration of the error console made ALFA experts not distracted with messages negligible in context of ALFA performance. Right up window shows the common dead time of the partition. In case of ALFA TDAQ overload, the busy time rises. Right bottom window is a terminal which allowed experts to run special scripts, e. g. resetting all plots in online monitoring.

Second monitor displayed three windows, Fig. E.2. Left window shows the interactive DCS view. It was used for the detector powering, configuration and if needed power-cycling of the apparatus and its infrastructure. Right up window presents the LHC Page 1 – main source of basic information about the common LHC state, used filling scheme and checking most important news from CCC. Right bottom window shows the file manager containing documents related the data-taking.

Fig. E.3 shows the Online Histogram Presenter (OHP) with four panels. The top left panel displays the MAPMTs map for all 8 detectors. It presents the configuration

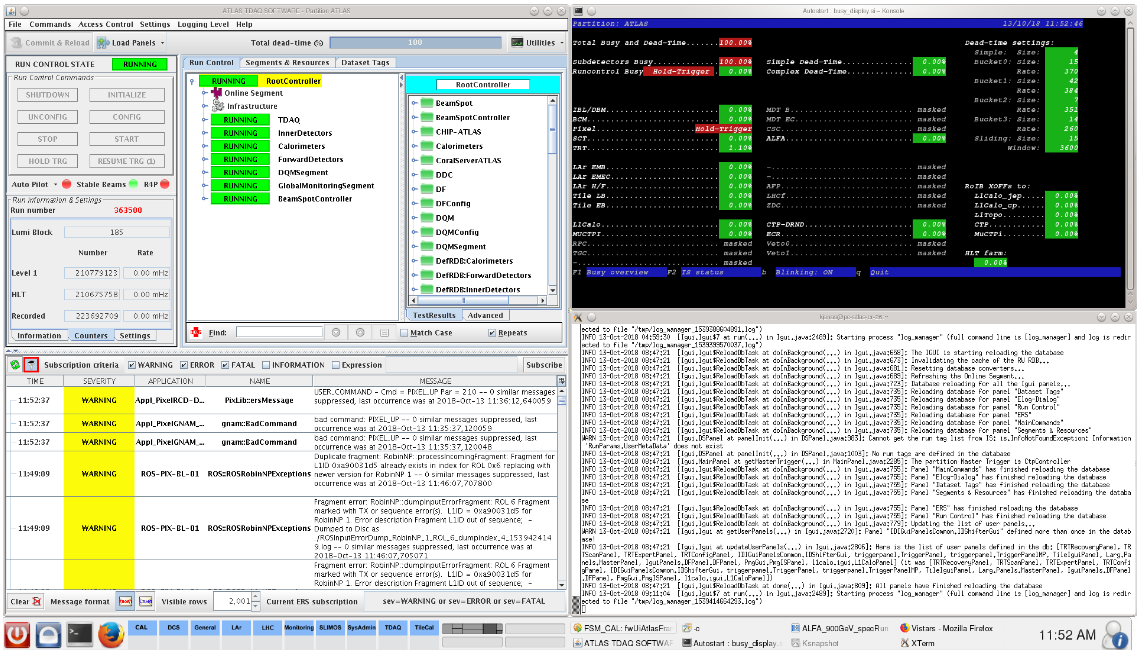

Figure E.1: Left window is an IGUI interface in observation mode. Top right one is a busy display. Bottom left is a user terminal.

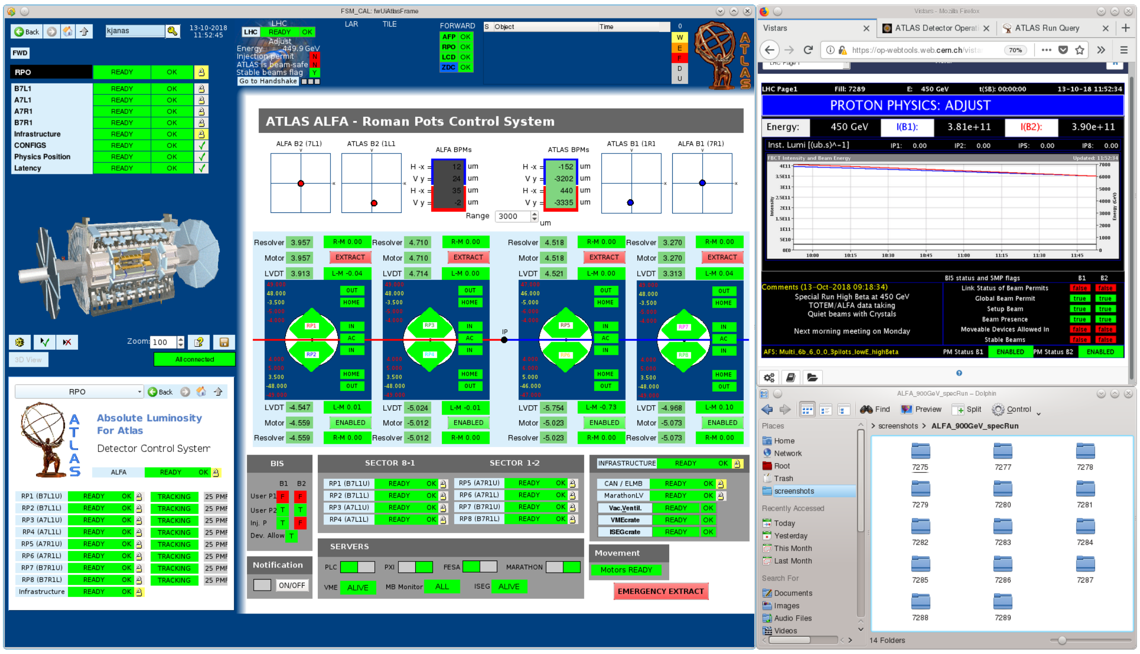

Figure E.2: Left window shows DCS interface. Top right is a LHC Page 1 display. Bottom right is a file manager.

state of the PMFs. Each square corresponds to one layer of the scintillating fibres. If a PMF is not configured then the corresponding square is empty. Moreover the pattern visible on the panel also gives some information about the state of the PMFs. Top right panel is related to the synchronisation monitor. Consists of four sub-panels. Top left sub-panel shows synchronisation errors in communication with PMFs. The state "*is not found*" means there are no synchronisation errors, all PMFs work fine. Top right sub-panel shows the trigger pattern. It informs whether all triggers are working, and if they are properly synchronised. Two bottom sub-panels displays amount of triggers in function of BCID for ARM0 and ARM1. It is visible, there are 5 bunches with same BCID – colliding ones and two smaller picks related to the non-colliding one from both beams. The bottom left panel shows the fast online track reconstruction. The bottom right panel shows U–V layers correlation. More counts in top right edge of each histogram in respect to the rest of bins refers to a good trigger latency setting.

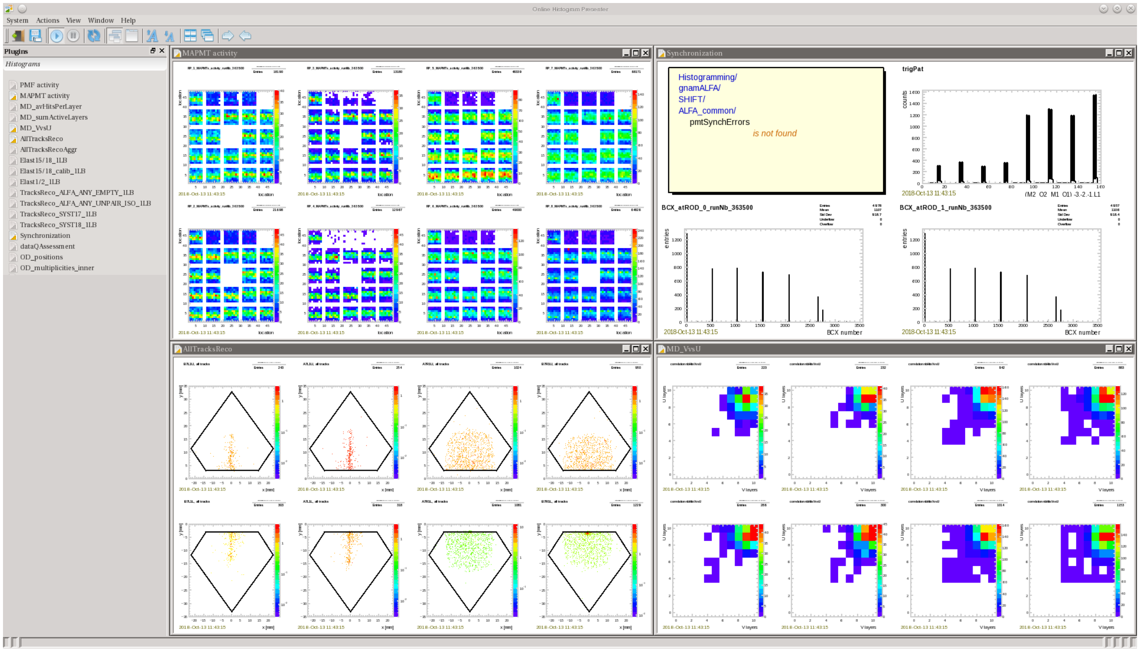

Histogramming/
gnamALFA/
SHIFT/
ALFA_common/
pmtSynchErrors
is not found

Figure E.3: Top left panels displays the MAPMTs map. Top right panel displays the trigger pattern. Bottom Left displays fast tracker reconstruction and bottom right panel shows the MD U–V correlation.

Fourth monitor shows the Trigger Rate Presenter, Fig. E.4. It consists of four panels. Left top and bottom panels show the raw trigger rates from all MDs and ODs, respectively. By observation of those rates experts could recognised which trigger caused problems, and which detector should be power-cycled. Right top panel shows the rates from the Minimum Bias Trigger Scintillator (MBTS) for beam 1 and beam 2. The last panel shows trigger rates ALFA_ELAST15 and ALFA_ELAST18 – the triggers generated by a coincidence of all detectors from ARM0 and ARM1, respectively, and also ALFA_SYST17 and ALFA_SYST18 which correspond to the coincidence of all upper and all lower detectors, respectively. These plots are a main subject of interest from the data quality point of view. On their basis one could estimate amount of the collected events, recognise the level of elastic signal (ALFA_ELAST15, ALFA_ELAST18) and the level of background (ALFA_SYST17 and ALFA_SYST18). Moreover, as these plots were used as a main indicator for re-scraping or the LHC re-fill need, also experts in CCC had eye on those.

Figure E.4: Top left – raw MDs trigger rates, bottom left – raw ODs trigger rates, top right – MBTS trigger rates, bottom left elastic and background trigger rates.

The fifth monitor shows four panels of OHP, Fig. E.5. Top left panel displays fast online reconstruction of the elastic events, while the bottom left panel presents the online fast reconstruction of all tracks. Both panels are reset every 10 lumiblocks (roughly every 10 minutes). Top right panel shows the distance between the upper and lower detectors measured by ODs. Fourth panel shows the data assessment which is a marker of data reconstruction errors.

The last monitor shows four OHP panels, Fig. E.6. Top left and right panels show the rates created by ALFA_CTPIN module from MDs and ODs respectively. Bottom left and right panels display the fast track reconstruction for all events and for elastic events, respectively. Both are reset every lumiblock.

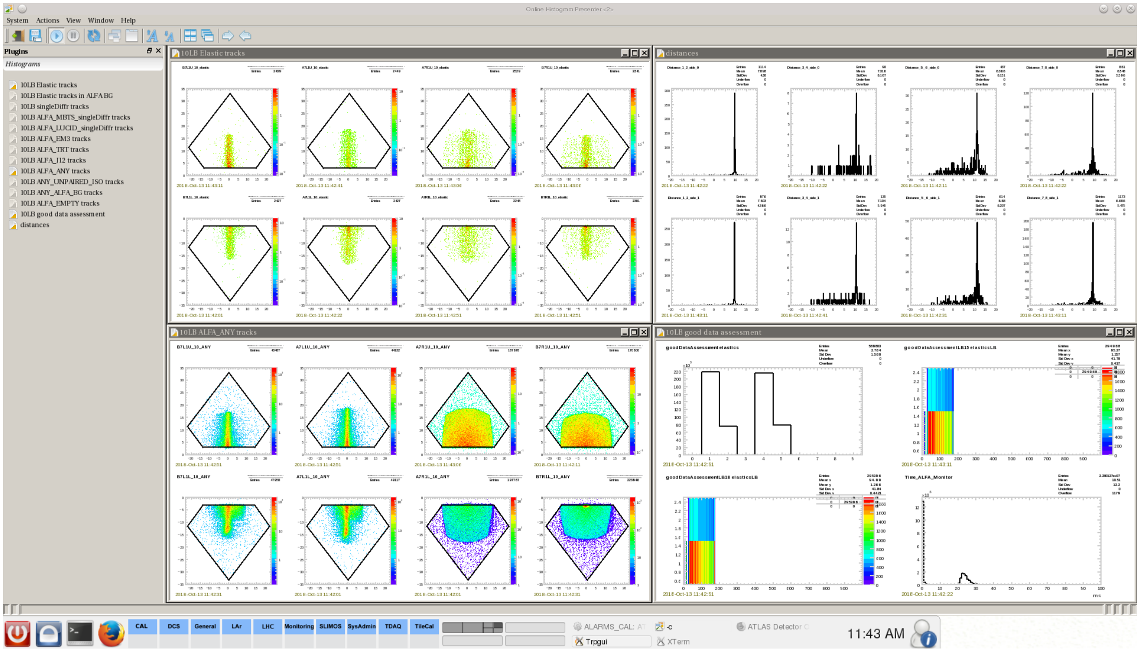

Figure E.5: Top left – fast online elastic tracks reconstruction, bottom left – fast online all track reconstruction, top right – online reconstruction of distances between upper and lower detectors, bottom right – data assessment.

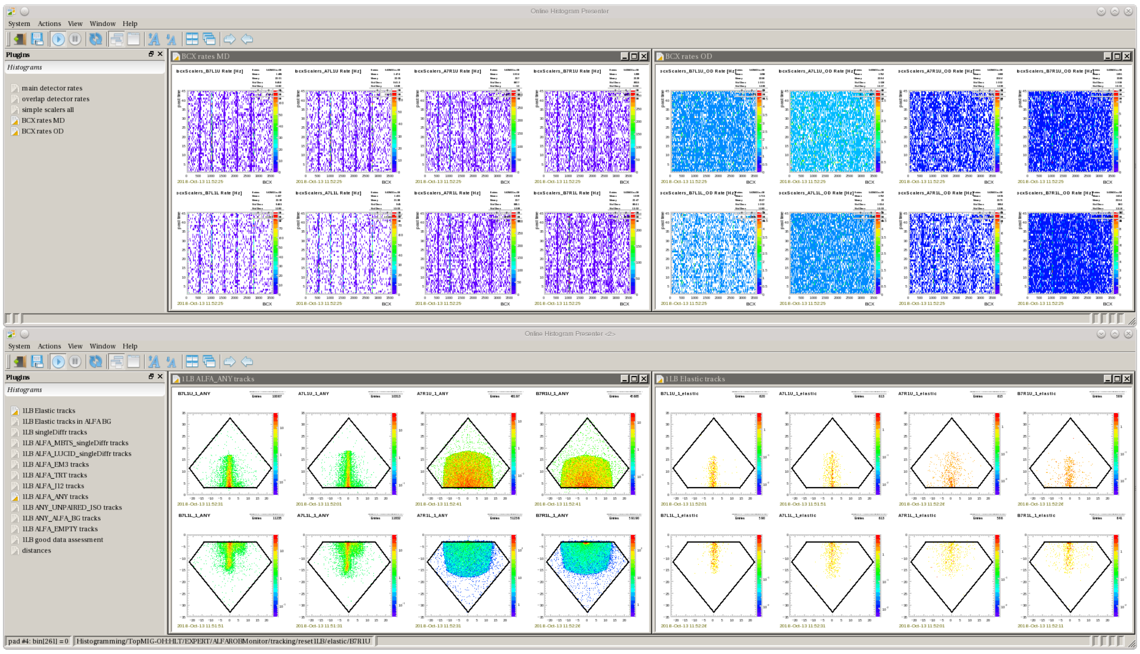

pad #4: bin[261] = 0

Histogramming/TopMIG-OH:HLT/EXPERT/ALFAROBMonitor/tracking/reset1LB/elastic/B7R1U

Figure E.6: Top left and right panels show rates created by ALFA_CTPIN module from MDs and ODs respectively. Bottom left and right panels display fast track reconstruction for all events and for elastic events, respectively.

Bibliography

[1] M. Risse *et al.*, “Primary Particle Type of the Most Energetic Fly’s Eye Air Shower,” *Astroparticle Physics*, vol. 21, p. 479, August 2004.

[2] O. S. Bruning *et al.*, *LHC Design Report Vol.1: The LHC Main Ring.* Geneve: CERN, June 2004.

[3] J. Wenninger, “Operation and Configuration of the LHC in Run 2,” *CERN*, March 2019.

[4] E. Mobs, “The CERN Accelerator Complex – August 2018,” August 2018.

[5] R. Ballabriga, M. Campbell, and X. Llopart, “ASIC Developments for Radiation Imaging Applications: The Medipix and Timepix Family,” *Nucl. Instrum. Methods Phys. Res., A*, vol. 878, pp. 10–23, 2018.

[6] H. Wiedemann, *Particle Accelerator Physics; 4th ed.* Berlin: Springer, 2015.

[7] M. Gyr, “Polarities of LHC Septum Magnets MSI and MSD,” *CERN*, April 2008.

[8] R. Steerenberg *et al.*, “Operation and Performance of the CERN Large Hadron Collider During Proton Run 2,” *JACoW Publishing*, 2019.

[9] H. Damerau, S. Hancock, A. Lasheen, and D. Perrelet, “RF Manipulations for Special LHC-Type Beams in the CERN PS,” in *Proceedings, 9th International Particle Accelerator Conference (IPAC 2018): Vancouver, BC Canada, April 29-May 4, 2018*, p. WEPAF063, 2018.

[10] K. Wille, *The Physics of Particle Accelerators: an Introduction.* Oxford: Oxford Univ. Press, 2000.

[11] H. Damerau, A. Lasheen, and E. Shaposhnikova, “Higher-Harmonic RF System for Landau Damping in the CERN PS,” in *Proceedings, 9th International Particle Accelerator Conference (IPAC 2018): Vancouver, BC Canada, April 29-May 4, 2018*, 2018.

[12] ATLAS Collaboration, “The ATLAS Experiment at the CERN Large Hadron Collider,” *JINST*, vol. 3, p. S08003, 2008.

[13] ATLAS Collaboration, *ATLAS: Detector and Physics Performance Technical Design Report. Volume 1.* No. CERN-LHCC-99-14, ATLAS-TDR-14, May 1999.

[14] T. Schörner-Sadenius, *The Large Hadron Collider: Harvest of Run 1.* Berlin: Springer, 2015.

[15] ATLAS Collaboration, "ATLAS Insertable B-Layer Technical Design Report," Tech. Rep. CERN-LHCC-2010-013. ATLAS-TDR-19, September 2010.

[16] G. Aad *et al.*, "ATLAS Pixel Detector Electronics and Sensors," *JINST*, vol. 3, p. P07007, 2008.

[17] J. Jackson, "The ATLAS Semiconductor Tracker (SCT)," *Nuclear Instruments and Methods in Physics Research Section A: Accelerators, Spectrometers, Detectors and Associated Equipment*, vol. 541, no. 1, pp. 89 – 95, 2005.

[18] V. A. Mitsou, "The ATLAS Transition Radiation Tracker. The ATLAS Transition Radiation Tracker," Tech. Rep. hep-ex/0311058, CERN, Geneva, Nov 2003.

[19] ATLAS Collaboration, *ATLAS Liquid-Argon Calorimeter: Technical Design Report.* Technical Design Report ATLAS, Geneva: CERN, 1996.

[20] ATLAS Collaboration, *ATLAS Muon Spectrometer: Technical Design Report.* Technical Design Report ATLAS, Geneva: CERN, 1997.

[21] ATLAS Collaboration, "ATLAS Forward Detectors," June 2018.

[22] L. Fabbri, "LUCID: the ATLAS Luminosity Detector," tech. rep., CERN, Geneva, September 2018.

[23] L. Adamczyk *et al.*, "Technical Design Report for the ATLAS Forward Proton Detector," Tech. Rep. CERN-LHCC-2015-009, ATLAS-TDR-024, 5 2015.

[24] ATLAS Collaboration, "Performance of the Minimum Bias Trigger in pp Collisions at $\sqrt{s} = 900$ GeV," Tech. Rep. ATLAS-CONF-2010-025, CERN, Geneva, July 2010.

[25] ATLAS Collaboration, "Performance of the Minimum Bias Trigger in p-p Collisions at $\sqrt{s} = 7$ TeV," Tech. Rep. ATLAS-CONF-2010-068, CERN, Geneva, Jul 2010.

[26] V. Cindro *et al.*, "The ATLAS Beam Conditions Monitor," *Journal of Instrumentation*, vol. 3, pp. P02004–P02004, February 2008.

[27] M. Červ, "The ATLAS Diamond Beam Monitor," *Journal of Instrumentation*, vol. 9, pp. C02026–C02026, February 2014.

[28] ATLAS Collaboration, "Trigger Menu in 2018," Tech. Rep. ATL-DAQ-PUB-2019-001, CERN, Geneva, Oct 2019.

[29] J. M. Campbell, J. W. Huston, and W. J. Stirling, "Hard Interactions of Quarks and Gluons: A Primer for LHC Physics," *Rept. Prog. Phys.*, vol. 70, p. 89, 2007.

[30] ATLAS Collaboration, "Performance of the ATLAS Trigger System in 2015," *Eur. Phys. J.*, vol. C77, no. 5, p. 317, 2017.

[31] CERN, "The Worldwide LHC Computing Grid | CERN." https://home.cern/science/computing/worldwide-lhc-computing-grid. Accessed: 2020-09-03.

[32] ATLAS Collaboration, "ATLAS DAQ, EF, LVL2 and DCS: Technical Progress Report," Tech. Rep. CERN-LHCC-98-016, CERN, Geneva, Jun 1998.

[33] A. Barriuso Poy *et al.*, "The detector Control System of the ATLAS Experiment," *JINST*, vol. 3, p. P05006, 2008.

[34] "Road Vehicles — Controller Area Network (CAN)," standard, International Organization for Standardization, Geneva, CH, March 2015.

[35] B. I. Hallgren, H. Boterenbrood, H. J. Burckhart, and H. Kvedalen, "The Embedded Local Monitor Board (ELMB) in the LHC Front-end I/O Control System," *TDR*, 2001.

[36] Siemens, "SIMATIC WinCC V7 | Simatic SCADA Systems." `https://new.siemens.com/global/en/products/automation/industry-software/automation-software/scada/simatic-wincc-v7.html`, 2020. Accessed: 2020-08-22.

[37] P. Jenni, M. Nordberg, M. Nessi, and K. Jon-And, *ATLAS Forward Detectors for Measurement of Elastic Scattering and Luminosity.* Technical Design Report ATLAS, Geneva: CERN, 2008.

[38] S. van der Meer, "Calibration of the Effective Beam Height in the ISR," Tech. Rep. CERN-ISR-PO-68-31. ISR-PO-68-31, CERN, Geneva, 1968.

[39] V. Papadimitriou, "Luminosity Determination at the Tevatron," in *LHC Lumi Days*, 3 2011.

[40] J. C. Denard, "Beam Current Monitors," *CERN Accelerator School Proceedings*, 2009.

[41] I. Brock *et al.*, "Luminosity Measurement in the L3 Detector at LEP," *Nucl. Instrum. Meth. A*, vol. 381, pp. 236–266, 1996.

[42] L. Adamczyk *et al.*, "Measurement of the Luminosity in the ZEUS Experiment at HERA II," *Nucl. Instrum. Meth. A*, vol. 744, pp. 80–90, 2014.

[43] A. Donnachie and P. V. Landshoff, "Total Cross Sections," *Phys. Lett. B296*, 1992.

[44] H. Stenzel, "Private communication."

[45] G. B. West and D. R. Yennie, "Coulomb Interference in High-Energy Scattering," *Phys. Rev. 172*, 1968.

[46] C. Bourrely, J. Soffer, and T. T. Wu, "Impact-Picture Expectation for Very High-Energy Elastic pp and $\bar{p}p$ Scattering," *Nucl. Phys. B247*, 1984.

[47] TOTEM Collaboration, "First determination of the ρ parameter at $\sqrt{s} = 13$ TeV: probing the existence of a colourless C-odd three-gluon compound state," *Eur. Phys. J. C*, vol. 79, no. 9, p. 785, 2019.

[48] P. Grafström, "Impact of Different Scenarios of the σ_{tot} Energy Dependence on $\rho =$ Re f/Im f, Workshop on QCD and Diffraction at the LHC," *Cracow, 15-17 Nov.*, 2018.

[49] H. Stenzel, "Measurement of the Total Cross Section From Elastic Scattering in pp Collisions at $\sqrt{s} =$ 7TeV With the ATLAS Detector," Tech. Rep. ATL-PHYS-PROC-2014-128, CERN, Geneva, September 2014.

[50] ATLAS Collaboration, "Measurement of the Total Cross Section From Elastic Scattering in pp Collisions at $\sqrt{s} = 8$ TeV with the ATLAS detector," *Phys. Lett. B*, vol. 761, pp. 158–178, 2016.

[51] TOTEM Collaboration, "Measurement of Proton-Proton Inelastic Scattering Cross-Section at $\sqrt{s} = 7$ TeV," *EPL*, vol. 101, no. 2, p. 21003, 2013.

[52] TOTEM Collaboration, "Luminosity-Independent Measurement of the Proton-Proton Total Cross Section at $\sqrt{s} = 8$ TeV," *Phys. Rev. Lett.*, vol. 111, no. 1, p. 012001, 2013.

[53] ATLAS Collaboration, "Measurement of the Total Cross Section From Elastic Scattering in pp Collisions at $\sqrt{s} =$ 7TeV With the ATLAS Detector," *Nuclear Physics B*, vol. 889, December 2014.

[54] "Giuseppe Cocconi (1914 - 2008). Giuseppe Cocconi (1914 - 2008)," p. 6, November 2008.

[55] National Instruments , "PXI Systems." `https://www.ni.com/pl-pl/shop/pxi.html`, 2020. Accessed: 2020-09-28.

[56] Kuraray Co. LTD, "Kuraray Plastic Scintillating Fibers." `http://kuraraypsf.jp/pdf/all.pdf`, 2020. Accessed: 2020-08-30.

[57] Eljen Technology, "General Purpose Plastic Scintillator." `https://eljentechnology.com/images/products/data_sheets/EJ-200_EJ-204_EJ-208_EJ-212.pdf`, 2020. Accessed: 2020-08-30.

[58] A. Braem and Others, "Trigger Counter Studies For the ALFA Detector," Tech. Rep. ATL-LUM-PUB-2009-001. ATL-COM-LUM-2009-005, CERN, Geneva, March 2009.

[59] Hamamatsu Photonics K. K., "Metal Package Photomultiplier Tube R9880U Series." `http://kuraraypsf.jp/pdf/all.pdfhttps://www.hamamatsu.com/resources/pdf/etd/R9880U_TPMH1321E.pdf`, 2019. Accessed: 2020-09-06.

[60] Hamamatsu Photonics K. K., "Metal Package Photomultiplier Tube R7400 Series." `https://ctf3-tbts.web.cern.ch/instr/PMT/R7400U_TPMH1204E07.pdf`, 2004. Accessed: 2020-09-06.

[61] Hamamatsu Photonics K. K., "Multianode Photomultiplier Tube Assembly H7546A, H7546B." `https://www.hamamatsu.com/resources/pdf/etd/H7546A_H7546B_TPMH1240E.pdf`, 2007. Accessed: 2020-09-06.

[62] Piyu Dhaker, "Introduction to SPI Interface." `https://www.analog.com/en/analog-dialogue/articles/introduction-to-spi-interface.html`. Accessed: 2021-11-07.

[63] CERN, *CAS - CERN Accelerator School: Course on Superconductivity for Accelerators*, (Geneva), CERN, 2014. Comments: 23 lectures, 592 pages, published as CERN Yellow Report https://cds.cern.ch/record/1507630?ln=en.

[64] R. Bruce, D. Mirarchi, and H. Garcia Morales, "Private communication."

[65] CERN, *Concept of Luminosity*, (Geneva), CERN, 2006.

[66] P. Belanger *et al.*, "MD2036: UFO Dynamics Studies and UFO Fast Detection," Tech. Rep. CERN-ACC-2018-0009, CERN, Geneva, Sep 2017.

[67] C. Bracco, *Commissioning Scenarios and Tests for the LHC Collimation System.* PhD thesis, EPFL, August 2009. Presented on 29 Jan 2009.

[68] K. L. F. Bane, "A Simplified Model of Intrabeam Scattering," in *8th European Particle Accelerator Conference (EPAC 2002)*, pp. 1443–1445, 6 2002.

[69] F. Zimmermann and M. P. Zorzano-Mier, "Touschek Scattering in HERA and LHC," Tech. Rep. LHC-PROJECT-NOTE-244, CERN, Geneva, Dec 2000.

[70] CERN, *LHC Workshop on Experimental Conditions and Beam-Induced Detectors Backgrounds*, (Geneva), CERN, 2009.

[71] ATLAS Collaboration, "Characterisation and Mitigation of Beam-Induced Backgrounds Observed in the ATLAS Detector During the 2011 Proton-Proton Run," *JINST*, vol. 8, p. P07004, 2013.

[72] E. B. Holzer *et al.*, "Design of the Beam Loss Monitoring System for the LHC Ring," *Proceedings of EPAC*, p. 3, 2004.

[73] S. Redaelli, "Beam Cleaning and Collimation Systems," in *2014 Joint International Accelerator School: Beam Loss and Accelerator Protection*, pp. 403–437, 2016.

[74] D. Mirarchi, B. Dziedzic, K. Korcyl, *et al.*, "Reducing Beam-Related Background on Forward Physics Detectors Using Crystal Collimation at the Large Hadron Collider1," *Physical Review Applied*, vol. 14, 12 2020.

[75] D. Mirarchi, *Crystal Collimation for LHC.* PhD thesis, Imperial College London, March 2015. Presented 18 Jun 2015.

[76] A. Bertarelli and R. Perret, "LHC Collimator Design," 2004.

[77] C. Assmann, "Collimators and Beam Absorbers for Cleaning and Machine Protection," *Chamonix*, 2005.

[78] ATLAS Collaboration, "Comparison Between Simulated And Observed LHC Beam Backgrounds in the ATLAS Axperiment at $E_{\text{beam}} = 4$ TeV," *JINST*, vol. 13, no. 12, p. P12006, 2018.

[79] A. W. Chao, , and Others, *Handbook of Accelerator Physics and Engineering 2nd ed.* Singapore: World Scientific, 2013.

[80] M. Tanabashi *et al.*, "Review of particle physics: Particle data group," *Physical Review D*, vol. 98, p. 2000, August 2018.

[81] M. Albrow *et al.*, "CMS-TOTEM Precision Proton Spectrometer," Tech. Rep. CERN-LHCC-2014-021. TOTEM-TDR-003. CMS-TDR-13, CERN, Sep 2014.

[82] G. Azzopardi, *Automation of the LHC Collimator Beam-Based Alignment Procedure for Nominal Operation.* PhD thesis, University of Malta, September 2019. Presented 10 Jan 2020.

[83] N. V. Mokhov and T. Weiler, "Machine-inudced backgrounds: Their origin and loads on atlas/cms," in *Fermilab-Conf-08-147-APC*, May 2008.

[84] ATLAS Collaboration, “Beam Backgrounds in the ATLAS Detector During LHC Loss Map Tests at $\beta^* = 40$ cm and $\beta^* = 80$ cm at $E_{beam} = 6.5$ TeV,” Tech. Rep. ATL-DAPR-PUB-2017-001, CERN, Geneva, October 2017.

[85] ATLAS Collaboration, “Measurement of Beam Background in Special High-β^* LHC Runs at $\sqrt{s} = 900$ GeV Using the ATLAS–ALFA Detectors,” Tech. Rep. ATL-FWD-PUB-2020-001, CERN, Geneva, May 2020.

[86] W. Iwanski, S. Jakobsen, K. Korcyl, and J. Oechsle, “Functionality and performance of the ALFA_CTPIN module,” *PoS*, vol. TWEPP-17, p. 142, 2017.

[87] MAXIM Integrated, “MAXIM EE Glossary.” `https://www.maximintegrated.com/en/glossary/definitions.mvp/terms/all`. Accessed: 2021-08-07.

[88] P. Borrego-Amaral *et al.*, “The ATLAS Local Trigger Processor (LTP) 016,” Tech. Rep. CERN-ATL-COM-DAQ-2004-025, CERN, Geneva, 2004.

[89] B. Dziedzic and K. Korcyl, “A New Approach to the ALFA Trigger Simulator,” *Acta Phys. Pol. B*, vol. 47, pp. 1655–1660. 6 p, 2016.

[90] I. Soloviev and Others, “ATLAS Operational Monitoring Data Archival and Visualization,” *EPJ Web of Conferences*, vol. 245, p. 01020, January 2020.

[91] R. Prenki, “ATLAS Trigger Rate Presenter,” tech. rep., CERN, Geneva, 2013.

[92] B. S. Dziedzic, “Using ALFA Detectors for the LHC Beam Background Measurements,” tech. rep., CERN, Geneva, June 2019.

[93] S. Shukla, *Measurements on Small Angle Elastic Scattering From pp and Anti-pp Collisions at the ISR.* PhD thesis, Northwestern U., 1986.

[94] H. Stenzel, “Total Cross Section and Elastic Scattering from TEVATRON to LHC,” in *International Conference on the Structure and Interactions of the Photon and 18th International Workshop on Photon-Photon Collisions and International Workshop on High Energy Photon Linear Colliders*, pp. 308–315, July 2009.

[95] A. Jeff, “Ghosts and Satellites Measured With the LHC LDM,” in *LHC Lumi Days 2012*, 2012.

[96] H. Burkhardt, “Private communication.”

[97] S. Jakobsen, “ALFA Trigger Situation.” `https://indico.cern.ch/event/129121/contributions/1346898/attachments/87747/125687/ALFA_triggers_27-07-2011_.pdf`. Accessed: 2020-09-12.

[98] H. Garcia Morales *et al.*, “Special Collimation System Configuration for the LHC High-Beta Runs,” in *9th International Particle Accelerator Conference*, p. MOPML012, 2018.

[99] SixTrack, “SixTrack | LHC@home.” `http://lhcathome.web.cern.ch/projects/sixtrack`. Accessed: 2020-02-10.

[100] H. G. Morales *et al.*, “Recent Progress on the Collimation System for Special Physics Run at injection.” `https://indico.cern.ch/event/752722/contributions/3118631/attachments/1709469/2755426/slides_ColWG_high-beta.pdf`. Accessed: 2020-09-23.

[101] S. Jakobsen, “Test of background reduction for alfa.” `https://indico.cern.ch/event/680846/contributions/2791920/attachments/1558811/2452792/ALFA_collimation_feedback_version4.pdf`, Nov 2017.

[102] E. Bravin, G. Burtin, A. Fisher, A. Guerrero, A. Jeff, T. Lefevre, A. Goldblatt, and F. Roncarolo, “First Beam Measurements with the LHC Synchrotron Light Monitors,” p. 3 p, May 2010.

[103] K.-H. Hiller, “ALFA 900 GeV review.” `https://indico.cern.ch/event/787251/contributions/3290577/attachments/1783206/2902066/ALFA_900GeV_program_V3.pdf`. Accessed: 2020-09-21.

[104] B. Dziedzic and K. Korcyl, “The ALFA Trigger Simulator,” *Acta Phys. Pol. B*, vol. 46, pp. 1271–1277, 2015.

[105] B. Dziedzic and K. Korcyl, “Arch Linux ARM w kontroli systemu wbudowanego na przykładzie S3T dla detektora ATLAS/ALFA,” *Monografia / Politechnika Krakowska im. Tadeusza Kościuszki. Podstawowe Nauki Techniczne*, 2016.

[106] AVNET Inc., “Zedboard (zynq evaluation and development) hardware user’s guide.” `http://zedboard.org/sites/default/files/documentations/ZedBoard_HW_UG_v2_2.pdf`. Accessed: 2021-01-15.

[107] M. Lisowska, “ALFA_LED – Remote Control Boards – Switch on/off and Reset.” `https://indico.cern.ch/event/612336/contributions/2497689/attachments/1423890/2183745/ALFA_LED_Lisowska_17Mar8.pdf`. Accessed: 2021-01-15.

[108] Xilinx Inc., “Zynq-7000 SoC Data Sheet Overview.” `https://www.xilinx.com/support/documentation/data_sheets/ds190-Zynq-7000-Overview.pdf`, July 2018.

[109] ARCH Linux ARM community, “ARCH Linux ARM.” `https://archlinuxarm.org/`. Accessed: 2020-01-10.

[110] R. B. et. all, “ROOT – An Object Oriented Data Analysis Framework, Release v6.18/04.” `https://root.cern/`. Accessed: 2020-05-03.

[111] E. F. Eisenhandler and S. Willocq, “ATLAS Style Guide,” tech. rep., CERN, Geneva, June 2008.

[112] Qt Group, “Cross-Platform Software Development for Embedded and Desktop.” `https://www.qt.io/`. Accessed: 2021-05-03.

[113] A. Almeghari, *Radiation Resistance of the ATLAS-ALFA Electronics and Trigger Efficiency Analysis at* $\sqrt{s} = 13 TeV$ *and* $\beta^* = 2.5$ *km.* PhD thesis, The Islamic University–Gaza, Mau 2018.